Universidad de Valladolid

INSTITUTO DE OFTALMOBIOLOGÍA APLICADA

TESIS DOCTORAL:

ANTERIOR SEGMENT TOPOGRAPHY AND ABERRATIONS FOR CLINICAL APPLICATIONS

Presentada por PABLO PÉREZ MERINO
para optar al grado de doctor por la
Universidad de Valladolid

Dirigida por:

SUSANA MARCOS CELESTINO

Universidad de Valladolid

Impreso 2T

AUTORIZACIÓN DEL DIRECTOR DE TESIS

(Art. 2.1. c de la Normativa para la presentación y defensa de la Tesis Doctoral en la Uva)

Dña. SUSANA MARCOS CELESTINO con D.N.I. nº 07954600G, Profesora de Investigación en el Instituto de Óptica "Daza de Valdés" del Consejo Superior de Investigaciones Científicas (CSIC), susana@io.cfmac.csic.es, como Directora de la Tesis Doctoral titulada "Anterior segment topography and aberrations for clinical applications", presentada por D. PABLO PEREZ MERINO, alumno del programa de CIENCIAS DE LA VISIÓN impartido por el departamento INSTITUTO UNIVERSITARIO DE OFTALMOBIOLOGÍA APLICADA, FACULTAD DE MEDICINA, autoriza la presentación de la misma, considerando que la tesis presenta resultados originales y novedosos para la comprensión de las aplicaciones clínicas de las patologías del segmento anterior más frecuentes del ojo, utilizando tecnologías estado-del-arte (Trazado de Rayos Laser y Tomografía de Coherencia Óptica), con impacto en la comunidad científica, clínica e industrial, a través de publicaciones en revistas internacionales de alto impacto y comunicaciones en congresos nacionales e internacionales.

Valladolid, 16 de septiembre de 2015

El Director de la Tesis,

Fdo.: Susana Marcos Celestino

SRA. PRESIDENTA DE LA COMISIÓN DE DOCTORADO

a mis padres, Pablo y Ramoni

a Ana

Table of Contents

ANTERIOR SEGMENT TOPOGRAPHY and ABERRATIONS for CLINICAL APPLICATIONS

Chapter I. INTRODUCTION

Key words

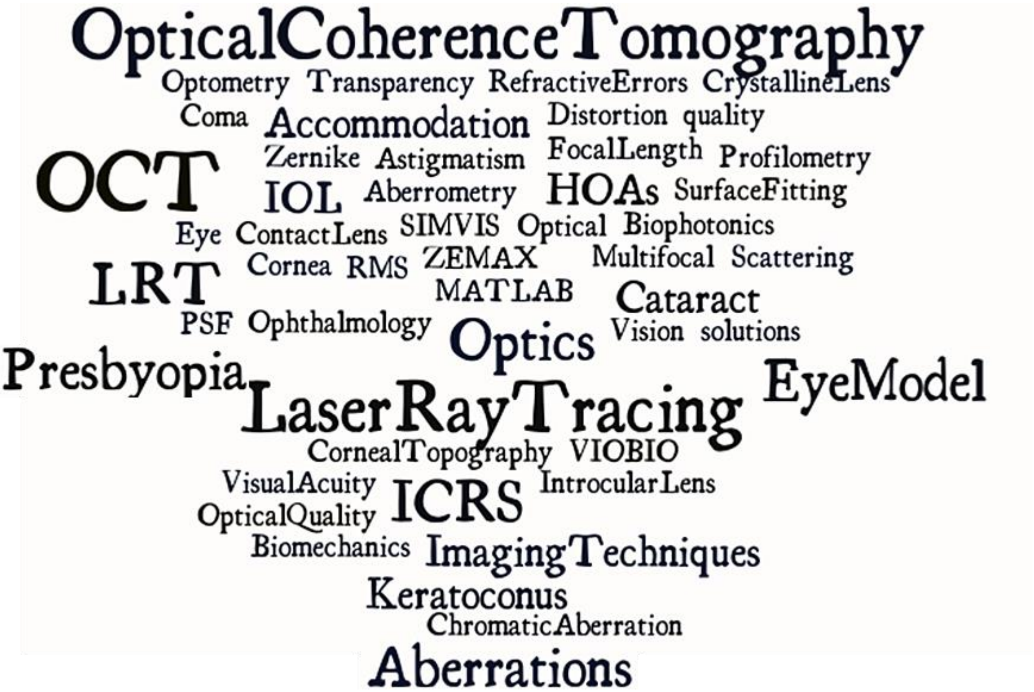
OpticalCoherenceTomography
Optometry Transparency RefractiveErrors CrystallineLens
Coma Accommodation Distortion quality
OCT
Zernike Astigmatism FocalLength Profilometry
IOL Aberrometry HOAs SurfaceFitting
Eye ContactLens SIMVIS Optical Biophotonics
LRT
Cornea RMS ZEMAX Multifocal Scattering
MATLAB Cataract
PSF Ophthalmology Optics Vision solutions
Presbyopia
LaserRayTracing
EyeModel
CornealTopography VIOBIO
VisualAcuity ICRS IntrocularLens
OpticalQuality
Biomechanics ImagingTechniques
Keratoconus
ChromaticAberration
Aberrations

List of commonly used abbreviations and variables

Abbreviatons

Imaging Techniques

OCT = Optical Coherence Tomography
TD-OCT = Time-Domain OCT
SD-OCT = Spectral-Domain OCT
SS-OCT = Swept-Source OCT
LRT = Laser Ray Tracing
H-S = Hartmann-Shack
UBM = Ultrasound biomicroscopy
MRI = Magnetic Resonance Imaging
PCI = Partial Coherence Interferometry

Optical Terms

IR = Infrared
CCD = Charge Couple Device
LED = Light Emitting Diode
SLD = Superluminiscent Diode
DLP = Digital-Light-Processing
NA = Numerical Aperture
BS = Beam Splitter
FC = Fiber Coupler
OI = Optical Isolator
PC = Polarization Controller
M = Mirror
L = Lens
NDF = Neutral Density Filter
SNR = Signal-to-Noise Ratio
HOAs = High-Order Aberrations
LCA = Longitudinal Chromatic Aberration
TCA = Transverse Chromatic Aberration
GRIN = Gradient Index
DoF = Depth-of-Focus

General

2-D = Two-dimensions
3-D = Three-dimensions
i.e. = *id est*, this is
e.g. = *exempli gratia*, for example
vs = *versus*, compared to
VA = Visual Acuity
BCVA = Best-Corrected VA
D = Diopters
N = Nasal
T = Temporal
S = Superior
I = Inferior
H = Horizontal
V = Vertical
OFZ = Organelle-Free Zone (crystalline lens)
AL = Axial Length
ACD = Anterior Chamber Depth
LT = Lens Thickness

Clinical treatments

IOL = Intraocular Lens
A-IOL = Accommodating-IOL
ICRS = Intracorneal ring segment
CL = Contact Lens
PPMA = Polymethyl-methacrilate

Wavefront Analysis

FFT = Fast Fourier Transform
FWHM = full-width-half-minimum
RMS = Root Mean Square
PSF = Point Spread Function
SR = Strehl Ratio
MTF = Modulation Transfer Function
CSF = Contrast Sensitivity Function
OTF = Optical Transfer Function
VSOTF = Visual Strehl OTF

Variables

Coefficients and indices

$n, m, j, \ldots$ = index names
N, M = maximum index/number

General Optical Variables

λ = Wavelength
κ = Wavenumber (propagation constant)
ω = angular frequency
υ = frequency
R, r = Radius
C = Curvature (=1/R)
K = Conic constant
p = p-value, asphericity
Q = Q-value, asphericity
$W(x,y)$ = Wave aberration in Cartesian coordinates
Z_n^m = Zernike polynomial in Cartesian coordinates
c_n^m = Zernike coefficient (order, n; frequency, m).
φ = phase (wavefront aberration)
A = Amplitude
I = Intensity
E = Electric field
d = Thickness of optical medium
f = Focal length
n = refractive index
DoF = Depth-of-focus

Units

s = seconds
mm = milimeters
μm = microns
nm = nanometers
deg = degrees

Coordinates

o = origin
X, Y, Z = Cartesian coordinates
ρ, θ = Polar coordinates

Motivation

The *eye* is one of the most elegantly built organs of the human body playing a triple role in gathering information of the external world, coding it and relying to the brain. It has a relatively simple optical design with incredible functionality; only two lenses (*cornea* and *crystalline lens*) set the physical rules for image-forming onto the retina. However, the eye is far from a perfect optical system since imperfections in the cornea and in the crystalline lens shape induce focusing errors and image degradation, known as *optical aberrations.*

State-of-the-art *aberrometry* provided a detailed analysis of the optical aberrations of the whole eye in normal subjects and in certain ocular conditions such as accommodation, aging, corneal degeneration and cataract surgery. Whereas different aberrometers allow measuring the optics of the eye, the relative contribution of the corneal and crystalline lens surfaces themselves to the optical quality of the eye is still poorly understood.

The aberrations of the cornea can be estimated from three-dimensional (3-D) measurements of the corneal shape. However, due to limitations of the commercial available anterior segment techniques (i.e., low resolution, high acquisition time, limited depth range and inherent distortion of the imaging systems), knowledge of *in vivo* geometrical parameters of the crystalline lens is only limited to 2-D measurements or axial distances. Hence, *optical coherence tomography (OCT)* presents several advantages over other imaging techniques (higher speed, resolution and depth range) for a 3-D accurate measurement of the anterior segment geometry.

Understanding the link between optical aberrations and anterior segment geometry is key for comprehending how the eye works and for modeling the optics of an individual eye. The eye has many innate adaptations that minimize optical aberrations. In most normal young eyes, the magnitude of aberrations of the cornea is larger than for the whole eye, indicating a significant role of the crystalline lens in compensating corneal aberrations. But, due to geometrical and structural changes this ocular compensation gets disturbed in different anterior segment conditions, such as *keratoconus*, *presbyopia* and *cataract*. While keratoconus degrades the corneal shape progressively and consequently vision in the adolescence; presbyopia and cataract are conditions related to aging that affect the crystalline lens and degrade vision.

With the advance in imaging techniques and new designs and materials, different solutions appeared for improving the visual quality, proposing *intracorneal ring segments (ICRS)* in keratoconus and *accommodative intraocular lens (A-IOL)* in presbyopia and cataract. However, although these approaches are currently used in the clinical practice, the mechanism of action and the benefit of these solutions are not yet fully understood. Thus, the development of *customized solutions* and eye models using individual geometrical data, the final 3-D location of the proposed solution (ICRS and IOL) and encompassing individual ocular aberrations address a currently unmet need.

In this thesis we analyzed the *geometrical properties* of the anterior segment of the eye and its link to the *optical quality* of the whole eye in different clinical situations. We use novel and validated methodology, the *laser ray tracing technique (LRT)*, for measuring the optical quality of the whole eye, and the distortion-corrected *OCT*, for analyzing accurately and three-dimensionally the geometrical properties of the anterior segment of the eye in different clinical applications. We studied longitudinally the geometrical and optical properties of keratoconus before and after ICRS surgery, and we quantified in 3-D the changes in ICRS position inside the cornea with time and the effect of ICRS on the geometry and optics of the cornea. Also, we evaluated *in vivo* the topographical changes of the crystalline lens surface with accommodation. We analyzed the 3-D location and the optical impact of accommodative IOLs after cataract surgery. And, finally, we analyzed *in vivo* the longitudinal chromatic aberration in pseudophakic patients.

Chapter I. ***INTRODUCTION***

In this introductory chapter we present a description of the optics of the eye, with special focus on the cornea and the crystalline lens. The refractive errors and ocular aberrations will be pointed out; and an overview of quantitative anterior segment imaging systems and the ocular aberrometry techniques will be described. We introduce some common pathologies and conditions in the anterior segment of the eye and their treatment. We also present the open questions, the goals and the hypothesis addressed in this thesis.

1.1. The optics of the human eye

> *"to be sought in the structure and functioning of the eye itself..."*
>
> *J. Kepler. "Ad Vitellionem paralipomena", 1604[Kepler, 1604]*

Human vision is a complex process that involves numerous components of the eye and the human brain. Briefly, in the eye, light from the visible spectrum is directed and refracted by two optical and transparent elements, the cornea and the crystalline lens, which project the images of the outside world on the retina. In the retina, cones and rods samples the light distribution, and then the light is absorbed and converted into chemical and electrical signals (visual signals) by the retinal layers. These visual signals are transmitted by the optic nerve into the visual cortex for further processing and final perception of the visual information.

1.1.1. Historical introduction

From ancient time, Assyrian, Greek and Roman philosophers and physicists have tried to explain the visual process. Aristotle was the first who tried to explain the optical defects of vision questioning with his coetaneous why vision differs among individuals. In the 11th century, Alhazen [Ibn al-Haytham, 1028-1038] adopted Aristotle´s theory of visual optics, Ptolemy´s theory of optics and Galen´s ideas on visual anatomy and conducted several experiments involving a dark room with a hole in it, proposing finally how the eye works by comparing the eye to a "dark chamber". Alhazen established the stage for subsequent developments in physiological optics for future generations. However, before the 17th century the mechanism of vision remained largerly unexplained, with first modern theories appearing at Galileo´s time with the development of his telescope. In 1604, Johannes Kepler [Kepler, 1604] proposed a full ray tracing model of the eye and described the use of spherical lenses to correct myopic and hyperopic refractive errors. In 1619, Christoph Scheiner experimentally verified Kepler´s theory and was the first to investigate the accommodation eye at different distances. And, in 1623, Benito Daza de Valdés described a measuring unit for grading lenses in his book (*Uso de los anteojos*); the unit was based on a Spanish medieval linear unit (the *vara*), the vara (836 mm, in the metric scale) was equal to 1.1967 diopters. Daza de Valdés described precise measurements and prescriptions for myopia, hyperopia and, also, presbyopia, being pioneer in quantifying the needed correction of refractive errors. In the centuries that followed, different major scientists developed the understanding in physiological optics. Thomas Young studied astigmatism, aberrations and was the first to recognize loss of accommodation with age in his treatise *"On the mechanism of the eye"*.

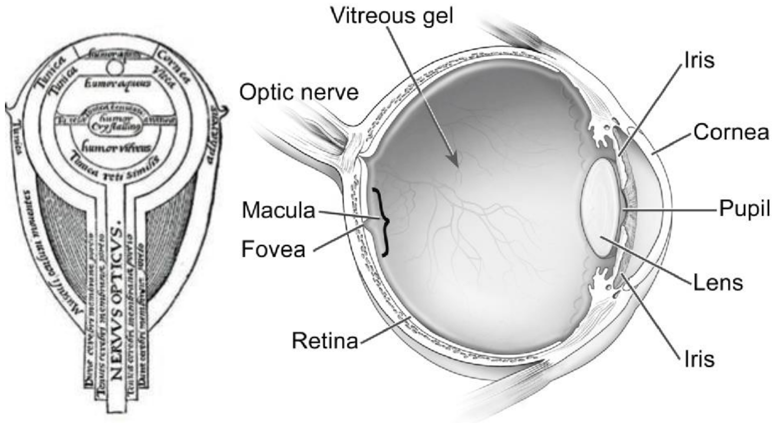

Figure 1.1. Left: The eye in *Opticae thesaurus Alhazeni Arabis (1572)*; Wellcome Library, London. Right: Schema of the human eye adapted from an image of the National Eye Institute Catalog (number NEA09).

1.1.2. Cornea

The majority of the refracting power of the eye is provided by the cornea, the transparent and curved “window” at the front of the eye [Beems & Van Best, 1990; Benedek, 1971; Hart & Farrell, 1968; Jakus, 1962; Jester, 2008; Maurice, 1957]. It fulfills a dual role, acting as both the primary refractive element and as a physical barrier to maintain ocular integrity; the cornea is a viscoelastic tissue that responds to the presence of external and internal forces [Dupps Jr & Wilson, 2006; Elsheikh et al., 2008; Kling et al., 2009; Meek & Knupp, 2015; Meek & Newton, 1999; Roberts, 2000].

Histologically, the cornea is an inhomogeneus cellular and fibrillar structure composed of five layers: epithelium, Bowman´s layer, stroma, Descemet´s membrane and endothelium. The cornea mainly contains water (78%), regularly arranged collagen fibrils, proteoglycans and keratocytes. Each corneal layer has its own refractive index, but since the stroma is by far the thickest layer, its refractive index dominates (1.376).

The *epithelium* protects the rest of the cornea providing a barrier against water, larger molecules and toxic substances. It consists approximately of six layers of cells, and only the innermost layer of these cells is able to show cell division. Once the cells are formed, they move gradually towards the surface as the superficial cells are shed. *Bowman´s layer* is 8-14 µm thick, and consist mainly of randomly arranged collagen fibrils. The bulk of the cornea is formed by the *stroma*, which in the human adult is approximately 450-550 µm thick centrally (approximately 90% of corneal thickness) and consists predominantly of flattened and stacked collagenous lamellae (200-250 layers). The stroma is considerably thicker in the periphery (550-750 µm). This arrangement maintains an ordered transparent structure while also enhances mechanical strength. *Descemet´s membrane* is the basement of the endothelial cells. The *endothelium* consists of a single layer of cells, which are hexagonal and fit together like a honeycomb. The endothelium regulates the fluid balance of the cornea in order to maintain the stroma hydration (at about 78%) and thus retain transparency [Atchison & Smith, 2000; Knupp et al., 2009; Maurice, 1957; Meek & Knupp, 2015; Morishige et al., 2007].

Stromal collagen assembles to form long fibrils that in the human cornea show a uniform diameter of approximately 31-34 nm, and are separated by 20-50 nm. Collagen fibers are approximately 1-2 µm thick, 10-200 µm wide and are thought to traverse the entire cornea from limbus to limbus [Polack, 1961]. The fibrils within a layer run parallel to each other, they are inclined at large angles to fibrils in adjacent lamellae and are uniform in size and spacing. Collagen fibrils are generally organized into independent bundles or fibers, lamellae. The regular arrangement of collagen fibrils in each stromal lamellae is the main responsible for the transparency of the cornea and the alternating orientation provides its shape and mechanical stability [Boote et al., 2005; Jester, 2008; Knupp et al., 2009; Meek & Knupp, 2015; Morishige et al., 2011].

Due to the corneal shape and the difference of refractive index between the cornea (1.37) and the air (1.0), the cornea contributes about two-thirds of the refractive power for the relaxed eye, approximately 42 D, with anterior and posterior paraxial powers of about +48 D and -6 D, respectively. The adult human cornea is smaller in the vertical diameter (9-11 mm) than in the horizontal diameter (11-12 mm). Both anterior and posterior corneal surfaces have a regular and stable shape in normal population, presenting convex and aspheric surfaces (flattening away from the corneal apex) [Atchison & Smith, 2000]. Corneal shape varies with age and across individuals [Allison & Brennan, 1997; Dubbelman & Heijde, 2001; Guirao & Artal, 1999a; Navarro et al., 2013].

Because of its accessibility, the anterior corneal surface has been widely studied. In a normal population, the central radius (3-mm optical zone) is around 7.5 and 8.0 mm. Although the posterior corneal surface is less accessible and represents a lower contribution to the ocular optics (due to a smaller difference between corneal and aqueous humor), its contribution is not negligible, as has been shown to compensate part of the irregularities of the anterior cornea, in particular astigmatism (31% [Dubbelman et al., 2006b]), spherical aberration (from 10% compensation to 26% addition [Sicam et al., 2006]) and vertical coma (from 3% [Dubbelman et al., 2007b] to 20% [Barbero et al., 2002b] compensation). The posterior corneal surface overall has a shorter radius of curvature, with a central radius between 5.9 and 6.7 mm. Neither the anterior nor the posterior surfaces are perfectly spherical due to the presence of asphericity and toricity (since the corneal surfaces usually presents different radius at vertical and horizontal meridians which produces astigmatism). Generally, in young eyes, the vertical meridian is steeper than the horizontal meridian, although this tendency reverses with age [Allison & Brennan, 1997; Baldwin & Mills, 1981; Dubbelman & Heijde, 2001; Lyle, 1971; Navarro et al., 2013].

It is commonly accepted that we can consider the equation of a conicoid for representing the corneal shape [Perez-Escudero et al., 2010]. The equation 1 provides the analytical expression of a conicoid, where ρ are the polar coordinates ($\rho = X^2+Y^2$), z is the axial coordinate, R is the radius of the surface and Q is the conic constant ($Q<-1$ hyperboloid, $Q=-1$ paraboloid, $-1<Q<0$ ellipsoid (Z axis is the major axis), $Q=0$ sphere, $Q>0$ ellipsoid (X-Y plane is the major axis).

Equation 1.1: $$\rho - 2zR + (1 + Q)z^2 = 0$$

The average anterior corneal radius R and asphericity Q are 7.7 mm and -0.25 in a normal population, respectively, this shape corresponds to a prolate ellipsoid, i.e., the cornea flattens towards the periphery. The average posterior corneal radius R and asphericity Q are 6.4 mm and 0.3 in a normal population, respectively.

Corneal thickness has been widely studied, in the central cornea thickness is on average 523±39 µm, and it thickens towards the periphery (660±76 µm) [Atchison & Smith, 2000].

1.1.3. Crystalline lens

The crystalline lens is the responsible for the remaining refraction of the eye, i.e. approximately one-third of the refractive power (on average, 14 D), and it has the capability in young subjects of focusing objects at different distances, a mechanism known as *accommodation* [Charman, 2009; Glasser & Campbell, 1998b].

Histologically, the crystalline lens is composed by the lens capsule, the lens epithelium and the lens fibers. The lens consists largely of lens fiber cells forming the nucleus and cortex. The crystalline lens is covered by an external capsule, located between the iris and the vitreous humor and attached to the cilliary processes by thin filamentous zonules. The crystalline lens is transparent due to its avascularity, lack of organelles, regular organization of the cells, fibers and proteins and its narrow inter-fiber spaces [Atchison & Smith, 2000; Bassnett et al., 2011; Beebe, 2003; Benedek, 1971; Mathias et al., 1997; Trokel, 1962].

The lens *capsule* is a multicellular organ surrounded by a basal lamina with an anterior layer of cuboidal epithelium covering concentric layers of fibers. The lens capsule consists mostly of a well-organized matrix of collagen IV, enactin and laminin. The capsule is produced continuously during life by the lens epithelium, which growths in a lamellar fashion along the lens. The anterior lens capsule is thicker than the posterior one. It is elastic in nature and prevents high molecular-weight substances from entering the lens [Beebe, 2003].

The lens *epithelium* is a single layer of cuboidal cells located between the lens fibers and the lens capsule on the anterior half of the lens. The epithelial cells contain different organelles for both aerobic and anaerobic metabolic activity. At the cellular level, there is limited light-scattering because of the organized distribution of the cellular organelles, which are relatively sparse in the central epithelium.

At the equator, away from the light path, epithelial cells undergo mitotic division and differentiate into *lens fibers* [Beebe, 2003]. Newly laid fibers crowd and compact previous fibers, thus the oldest are the most central (nucleus) and are the outermost fibers the most recently formed fibers (constituting the lens cortex) [Beebe, 2003; Wride, 2011]. High concentrations of crystallin proteins in the lens fibres contribute to lens transparency [Michael & Bron, 2011].

The crystalline lens has a higher refractive index than its surroundings, resulting from the high concentration of α- β- and δ-crystallins in the lens fiber cytoplasm. The crystalline lens shows a *gradient-index (GRIN)* distribution. The nucleus of the lens shows the highest refractive index, whereas the more peripheral fibers from the cortex present the smallest refractive index in the lens [Atchison & Smith, 1995; de Castro et al., 2011; Goncharov & Dainty, 2007; Siedlecki et al., 2012; Von Helmholtz, 1909]. Furthermore, the distinctive concentration of different proteins produces changes in the refractive index across layers [Beebe, 2003]. Recently, de Castro et al. [de Castro et al., 2010] reported index variation in the nucleus with values ranging from 1.434 to 1.413 and in the lens cortex with values ranging from 1.386 to 1.376, showing a monotonic decrease in young crystalline lens and a plateau-like functioning in older crystalline lens. To date, most GRIN measurements (and all through optical measurements) have been performed *ex vivo* [Birkenfeld et al., 2013; de Castro et al., 2011; Jones et al., 2007], so for *in vivo* crystalline lens studies an equivalent refractive index (Uhlhorn´s formulae) is commonly used [Uhlhorn et al., 2008].

Due to its inaccessibility, the *in vivo* geometrical parameters of the crystalline lens are limited in the literature. Rosales et al. [Rosales et al., 2006; Rosales & Marcos, 2009] using distortion-corrected Scheimpflug camera reported averaged values of the crystalline lens radius for the anterior surface (11.1±1.1 mm) and for the posterior surface (6.1±0.5 mm). Dubbelman et al. (Dubbelman & Heijde, 2001) described age-related expressions for the anterior and posterior crystalline lens surfaces respectively (R=12.9-0.057*age, anterior; R=6.2-0.012*age, posterior), and reported an average conic constant value of -4 and -3 for the anterior and posterior lens, respectively. Average lens thickness values range between 3.06 mm to 4.19 mm at 30 years old of age with a mean increase of 24 µm/year [Dubbelman & Heijde, 2001]. Recently, Ortiz et al. [Ortiz et al., 2012b] quantified the crystalline lens geometrical properties with distortion-corrected Optical Coherence Tomography (OCT) and reported the first *in vivo* report of 3-D surface elevation maps of the anterior and posterior lens surfaces. Ortiz et al. [Ortiz et al., 2012b] described a perpendicular orientation of the astigmatism *vs* the posterior lens surface in young subjects.

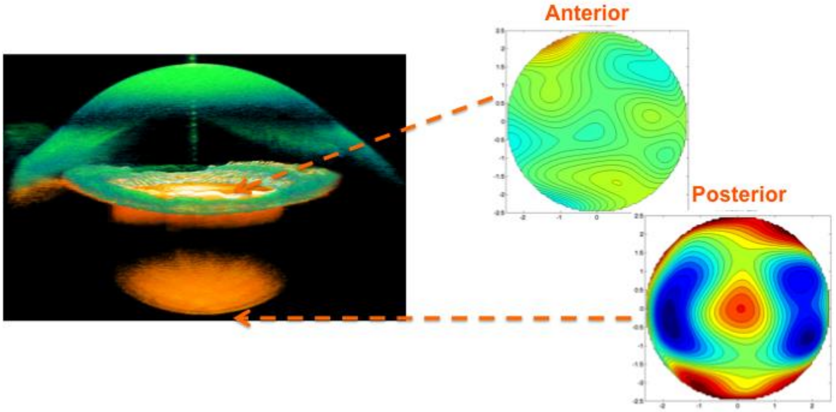

Figure 1.2. 3-D *in vivo* anterior segment volume and the corresponding crystalline lens elevation maps (OCT-distorsion corrected, [Ortiz et al., 2012b]).

Internal astigmatism may be produced by the toricity of the crystalline lens surfaces [Dunne et al., 1996; Keller et al., 1996] or by a tilt of the lens [Rosales & Marcos, 2006]. Aberration analysis between different ocular elements has shown compensation in corneal astigmatism and high-order aberrations by the crystalline lens and a disruption in this balance as we age [Artal & Guirao, 1998; Artal et al., 2001b; Kelly et al., 2004a; Marcos et al., 2008; Mclellan et al., 2001; Tabernero et al., 2007]. Javal postulated a relationship between corneal and refractive astigmatism and proposed a compensation of -0.5 D of against-the-rule astigmatism by the internal optics. Elawad, in his PhD thesis [Elawad, 1995], and Dunne et al. [Dunne et al., 1996] measured the contribution of the different ocular components to residual astigmatism in human eyes, and found that whilst the astigmatic contributions of the posterior corneal and posterior lens surfaces were found to be predominantly inverse (with the steeper meridian in the horizontal axis), direct astigmatism came from the anterior lens surface, although they recognized that the techniques used in their studies were subject to cumulative errors. Artal et al. [Artal et al., 2001a] and Kelly et al. [Kelly et al., 2004a] found significant negative correlation for corneal horizontal/vertical astigmatism, lateral coma and spherical aberration and the internal optics, indicating a fine-tuned compensation process between the cornea and the lens in the young unaccommodated state. The GRIN has been shown experimentally to play a major role in the negative sign of the spherical aberration of the young crystalline lens [Birkenfeld et al., 2014; de Castro et al., 2013; Smith & Atchison, 2001].

Accommodation, presbyopia and cataract will be treated in section 1.8.

1.1.4. Pupil

The diameter of the incoming beam of light into the eye is controlled by the iris, which contracts and dilates according to the surrounding light and it acts as the pupil. From geometrical considerations, the quantity of light from any object reaching the retina is proportional to the area of the pupil [Atchison & Smith, 2000].

1.1.5. Axes of the eye

The eye is not a centered and rotationally symmetric optical system. The curvature centers of the ocular surfaces as well as the fovea do not lie in a common axis. The fovea is located 1-2 mm temporalward from the intersection of the optical axis with the retina. Thus, in connection with the schematic eye, several other axes were defined: *optical axis* (line joining center of curvature of the corneal and lens surfaces), *pupillary axis* (line joining center of pupil and centers of curvature of anterior corneal surface), *primary line of sight* (line joining fixation point and center of the entrance pupil) and *visual axis* (line joining fixation point and nodal point). The line of sight is the reference that will be used for the analysis of ocular aberrations. And thus, *angle kappa* is the angular distance (in the object space) between the line of sight and the pupillary axis [Artal & Tabernero, 2010; Atchison & Smith, 2000; Berrio et al., 2010].

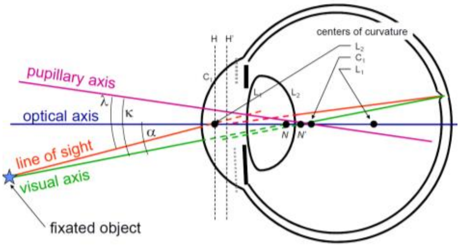

Figure 1.3. Illustration of the axis of the eye.

1.2. Refractive errors

> *"Los grados de los antojos, son vnas porciones o partes de esferas, q se van disminuyendo, desde vna esfera de dos varas de diámetro, hasta otra tan pequeña, como el diámetro que tiene la redódez del ojo; y los grados van creciendo según se va disminuyendo, ó achicando estas esferas y sus diámetros: cuyas por porciones cóncavas o convexas, se van pasando a las formas donde se labran los antojos, de tal manera que la diferencia de diámetro que tiene la mayor esfera á la menor, se divide en treynta partes, a las quales llamamos grados, començando su numero desde la porción de la mayor esfera, y feneciendo el numero treinta, en la porción de la menor que es la del ojo: Y estos treinta grados, son bastantes para medir y ajustar qualquiera cortedad de vista por mucha q sea porque todas las vistas que comiençan a usar antojos…"*
>
> *B. Daza de Valdés. "Uso de los antojos", 1623 [Daza de Valdés, 1623]*

Refractive errors are the most common cause of reduced vision and normally are easily corrected by adding lenses in front of the eye. Refractive errors can be defined from an optical point of view as the refractive condition in which best focus for distant objects is not located on the retina of the relaxed eye and refractive errors are generally divided into defocus and astigmatism:

There are two types of defocus: *myopia* and *hyperopia*. Myopia, or nearsightedness, is present when the focus of the eye falls in front of the retina causing a spherically defocused image. By contrast, hyperopic eyes have difficulties to resolve close objects, because the image falls behind the retina causing also a spherically defocused image and distant objects can only be focused with accommodation. Defocus is sometimes accompanied by astigmatism.

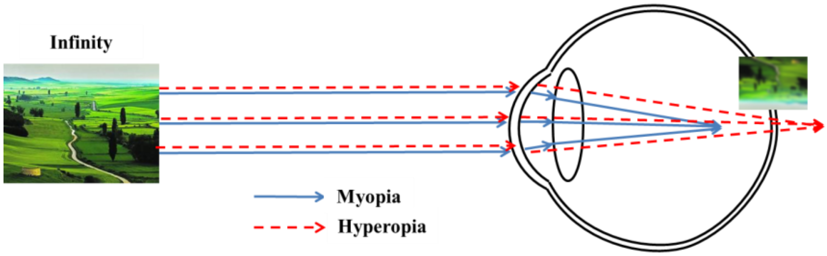

Figure 1.4. Illustration of myopia and hyperopia.

Astigmatism is a symptom of asymmetry in the optics of the eye, where the refractive power in one meridian is different in the power in the perpendicular meridian (this will result in two lines of foci, and therefore an orientation dependent blur of the image).

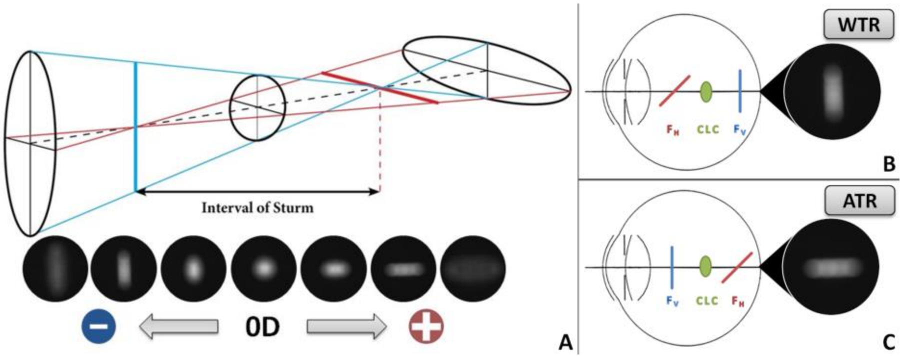

Figure 1.5. (A) Series of "retinal" images of a circular spot captured in the CCD camera at the focal plane of a lens acting as an artificial eye (Z_2^2 = 0.92 µm, 6-mm pupil diameter). (B) Illustration of the astigmatic foci in a myopic with the rule astigmatism. (C) Illustration of the astigmatic foci in a myopic against the rule astigmatism [Marcos et al., 2015].

1.3. Optical aberrations

> *"My eye, in a state of relaxation, collects to a focus on the retina, those rays diverge vertically from an object at the distance of ten inches from the cornea, and the rays which diverge horizontally from an object at seven inches distance…"*
>
> *"When I look at a minute lucid point, such as the image of a candle in a small concave speculum, it appears as a radiated star, as a cross, or as an unequal line, and never as a perfect point…"*
>
> *T. Young. "On the mechanism of the eye", 1801 [Young, 1801]*

The image-forming properties of any optical system can be described in terms of wave aberration. Light can be considered as a series of waves coming from a source. In aberrations-free optical systems all the parallel rays will intersect the retina at the same point, or equivalently, all the imaging wavefronts will be spherical and centered in the image point. However, an imperfect lens will impose phase distortions on the plane waves, there is no longer a point focus and the different rays will intersect the image plane at different points (the wavefronts will no longer be spherical). The difference between the distorted waves and the ideal waves is the wavefront aberration, representing the distortions of the wavefront (surface containing points with the same phase and orthogonal to the propagation axis) in the pupil plane as it goes through the optical system. Aberrations can be divided into chromatic and monochromatic aberrations [Born & Wolf, 1993; Campbell & Gubisch, 1966].

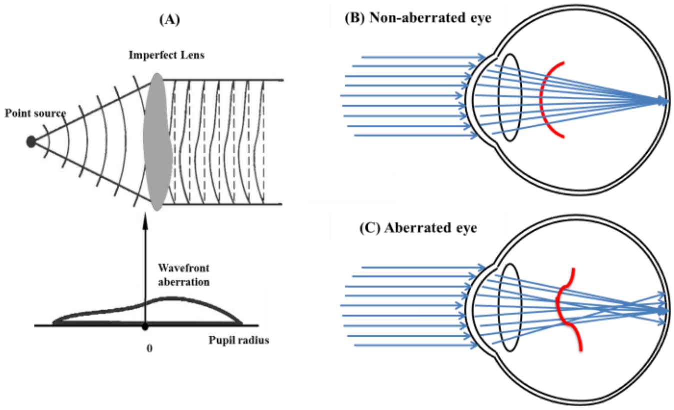

Figure 1.6. (A) Illustration of wavefront aberrations. (B) Schematic representation of a non-aberrated eye. (C) Schematic representation of an aberrated eye.

Chromatic aberrations are a consequence of the dispersion (variation of refractive index with wavelength) of the refractive media of an optical system. The average index of refraction in the eye varies from 1.3404 for blue (450 nm) to 1.3302 for red (700 nm). This means that the eye is about 1.5 D more myopic in blue light than in red.

There are two types of chromatic aberrations: *longitudinal* and *transversal*. Longitudinal chromatic aberration (LCA) is produced because the different wavelengths are focused at different image planes, and can be quantified as the variation in power with wavelength. Whereas transverse chromatic aberration (TCA) is produced when obliquely incident rays are focused at different transverse positions within the image plane (being critical the object location in the visual field and the pupil position within the eye). LCA affects image contrast through the mechanism of defocus and TCA affects image phase through the mechanism of displacement [Bedford & Wyszecki, 1957; Bradley, 1992; Howarth, 1984; Howarth & Bradley, 1986; Marcos et al., 1999; Marcos et al., 2001; Simonet & Campbell, 1990].

LCA has been measured by using psychophysical techniques (e.g., Badal optometer [Bobier & Sivak, 1978a; Morrell et al., 1991], Spatially Resolved Refractometry [Marcos et al., 1999]) and objective reflectometric techniques (e.g. Hartmann-Shack [Vinas et al., 2015] and Laser Ray Tracing [Llorente et al., 2003]).

Monochromatic aberrations are those present when only one wavelength is considered, and arise from the geometry, irregularities, tilts and decentrations of the components of the optical system (cornea and crystalline lens). The magnitude of the monochromatic aberrations in the eye depends on a variety of factors such as accommodation, pupil size, aging, refractive state and retinal eccentricity [Applegate et al., 2000; Guirao & Artal, 1999b; Howland & Howland, 1977; Marcos et al., 2001; Mclellan et al., 2001; Navarro et al., 1998; Plainis & Pallikaris, 2006; Porter et al., 2001; Thibos & Hong, 1999].

Interestingly, in the young eye the magnitude of aberrations is larger in the cornea and the internal optics separatley than in the complete eye as a result of compensatory effects in horizontal/vertical astigmatism, spherical aberration and lateral coma [Artal et al., 2001b; Kelly et al., 2004a].

The wave aberration of a general optical system can be described mathematically by a polynomial series. Zernike polynomial expansion has become the standard for representing wave aberration data because they form an orthogonal set over a circle of unit radius, and aberrations are usually referred to circular pupils [Mahajan, 1994; Malacara et al., 1990].

The Zernike polynomials (Z_n^m, corresponding to the radial order *n* and the meridional frequency *m*) were described by Frits Zernike in 1934 [Zernike, 1934]. An interesting feature of the Zernike polynomials is that some terms are directly related to commonly known ocular aberrations [Thibos et al., 2004a]. For example, structural abnormalities of the eye, such as myopia, hyperopia and astigmatism, appear in the 2nd order of this expansion. Further, Zernike terms represent higher-order aberrations such as *spherical* aberration (arising from the asphericity of the optical surfaces) and *coma* (mainly associated to local irregularities, tilt and decentration of the surfaces of the optical system).

A wave aberration, *W(x,y)*, can be described as a summation of Zernike polynomial functions weighted by the Zernike coefficients, which indicate the magnitude of each particular aberration present:

Equation 1.2: $$W(x,y) = \sum_{n,m} c_n^m Z_n^m(x,y)$$

The deviation from a monochromatic perfect spherical wavefront can be denoted by *W(x,y)*, where *W(x,y)* is the wave aberration expressed in Cartesian coordinates, $Z_n^m(x,y)$ the Zernike polynomial expressed in Cartesian coordinates, and c_n^m are the corresponding Zernike coefficients for radial order *"n"* and meridional frequency *"m"*.

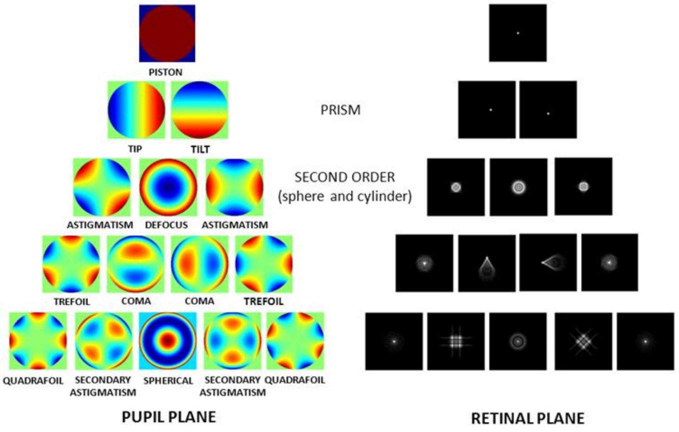

Figure 1.7. Representation of the Zernike base functions (15th coefficients) and their corresponding point-spread functions (*Taken from Vera-Díaz F and Doble N, The human eye and adaptive optics, Topics in adaptive optics, 2012).*

From the wave aberration coefficients, different optical quality descriptors can be directly derived after mathematical operations. The two classic descriptors are the Modulation Transfer Function (MTF) and the Point Spread Function (PSF). The MTF quantifies the loss in contrast associated to each spatial frequency, the higher the MTF the better the image provided by the system. The PSF is the impulse response of the system, i.e., the degraded image of an ideal point as imaged by the system. The Root Mean Square (RMS) is also a common descriptor, it is defined as the root square of the variance of the wave aberration and is typically used as the global metric for the optical quality [Applegate et al., 2003a; Applegate et al., 2003b]. Furthermore, the retinal image associated with any observed image can be simulated by convolving the ideal image with the PSF of the system [Cheng et al., 2003b; Guirao & Williams, 2003].

In the Chapter II we will describe the optical quality metrics descriptors analyzed in this thesis.

1.4. State-of-the art of aberrometers

Ocular aberrations are currently measured by using different techniques. Although aberrometers measure ray aberrations as a function of pupil position, differences across instruments arise from their psychophysical (requiring the participation of the subject) or objective (based on the light reflected off the retina) nature of the technique, and the “ingoing” (aberrations measured as the test beam goes into the eye) or “outgoing” (as the wavefront emerges from the eye) direction of the measurement [Arnulf & Dupuy, 1956; Burns & Marcos, 2001; Howland, 2000; Liang et al., 1994; Liang & Williams, 1997a; Losada & Navarro, 1998; Marcos et al., 2002; Moreno-Barriuso & Navarro, 2000; Smirnov, 1961; Thibos et al., 1999]. The most relevant aberrometers are *Hartmann-Shack (H-S)* and *Laser Ray Tracing (LRT)*.

The H-S is an objective “outgoing” aberrometry technique [Hartmann, 1900, 1904; Shack, 1971]. It is based on the measurement of ray deviations at different pupil positions of a wave reflected by the retina from a light point source. A microlens array, placed on a pupil conjugate plane, focused multiple spots (one per lenslet) onto a CCD camera. Each lenslet samples a small part of the wavefront corresponding to a certain pupil location. A regular pattern of spots would be obtained for an ideal non-aberrated eye, while the presence of aberrations produce an irregular pattern of spots. The deviations of each spot from the ideal position are linearly proportional to the derivative of the wave aberration. An array of the image shifts across the entire pupil is collected and a reconstruction algorithm is applied to obtain the wavefront. H-S has two main advantages over sequential techniques such as LRT: (1) it samples the pupil with a high fill factor, (2) high-speed (miliseconds).

The LRT is an objective “ingoing” technique and it is based on the light entering into the eye through different pupil positions [Molebny et al., 1997; Navarro & Losada, 1997]. The deviation of the test ray from the principal ray is detected by a CCD camera placed on a plane conjugated to the retina. A galvanometer X-Y scanner allows to scan sequentially a narrow light beam across the pupil in a brief period of time. As each ray goes through a different optical path, the image on the retina suffers a shift that is linearly proportional to the wavefront slope at the corresponding pupil position. From the sequence of the image shifts, the ocular wavefront can be reconstructed. Because the light source is projected sequentially, LRT allows a very large dynamic range and the entire pupil can be used; however, the sequential nature makes it slow (1.5 s *vs* 45 ms) in comparison with H-S.

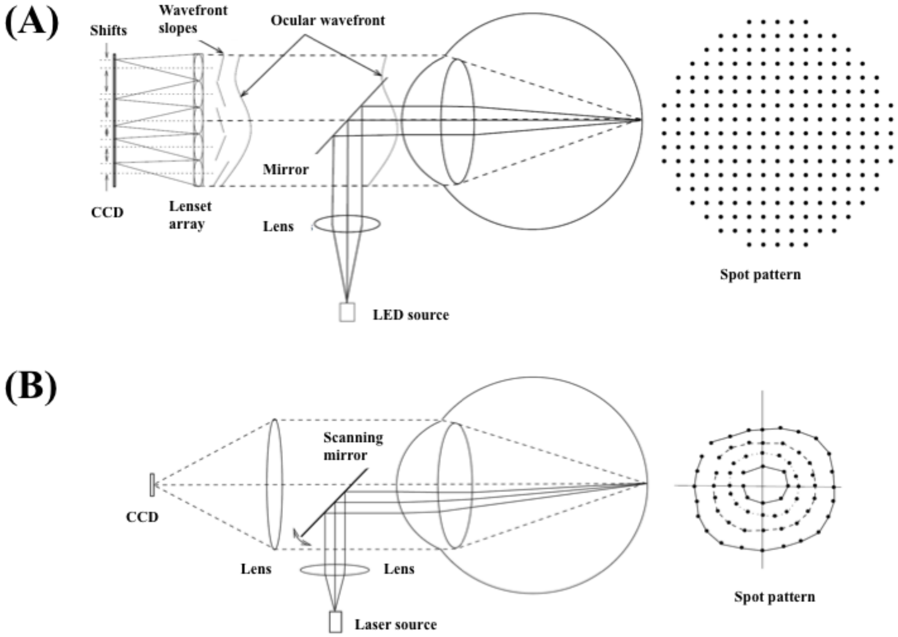

Figure 1.8. (A) Scheme of H-S. (B) Scheme of LRT

A custom-developed LRT is the technique of choice to quantify the ocular aberrations in this thesis, and the actual laboratory implementation will be described in Chapter II.

1.5. State-of-the art of quantitative anterior segment imaging techniques

1.5.1. Elevation-based corneal topography

There are several techniques to measure the corneal topography: specular reflection, scattered light and Scheimpflug imaging [Mejia-Barbosa & Malacara-Hernandez, 2001].

The *specular reflection* technique considers the anterior corneal surface as a convex mirror, as in the Placido disk-based systems. This method uses the analysis of reflected images of multiple concentric rings (alternating black and white rings) projected on the cornea. The concentric rings target has a hole in its center through which the observer/camera can visualize the reflected image from the cornea. The corneal shape is reconstructed in Placido disk topography assuming reflection principles only valid for rotation-symmetric surfaces [Massig et al., 2005; Rand et al., 1997]. However, the accuracy of this method has some controversy since for non-rotation symmetric surfaces (as the cornea) skew-ray reflections produces crossing points, ambiguity and inaccuracy in corneal surface analysis [Klein, 1997; Massig et al., 2005; Sicam & Van der Heijde, 2006]. In addition, Placido-disk topography does not directly picture actual corneal shape or true elevation topography.

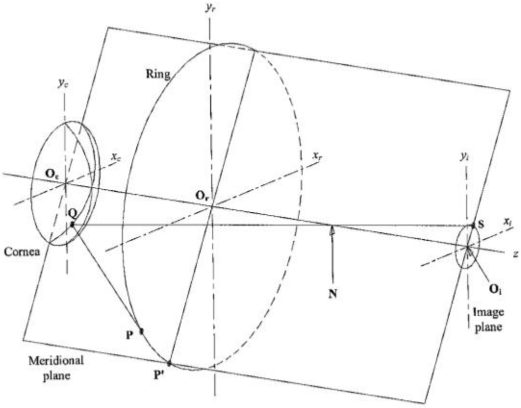

Figure 1.9. Geometry of the optical system for corneal topography in Placido-disk. A light ray that emerges from a ring at P reflects off the cornea at Q and reaches the image plane at S following the path QNS. The meridional plane is the plane that contains the optical axis, so here the reflected ray QS is a meridional ray, whereas the incident ray PQ is a skew ray (*Taken from Mejía-Barbosa and Malacara-Hernández).[Mejia-Barbosa & Malacara-Hernandez, 2001]*

The *scattered light* technique uses the scattering phenomenon of the light when it is transmitted in an optical medium. Part of this light emerged through ocular surfaces and it is captured by an optical method. This technique is used in the slit-lamp systems (Orbscan, *Bausch and Lomb, Rochester, NY, USA*). The Orbscan uses two slit-lamp projectors that are calibrated at 45 deg to the right or left of the optical axis of the camera-eye system. Each slit projects 20 slit beams across the whole width of the cornea, taking about 5000 points and obtaining anterior and posterior corneal topography. However, the Orbscan is a time-consuming technique (~2 seconds) and it is sensitive to motion artifacts.

The *Scheimpflug imaging* technique images the anterior segment of the eye using the Scheimpflug principle. The principle is named due to Theodor Scheimpflug and explained a method to increase the depth of focus. The Scheimpflug principle states that when the object plane, the lens plane and the camera plane are all allowed to form converging lines, then everything in the object plane will be in focus. The Pentacam *(Oculus Inc., Lynnwood, Wash, USA)* is the commercial Scheimpflug camera. The Scheimpflug camera rotates 360 degrees around a single fixation point as the patient focuses on a central light source, obtaining 50 images over a two-second period. The Pentacam generates 25000 true elevation points for each surface, including the center of the cornea. However, Pentacam suffer optical and geometrical distortion since it did not show a constant magnification and each surface is seen through previous refractive surfaces. Distortion correction of the images allowed accurate study of the posterior corneal surface and lens [Dubbelman et al., 2005; Rosales & Marcos, 2009].

Assuming that the corneal surface is given by *z=f(x,y)* in a Cartesian system with first and second derivaties continuous at any point, there are three ways for representing corneal topography [Sicam & Van der Heijde, 2006]:

By the *surface elevation f(x,y)* with respect to a reference surface (plane, sphere). A typical reference sphere is one with the minimum standard deviation with respect to the corneal surface and with the same optical axis. The best-fit sphere for calculating the topography of the cornea is calculated using a least-squares method.

By the *local slopes* with respect to the reference sphere since at any point on the surface the slope is a function of the direction.

By the *local curvature*, for a given point there is a maximum value in a certain direction and a minimum value in the perpendicular direction.

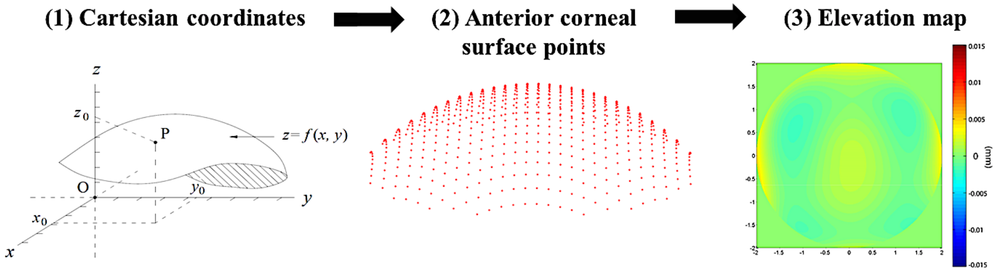

Figure 1.10. Cartesian coordinates (a point of the surface is described by three linear coordinates: *x*, *y*, *z*), corneal surface points and its corresponding elevation map (normal cornea).

1.5.2. Optical Coherence Tomography (OCT)

The working principle of the *Optical Coherence Tomography (OCT)* is based on low coherence interferometry and is commonly performed by using a Michelson interferometer.

In the Michelson interferometer, a lens collimates light from a source and transmits it through a beam splitter. The two separated beams are coherent and are reflected from two flat mirrors (M1 and M2) and returned to the beam splitter (BS). There, the two beams recombine and equal fractions are again transmitted and reflected. The transmitted fractions are the ones of interest. Because of the coherence the combined amplitudes may be added, and the addition is vectorial because, unless the two arms are of exactly equal length, there is a phase-difference between the two components and they may reinforce or cancel each other out if the path-difference is an integer or half-integer number of wavelengths. If the light is monochromatic, the transmitted intensity varies sinusoidally as one of the reflectors is moved uniformly to change the path-difference.

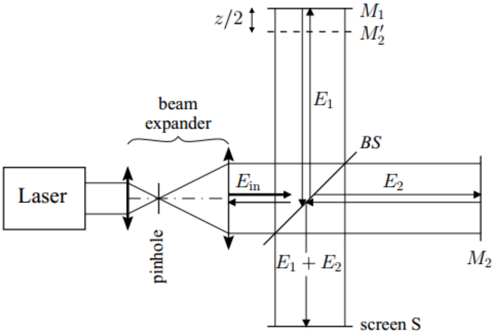

Figure 1.11. Scheme of the Michelson intereferometer and the corresponding electric field in the light wave.

The functional form of the electric field in a light wave is:

Equation 1.3: $$E_{in} = E_0\, e^{i(\omega t - kz_0)}$$

$$E_1 = |E_1|e^{i(\omega t - kz_1)}\ travelling\ BS - M_1 - BS - \ldots$$

$$E_2 = |E_2|e^{i(\omega t - kz_2)}\ travelling\ BS - M_2 - BS - \ldots$$

where, $\omega=2\pi\upsilon$ is the angular frequency (υ, frequency of the light wave), and $\kappa=2\pi/\lambda$ is the propagation constant (κ, it contains information regarding the wavelength).

Both reference and signal beams are combined at the beam splitter (BS). The output of the interferometer is the sum of the electromagnetic fields from the reference beam and the signal beam reflected from the tissue:

Equation 1.4: $$I = |E_1 + E_2|^2 = I_1 + I_2 + \sqrt{I_1 I_2}\,e^{i(-kz_1 + kz_2)} + \sqrt{I_1 I_2}\,e^{i(kz_1 - kz_2)} =$$
$$I_1 + I_2 + 2\sqrt{I_1 I_2}\cos kz$$

A detector (S) measures the field of the optical beam. The superimposed waves produce interference fringes on the detector. These distinctive fringes enable the determination of the location at which light is reflected back and the measurement of the depth profile of the scattering amplitude. When several wavelengths are present, the output signal contains a range of frequencies with amplitudes corresponding to the intensities of the various spectral components. Fourier analysis of the signal can thus recover the spectrum of the source and accurate measurements became possible with computing functions (e.g., Fast Fourier Transform, FFT).

OCT is based on a classic optical technique known as low-coherence interferometry. Low-coherence interferometry was used in photonics to measure optical echoes and backscattering in optical fibers and its basic principle rely on the interferometric properties of a broadband light source. The first biological application of low-coherence interferometry was reported by Fercher et al. in 1988 [Fercher et al., 1988], for measuring the eye axial length.

OCT is an important biomedical imaging technique being extensively developed since the early 90s. The optical sectioning ability of the OCT was soon recognized and exploited to image *in vivo* microscopic structures in tissue at depths beyond conventional confocal microscopes. Compared with other imaging techniques, OCT has the following important advantages: (1) the laser source is usually infrared, so, with controlled power, it is not harmful to human tissue and comfortable for the patient; (2) the system is based on low-coherence interferometer and the resolution is limited by the coherence length of the laser, thus high resolution (1-10 µm) can be achieved; (3) the system can be fiber based, therefore it could be easily made compact and low cost OCT; (4) real-time imaging can be achieved; and (5) higher speed over other imaging technologies. Because of these advantages, OCT has been established as an important tool in biomedical imaging area, especially in the ophthalmology field (being now very common in the clinic).

OCT technology can be divided into two distinct groups: time-domain (TD) and spectral-domain (SD) OCT. In TD-OCT, the autocorrelation of the light field is measured directly by a mechanical axial movement of the reference mirror, which corresponds to the depth-scanning signal of the sample [Fercher et al., 1993; Huang et al., 1991; Izatt et al., 1994; Swanson et al., 1993].

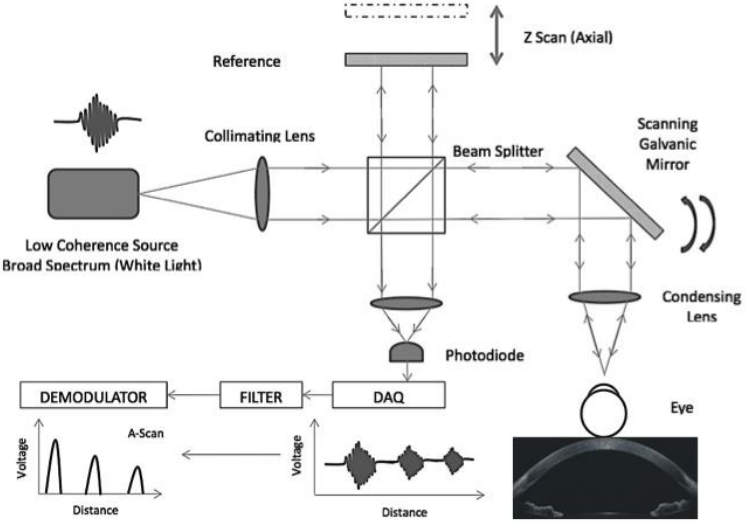

Figure 1.12. Time-Domain OCT *(adapted from T.E. Drew thesis)*

In contrast, in SD-OCT, the autocorrelation is calculated by means of the Fourier transform of the power spectral signal, which is measured directly. Modern OCT systems are usually not based on time-domain principle but rather on SD-OCT shows higher speed (there is no dependency of an axial movement of the reference mirror) and significant sensitivity improvement for the same laser power. SD-OCT can be implemented by setting up a spectrometer (SD) to detect the interference signal [Grulkowski et al., 2009; Wojtkowski et al., 2003; Wojtkowski et al., 2002] or using a swept source (SS) to scan the frequency of the laser [Chinn et al., 1997; Choma et al., 2003; Yun et al., 2003]. Due to its higher speed (up to 1.68 MHZ) and depth range (up to 50 mm) SS-OCT is the latest milestone in ocular imaging [Grulkowski et al., 2012].

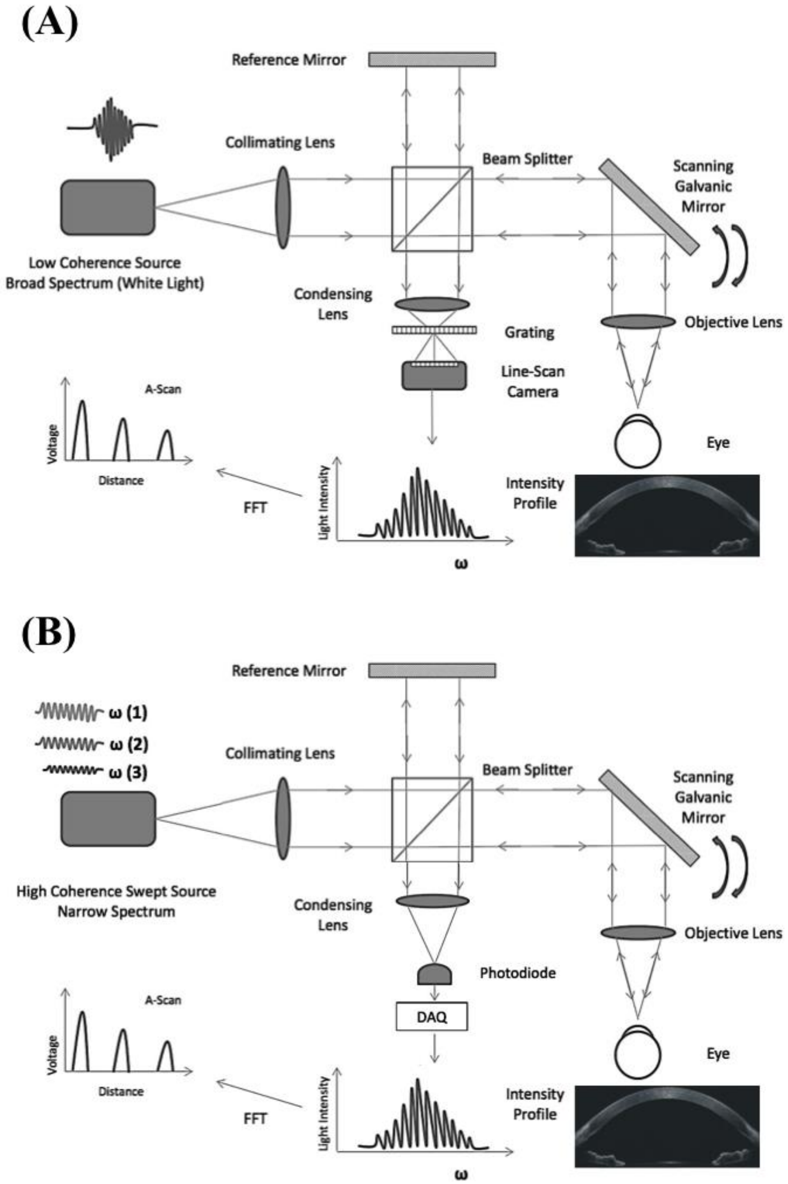

Figure 1.13. (A) Spectral-Domain OCT. (B) Swept-Source OCT *(adapted from T.E. Drew thesis).*

OCT has been extensively used to study the retina, and less extent, in the last decade, to image the anterior segment. However, as in all optical techniques aiming at direct imaging of the posterior corneal surface and crystalline lens, images are distorted by the refraction of the rays at the cornea and lens. Also, the scanning system induces distortion, fan distortion (resulting in a combination of geometric aberrations, including field distortion, astigmatism, and spherical aberration). Correction algorithms have been recently applied to extract accurate information of the cornea [Ortiz et al., 2012a; Ortiz et al., 2010; Ortiz et al., 2009a, 2009b; Zhao et al., 2010] and the whole anterior segment [Ortiz et al., 2013; Ortiz et al., 2012b].

A custom-developed SD-OCT is the technique of choice to quantify the geometry and biometry of the anterior segment of the eye in this thesis, and the actual laboratory implementation will be described in Chapter II. Pentacam and Placido disk-based corneal topography were used in this thesis for validating OCT-based *in vivo* corneal topography.

1.6. Customized eye modeling: linking geometry and aberrations

Eye models based on anatomic data have become essential to understand the link between geometrical and optical properties of the human eye. The first paraxial eye models were developed by Moser (1844), Listing (1851), Gullstrand [Gullstrand, 1909] and Le Grand [Le Grand, 1956]. Early paraxial models used spherical surfaces and focused on paraxial computations such as focal length and image locations (focal points, principal points and nodal points). However, although paraxial models serve as an approximation of the real dioptric system of the eye, those are idealized models unable to predict individual optical responses.

Geometric optics assumes that the wavelength of the light is sufficiently small, so light propagation can be described in terms of rays. The path of the rays is determined by reflection and refraction. A ray obeying Snell´s law is called real ray. Analyzing optical systems by tracing many real rays is therefore known as real ray tracing, and in terms of geometrical optics every deviation from a perfect optical system can be quantified as optical aberrations.

Modeling the optics of an individual patient´s eye and predicting the resulting optical performance addresses a current unmet need in visual optics. With the advance in imaging techniques, more sophisticated eye models (multi-surface eye models) are in constant development allowing realistic individual simulations of the ocular properties such as ocular aberrations (monochromatic and chromatic), by incorporating patient´s based eye biometry (corneal thickness, ACD, lens thickness and axial length), ocular angles, eccentricities and the geometrical and optical characteristics of the ocular elements (cornea and crystalline lens/IOL).

Table 1.1. Summary of the features eye-models based on average population data (adapted from Sheehan thesis).

Model (Year)	***Surfaces***		***Lens***	***Accomm***	***Domain***		***Dispe_ rsion***	***Age***	***Amet_ ropic***
	Sph	*Asph*			*On-axis*	*Off-axis*			
Gullstrand (1909)	6	-	shell	Yes	Yes	-	-	-	-
Le Grand	4	-	-	Yes	Yes	-	-	-	-
Emsley (1952)	1	-	-	-	Yes	-	-	-	-
Lotmar (1971)	3	1	-	-	Yes	Yes	-	-	-
Drasdo & Fowler (1974)	-	4	-	-	Yes	Yes	-	-	-
Kooijman (1983)	-	4	GRIN	-	Yes	Yes	-	-	-
Pomerantzeff (1984)	-	2	shell	-	Yes	Yes	-	-	-
Navarro (1985)	1	3	-	Yes	Yes	Yes	Yes	-	-
Blaker (1991)	-		GRIN	Yes	Yes	-	-	Yes	-
Smith (1992)	2	2	GRIN	-	Yes	-	-	Yes	-
Thibos - Indiana (1992)	-	1	-	-	Yes	Yes	Yes	-	-
Liou & Brennan (1997)	-	2	GRIN	-	Yes	Yes	Yes	-	-
Masajada & Kasprzak (2002)		4	GRIN	Yes	Yes	-	-	-	-
Siedlecki (2004)	-	4	GRIN	-	Yes	-	-	-	-
Norrby (2005)	-	4	-	Yes	Yes	Yes	-	Yes	-
Atchison (2006)	-	5	GRIN	-	Yes	Yes	Yes	-	Yes
Goncharov & Dainty (2007)	-	4	GRIN	-	Yes	Yes	-	-	-
Navarro (2007)	-	4	GRIN	Yes	Yes	Yes	-	Yes	-
Campbell (2010)	-	4	Shell	Yes	Yes	Yes	-	Yes	-
Rozema (2011)	-	4	-	-	Yes	-	-	-	-
Chen (2012)		4	Shell	Yes	Yes	-	-	-	KC
Polans (2015)	-	4	GRIN	Yes	Yes	Yes	Yes	Yes	-

Most of current generic eye modeling requires the assistance of ray tracing computational programs (such as ASAP (Breault Research Organization, Inc., Tucson, AZ), ZEMAX (Radiant ZEMAX; Focus software, Tucson, AZ), Code V (Optical Research Associates, Pasadena, CA) or OSLO (Lambda Research Corporation, Littleton, MA)) and optical optimization by integrating a merit function in order to approach the specific targets (e.g. best focal position and optical quality metrics).

The incorporation of the geometry and aberrometry experimental data into computational simulations has recently demonstrated fully customized procedures for ray-tracing IOL power calculation [Rosales & Marcos, 2007; Tabernero et al., 2006].

Table 1.2. Pseudophakic eye models based on ray-tracing IOL power calculation. sph=spherical; asph=aspherical.

Model (Year)	*Cornea*	*IOL*
Rosales et al. (2007)	Placido-disk (ant)	2 models (sph, asph)
Barbero & Marcos (2007)	Theoretical (ant and post)	2 models (sph, custom)
Einighammer et al. (2009)	Placido-disk (ant)	4 models (sph, asph, toric)
Canovas et al. (2011)	Placido-disk (ant)	1 model
Zhu et al. (2011)	OCT	Theoretical
Ribeiro et al. (2012)	ORBSCAN (ant and post); post-LASIK	1 model
Fernández et al. (2013)	Theoretical (ant and post)	1 model (multifocal)
Zhang et al. (2015)	Theoretical (Hwey-Lan Liou)	2 models (sphr, toric)

1.7. Anterior segment conditions and clinical applications studied in this thesis

The measurement of the anterior segment geometry and aberrations in normal eyes is important in understanding the contribution of every optical component to retinal image quality. Still, the acquisition of accurate measurements in pathological eyes or in eyes treated with different ocular procedures is critical for the evaluation of the geometry of the optical components (cornea and implant, and crystalline lens and implant), the 3-D positioning of the implant in the eye, and finally, the contribution of the clinical solution to ocular aberrations.

1.7.1. Cornea *(Keratoconus & Intracorneal Ring Segment (ICRS) treatment)*

> *"I therefore held a candle at the distance of fifteen inches from the cornea, and keeping my eye in the direction of the reflected rays, I observed the variations in the size and form of the image of the candle. The reflected image regularly decreased when it passed over the most convex parts of the cornea; but when it came to the part nearest the nose, it alternately expanded and contracted, and suffered such derangements, as to indicate the presence of a number of spherical eminences and depressions, which sufficiently accounted for the broken and multiplied images of luminous objects…"*
>
> *J. Wardrop. "Essays on the Morbid Anatomy of the Human Eye", 1808 [Wardrop, 1808]*

Keratoconus derives from the Greek words *Kerato* (cornea) and *Konos* (cone) and it is a corneal condition affecting primarily young patients with a prevalence about 1 per 2000 in the general population, being this prevalence 6 times greater in India [Gokhale, 2013]. It is caused by the progressive and asymmetric weakening of corneal tissue, in which gradual thinning lead to a cone-like appearance of the cornea, manifesting irregular astigmatism, myopia and high levels of high-order aberrations.

Symptoms of keratoconus vary and depend on its stage [Nordan, 1997; Rabinowitz, 1998]. In early stages, it results difficult to differentiate keratoconus from other ocular refractive conditions (such as astigmatism) in typical routine eye exams, so highly sensitive corneal topography might be really helpful in its diagnosis. Furthermore, although the detection in advanced stages is usually easier because of distorted vision and topographical signs, highly deformed corneas cannot be assessed precisely because of inherent limitations of the imaging techniques (e.g., resolution or acquisition time) or aberrometers (e.g., dynamic range).

1.7.1.1. Keratoconus: topography and pachymetry

The characteristic changes in both anterior and posterior corneal surfaces leads to changes in corneal thickness, which can be assessed by means of corneal topography and pachymetry. In most keratoconic patients, the anterior corneal topographic map is characterized by focal steepening with a dioptric power greater than 46 D, corneal thinning and astigmatism. The cone vertex is typically displaced toward the lower mid-peripheral region in either the nasal and temporal quadrant. There is usually a vertical asymmetry with a certain diagonal angle. All of these topographic and pachymetric alterations in keratoconus appear as a consequence of the biomechanical changes that occur in the corneal structure [Meek et al., 2005]. The topographical pattern is usually similar in both eyes, although one of them may show a more advanced state [Nordan, 1997; Rabinowitz, 1998].

For early keratoconus diagnosis, different descriptors based on anterior corneal topography were developed during the 90s with the first videokeratographers: central corneal power (*central K*: descriptive of central steepening), Inferior-Superior values (*I-S dioptric asymmetry*), surface asymmetry index (*SAI*), specific index quantifying irregular astigmatism (*SRAX*, skewed radial axis) and KISA% index [Li et al., 2009; Maeda et al., 1994; Rabinowitz, 1995].

The development of new commercial imaging techniques (Orbscan II and Pentacam Scheimpflug camera) and the advance in new surface detection algorithms has made possible the topographic analysis of the posterior cornea. Tomidokoro et al. [Tomidokoro et al., 2000] reported that irregular astigmatism of the posterior corneal surface is one of the first sign of keratoconus; Chen and Yoon [Chen & Yoon, 2008] showed that the posterior corneal surface was significantly more irregular than the anterior corneal surface in keratoconus. Regarding corneal pachymetry, significant differences have been reported between normal subjects and keratoconus, showing also differences across different keratoconus stages [Rabinowitz et al., 1998]; and Saad and Gatinel [Saad & Gatinel, 2010] showed that corneal thickness and curvature measurements over the entire cornea centered on the thinnest point are valid metrics for diagnosing earlier keratoconus stages.

However, some studies reported poor repeatability and variability in the analysis of keratoconus using Orbscan and Pentacam (especially in the posterior corneal surface), being this variability possibly associated to interpolation errors attributable to meridional sampling approaches, relatively long acquisition times, and errors in optical distortion correction, particularly challenging with highly deformed corneas [Read et al., 2009; Shankar et al., 2008].

Due to its higher speed, depth range and resolution, OCT has been positioned as a promising technique for quantifying both corneal surfaces in keratoconus [Gorgun et al., 2012; Karnowski et al., 2011; Li et al., 2008; Ortiz et al., 2011; Qin et al., 2013; Read et al., 2009]. Li et al. [Li et al., 2008; Li et al., 2006] reported for first time quantitative abnormal corneal thinning in keratoconus based on OCT by analyzing only 8 cross-sectional OCT images and mapped the corneal epithelial thickness [Li et al., 2012]. Karnowski et al. [Karnowski et al., 2011] showed 3-D quantitative corneal analysis in a keratoconic subject based on SS-OCT. Nakagawa et al. [Nakagawa et al., 2011] measured forty keratoconic eyes and showed good agreement between OCT and Pentacam. And, Szalai et al. [Szalai et al., 2012] compared anterior segment measurements (anterior and posterior corneal radius, corneal thickness and anterior chamber depth) between SS-OCT and Scheimpflug in normal and keratoconus and found statistically significant differences between instruments in all parameters. As we described in section 1.5.2., OCT images are generally subject to distortions. Because of these distortions, OCT images need to be corrected for an accurate quantification. To date, the only study showing 3-D quantitative keratoconus properties using OCT after full distortion correction was performed in our group by Ortiz et al. [Ortiz et al., 2012a], on a single patient.

1.7.1.2. Keratoconus: aberrations

The progressive distortion of the cornea leads to abnormal corneal topography and results in irregular astigmatism, progressive myopia and increased high-order aberrations, with consequent loss of vision. Previous studies based on H-S [Maeda et al., 2002] and LRT [Barbero et al., 2002a] ocular aberrometry showed differences between normal and keratoconic eyes, being approximately 5.5 times higher in keratoconus. Both studies found significant high values in astigmatism and coma (particularly, vertical coma). Maeda et al. [Maeda et al., 2002] reported that coma-like aberrations were 2.32 times larger than spherical-like aberrations in keratoconic eyes. Trefoil, tetrafoil and secondary astigmatism terms were also higher and variable in keratoconus [Alio et al., 2011; Alio & Shabayek, 2006; Barbero et al., 2002a; Maeda et al., 2002].

Although the anterior corneal surface supposes the dominant factor to corneal aberrations, posterior corneal aberrations have a remarkable implication in ocular aberrations, especially in keratoconus. However, few studies measured the contribution of the anterior and posterior corneal surfaces to total aberrations. Chen and Yoon [Chen & Yoon, 2008] (using Orbscan) demonstrated stronger compensation effects of the posterior corneal surface in keratoconus than in a normal population (around 20% of anterior corneal astigmatism and coma). Nakagawa et al. (using Pentacam) showed that the axes for coma in the anterior (63.6 deg) and posterior (241.9 deg) surfaces were in opposite directions. Piñero et al. [Pinero et al., 2009a] (using Pentacam) showed higher levels of aberrations (particularly for coma-like aberrations) in the posterior corneal surface when compared with the anterior corneal surface in normal and keratoconus eyes.

1.7.1.3. Keratoconus treatment: Intracorneal Ring Segments (ICRS)

The hallmark of keratoconus is the presence of irregular corneal astigmatism and the increase of high-order aberrations (particularly vertical coma, Z_3^{-1}), making difficult its correction with spectacles or contact lenses alone when the disease is in advanced stage. Managing keratoconus would benefit from the reinforcement of the cornea using an additive technique. Surgical treatments to stabilize or delay the progression of keratoconus before a corneal transplant involve the implantation inside the cornea of intracorneal ring segments (ICRS) [Colin et al., 2000] or the application of collagen cross-linking [Spoerl et al., 1998]. In this thesis we make use of our custom-developed LRT and OCT methodology to evaluate the ICRS treatment (Chapter III).

ICRS are PMMA segments with variable form (triangular, hexagonal and oval), arc length and width, and are inserted to the cornea through a manually [Colin et al., 2000] or femtosecond laser [Shabayek & Alio, 2007] made channel in the corneal stroma according to empirical nomograms, in one or two sides of the pupil.

ICRS act as spacer elements between the bundles of corneal lamellae, inducing shortening of the central corneal arc length and, as consequence, producing a flattening of the anterior cornea. Furthermore, ICRS are expected to increase the biomechanical stability and to improve the optical quality of the cornea by increasing corneal symmetry [Colin et al., 2000; Pinero et al., 2009b; Vega-Estrada et al., 2013].

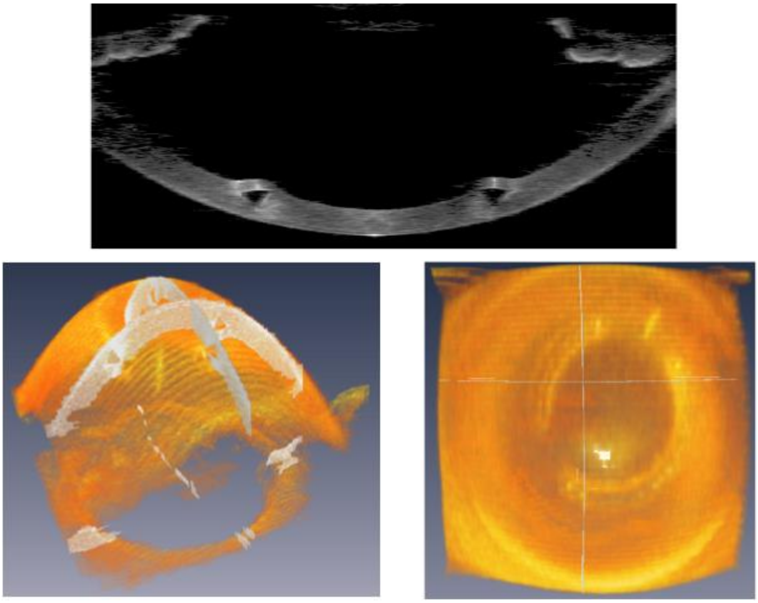

Figure 1.14. (Top) OCT cross sectional image showing the ICRS inside the cornea. (Bottom) 3-D illustration of ICRS inside the cornea (obtained with OCT and illustrated with AMIRA software).

Assessment of ICRS implantation has been performed using different imaging techniques including slit scanning corneal topography [Dauwe et al., 2009], Scheimpflug imaging [Torquetti & Ferrara, 2010], ultrasound biomicroscopy [Reinstein et al., 2010; Reinstein et al., 2001] and OCT [Gorgun et al., 2012; Ortiz et al., 2012a]. Additionally, few studies in the literature have examined aberrations in keratoconic patients implanted with ICRS.

Most studies analyzed changes in the anterior cornea only, with only very few studies addressing the posterior cornea. These studies reported a mean flattening of the anterior cornea by 2.5 D, showing large variability in the corneal response across subjects (from an increase of 2.5% to a decrease of 18% in the topographic K-values after 90 days ICRS implantation [Shabayek & Alio, 2007]). The only previous study investigating the posterior corneal surface in corneas implanted with ICRS reported a significant flattening of approximately 0.25 mm using Scheimpflug imaging [Sogutlu et al., 2007].

Dauwe et al. [Dauwe et al., 2009] suggested that thickness redistribution after ICRS implantation might be a delay factor in keratoconus progression, since as the cornea thickens in the weakened areas, the stress may be redistributed and the decompensatory keratoconus cycle might be delayed. However, this hypothesis has not been yet demonstrated. In fact, there is controversy on the long-term effects with some studies showing stabilization [Torquetti et al., 2014; Vega-Estrada et al., 2013] and others regression [Alio et al., 2014; Vega-Estrada et al., 2015] after ICRS surgery.

Potential changes in the expected ICRS depth have been associated to post-surgical complications. Rotation or migration of the ICRS post-surgery has been described as consequence of the physiological stress and the wound healing response [Perez-Merino et al., 2010]. Naftali and Jabaly-Habib [Naftali & Jabaly-Habib, 2013] using commercial OCT reported significant differences between the planned and measured ICRS depth (~120 µm), although part of this discrepancy might be due to the inherent distortion associated to OCT. Recently, Ortiz et al. [Ortiz et al., 2012a] measured accurately the location of ICRS in 3-D using distortion-corrected OCT.

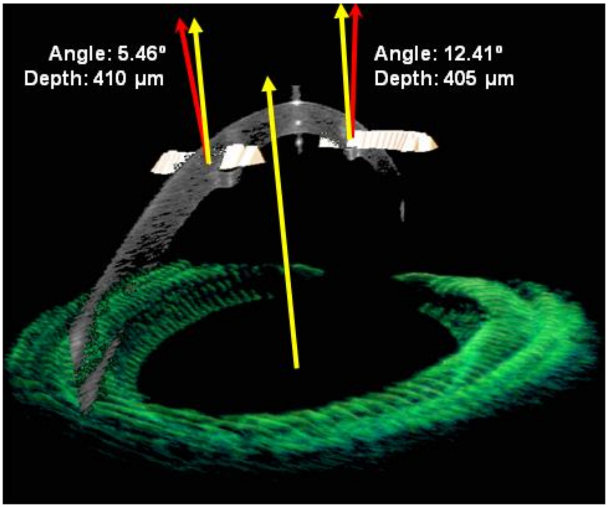

Figure 1.15. OCT 3-D *in vivo* positioning of the ICRS inside the cornea (orientation and depth). [Ortiz et al., 2012a]

While the literature reporting clinical visual performance after ICRS implantation is extensive, only two studies evaluate wavefront aberrations, showing contradictory results. Piñero et al. [Pinero et al., 2010] reported a significant improvement in anterior corneal astigmatism (3.21±2.16 µm preoperative, 2.50±1.73 µm post ICRS) and a reduction of coma-like anterior corneal aberrations (3.46±1.86 µm preoperative, 2.94±1.45 µm post

ICRS) and of anterior corneal HOAs (3.73±1.97 µm preoperative, 3.24±1.44 µm post ICRS) 3-months post ICRS implantation, for 6-mm pupils. In contrast, Chalita and Krueger [Chalita & Krueger, 2004] reported an increase in ocular HOA in the ICRS-implanted eye, when compared to the non-treated fellow eye.

Quantitative image-based and aberrometry techniques are helpful to evaluate objectively the performance of ICRS, but different studies also proposed analytical or numerical methods to model the response of the cornea to the ICRS and improve the implantation nomograms [Dauwe et al., 2009; Kling & Marcos, 2013; Pinsky et al., 2005]. These studies suggested a linear relationship between refractive change and ICRS height (the higher, the more effective) and optical zone (the smaller, the more effective).

1.7.2. Crystalline lens *(Accommodation, Presbyopia, Cataract)*

With age, two crucial features of the crystalline lens decline due to biochemical and biophysical changes. A progressive loss of transparency is accompanied by a fall in the rate and amplitude of accommodation. The latter is the basis of presbyopia, which reaches its top by the age of 50. The biochemical and cellular changes that result in the loss of transparency are known as cataract.

1.7.2.1. Accommodation

Accommodation is the dioptric change in power of the eye to provide clear and sharp retinal image for all distances, accommodation is also often described as being linked with convergence and pupil constriction. The primary stimulus for accommodation is blur vision, with lesser roles played by apparent perceived distance, chromatic aberration, non-symmetric aberrations and spherical aberration [Atchison, 1995; Charman, 2008].

When the young eye is relaxed and focused for distance, the ciliary muscle is relaxed, resting tension on the zonular fibers spanning the circumlental space and inserting around the lens equator apply an outward directed tension around the lens equator through the lens capsule to hold the lens in a relatively flattened and relaxed state. During accommodation, the ciliary muscle contracts, the inner apex of the ciliary muscle moves forward and towards the axis of the eye. This inward movement of the apex of the ciliary muscle stretches the posterior attachment of the ciliary muscle relaxing the tension on the zonular fibers and changing the crystalline lens geometrical properties (by increasing the convexity of its surfaces). The lens capsule provides the force to cause the lens to become accommodated. During accommodation, lens diameter decreases, lens thickness increases, anterior and posterior lens radii become steeper and anterior chamber depth decreases. In addition to the dioptric changes due to curvature and axial variations, a modification in the refractive index gradient was also found [Garner & Smith, 1997]. These changes overall contribute to 10-15 D of accommodative amplitude in the young adult eye, diminishing to <2 D by middle age [Ostrin & Glasser, 2004].

The accommodative response is the actual amount of accommodation produced by the lens for a given stimulus, i.e., the least accommodation required to obtain a sharp image. It is normally limited by the depth-of-focus (which is dependent on pupil size, residual defocus, astigmatism and high-order aberrations) and the inability to detect small amounts of blur. At distance, the eye usually overaccommodates, while at near underaccommodates, creating a lag of accommodation [Charman, 2008].

Most of clinical evaluations assessing the amplitude of accommodation are primarily based on the patient´s visual function: i.e. test of near visual acuity, reading test, through focus curves, convergence or subjective measurements of accommodation (e.g., by adding plus or minus lenses). However, these measurements do not differentiate the functional range of near vision attributable to the depth-of-focus of the eye.

Several techniques have been used to assess accommodation objectively using ultrasound biomicroscopy [Ramasubramanian & Glasser, 2015], low-coherence interferometry [Bolz et al., 2007; Drexler et al., 1997; Drexler et al., 1998], magnetic resonance imaging [Jones et al., 2007; Kasthurirangan et al., 2011], Purkinje imaging [Rosales et al., 2006], Scheimpflug imaging [Dubbelman et al., 2005; Koretz et al., 1997] and OCT [Gambra et al., 2013; Leng et al., 2014; Ruggeri et al., 2012; Shao et al., 2015]. Several of these techniques allowed quantifying the geometrical properties of the crystalline lens and the changes with accommodation. Alternatively, dynamic autorefraction and aberrometry [Gambra et al., 2009] have proved also rapid and repeatable measurements to objectively assess the accommodative response.

The changes in crystalline lens radius during accommodation in young subjects are greater for the anterior surface than for the posterior lens surface. Dubbelman et al. [Dubbelman et al., 2005] using 2-D cross-sectional Scheimpflug images reported rates of 0.61±0.15 mm/D for the anterior and 0.13±0.06 mm/D for the posterior lens radius. Rosales et al. [Rosales et al., 2006] measured the radius of the anterior and posterior lens surface with accommodation using Scheimpflug and Purkinje imaging and found a decrease of 0.64 mm/D (Scheimplfug) and 0.57 mm/D (Purkinje) for the anterior lens and 0.23 mm/D (Scheimplfug) and 0.57 mm/D (Purkinje) for the posterior lens, for an 8-D accommodative demand range. Gambra et al. [Gambra et al., 2013] reported measurements in eyes as a function of accommodation using distortion-corrected OCT and found a decrease of 0.73 mm/D and 0.20 mm/D for the anterior and posterior lens radius, respectively. And, Shao et al. [Shao et al., 2015] using 2-D OCT reported rates of 1.06 mm/D and 0.29 mm/D for the anterior and posterior lens radii.

Different studies also reported static (anterior chamber depth (ACD) and lens thickness) and dynamic (fluctuations) changes with accommodation [Dubbelman et al., 2005; Gambra et al., 2013; Kasthurirangan et al., 2011; Leng et al., 2014]. On average, ACD decreases 0.057 mm/D, lens thickness increases 0.081 mm/D and lens fluctuations changes 0.044 D/D of accommodative demand (driven primarily by the posterior lens surface) [Gambra et al., 2013].

Because of structural changes in the crystalline lens (shape, position and refractive index) that occur during accommodation, wave aberrations are expected to change. Spherical aberration has been reported to shift towards negative values, and different studies also showed changes in coma, trefoil and astigmatism, but the direction of the change was variable [Chen et al., 2006; Gambra et al., 2009; He et al., 2000b; Radhakrishnan & Charman, 2007].

Information on the crystalline lens provided by commercial or custom-developed instruments is generally limited to axial properties or to measurements of the anterior and posterior lens radius of curvature from single cross-sections, not revealing topographic features of the lens. In this thesis we make use of our custom-developed OCT in the *in vivo* analysis of crystalline lens topography with accommodation (Chapter IV).

1.7.2.2. Presbyopia

> *"It may be observed that old people hold objects that they wish to examine further from the eye…If anyone examines letters or other minute objects through the medium of crystal or glass or other transparent substance, if it be shaped like the lesser segment of a sphere, with the convex side being towards the eye, and the eye being in the air, he will see the letters far better, and they will seem larger to him…For this reason, such an instrument is useful to old persons…"*
>
> *R. Bacon. "Opus Majus", around 1250*

The basis of presbyopia development is crystalline lens hardening. The lens becomes too stiff to respond by bulging when tension is removed. The most likely cause for lens hardening is changed of the highly concentrated proteins within the fiber cells, thus altering the physical proteins of the cytosol [Truscott & Zhu, 2010].

Dubbelman and Van der Heijde [Dubbelman & Heijde, 2001] reported a slight decrease of the anterior and the posterior lens radius of curvature with age (0.057 mm/age and 0.012 mm/age, respectively), using Scheimpflug imaging technique. Additionally, with age there is also an increase of lens thickness and a decrease of the ACD. Birkenfeld et al. [Birkenfeld et al., 2014] showed a decrease of the GRIN compensatory role on spherical aberration with age.

The optical performance of the eye also changes with age. Due to the disruption of the compensatory effect between the anterior cornea and the internal aberrations there is an increase in high order aberrations [Glasser & Campbell, 1998a; McLellan et al., 1999]. In particular, the spherical aberration and horizontal coma tend to increase in older eyes [Piers, 2002; Pierscionek, 1996]. Tabernero et al. [Tabernero et al., 2007] showed that the RMS of the higher order ocular and corneal aberrations increased with age at a rate of 0.0032 µm/year and 0.0015 µm/year, respectively. In this study, the authors did not observed changes in the optical alignment with age (i.e., the angle kappa remains stable), assuming therefore that variations in the crystalline lens shape with age might explain most of the increment of ocular aberrations.

1.7.2.2.1. Presbyopia solutions

Presbyopia becomes an apparent problem for most people in their forties when they can no longer see clearly daily near tasks and need to seek a solution by using external (spectacles or contact lenses) or internal (corneal refractive surgery or IOL) corrections.

The easiest solution is conventional single-vision reading spectacles, but this solution does not allow sharp vision at intermediate or far vision. Different available solutions for presbyopia are based on different principles: *alternating vision* (implying changes of gaze:

bifocal lenses or progressive spectacles), *monovision* (one eye is corrected for distance vision and the other for near vision: contact lenses, IOLs, corneal inlays or corneal laser refractive surgery) and *simultaneous vision* (the eye is corrected for distance and near vision simultaneously: contact lenses or IOLs) [Ahmad et al., 2014; Bennett, 2008; Brown et al., 1987]. In addition, surgical options to restore or enhance the accommodative ability of a presbyopic eye by mimicking the crystalline lens (*accommodative IOLs*) are currently under development [Beiko, 2007; Glasser, 2008].

In this thesis we will focus on *accommodative IOLs* as a solution for presbyopia.

Accommodative IOLs

Accommodative IOLs (A-IOLs) that attempt at changing either their position and/or shape in response to ciliary muscle contraction are at the forefront of much ongoing research to restore true accommodative function to presbyopic eyes. Currently, there are multiple strategies from laboratory-based to commercial models attempting functional accommodative capacity in presbyopic/cataract patients, including flexible haptics, moldable gels and fluid displacements, with either single monofocal IOLs, dual IOLs or gel-filled lenses [Glasser, 2008]. Additionally, several studies have explored the concepts of lens softening (reducing lens stiffening by photodisruption) and lens refilling of the capsular bag with gel-like polymers that mimic the crystalline lens [Nishi et al., 2009]. However, to date, most designs in practice rely on an axial shift of the IOL in response to an accommodative stimulus:

(1) *single optical element* expected to move axially forward and backwards (BioCom Fold, by Morcher GmbH; 1CU, by Human Optics AG; Crystalens A-IOL, by Bausch & Lomb; Tetraflex, by Lenstec, Inc; OPAL, by Bausch & Lomb; C-Well, by Acuity Ltd; Quest Vision lens, by AMO; TekClear, by Tekia) [Cumming et al., 2006].

(2) *two optical elements* expected to axially increase their separation (e.g., Synchrony, by AMO; Sarfarazi dual-optic A-IOL, by Bausch & Lomb; Turtle A-IOL based on Alvarez´s lens principle) [McLeod et al., 2007].

In the A-IOL, the degree of the accommodative effect is proportional to the dioptric power, its mechanism of action and the lens and its movement. Ho et al. predicted with ray-tracing that single optical A-IOL might provided up to 1.0 D of accommodation (axial shift 1.2 D/mm), whereas the range for two optical elements A-IOLs is up to 3.0 – 4.0 D (axial shift 3.0 D/mm). Also, for a maximum accommodation, the final position of the A-IOL should be placed close to the posterior capsule.

However, to date, the *in vivo* efficacy of A-IOLs designs remains unclear. Different studies have shown than the subjective accommodative response after Crystalens A-IOL implantation ranged from 0.44 to 2.36 D, which was close to the magnitude of depth-of-focus of standard monofocal IOLs (ranging from ±0.85 D to 1.82 D) [Beiko, 2013; Macsai et al., 2006]. While subjective measurements assess visual performance at different distances, the results provided by these tests cannot generally conclude whether the lenses are actually working according to their functional mechanism, since these methods do not differentiate the functional range of near vision attributable to the depth-of-focus of the eye [Leydolt et al., 2009; Marcos et al., 2005b; Tahir et al., 2010; Tucker & Rabie, 1980].

Alternatively, dynamic autorefraction demonstrated rapid, objective and repeatable techniques to assess the accommodative response [Choi et al., 2000]. Langenbucher et al. [Langenbucher et al., 2003] showed a mean accommodative response of 1.00±0.44 D using photorefraction in patients implanted with the 1CU A-IOL (HumanOptics AG, Erlangen, Germany); whereas, Zamora-Alejo et al. [Zamora-Alejo et al., 2013] showed no change with accommodative effort in the spherical equivalent in patients implanted with the Crystalens HD.

As described in the accommodation sub-section, different factors, such as pupil size, residual defocus, astigmatism and high-order aberrations, may contribute to an expansion of the ocular depth-of-focus. Aberrometry therefore appears as a highly suitable objective technique to evaluate the optical performance of A-IOLs, including potential accommodative responses and the factors that may result in a potential pseudoaccommodation [Marcos et al., 2005a; Mclellan et al., 2001]. Static and dynamic aberrometry have been used in the past to assess the change of aberrations with aging or accommodation, as well as the impact of aberrations on the accommodative lag [Gambra et al., 2009; He et al., 2000b; Hofer et al., 2001; Lopez-Gil et al., 2007]. In addition, aberrometry has been extensively used to evaluate the optical performance in patients implanted with monofocal IOLs [Barbero, 2003]. However, whereas optical bench studies and ray-tracing simulations analyzed optical quality in A-IOLs [Ho et al., 2006; Kim et al., 2011; Pepose et al., 2012; Zheleznyak et al., 2012], there are few reports in the literature on the optical aberrations in eyes implanted with A-IOLs. Using dynamic Hartmann-Shack aberrometry, Dick and Kaiser [Dick & Kaiser, 2002] found small changes in defocus in patients implanted with the Crystalens AT-45 (Bauch&Lomb, Rochester, NY) and 1CU (HumanOptics AG, Erlangen, Germany) A-IOLs. Ehmer et al. proved a low degree of accommodation of Synchrony dual-optic A-IOL, they found amplitudes of accommodation of 1 D for an accommodative stimulus of 3 D. Wolffsohn et al. [Wolffsohn et al., 2010] reported some changes in ocular aberrations (defocus, astigmatism, coma and trefoil) with increased accommodative demand in patients implanted with the Tetraflex A-IOL (model KH-3500; Lenstec, ST. Petersburg, FL).

In addition to objective visual function analysis, an objective way to evaluate whether A-IOLs are operating as expected by design is its direct intraocular visualization. With the use of ultrasound biomicroscopy (UBM), Marchini et al. [Marchini et al., 2004] reported a forward mean shift of 0.32 mm at 1 month (with several eye showing backward shifts). With low-coherence intereferometry (PCI), Stachs et al. [Stachs et al., 2006] reported a forward mean shift of 0.24 mm under pilocarpine-induced accommodation and Koeppl et al. [Koeppl et al., 2005] detected only negligible counterproductive backward movement of the Crystalens AT-45. Also, apart from potential shifts of the A-IOLs in the axial direction, observational studies have also reported cases of asymmetric vaulting of the IOL, known as “Z syndrome” (the lens tilt is likely caused by capsular contraction or asymmetric fibrosis in the haptic region).

In this thesis we make use of our custom-developed LRT (objective accommodative response and optical aberrations) and OCT (3-D positioning) methodology for evaluating the efficacy of a single optical element A-IOL (Chapter V).

1.7.2.3. Cataract (Intraocular Lens)

> *"A new operation is described whereby an artificial lenticulus is inserted in the eye after cataract extraction. Excellent function can be obtained, and a lens has been known to remain in position without causing inflammation for at least two years…"*
>
> *H. Ridley. "Intra-ocular acrylic lenses after: a recent development in the surgery of cataract", Brit J Ophthal, 1952*

Age-related cataract is a cause of blindness on a global scale (43% of worldwide blindness) due to biological aging, genetic and environmental factors of the crystalline lens, such as protein aggregation, oxidative stress and increase in high molecular weight and increase in water content. There are several distinct forms of age-related cataract, whose morphologies imply different etiologies of different lens regions: nuclear and cortical cataracts [Michael & Bron, 2011; Truscott & Zhu, 2010].

Cataract surgery is one of the oldest surgical procedures known, first documented in the 5th century BC in Egypt. However, the substitution of the opacified crystalline lens by an intraocular optical element it was not done until the mid of the 20th century, when Sir H. Ridley first introduced an artificial IOL [Ridley, 1952]. Since then, cataract surgery with intraocular lens (IOL) implantation has become a routine surgical procedure.

A typical IOL structure is composed by two main parts: the body (the optic of the lens) and the haptics (the struts). IOLs must satisfy specific requirements in terms of optical performance, mechanical properties, biocompatibility, shelf-life and transportability. There are several IOL designs and/or models available in the market: *monofocal* (spherical, aspherical), *multifocal* (concentrical zones of differing refractive power, diffractive optics), *toric* and *accommodative* (curvature changes of the lens surfaces and/or axial displacement of the optical elements).

Traditional IOLs are monofocal and spherical, and only correct defocus for far vision, achieving almost far-emmetropic distance refractions in the majority of cases. However, with the current advances and the great variety in design, materials, imaging techniques, femtosecond surgery and the patient´s demands, the concept of *"premium IOLs"* has been coined [Atchison, 1989; Atchison, 1991; Glasser, 2008; Holladay et al., 2002; Norrby et al., 2007; van der Mooren et al., 2015]. "Premium IOLs" include all toric, aspheric, multifocal and accommodative designs.

State-of-the-art of toric [Novis, 2000] and aspheric IOL [Wang et al., 2012] designs aim at compensating the astigmatism and spherical aberration of the cornea, respectively. Furthermore, because of the replacement of the crystalline lens by an IOL modifies the chromatic dispersion properties of the eye, new materials (with different Abbe number) and designs aim also at correcting the chromatic aberration of the eye [Weeber & Piers, 2012].

To date, there are different formulas for IOL power calculation [Fyodorov et al., 1975; Loyd & Gills, 1986]. SRK [Sanders et al., 1981] and SRK-II [Sanders et al., 1988] are regression formulas based on statistical retrospective analysis of post-operative data; and SRK-T generally uses a thin lens approach and different approximations for the cornea and lens in the paraxial regime [Sanders et al., 1990]. These formulas require pre-operative data of axial length and corneal power. However, compared to the sophisticated technologies and surgical skills involved in cataract surgery, more factors (e.g., corneal elevation, ACD, IOL model and ocular alignment) can be included to predict with higher accuracy the estimated lens position (ELP) and the final visual performance (especially in odd cases (keratoconus) or in patients treated with refractive surgery) [Aramberri, 2003; Canovas & Artal, 2011; Hoffer, 1993; Hoffer et al., 2015; Holladay et al., 1988; Norrby et al., 2007; Ortiz et al., 2013; Rosales & Marcos, 2007; Savini & Hoffer, 2011].

Improvements in aberrometry and in biometry imaging techniques has opened the possibility of considering new factors for providing a better IOL power calculation and finding the proper IOL placement. Ray-tracing allows for exact calculations, retaining only the errors inherent to biometrical measurements, being a better competitor compared with paraxial optical methods [Barbero & Marcos, 2007; Canovas & Artal, 2011; Einighammer et al., 2009; Ortiz et al., 2013; Piers et al., 2004; Rosales & Marcos, 2007; Zhu et al., 2011].

Double-pass retinal image quality was first used to evaluate objectively optical quality after cataract surgery. Barbero et al. [Barbero, 2003] and Guirao et al. [Guirao et al., 2002] measured for first time *in vivo* corneal and total aberrations after cataract surgery, showing the contribution of the IOL to total aberrations and the effect of the corneal incision. Piers et al. [Piers et al., 2004; Piers et al., 2007] showed that correcting ocular spherical aberration improved spatial vision in the best-focus position without compromising the subjective tolerance to defocus. Recently, Barbero et al. [Barbero et al., 2011] designed isoplanatic aspheric monofocal IOLs for compensating optical aberrations on- and off-axis. To date, there is also ongoing research in compensating monochromatic and chromatic high order aberrations; however, chromatic aberration correction might have an effect on depth of focus and therefore in visual performance [Weeber & Piers, 2012]. In this thesis we make use of our custom-developed LRT to evaluate *in vivo* the longitudinal chromatic aberration in patient implanted with different IOL designs (Chapter VI).

Whereas the description of the optical performance of these patients is interesting, the evaluation of the pre-operative biometrical parameters and the identification of the sources of the aberrations (e.g., corneal incision, crystalline lens location and volume, capsule, IOL location, tilt, decentration, IOL material) are essential for customizing cataract surgery [Phillips et al., 1988; Rosales & Marcos, 2007]. Recently, Ortiz et al. [Ortiz et al., 2013] for the first time showed with distortion-corrected OCT a full 3-D quantitative analysis of the anterior segment geometry of patients before and after cataract surgery, describing with a single instrument: corneal geometry, corneal thickness, anterior chamber depth/lens position, lens thickness/IOL thickness, lens tilt and decentration, IOL tilt and decentration.

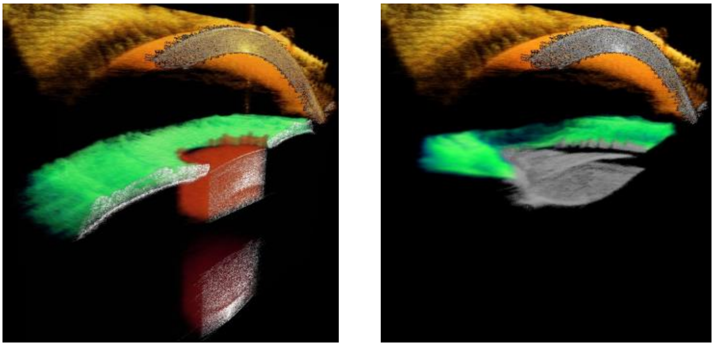

Figure 1.16. OCT 3-D *in vivo* biometry before and after cataract surgery (left: crystalline lens; right: IOL).

1.8. Open questions addressed in this thesis

Accurate optical and geometrical characterization of the anterior segment of the eye will not only increase knowledge on the contribution of every optical element (cornea and crystalline lens) to ocular optical quality, but will also have an impact on the understanding of the mechanism of action of different clinical treatments (intracorneal ring segment and intraocular lenses) for different conditions and/or pathologies of the eye (keratoconus, presbyopia and cataract).

In this thesis we use novel technology to characterize optically and structurally the anterior segment of the eye in a series of very prevalent conditions and their surgical corrections.

Keratoconus and ICRS treatment: ICRS is a well-tolerated and effective treatment for keratoconus, offering in most cases long-term improvement in refractive and keratometric measurements. However, to date, surgical ICRS nomograms are rather qualitative, based on few input data and there is no a universal standard protocol for ICRS implantation. Furthermore, there is little knowledge on the achieved optical quality and the mechanism of action of the ICRS implanted in the cornea and its effect on both anterior and posterior corneal surfaces. So, new objective methods for ICRS evaluation are needed in order to improve the predictability of the surgical technique.

Some unsolved questions are: *What is the longitudinal effect of the ICRS on both anterior and posterior corneal surfaces? Are ICRS stable inside the cornea with time? Does a redistribution of the corneal thickness occur after ICRS implantation? Does ICRS implantation delay keratoconus progression? What is the optical quality of keratoconus patients before and after ICRS implantation?*

Accommodation: To date, most of *in vivo* biometric information in the accommodating crystalline lens is limited to axial biometry (e.g., crystalline lens thickness) and radius of curvature, however there is limited information on 3-D crystalline lens shape in the relaxed and/or accommodated state.

A deeper analysis of 3-D lens shape and geometry is crucial for understanding its optical properties, and will help to understand *(1) the compensatory role of the crystalline lens aberrations to corneal aberrations (in particular, astigmatism and spherical aberration), (2) the mechanisms of accommodation of the crystalline lens, (3) the role of the crystalline lens in the development of refractive errors (e.g., myopia), (4) the age-related changes of the crystalline lens optics and (5) will help to increase the predictability of intraocular lens (IOL) implantation.*

Presbyopia/Cataract and Intraocular lenses: Customized IOL designs are intended to mimic the natural young crystalline lens properties. Currently, there are different IOL designs aiming at correcting spherical aberration, compensating chromatic aberration, providing multifocality and/or restoring accommodation. Thus, accurate biometric anterior segment parameters and ocular aberrations are crucial for designing the optimum IOL and for planning the cataract surgery.

However, there are still different open questions: *What is the optical quality of IOL patients? Do the accommodative IOLs perform as expected? Do the accommodative IOLs provide objective accommodative range? What is the depth-of-focus of patients implanted with IOLs? To what extent chromatic aberration changes with IOL implantation? What is the role of chromatic aberration in pseudophakic patients?*

1.9. Goals of this thesis

The main purpose of the thesis is the understanding of the relationship between the optical quality and the geometrical properties in clinical applications for the anterior segment of the eye.

The specific goals are:

1. To establish Laser Ray Tracing and OCT as validated imaging techniques for objective measurements of ocular aberrations and the anterior segment geometry of the eye. To design an external accommodative/fixation channel in both systems and to establish the *in vivo* experimental protocols for measuring accommodation in young subjects and for measuring clinical patients (keratoconus & ICRS, presbyopia and cataract & A-IOL/IOL).

2. To develop an algorithm for the evaluation of OCT-based corneal aberrations. Accuracy and possibilities of the methodology will be tested by comparing corneal to total aberrations (Laser Ray Tracing) in keratoconus subjects (before and after ICRS implantation).

3. To investigate longitudinally the effect of ICRS on keratoconic corneas by accurate evaluation of corneal geometrical changes and ICRS monitoring using 3-D quantitative OCT.

4. To study the optical performance of keratoconus before and after ICRS implantation.

5. To study *in vivo* the topographical changes of the crystalline lens with accommodation.

6. To evaluate the 3-D IOL position, objective accommodative response, optical performance and depth of focus in eyes implanted with accommodative IOLs.

7. To measure *in vivo* and objectively chromatic aberrations in patients implanted with IOLs.

1.10. Hypothesis

Combining technological advances in aberrometry and OCT imaging techniques with dedicated processing tools will lead to understand the links between optical and structural properties in the accommodating eye, as well as in clinical eyes before and after treatment. These advances will contribute to customize diagnosis and correction.

1.11. Structure of this thesis

The body of this thesis is structured as follows:

The current introductory chapter ***(Chapter I)*** presents the background, state of the art and motivation of the thesis.

Chapter II presents a description of the methods used throughout this thesis and common to the different studies, including a description of the Laser Ray Tracing (for ocular aberration measurements), a description of the SD-OCT (for geometrical and aberration measurements of the anterior segment of the eye), and its calibrations, validation and processing tools. Finally, a description of the optical quality metrics is also showed.

Chapter III validates the OCT as a corneal aberrometer by comparing corneal aberrations (OCT) to total aberrations (LRT) on eyes with predominantly corneal aberrations (keratoconus, before and after ICRS surgery). Also, this chapter presents longitudinal measurements of keratoconic corneas upon ICRS implantation to characterize the geometrical properties, anterior and posterior corneal surface shape and the 3-D positioning of the ICRS with time.

Chapter IV presents *in vivo* OCT measurements of anterior and posterior crystalline lens surface elevation in accommodating eyes and shows relationships between anterior segment surfaces. These measurements allow a better understanding of the contribution of the different ocular components to overall optical quality of the eye in the relaxed and accommodated state.

Chapter V presents measurements *in vivo* of the optical aberrations (LRT) and geometrical properties (OCT) in patients implanted with the accommodative IOL (Crystalens AO) for different accommodative demands. Objective measurements of the accommodative response and direct 3-D intraocular visualization will shed light into the mechanism of action of the accommodative IOLs.

Chapter VI explores the role of longitudinal chromatic aberration (LCA) in eyes implanted with different IOL models. The impact of LCA on retinal image quality was analyzed to better understand the optical implications of IOL.

Finally, the ***Epilogue*** enumerates the conclusions of the thesis and identifies the new open questions arising from this work that can be addressed in future work

Chapter II. ***MATERIAL & METHODS***

In this chapter we will describe the custom-developed experimental techniques and the routines used in this thesis. Specifically, the custom-Laser Ray Tracing (LRT) technique used to measure the ocular aberrations (in Chapters III, V and VI) and the custom SD-OCT to measure the 3-D geometrical properties of the anterior segment of the eye (in Chapters III, IV and V).

The author of this thesis has been the main contributor in redesign and modifying those instruments, implementing fixation/accommodation external channels in the LRT and OCT, developing specific algorithms for analyzing aberrations with OCT, designing the experiments and developing the measurement protocols. He led, in collaboration with Carlos Dorronsoro, Lourdes Llorente and Susana Marcos, the modification, adaptation and calibration of the LRT system for measuring aberrations with accommodation and in prevalent anterior segment conditions (such as keratoconus and IOL patients). He also developed, calibrated and tested the custom-SD OCT system in collaboration with Ireneusz Grulkowski, Michalina Gora and Maciej Wojtowski from Nicholaus Copernicus University (Torun, Poland) and Sergio Ortiz, Damian Siedlecki, Enrique Gambra, Alberto de Castro and Susana Marcos at the Visual Optics and Biophotonics Lab (Madrid, Spain).

2.1. Laser Ray Tracing (LRT): ocular aberrations

The experimental measurements of ocular aberrations in this thesis were performed using Laser Ray Tracing (LRT) technique with new implementations (e.g., accommodation channel, retinal camera, Badal system). The technique has been described in detail in previous theses (Lourdes Llorente and Carlos Dorronsoro).

2.1.1. LRT: basic concepts

The LRT technique was first applied to measure ocular aberrations in human eyes in 1997 [Molebny et al., 1997; Navarro & Losada, 1997]. LRT is a double pass technique, since light is delivered into the eye and the reflection from the retina is captured on a CCD camera.

In the *first pass*, the pupil of the eye is sequentially sampled with laser pencils parallel to the optical axis. Each ray is deflected by a specific angle α depending on the slope of the wavefront at a particular point on the pupil plane (defined by the optical characteristics of the surfaces it goes through), and therefore will impact the retina at a specific point. In an aberration-free system, all rays superimpose on the same retinal location. However, when optical aberrations are present, the rays hit the retina at different positions.

In the *second pass*, the light is reflected off the retina, exiting the eye through the whole pupil, and forming an aerial image of the double-pass (on *one-and-a-half-pass*) point spread function (PSF) on a plane conjugated with the retina, but tilted an angle α from the chief ray (entering the eye through the pupil center). Angle α is proportional to the slope of the wavefront at the point where the incoming beam entered the eye. This image is collected by a high-resolution cooled CCD camera. Although in this second pass the aberrations of the eye affect the PSF, its position relative to the reference is not affected (as long as the PSF is contained within the isoplanatic area of the retina). Therefore, the angles are preserved, and the ray (transverse) aberration can be computed from the distance between the position (centroid) of the aerial image corresponding to each pupil location, and that corresponding to the aerial image for the reference ray (chief ray).

The sampled pupil size is defined by the diameter of the sampling pattern projected on the pupil, and therefore, can be controlled by software (as long as the pupil is at least of the same diameter to be programmed).

The reconstruction of the wavefront from the slopes of the wavefront, measured at each point, is performed considering that the local slope of the wavefront (partial derivatives) is proportional to the ray aberration.

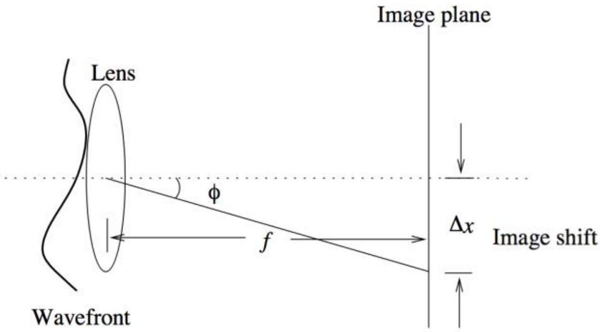

Figure 2.1. Illustration of wavefront slope and image shift through a lens.

The image shift is linerarly proportional to the angle ϕ and the focal length f. With a theoretical derivation, the image shifts in x and y directions are related to the average wavefront slopes in x and y directions, respectively, as:

Equation 2.1: $$\Delta x' = \frac{1}{R_p}\frac{\partial W(\overline{\xi},\overline{\eta})}{\partial \xi}; \quad \Delta y' = \frac{1}{R_p}\frac{\partial W(\overline{\xi},\overline{\eta})}{\partial \eta}$$

where $\xi=\xi/R_p$ and $\eta=\eta/R_p$ are dimensionless canonical pupil coordinates and R_p is the pupil radius.

The wave aberrations are reconstructed by integrating the slopes of an array of beams intersecting the eye´s entrance pupil. Usually, least-square estimation is used for phase reconstruction. A modal reconstruction based on the expansion of the derivatives of the wave aberration as a linear combination of a set of basic functions (the derivatives of Zernike polynomial expansion) was used for analyzing wavefront aberrations.

2.1.2. LRT: setup

The LRT consist of three channels:

(1) *Illumination channel* (incoming rays), with two possible light sources (green: 532 nm; infrared: 786 nm).

(2) *Pupil and Retinal channel* (outgoing). Pupil camera captures the corresponding image of the eye´s pupil simultaneously with the retinal spots on the retinal CCD. Retinal camera captures the light reflected back from the retina

(3) *Accommodation/Fixation channel*. An open-field external fixation channel was incorporated to stimulate accommodation. The subjects viewed the stimulus monocularly and the desired accommodative demand was produced by changing the fixation distance (allowing static measurements of aberrations under steady accommodation).

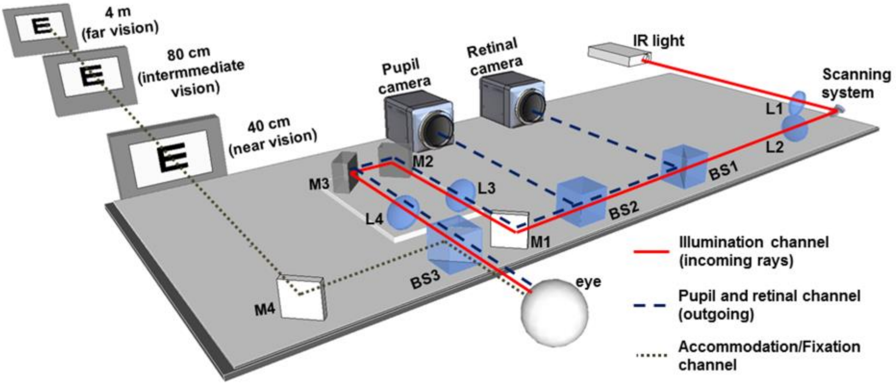

Figure 2.2. Scheme of the custom-LRT at the VioBio lab (Instituto de Óptica "Daza de Valdés").

The light source can be selected between two diode lasers emitting in green (532 nm; Brimrose, Baltimore, MA, USA) and infrared wavelengths (786 nm; Schäfter+Kirchhoff, Hamburg, Germany). Both lasers are attenuated below safety limits using neutral density filters: the maximum permitted exposure power thresholds for 532 nm and 786 nm are 6.9 µW and 7.6 µW respectively. Exposure times for a typical run with 37 samples were about 1.5 seconds, being controlled by an electronic shutter (Vincent Associates, Rochester, NY, USA).

The XY scanner (mod. 6210, Cambridge Technologies, Lexington, USA) consists of two rotating mirrors that deflect the incoming unexpanded laser pencil in such a way that in combination with collimating lenses (L1 and L2, f'=50.8 mm) compose the sequential sample pattern. Due to the distance between the two mirrors (~5 mm), some astigmatism is induced in the system, and therefore a trial lens attached to the collimating lens (2.25 D at 90 deg) is used to compensate this astigmatism. Lens L1 (f'=50.8 mm) forms the image of the laser waist on the scanner in order to obtain the smallest sampling aperture on the pupil plane (~400 µm). Different sampling patterns can be configured in the scanner. In this thesis we only uses the hexagonal pattern (37 rays).

Channels 1 and 2 share a Badal system for defocus compensation. The Badal system is formed by lenses (L3 and L4; f'=100 mm; that form an afocal system of magnification x1) and mirrors (M1, bends the optical path to obtain a more compact device, and M2 and M3, compose the focusing block). The Badal system allows changing the vergence of the rays (and hence defocus) without changing magnification (by moving the mirrors instead of the lenses), ensuring therefore that the pupil magnification or the sampling density will not be affected by defocus correction. Spherical error correction ranging from -12 D to +12 D can be induced with this system to allow measurements on keratoconic eyes. P, marks the position of a pupil conjugate planes; and R, marks the position of retinal conjugate planes. The versatility of the LRT and its dynamic range allow us measurements on keratoconic corneas

The light reflected off the retina is collected by a cooled highly sensitive CCD camera (12 bits, 30 frames per second with 2x2 binning, 1024x1024 pixels, pixel size: 14 µm x 14 µm, nominal maximum quantum efficiency: 20% (700 nm). Model 1M15, Dalsa, Waterloo, Canada), conjugate to the eye retinal plane (retinal channel). In addition to record aerial images, this camera can display them in real time allowing to find objectively the best focus position while assessing the aerial image for a centered ray. During the measurement, the retinal camera is synchronized with the scanner and the pupil camera.

In the pupil channel, a CCD (8 bits, 60 Hz (video), 646 (horizontal) x 485 (vertical) pixels, pixel size: 7.4 µm x 7.4 µm. Model XC-55, Sony Corp., Tokyo, Japan) continuously monitors the pupil and records pupil images during the measurement. Pupil monitoring prior to the measurement helps to verify that everything is ready for the measurement, assisted by marks superimposed on the pupil image in the control program: pupil located on the corresponding plane (pupil edges focused), alignment of the center of the pupil and the optical system (centration cross), suitability of the sampling pattern to the pupil diameter (small circumferences of different diameters to estimate pupil size). This pupil control becomes critical for avoiding back-reflected light from the edges of the ICRS and the IOL.

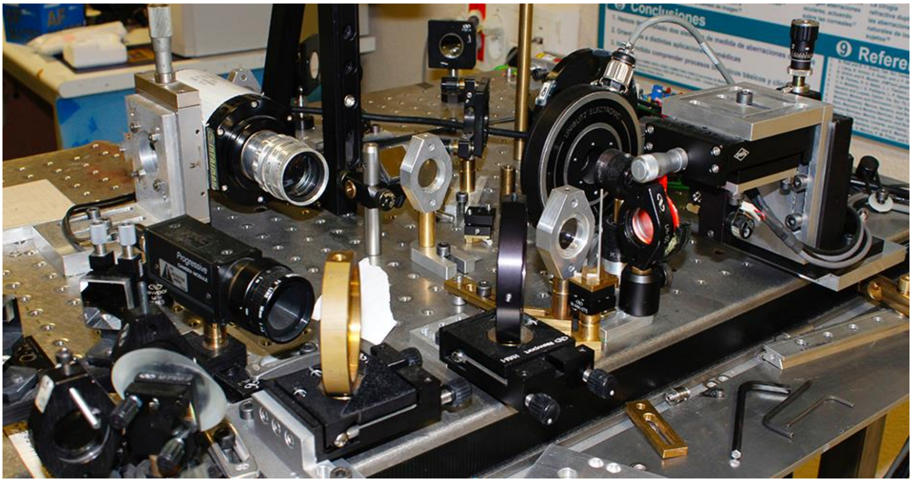

Figure 2.3. Custom-LRT at the VioBio lab (Instituto de Óptica “Daza de Valdés”).

2.1.3. LRT: control and analysis software

The control and analysis software used in this thesis was developed previously in our group by Lourdes Llorente and Carlos Dorronsoro theses. The control software development was written in Visual Basic (Microsoft Corp., USA) combined with Matlab (Mathworks, Natik, MA) scripts.

The system control software operates and synchronizes the different elements (scanner, shutter and cameras) for the measurement, assisting in some other operations such as alignment of the pupil and the optical system. Measurements, calibration parameters and measurement conditions are saved in a structured way using excel files.

The software to estimate the ocular aberrations from the set of aerial images was developed in Matlab (Mathworks, Natik, MA). In brief, raw images are processed in order to isolate each aerial image and locate the corresponding centroid. Then, the relative distance of each centroid to that of the central ray is calculated (transverse aberration), and the wave aberration is then estimated by fitting the transverse aberration corresponding to each sampled point to the derivatives of the Zernike polynomials, using a least squares method.

2.1.4. LRT: calibration

Two parameters (offset and slope) driving each scanner response to digital signals were set up in order to use image plane coordinates instead of electrical voltages. The offset was chosen to obtain a laser beam aligned with the optical axis of the setup when coordinates (0,0) were selected. The slope, or ratio *scanner_voltage / laser_displacement*, it was selected to obtain the displacement of the laser spot necessary to obtain the desired pattern. For this purpose, a screen with a square grid pattern (1 mm squares) was placed at the pupil plane with the shutter open to see both the spot and the grid. The ratio *scanner_voltage / laser_displacement* was calculated as 1/10 of the voltage needed to move 10 mm the laser spot impacting on the screen (as observed by the camera) and taking the grid as a reference.

The equivalence between pixels and deviation angles in the retinal camera images was determined by imaging a metal caliper in a plane conjugate to the sensor, i.e. at the focal point of lens L3. We estimated that each pixel in the image subtends 0.37 mrad. This value is used in the processing program to compute transverse ray aberration from the deviations of the spots in the CCD.

The pupil camera is used to ensure alignment of the eye pupil with the optical axis of the system, to visualize the sampling pattern superimposed to the pupil, and to assess distances, such as the pupil diameter or pupil misalignment. We ensured that the centration reference is superimposed with the optical axis, by placing a screen at the pupil position and imaging a laser beam with the scanner is in its centered position. The position of the spot in the image is calibrated as the instrument axis. We calibrated the scale (equivalence between pixels and millimeters at the pupil plane of the camera) by imaging a graph paper screen.

As previously mentioned, some astigmatism is induced by the scanner due to the distance between its two rotating mirrors. The theoretical astigmatism induced due to the distance between the mirrors of the scanner (d=4.9 mm) depends also on the focal length of the collimated lens used (f'=50.8 mm).

Equation 2.2:

$$Astigmatism\ scanner = \frac{d}{\left(f' + \frac{d}{2}\right)\left(f' - \frac{d}{2}\right)} = 1.88\ D$$

Some astigmatism can also be introduced by other elements of the setup, such as lenses not completely perpendicular to the optical axis. We then estimated the residual astigmatism by measuring the aberrations of a non-aberrated artificial eye. We computed the value of the astigmatism from the coefficients Z_2^{-2} and Z_2^{2} (oblique and perpendicular astigmatism respectively) using the equation:

Equation 2.3: $$J_0 = \frac{-2\sqrt{6}Z_2^2}{R^2}\ ;\ J_{45} = \frac{-2\sqrt{6}Z_2^{-2}}{R^2}\ ;\ C = -2\sqrt{J_0^2 + J_{45}^2}\ ;\ \alpha = \frac{1}{2}\arctan\frac{J_{45}}{J_0}$$

> where R is the pupil radius, Z_2^{2} the H/V (horizontal/vertical) astigmatism (Zernike coefficient) and Z_2^{-2} the oblique astigmatism (Zernike coefficient).

A cylindrical trial lens of -2.25 D (axis at 90 deg), placed right after the collimation lens (L2) of the scanner minimized the astigmatism.

We verified that the sampling pattern selected (37 spot positions) was precisely delivered, by projecting the beams on a screen at the pupillary plane and analyzing the images captured by the pupil camera. The mean deviation from the expected position across all 37 spot positions was 0.05±0.04 mm (0.08±0.05 mm and 0.03±0.02 mm for X and Y coordinates respectively). These differences are smaller than those typically resulting in real eye measurements due to motion artifacts.

In addition, to make sure that the processing program was correct; we confirmed that when computing transverse ray aberrations from the wave aberration (obtained after processing the experimental data), the corresponding spot diagram position matched the spot diagram obtained experimentally.

The Badal system included in the setup to compensate defocus was also calibrated. Moving the translational stage with two mirrors (focusing block) introduces a change in vergence that, for a focal length of 100 mm for each Badal lens, corresponds to 0.2 D/mm (1 D each 5 mm). The 0 D position in the focusing block scale was determined using a non-aberrated emmetropic artificial eye. Trial lenses in front of the artificial eye were used to check the compensation of defocus by the focusing block.

We also measured the aberrations of the nominally aberration-free artificial eye. For 3rd and higher-order aberrations we found that the RMS departure of the wavefront from the reference sphere was much less than $\lambda/14$ (Marèchal criterion). For 2nd order aberrations (defocus and astigmatism), the residual values were subtracted from the measured values.

2.2. Spectral Domain Optical Coherence Tomography

2.2.1. SD-OCT: custom-setup

The SD-OCT system consist of roughly the same components: (1) light source, (2) interferometer, (3) galvanic scanning mirrors, (4) digital capture system, (5) processing system, and (6) focusing optics. A schematic diagram of the SD-OCT system used in this thesis can be seen in Figure 2.4.

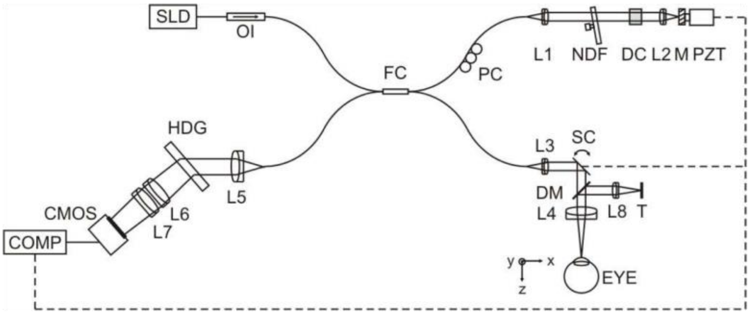

Figure 2.4. Experimental custom SD-OCT set-up, components: SLD superluminiscent diode, OI-optical isolator, FC- 80:20 Fiber coupler, PC-polarization controller, NDF-Neutral density filter, DC-dispersion compensator, DM-Dichroic mirror, T-Target, HDG-holographic volume diffraction grating, CMOS linescan camera, COMP computer.

The set-up is based on a fiber-optics Michelson interferometer configuration with a *superluminescent diode SLD* (λ_0 = 840 nm, $\Delta\lambda$ = 50 nm; Superlum, Ireland) as a light source, followed by an optical isolator (OI) joined by a fiber mate to a 80:20 fiber coupler (FC) in order to avoid the backreflected light from the reference and sample arms returning to the SLD. The light is split by the fiber coupler in two arms (reference and sample arms).

The *reference arm* consists of a polarization controller (PC) to optimize detection performance, a converging lens (L1) to produce a collimated beam, a neutral density filter (NDF) to increase or decrease the power of light in the reference arm, and a converging lens (L2) that focuses the light on the mirror (M).

The *sample arm* consists of a converging lens (L3) that collimates the light onto a XY galvanometric optical scanner to produce the horizontal/vertical raster of the sample, and finally a converging lens of 75 mm of focal length (L4) to collimate the chief rays of the beams and to focus the irradiance impinging the sample.

The light backreflected from both reference and sample arms is then recombined by the fiber coupler and it is led to the detection unit, which consists of a converging lens (L5, f'=XX mm) to collimate the light.

Finally, the *detection arm* of the OCT is composed by a spectrometer consisting of diffraction grating (plus two converging lenses, L6 and L7, to collimate the light) and a 12-bit line-scan CMOS camera with 4096 pixels (Basler sprint spL4096-140k; Basler AG, Germany).

The maximum effective acquisition speed of this system is up to 150000 A-Scans/s, although the typical speed used for the experiments in this thesis was 25000 A-Scans/s, since this configuration showed a very good balance between acquisition speed and resolution. The axial range of the instrument is 7 mm, and the theoretical axial resolution 3.4 µm in air. The signal to noise ratio (SNR) of the instrument was calibrated to be 97 dB.

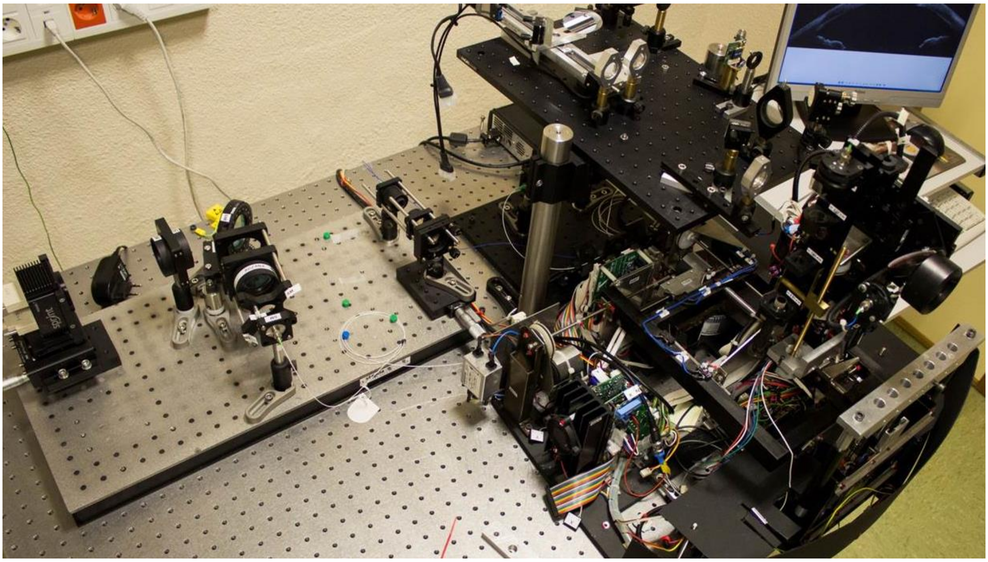

Figure 2.5. Custom SD-OCT at the VioBio lab (Instituto de Óptica "Daza de Valdés").

By performing multiple low coherence interferometry measurements at different lateral coordinates on a sample, a three-dimensional cross-sectional image of the scattering amplitude can be constructed.

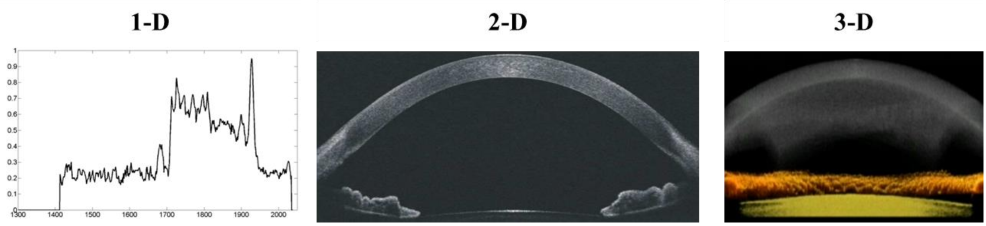

Figure 2.6. Left: 1-D, Axial (Z) scanning (Illustration of an A-Scan belonging to the corneal surface). Centre: 2-D, Axial (Z) scanning and transverse (X) scanning (Illustration of a B-Scan showing the cornea, iris and the anterior lens surface). Right: 3-D, Axial (Z) scanning and XY scanning (Illustration of the corneal, iris and anterior lens surface volume).

For measuring purposes, an additional beam splitter was placed in the sample arm in order to incorporate the *accommodation/fixation channel*. In this channel, a Badal system mounted on a motorized stage (VXM-1, Velmex) was used for compensating spherical refractive errors and for inducing accommodative demands. The Badal system is composed by two achromatic doublets of equal focal lengths (f´=150 mm), that form an afocal system of magnification x1, and two flat mirrors, which can be moved to change the optical path between the lenses. Vergence was changed with the Badal system from -10 D to 10 D and compensated with trial lenses placed on a pupil plane. In all conditions, the image remained in focus (in 1-D steps). A VisualBasic.Net software program wrote by Enrique Gambra to control the diopter steps in the Badal system.

The visual fixation stimulus is presented on an external screen controlled by a picoprojector. It consists of a white Snellen E (20/25 visual acuity) over a black background. Firstly, the target is aligned with the OCT axis and, secondly, for measuring in the line of sight we developed a script written in Matlab able to move the target each 0.5 pixels in the horizontal and vertical meridians.

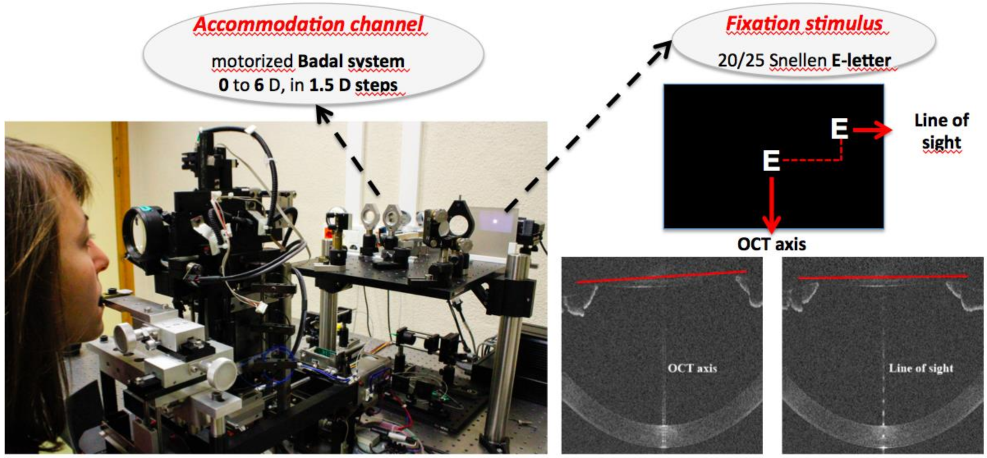

Figure 2.7. External accommodation and fixation channel implemented on the OCT. Illustration of the moving stimulus for further eye alignment.

2.2.2. SD-OCT: distortion correction

OCT images are generally subject to distortions: (1) *fan distortion*, arising from the scanning architecture, and resulting in a combination of geometrical aberrations, including field distortion, astigmatism and spherical aberration and (2) *optical distortion*, arising from refraction at the optical surfaces. Due to these distortions, OCT images need to be corrected for quantification. Fan (following instrument calibration) and optical distortion (through preceding surfaces) are corrected using 3-D ray tracing analysis. To correct the distortion in the images acquired in this thesis we have used an algorithm developed previously in our laboratory by Sergio Ortiz [Ortiz et al., 2010; Ortiz et al., 2011; Ortiz et al., 2009b] and modified by Eduardo Martinez-Enriquez [Pérez-Merino et al., 2015].

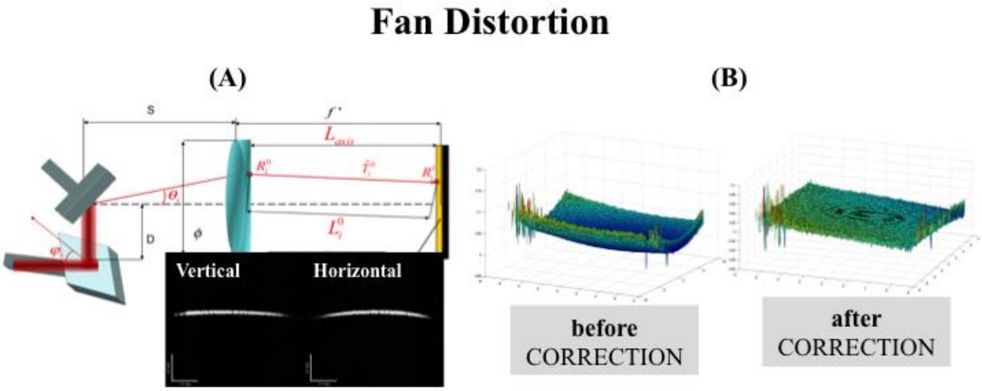

Figure 2.8. Fan distortion correction. (A) Separation of mirrors in the OCT scanning system results in different beam deflections after being refracted by a collimating lens, as a consequence a flat surface appeared curved in the horizontal and vertical meridians. (B) 3-D image of a plane mirror before and after fan distortion correction. Courtesy of Sergio Ortiz.

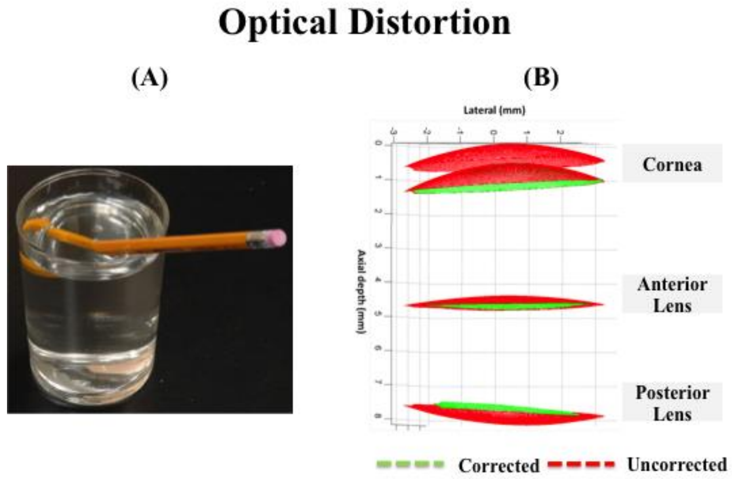

Figure 2.9. Optical distortion correction. (A) Illustration of optical distortion of a pencil in different refractive indexes (air and water). (B) Illustration of the effect of the 3-D distortion correction on the anterior segment surfaces (all surfaces are corrected axially from refractive index. Green: corrected volumes; red: uncorrected volumes). Courtesy of Sergio Ortiz.

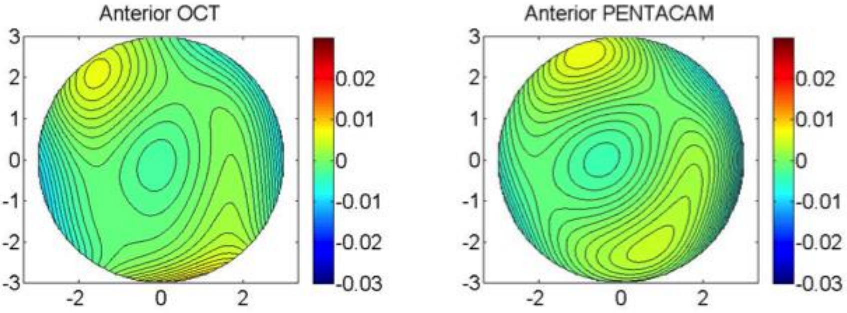

Figure 2.10. Validation of fan distortion correction in a normal subjetc (anterior corneal elevation map with OCT-distortion correction and Pentacam).

2.2.3. SD-OCT: image processing

The 3-D image processing tools developed to obtain quantitative information of the anterior chamber structures have been described by Ortiz et al. in prior publications [Ortiz et al., 2012a; Ortiz et al., 2013; Ortiz et al., 2012b; Ortiz et al., 2011]. Automatic image processing analysis includes *segmentation, data processing and quantification* of the anterior segment 3-D volumes. The corneal refractive index was taken as 1.376, the aqueous humor refractive index as 1.336, the crystalline lens refractive index was obtained from the age-dependent average refractive index expression derived by Uhlhorn et al. [Uhlhorn et al., 2008], in Chapter IV, and the clinical solutions refractive indices (ICRS, in Chapter III, and accommodative IOL, in Chapter V) were obtained from manufacturers. The routines were written in Matlab.

The algorithm is summarized in three different steps:

(1) 3-D image processing (*Volume clustering and multilayer segmentation):*

Volumes of connected points were identified as classes. The classes with a volume size below a certain threshold were eliminated. The threshold was estimated as a certain percentile within the range of 95-99% of the total number of connected points. After application of volume clustering, the number of classes was further reduced and the larger volumes (cornea, iris, crystalline lens, ICRS, IOL) were automatically classified. Once the volumes were classified, an algorithm based on first derivative boundary region identification extracted the position of the peaks of every A-scan and they were sorted by position and intensity.

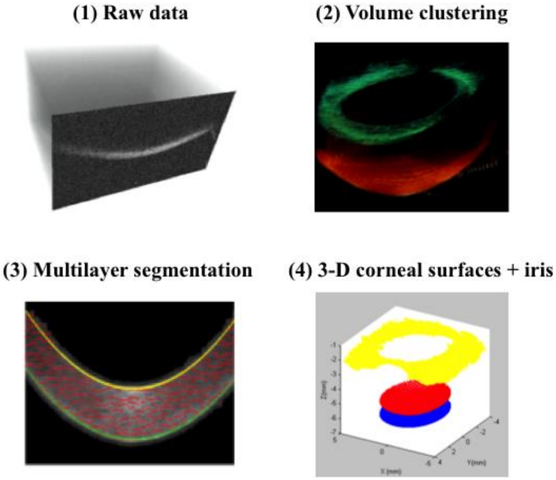

Figure 2.11. Illustration of the segmentation process.

(2). 3-D anterior segment data processing

Pupil center reference:

The pupil center was used to define the center of optical zone, and its center was considered as a fixed reference instead the corneal apex across measurements (pre-op and post-op). The pupil center was efficiently calculated from the clustered iris volume, by collapsing the cloud of points onto a 2-D image. The pupil center (lateral coordinates, Xpc and Ypc) and radii (Rx and Ry) were obtained from an ellipse fitting of the segmented edges using a Sobel edge detector. The evaluation of the plane at the estimated pupil lateral coordinates provided the axial component of the pupil center Zpc: $Zpc=-(AXpc+ BYpc+D)/C$. The coefficients A, B, C and D allows the calculation of the normal vector to the pupil plane, which provided the tilt angle of this plane with respect to the OCT coordinate system.

Specular reflection reference:

The specular reflection of corneal and lens/IOL images was also used as a fixed reference for further merging 3-D volumes.

Merging 3-D volumes:

We used the pupil and specular reflection points for merging anterior segment volumes. First, the corneal image was inverted, since for efficiency in the OCT focus range it was obtained in the opposite side of the Fourier transform. Then, the 3-D volumes of cornea/iris and posterior lens/iris were shifted to the pupil center reference with help of the specular reflections and rotated to superimpose the characteristic vectors of the corresponding pupil plane to those of the anterior lens-IOL/iris.

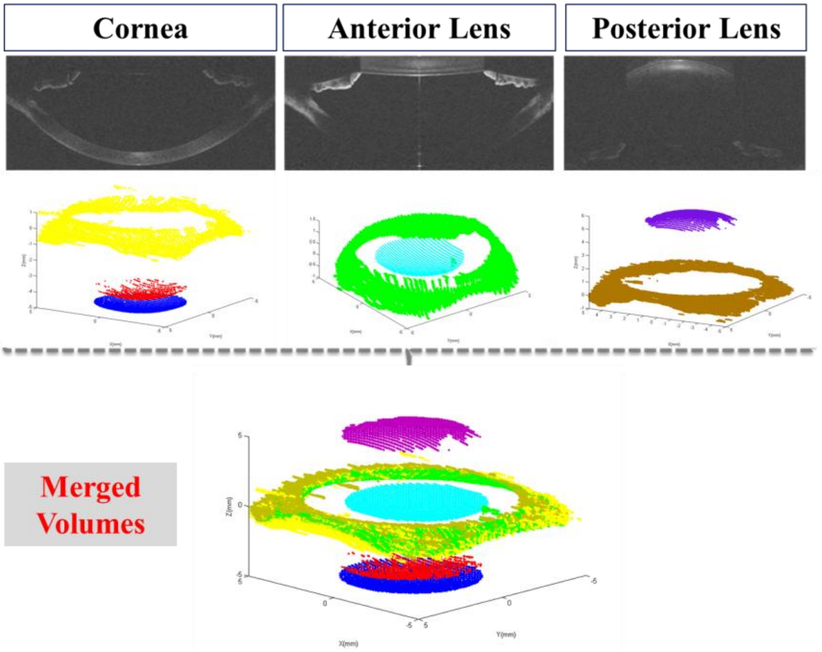

Figure 2.12. Illustration of the acquisition of an individual data collection of three volume acquisitions and merging to obtain a 3-D full anterior segment volume.

Distortion corrections (fan and optical):

Fan distortion correction was applied for the anterior cornea, and both fan and optical distortion corrections were applied for the multiple surfaces after the anterior corneal surface.

Geometrical distances calculation:

The optical distances were calculated by direct subtraction of the coordinates of the different surfaces.

(3) Surface analysis.

Surface fitting: sphere, ellipsoid, conicoid

Once the surfaces have been corrected from distortion, data were expressed in Euclidean coordinates and they were fitted by standard functions.

Sphere: from the sphere we obtained the radius (a) and the center of the sphere (x_0, y_0, z_0).

Equation 2.4: $$(x - x_0)^2 + (y - y_0)^2 + (z - z_0)^2 = a^2$$

Ellipsoid: from the ellipsoid we obtained 3 radii of curvature (a, b, c) and the center of the ellipsoid (x_0, y_0, z_0).

Equation 2.5: $$\frac{(x-x_0)^2}{a^2}+\frac{(y-y_0)^2}{b^2}+\frac{(z-z_0)^2}{c^2}=1$$

Conicoid: we assumed the ellipsoid definition, with $a=b$,

Equation 2.6: $$(x-x_0)^2+(y-y_0)^2-2(z-z_0)R+(Q+1)(z-z_0)^2=0$$

where (x,y) is the horizontal and vertical coordinates relative to their origin (x_0,y_0), and z and z_0 are the axial and axial origin coordinates. The fitting parameters are R and Q. R is the radius, $R=a^2/c$; Q is the conic constant, $Q=-(1-b^2/c^2)$.

Elevation and pachymetry maps

The maps were displayed in a square grid of 100x100 points in a 4 to 6-mm diameter, with respect to the pupil center. This representation did not require interpolation of the data, as the data were collected as a dense collection of B-scans, rather than across meridians.

The measured elevation was represented as the difference of corneal elevation from the reference sphere, where warm colors represented points that are higher than the reference surface and cool colors represented points below the reference. The pachymetry maps were calculated from direct subtraction of the posterior surface from the anterior surface, after distortion correction, and were represented using the HSV color map.

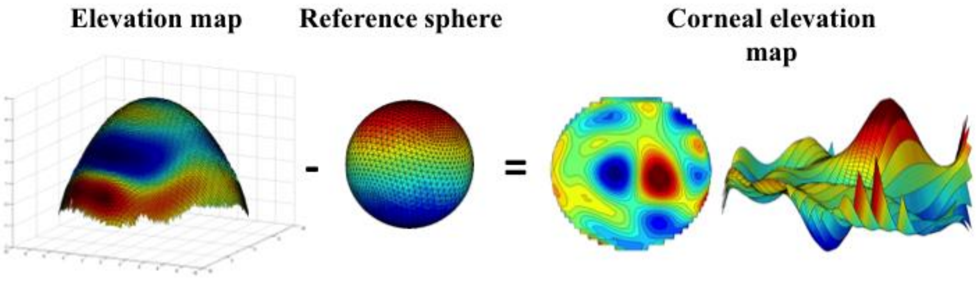

Figure 2.13. Illustration of the calculation of a topographic map as a direct subtraction of the elevation data minus the best fitted sphere.

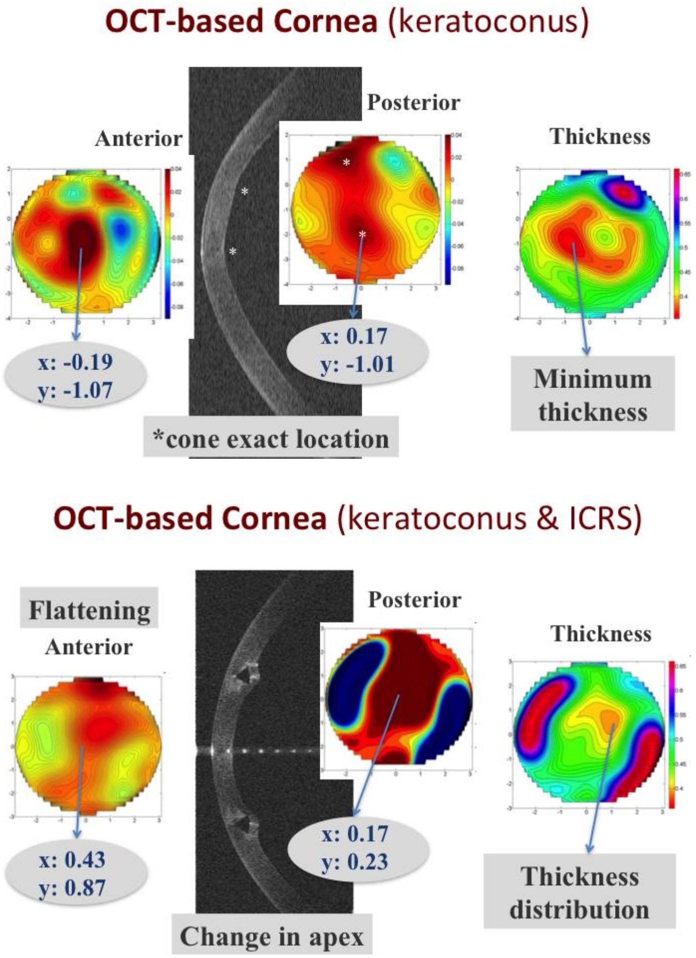
OCT-based Cornea (keratoconus)

OCT-based Cornea (keratoconus & ICRS)

Figure 2.14. Illustration of the elevation map in the anterior and posterior corneal surfaces and pachymetry in a keratoconic cornea before and after ICRS surgery.

Anterior segment biometry for clinical applications

The 3-D Euclidean distances were obtained by direct subtraction of the apices coordinates obtained from the fittings of the surfaces to spheres after optical distortion correction.

Crystalline lens/IOL decentration was defined as the lateral Euclidean distance between the crystalline lens/IOL center and the pupil center. Crystalline lens/IOL tilt was defined as the angle between the axis of the crystalline lens/IOL and the pupillary axis. The crystalline lens/IOL axis was defined as the vector that joins the apices of the anterior and posterior crystalline lens/IOL surfaces. The pupillary axis was defined as the vector that joins the center of curvature of the anterior cornea and the pupil center. The angle between axes was obtained by the scalar product of both vectors.

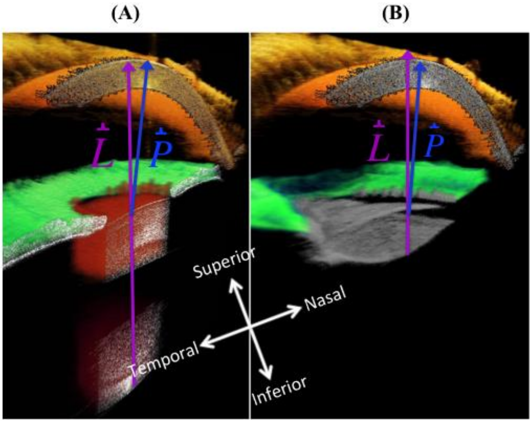

Figure 2.15. Illustration of the lens tilt evaluation: Pre-cataract surgery (a), and post-cataract surgery with IOL implantation (b). Vector P (in blue) is the pupillary axis, and L (in purple) is the Lens/IOL axis.

3-D ICRS positioning was described by the following parameters: 3-D ICRS depth (defined as the distance between the center of mass of the ICRS and the anterior corneal surface), and ICRS tilt (defined as the angle between the ICRS axis, normal to the ICRS plane, and the pupillary axis, normal to the pupil plane).

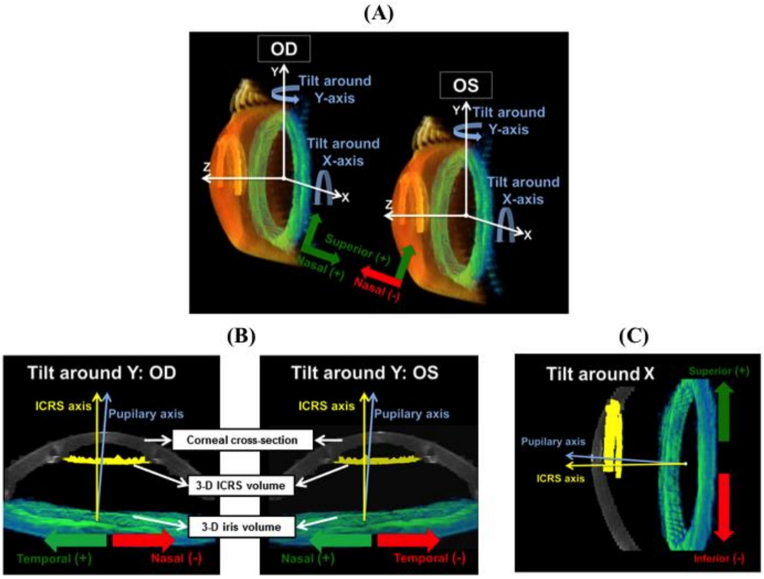

Figure 2.16. (A) Definition of the pupillary plane (and axis), ICRS plane (and axis) and ICRS tilt. (B) Sign convention ICRS tilt around the y-axis, for OD and OS. (C) Sign convention of ICRS tilt around the x-axis.

2.2.4. OCT-based corneal aberrometry

Corneal and ocular wave aberrations were computed directly from the ray tracing analysis. The elevation data obtained from OCT distortion-corrected corneal surfaces were fitted by Zernike polynomial expansion (up to 6th order) and exported to ZEMAX (Radiant ZEMAX; Focus software, Tucson, Arizona, USA) for virtual ray tracing analysis, by using a finite difference method to evaluate the normals to the surface.

A complete ray tracing procedure provides a discrete set of local measurements of the wave aberration. ZEMAX uses a modal reconstruction with a standard least squares algorithm fitting to a Zernike expansion. Matlab was used to create a suitable input file into ZEMAX for calculating corneal wavefront aberrations (ZEMAX DDE toolbox).

The object (light source) is set at infinity. The point source at infinity will be best focused on the retinal surface after iteration (we use the best focus position as is the position that minimizes the root-mean-square wavefront error). Refractive indices of 1.376 and 1.334 were used for the cornea and aqueous humor, respectively. Wave aberrations were calculated for IR LRT-wavelength (786 nm) in the pupil plane, placed at 3.47 mm from the anterior corneal surface (in keratoconic corneas), by tracing an array of 64x64 collimated through a 1-surface (anterior cornea only) or 2-surface (anterior and posterior cornea, separated by corneal thickness) eye model. In the 1-surface model, the refractive index after the anterior corneal surface was set to 1.334. The contribution of the posterior corneal surface was obtained from direct subtraction of the anterior corneal surface aberrations from corneal aberrations. Also, a 4-surface eye model (anterior and posterior cornea, anterior and posterior lens/IOL, separated by corneal thickness, ACD and lens/IOL thickness) was developed.

The merit function is defined by the operand “ZERN”. The parameters are set as Term = 1,2,3… in the order of Zernike coefficients in ZEMAX (by previous conversion from OSA to ZEMAX Zernike notation), Samp = 2 (pupil sampling = 64x64), field = 1 (only one field is set in our calculations), Type = 1 (Zernike Standard Coefficient), and Zernike coefficients of the wavefront aberrations are input at the column of the “target” values (the weight of each coefficient is set equally). Once the merit functions were set, the optimization is performed.

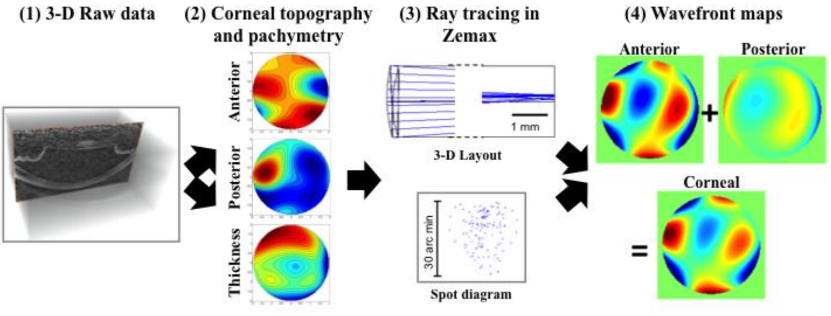

Figure 2.17. Illustration of the computation of corneal aberrations from OCT data.

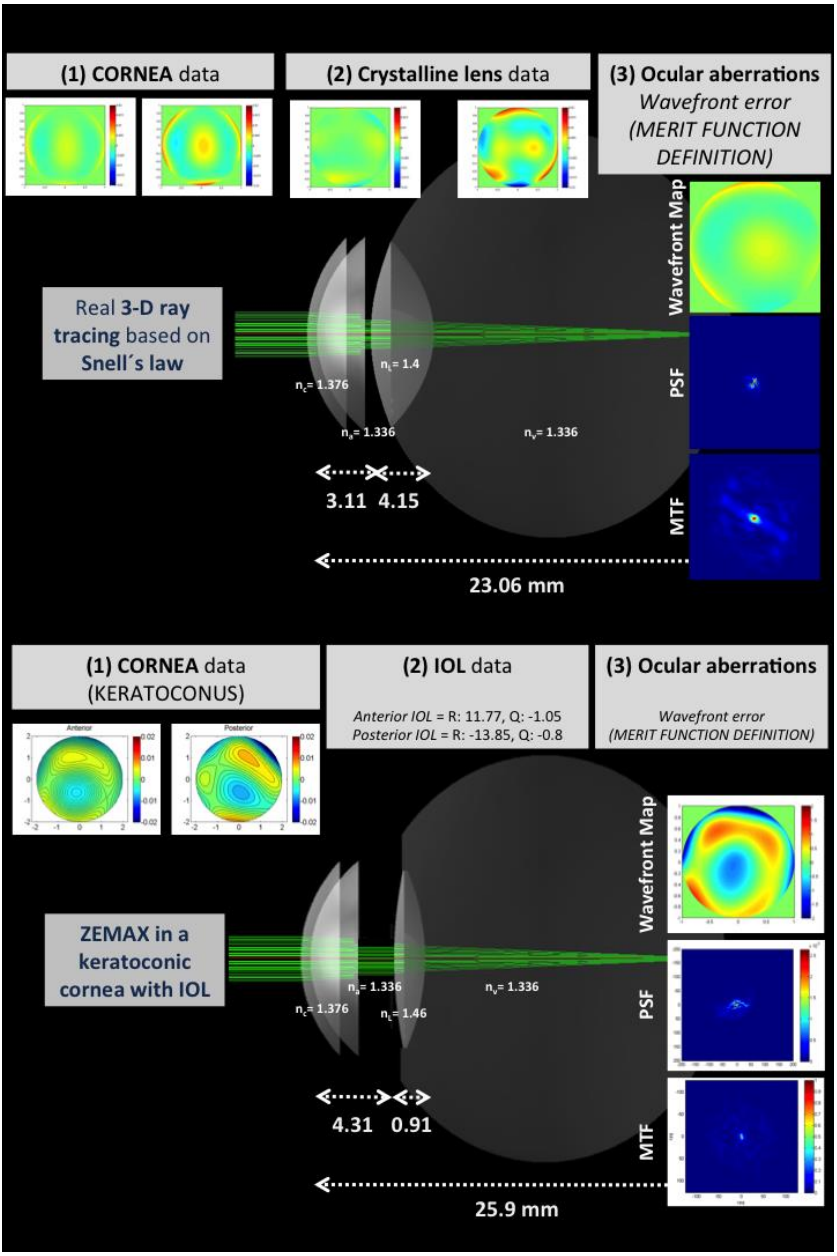

Figure 2.18. Illustration of the computation of total aberrations, PSF and MTF from OCT data (Zernike coefficients of the corneal and lens surfaces and axial distance, left eye). Top: left eye of the author; Bottom: keratoconus eye with IOL.

2.3. Optical quality metrics

We specified the optical quality of the eye in two different reference planes, defining: *pupil plane metrics* (e.g., Root Mean Square, RMS) and *image plane metrics* (e.g., Point Spread Function (PSF), Optical Transfer Function (OTF), Modulation Transfer Function (MTF), Strehl Ratio). Because of visual performance is a combined effect of retinal imaging and visual perception, the image plane metrics are in general better than the pupil plane metrics [Applegate et al., 2006; Cheng et al., 2003a; Cheng et al., 2004].

In this thesis we described the optical quality by using the following metrics: RMS, PSF, OTF, MTF, Strehl Ratio and Visual Strehl.

Root Mean Square (RMS) measures the deviation of the wavefront from a perfect plane wave. RMS is computed directly from the Zernike coefficients. The calculation of RMS error can be done either individually or grouped arbitrarily (coma, trefoil and spherical, among others). A flat wavefront has a RMS = 0, while an aberrated wavefront has a RMS > 0.

Equation 2.7:

$$RMS = \sqrt{\sum_{n,m} {c_n^m}^2}$$

where c_n^m is the Zernike coefficient corresponding to the order n and frequency m.

Point Spread Function (PSF) is the two dimensional distribution of light in the image plane, i.e. is the image of a point object through the optical system. The PSF for a perfect optical system (only limited by diffraction) is the Airy disk. The presence of ocular aberrations causes the light to spread out over an area and the corresponding PSF is considerably broader than the aberration-free PSF for the same pupil size, particularly for pupils higher than 3 mm.

Basically, the PSF is calculated as the squared magnitude of the inverse Fourier transform of the pupil function. The pupil function, *g(x',y')*, defines how light passes through the pupil (i.e. wavefront aberration and amplitude function weighted with the styles-Crawford effect) and it may be defined as 1 within the pupil area and 0 elsewhere.

Equation 2.8: *Pupil function:*

$$g(x',y') = p(x',y')\exp(i\frac{2\pi}{\lambda}\,W(x,y))$$

where *p(x',y')* is a circle that defines the aperture of the eye, *w(x',y')* is the wavefront aberration of the subject and λ the wavelength used for calculations (550 nm)

Equation 2.9:

$$PSF = |FT\big(g(x',y')\big)|^2$$

Optical Transfer Function (OTF), is the frequency response of an optical system. OTF is the autocorrelation of the pupil function, or equivalently, the Fourier transform of the PSF. The OTF is a complex function that measures the loss in contrast in the image of a sinusoidal target, as well as any phase shifts. The modulus of the OTF is the *Modulation Transfer*

Function (MTF), which represents the decrease in the contrast as a function of the spatial frequency.

Equation 2.10: $$OTF = FT(PSF)$$

Equation 2.11: $$\mathrm{MTF} = |OTF|$$

Strehl Ratio, is a scalar metric used to describe the quality of the PSF in an eye. Basically, the Strehl ratio describes the reduction in the peak power of the point image.

In the spatial domain, it can be calculated directly from the PSF. It is defined as the maximum value of the PSF in the presence of aberrations, normalized by the maximum of the diffraction limited PSF for the same pupil size (i.e., is the ratio of the PSF irradiance value at the ideal image point of an aberrated optical system to the PSF irradiance value at the ideal image point for an equivalent diffraction-limited system). The Strehl Ratio ranges from 0 to 1, with 1 defining a perfect optical system.

In the frequency domain, the Strehl Ratio is computed as the volume under the MTF of an aberrated system normalized by the diffraction-limited MTF, for the same pupil diameter.

Equation 2.12: $$Strehl\ Ratio = \frac{PSF_{aberrated}(x',y')}{PSF_{ideal}(x',y')}$$

As the Strehl Ratio includes in the calculation regions of the MTF with spatial frequencies beyond those relevant to the visual system, a new metric was introduced to adapt the definition to visual optics (Visual Strehl).

The *Visual Strehl* is computed as the volume under the visual MTF, obtained from the overlapping of the MTF with the inverse of a general neural transfer function, normalized to diffraction limit.

The neural sensitivity, function of the spatial frequency, is a common measurement of the neural performance. In a similar way as the optical MTF, it is possible to define and measure the neural MTF, and the product of the neural and optical MTFs gives the *Contrast Sensitivity Function (CSF)* of the eye.

Equation 2.13: $$\mathrm{CSF} = MTF_{optical} * MTF_{neural}$$

Equation 2.14: $$VSOTF = \frac{\int_{-\infty}^{\infty}\int_{-\infty}^{\infty} CSF_N(f_x,f_y) * |Re\{OTF(f_x,f_y)\}| df_x df_y}{\int_{-\infty}^{\infty}\int_{-\infty}^{\infty} CSF_N(f_x,f_y) * \{OTF(f_x,f_y)\} df_x df_y}$$

> where $\mathrm{OTF}(f_x,f_y)$ denotes the diffraction-limited OTF, $\mathrm{CSF}_\mathrm{N}(f_x,f_y)$ is the neural contrast sensitivity function, and (f_x,f_y) are the spatial frequency coordinates. Here, the VSOTF was based on calculated OTF across all spatial frequencies.

In several reports in this thesis, we have used Visual Strehl ratio as a metric, as it has been shown to hold the highest correlation variance against subjective acuity [Cheng et al., 2003b].

Finally, depth-of-focus was estimated from through-focus Visual Strehl (in 0.125 D defocus steps). All computations considered high-order aberrations (HOAs) up to 6^{th} order.

2.4. Subjects and protocol in measurements (LRT and OCT)

The procedures involving subjects were reviewed and approved by Institutional Bioethical Committees of the Consejo Superior de Investigaciones Científicas and the Fundación Jiménez Díaz and met the tenets of the Declaration of Helsinki. All patients were fully informed and understood and signed an informed consent before enrolment in the study.

Most of the LRT and OCT measurements were presented in this thesis were performed under pupil dilation (with one drop of tropicamide 1% in Chapter III and VI, and with one drop of phenylephrine in Chapter IV and V).

All subjects in the present thesis were selected patients from the Fundación Jiménez Díaz (Madrid, Spain) or normal volunteers. All participating subjects had a previous eye examination in the Fundación Jiménez Díaz. A total of 64 patients were measured in this thesis, distributed as follows:

- *Chapter III (LRT + OCT):* Nineteen keratoconic patients (before and after ICRS surgery) (19 eyes). OCT measurements were done in all subjects. LRT measurements were done in 8 eyes.
- *Chapter IV (OCT):* Seven normal young subjects (9 eyes).
- *Chapter V (LRT + OCT):* Eleven cataract patients (22 eyes) and nine normal young subjects (17 eyes). LRT and OCT measurements were done in all subjects.
- *Chapter VI (LRT):* Eighteen cataract patients (18 eyes).

In both LRT and OCT systems, measurements were acquired while the patient fixated at the stimulus (Snellen E or Maltese cross) presented on the fixation/accommodation channel at the best focus (the Badal system was first used to compensate the residual refractive error of the subject). Patients were stabilized by means of a bite bar and asked to fixate their gaze on the stimulus.

Set of images was captured approximately five seconds after blinking. And at least five repeated measurements were collected in each condition, and processed independently.

OCT measurements were collected with two 3-D configurations:

(1) *Chapter III and V*: 10x12-mm area, and consisted of a collection of 50 B-Scans composed by 360 A-Scans. The total acquisition time of a 3D data set was 0.72 s.
(2) *Chapter IV*: 10x10-mm area, and consisted of a collection of 50 B-Scans composed by 300 A-Scans. The total acquisition time of a 3D data set was 0.6 s.

The images of the cornea were acquired centered at the specular reflection, which was used as a reference in the image acquisition throughout the different sessions. And, additionally, the position of the fixating letters was moved across the display until the cornea and iris was aligned with the optical axis of the instrument, for ensuring a line-of-sight measurement reference (as it was described in Figure 2.7).

In OCT, the specifications of the spectrometer and light source do not allow sufficient axial range to capture all anterior segment surfaces in a single acquisition. To solve that, for IOL (Chapter V): two sets of 3-D images were captured sequentially: (1) cornea and (2) IOL, and for crystalline lens (Chapter IV): three sets of 3-D images were captured sequentially at 5 seconds after blinking: (1) cornea, (2) anterior lens and (3) posterior lens, rapidly shifting axially the plane of focus; all 3D sets of data contained the iris (as it was described in Figure 2.12).

OCT images containing artifacts (i.e., eyelids), which precluded corneal and lens surface analysis within the optical zone were excluded.

LRT measurements last approximately 1.5 s for an entire typical run. A sampling pattern consisted of 37 entry positions arranged in a hexagonal configuration within the pupil. The eye´s pupil was monitored during measurements with a CCD camera conjugate to the pupil, in order to ensure the correct alignment between the pupil center and the optical axis of the setup, and therefore a line-of-sight measurement reference. Pupil monitoring during the measurement allows to verify that no abnormalities, such as blinking, motion artifacts or tear problems occurred and to ensure the eye´s stability.

In addition to LRT and OCT other measurements were typically conducted on patients: axial length and anterior chamber depth with an IOL Master (Carl Zeiss, Germany), corneal topography with the Pentacam (Oculus, Germany) and autorefraction with an automatic refractometer (Model 597, Humphrey-Zeiss).

Chapter III. ***KERATOCONUS AND ICRS***

OCT-based Topography and Aberrometry in Keratoconus with Intracorneal Ring Segments

This chapter is based on the following publications:

1. ***Quantitative OCT-based Longitudinal Evaluation of Intracorneal Ring Segment Implantation in Keratoconus***, by P. Pérez-Merino, S. Ortiz, N. Alejandre, I. Jimenez-Alfaro and S. Marcos, in Investigative Ophthalmology and Visual Science (2013).
2. ***Ocular and Optical Coherence Tomography-Based Corneal Aberrometry in Keratoconic Eyes Treated by Intracorneal Ring Segments***, by P. Pérez-Merino, S. Ortiz, N. Alejandre, A. de Castro, I. Jimenez-Alfaro and S. Marcos, in American Journal of Ophthalmology (2014).

The contribution of Pablo Pérez-Merino to the study, in collaboration with other coauthors, was the literature search, the design of the experiments (in collaboration with Nicolás Alejandre), the customization of the measuring instruments (in collaboration with Sergio Ortiz), the data acquisition, the development of specific routines (in collaboration with Sergio Ortiz and Alberto de Castro) and the analysis of the data.

Keratoconus is a progressive corneal disorder that affects the shape and structure of the cornea. The distorted corneal geometry severely reduces the optical quality of the eye, making difficult its correction with spectacles or contact lenses [Nordan, 1997; Rabinowitz, 1998]. To date, ICRS are an increasingly used surgical alternative to delay corneal transplant and improve visual quality in keratoconus (by increasing corneal symmetry) [Pinero et al., 2010; Shabayek & Alio, 2007; Torquetti et al., 2014]. Several studies using slit-scanning corneal topography [Dauwe et al., 2009], Scheimpflug imaging [Torquetti & Ferrara, 2010] or ultrasound biomicroscopy [Reinstein et al., 2001] have reported anterior and posterior corneal geometry in keratoconus and its change upon ICRS implantation. However, these techniques include some inherent limitations that makes particularly challenging an accurate measurement in highly deformed corneas and in the presence of implants with a refractive index different from that of the cornea: (1) optical and geometrical distortion in the acquired images, (2) low resolution, (3) acquisition times exceeding typical eye motions, (4) poor repeatability in irregular corneas and (5) interpolation errors [Shankar et al., 2008].

As we mentioned in Chapter I and II, an excellent imaging alternative with improved acquisition time and resolution over other imaging techniques is OCT. OCT provides direct measurement of corneal elevation, and therefore is free from the skew ray ambiguity present in standard Placido disk topography. Besides, the rectangular and dense lateral scanning provides higher lateral resolution than a typical radial sampling (standard Placido disk) or meridional sampling (Scheimpflug imaging). Several OCT studies have reported thickness, power, curvature and topography in keratoconus, as well as the implantation depth of ICRS in keratoconic corneas [Gorgun et al., 2012; Karnowski et al., 2011; Lai et al., 2006; Li et al., 2008; Naftali & Jabaly-Habib, 2013; Szalai et al., 2012]. However, for accurate quantification, OCT images need to be distortion-corrected. Previous works of our group validated the repeatability and accuracy of our OCT system in corneal geometric measurements in normal [Ortiz et al., 2010; Ortiz et al., 2011] and in a keratoconic subject [Ortiz et al., 2012a].

While evaluating corneal topography and geometry allows monitoring the progression of keratoconus and the potential benefit of the treatment, a better understanding of the impact of the changes of corneal shape (by disease or treatment) is obtained by studying its aberrations, as these determine the optical quality. However, the evaluation of the optical performance in patients implanted with ICRS has been addressed only in few studies, which analyzed total [Chalita & Krueger, 2004] and anterior corneal aberrations [Pinero et al., 2009b; Pinero et al., 2010] and showed opposite results.

The combined measurement of corneal topography, corneal thickness and corneal aberrations with the same instrument will give insights on the performance of the ICRS treatment and the potential reasons behind the limited success of some of the procedures in some patients, as well as interactions between the aberrations produced by each optical element. Also, the 3-D ICRS characterization will shed light into ongoing debates on the stability of ICRS, and on reported complication such as ICRS rotation or migration. So, this information will be extremely valuable to understand the mechanism of action of ICRS and provide feedback to biomechanical models of the cornea and ICRS implants to increase the predictability of this treatment and finally get insights on the potential optical and visual benefits of the ICRS procedure.

In this chapter, we present, for the first time the longitudinal corneal quantification before and after ICRS implantation of geometric, topographic, pachymetric and ICRS location based on distortion-corrected OCT. Also, we demonstrated for the first time OCT-based corneal aberrometry and its application in keratoconic patients with ICRS. Corneal aberrations were compared with total aberrations measured with the LRT in the same patients. These comparisons allowed evaluating interactive effects of anterior cornea, posterior cornea and internal aberrations. In addition, the pre- and postoperative optical quality estimated from the measured aberrations was correlated with visual performance.

3.1. Material and methods

3.1.1. Patients

Ferrara-like ICRS (FerraraRing ; AJL Ophthalmics, Vitoria, Spain) were implanted in 19 corneas of 17 patients (ages ranging from 23–41 years) with diagnosed keratoconus (by an experienced corneal specialist, Dr. Nicolás Alejandre). The average age of the patients was 29.3±10.8 y.o. The study was revised and approved by the Institutional Review Boards of the Fundación Jiménez-Díaz, Madrid, Spain and followed the tenets of the Declaration of Helsinki. The subjects signed a consent form and they were aware of the nature of the study.

3.1.1.1. OCT-based Corneal Topography in Keratoconus and ICRS

10 eyes were analyzed pre- and postoperatively at 7, 30 and 90 days after ICRS implantation. Manual and femtosecond laser-assisted techniques were performed for implanting ICRS. Table 3.1 summarizes the clinical profile of the 10 patients and the specifications of the surgical procedure for ICRS implantation in each patient. Depending on the pre-operative corneal topography and refraction, one or two segments were implanted, equidistantly to the incision site. If the corneal coma axis and the flattest meridian differed less than 60 deg the incision was performed in the steepest meridian and a 160-deg segment was placed inferiorly (S#3,9). If anterior corneal astigmatism was higher than 5 D, an additional 90-deg segment was inserted superiorly (S#4,6,8 and 10). If the spherical equivalent was higher than 9 D a 120-deg segment was instead inserted superiorly (S#1). If anterior corneal astigmatism was lower than 3 D, coma was higher than 2 µm (for 5-mm diameter), the corneal coma axis and the flattest meridian differed more than 60 deg and BCVA was below 20/30, a 210-deg segment was placed inferiorly with its center along the corneal coma axis (S#5 and 7). If the patient showed a regular myopic astigmatism higher than 4 D, the incision was performed in the steepest meridian, and two 120-deg segments were inserted (S#2).

All eyes were examined before and after ICRS implantation at 7, 30 and 90 days. The study was approved by Institutional Review Boards and followed the tenets of the Declaration of Helsinki. The patients signed a consent form and they were aware of the nature of the study.

Table 3.1. Descriptive preoperative keratoconic parameters and surgical specifications for ICRS implantation (Part 1).

	Cone loc.*	VA (Pre)**	VA (Post) **	ICRS Technique	Optical zone (mm)	Seg_ment	ICRS thickness (µm)	ICRS arc length (deg)***	I_s (deg) ****	Planned depth (µm)
S#1	I-T	0.1	0.4	Manual	5	2	a:250; b:200	a:160; b:120	140	380
S#2	I-T	0.1	0.4	Femto	6	2	a:200; b:200	a:120; b:120	100	380
S#3	I	0.3	0.8	Femto	6	1	250	160	110	353
S#4	C	0.2	0.4	Manual	5	2	a:250; b:250	a:160; b:90	120	370
S#5	I-T	0.5	1.0	Femto	6	1	200	210	70	380
S#6	C-T	0.4	0.6	Femto	6	2	a:200; b:200	a:160; b:90	30	430
S#7	I-N	0.4	0.4	Femto	6	1	300	210	135	440
S#8	I-T	0.8	0.8	Manual	5	2	a:250; b:250	a:160; b:90	60	380
S#9	I-C	0.3	0.8	Manual	5	1	200	160	50	350
S#10	I-C	0.4	0.6	Femto	6	2	a:200; b:200	a:160; b:90	35	360

*Cone location: S=superior, I=inferior, N=nasal, T=temporal, C=central;
**VA= best-corrected distance visual acuity;
***a= left/superior segment, b= right/inferior segment.
****I_s= Incision site.

3.1.1.2. OCT-based Corneal Aberrometry in Keratoconus and ICRS

19 eyes were measured pre- and 90 days after ICRS implantation. Table 3.2 includes selected descriptive preoperative parameters and the specifications of the surgical procedure for ICRS implantation in each all patients (19 eyes).

Table 3.2. Keratoconic parameters and surgical/ICRS specifications (Part 2).

	Pre-op data			**ICRS parameters**					
	KC degree	Cone location*	K max (D)	ICRS technique	Optical zone (mm)	ICRS thickness (µm)	ICRS arc length (deg)**	Incision site (deg)	Planned depth (µm)
S#1	III	I-T	52.00	Femto	6	200	210	70	380
S#2	III	I-C	53.63	Femto	6	a:200; b:200	a:160; b:90	35	360
S#3	III	I-T	55.20	Femto	6	a:250; b:200	a:120; b:90	100	380
S#4	III	I-T	56.44	Manual	5	a:250; b:200	a:160; b:120	140	380
S#5	III	I-T	57.86	Femto	6	a:200; b:200	a:120; b:120	100	380
S#6	II	I-C	48.58	Femto	6	250	160	110	353
S#7	III-IV	C	62.35	Manual	5	a:250; b:250	a: 160; b:90	120	370
S#8	III-IV	I-N	58.93	Femto	6	300	210	135	440
S#9	III-IV	I-C	63.37	Manual	5	a:250; b:250	a:160; b:90	60	380
S#10	III	I-C	56.15	Manual	5	200	160	50	350
S#11	III-IV	I-T	59.04	Femto	6	a:250; b:250	a:120; b:120	115	380
S#12	III-IV	I-C	64.16	Femto	5	300	210	165	380
S#13	II	I-T	48.64	Femto	6	a:150; b:150	a:120; b:120	75	380
S#14	II-III	C	56.25	Femto	6	300	150	10	380
S#15	II	I-N	55.07	Femto	6	250	150	125	375
S#16	III	C	51.56	Femto	6	300	150	0	380
S#17	II	I-C	51.63	Femto	6	250	150	140	380
S#18	II	I-T	52.29	Femto	6	a:300; b:300	a:120; b:120	75	347
S #19	II	I-T	58.44	Femto	6	250	210	60	380

*Cone location: S=superior, I=inferior, N=nasal, T=temporal, C=central;
**a= left/superior segment; b= right/inferior segment.

3.1.2. Custom SD-OCT system

The OCT images were acquired using a custom developed SD-OCT system, previously described in chapter II.

Images were acquired while patients fixated a Maltese cross fixation stimulus presented on a mini-display (SVGA OLED LE 400; LiteEye Systems, Centennial, Colorado, USA) implemented in a secondary channel. The images of the cornea were acquired with respect to the anterior corneal specular reflection. Sets of 3-D images were captured approximately 5 seconds after blinking. Five repeated measurements were collected in each condition after inducing mydriasis with 1 drop of tropicamide 1%.

Measurements were collected in a 10x12-mm area, using a horizontal raster scan. Each 3-D data set consisted of a total of 50 B-scans composed by a collection of 360 A-scans. The total acquisition time of a 3-D data set was 0.72 seconds.

3.1.3. OCT Image Processing: Corneal Surface Analysis and ICRS segmentation

OCT images were denoised, clustered (cornea, iris and ICRS), segmented and corrected for fan and optical distortion. Figure 3.1 illustrates the image analysis in S#2.

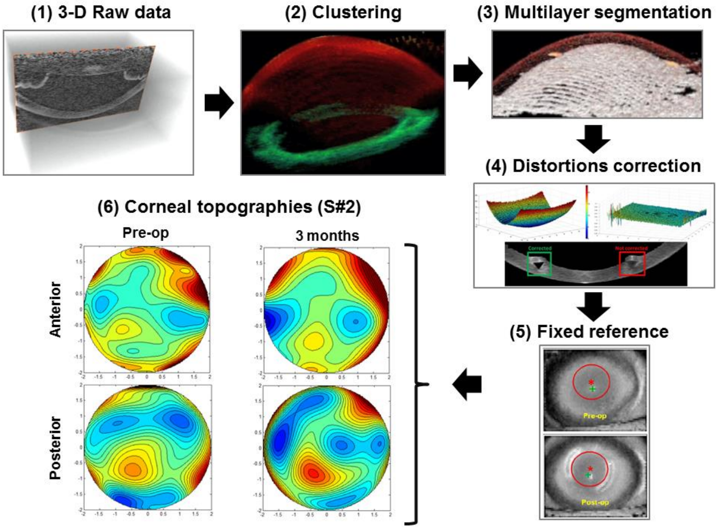

Figure 3.1. Illustration of the OCT image analysis and quantification in S#2.

The pupil center (obtained from the automatically identified iris volume) was used as a reference in the analysis of pre- and postoperative measurements. Corneal elevation maps were reported within the optical zone defined by the ICRS and the natural pupil. The center of the implanted ICRS was obtained from the automatically identified ICRS volume, and its shift from the pupil center estimated for registration of pre- and postoperative measurements. The optical zone is defined by the 4-mm diameter circular zone inside the circumference defined by the ICRS radius, and centered at the pupil center.

Corneal shape was described in terms of the radii of curvature and asphericities from fittings to a sphere and a ellipsoid (anterior cornea: R [sphere]; Rx and Ry, Qx and Qy [ellipsoid]; posterior surface: R [sphere]), and corneal elevation maps were also fitted to Zernike polynomial expansions (6th order) using the center of the optical ICRS zone described in the previous paragraph as the reference. This way, the same optical zone was analyzed in the pre- and postoperative conditions.

Topographic and thickness maps were displayed in a grid square of 100x100 points in the 4-mm of diameter optical ICRS zone in order to ensure quantitative analysis of the optical zone without the ICRS influence. Topographic maps were represented as the difference of corneal elevation data from the reference sphere, in the so called ‘‘height representation,’’ with warm colors representing points that are higher than the reference surface and cool colors representing points below the reference. Both anterior and posterior corneal surfaces were fitted by Zernike polynomial expansions (note that these are fits to surface elevations, not corneal wave aberrations). The symmetry of the corneal elevation maps was obtained using the Root Mean Square error (RMS) of the asymmetric terms of the corneal elevation Zernike expansion (RMS_asym). RMS_asym was therefore defined as the RMS for astigmatism, coma, trefoil, tetrafoil, pentafoil and hexafoil terms (Z_2^{-2}, Z_2^{2}, Z_3^{-3}, Z_3^{-1}, Z_3^{1}, Z_3^{3}, Z_4^{-4}, Z_4^{-2}, Z_4^{2}, Z_4^{4}, Z_5^{-5}, Z_5^{-3}, Z_5^{-1}, Z_5^{1}, Z_5^{3}, Z_5^{-5}, Z_6^{-6}, Z_6^{-4}, Z_6^{-2} Z_6^{2}, Z_6^{4}, and Z_6^{6}) of corneal height maps (not to be confused with wave aberration maps). RMS_asym was evaluated both including and excluding astigmatism coefficients.

Thickness maps were calculated from direct subtraction of the posterior corneal surface from the anterior corneal surface. RMS thickness maps were used to assess the regularity of the thickness distribution. RMS_thicknessmap is therefore defined as the deviation of the thickness maps from a uniform pachymetry across the cornea.

Corneal power (diopters, D) was calculated by using the paraxial formula with both the corneal (1.376) and the aqueous (1.336) refractive indices. All metrics were computed for a 4-mm optical ICRS zone.

3-D ICRS positioning was described by the following parameters: 3-D ICRS depth, defined as the distance between the center of mass of the ICRS and the anterior corneal surface, and ICRS tilt, defined as the angle between the ICRS axis (normal to the ICRS plane) and the pupillary axis (normal to the pupil plane). Positive tilts around X-axis indicate a forward tilt of the nasal part (OD) / temporal part (OS) of the ICRS plane with respect to the pupil plane. Positive tilts around Y-axis indicate a forward shift of the inferior part of the ICRS plane with respect to the pupil plane (Figure 2.16, Chapter II).

3.1.4. OCT Image Processing: Corneal Aberration Analysis

The elevation data from both corneal surfaces within a central 4-mm pupil diameter area (for ensuring quantitative analysis within the optical zone without the influence of ICRS) were fitted by Zernike polynomial expansions (up to sixth order) and exported to ZEMAX (Radiant ZEMAX; Focus Software, Tucson, Arizona, USA) for ray tracing analysis as described in Chapter II (Figure 2.17). Corneal aberrations were analyzed preoperatively and 3 months post ICRS implantation in 19 eyes.

3.1.5. Laser Ray Tracing: Total Aberration Analysis

Total wave aberrations were measured using custom LRT, which has been described in Chapter II.

Measurements were done under mydriasis (1 drop 1% tropicamide). The sampling pattern (37 rays in a hexagonal configuration) was adjusted by software to fit a 4-mm pupil centered at the pupil center. The pupil center reference allowed pre- and post-op comparisons, and the pupil diameter was selected to guarantee that post-op measurements fitted the optical zone defined by the inner diameter of the ICRS. Maximum energy exposure was 6.8 µW.

Prior to the measurement, the patient adjusted his/her subjective refraction using a Badal optometer. The Badal system had been modified for this study to allow correction of spherical errors up to -12 D, frequent in moderate to advanced keratoconus. All measurements were done under foveal fixation of a Maltese cross fixation stimulus. Total wave aberrations were fitted with 6th order Zernike polynomial expansions following OSA standards. Pre- and 3-month post-ICRS total aberrations were measured and analyzed in 8 patients.

3.1.6. Optical quality metrics

Wave aberrations were described in terms of individual Zernike coefficients or RMS. RMS was used to report the magnitude of high order aberrations (HOAs) excluding tilt, defocus and astigmatism, and of certain relevant aberrations (astigmatism, coma and trefoil). The Point-Spread-Function (PSF) and the Modulation Transfer Function (MTF) were computed from Zernike coefficients by means of Fourier optics using routines written in Matlab (MathWorks, Natick, MA), for 4-mm pupils. Optical quality was described in terms of the Visual Strehl Metric. Visual Strehl was computed as the volume under the Visual MTF (obtained from the overlapping of the MTF with the inverse of a general Neural Transfer Function), normalized to diffraction limit. Visual Strehl was evaluated through focus (considering HOAs, and canceling the astigmatic terms). The maximum value of the through-focus Visual Strehl curve was obtained as the best corrected optical quality metric. Visual Strehl metric has been shown to correlate best with logMAR visual acuity.

3.1.7. Visual Acuity measurement

Visual acuity was measured using a high contrast Snellen visual acuity test. Patients were tested at a distance of 4 m (13 feet) from the visual acuity chart. All measurements were performed with natural pupils under photopic conditions. Best corrected Visual Acuity was obtained for optimal spherical and cylindrical correction with spectacles, and given in logMAR units.

3.1.8. Statistical analysis

The changes in corneal geometry and ICRS position were analyzed statistically using an analysis of variance (ANOVA; general linear model for repeated measurements). Significant levels (ANOVA and pair-wise two tailed comparison t-test) were set at $p<0.05$. The statistical tests were performed using SPSS software (SPSS, Inc., Chicago, Illinois).

Univariate analysis (independent samples Student´s t-test) was used to evaluate differences between pre-operative and post-operative measurements in corneal aberrometry. Correlations (Pearson correlation coefficients) were assessed between OCT and Laser Ray Tracing aberration measurements. A p-value less than 0.05 was considered statistically significant in all comparisons.

3.2. Results

3.2.1. OCT-based Corneal Topography in Keratoconus & ICRS

3.2.1.1. Longitudinal changes of anterior corneal surface geometry and topography

Radius of curvature and asphericity of the anterior corneal surface were obtained from sphere (R) and biconicoid (Rx, Qx; Ry, Qy) fittings in a 4-mm optical ICRS zone.

Figure 3.2 (a) shows averaged horizontal and vertical anterior corneal radii of curvature (Rx and Ry) in each eye before and at 7, 30, and 90 days after ICRS implantation. The intrasubject repeatability in the estimated anterior radius of curvature across repeated measurements is high, with average standard deviations of 0.07 mm (pre-op), and 0.08 mm, 0.09 mm and 0.08 mm (at 7, 30 and 90 days post-op, respectively). We found significant overall flattening ($p<0.05$) of the anterior cornea one week following surgery in 8 out of 10 patients (all patients except for S#2 and S#3), with an average radius increase by 2.25%. In 6 of these patients there was further corneal flattening during the tested period, with an average radius increase by 5.5% at 90 days. S#2 and S#3 experienced an initial corneal steepening, followed by a corneal flattening, but the radius of curvature at 90 days was not statistically significantly different from pre-operative values. Figure 3.2 (b) shows ratio Rx/Ry pre- and post-operatively (7, 30, and 90 days). In 7 out of 10 patients (all except for S#2, S#7 and S#10), the ratio Rx/Ry decreased after ICRS implant. Four patients (S#3, S#5, S#6 and S#9) showed Rx/Ry ratios close to 1. On average, the difference in anterior curvature in the horizontal and vertical meridians decreased significantly from a mean pre-op value of 4.52±2.62 D to a mean 90-days post-op value of 2.81±2.39 D ($p<0.05$).

The overall anterior corneal flattening ranged from 8.9% to 2.2% across patients. We found a tendency for Rx to flatten more than Ry. Rx flattening ranged from 18.6% to 1.5% across patients, and Ry from 0.8% to 9.1%. Flattening in Rx was statistically significant at 7, 30 and 90 days, whereas changes in Ry were not statistically overall.

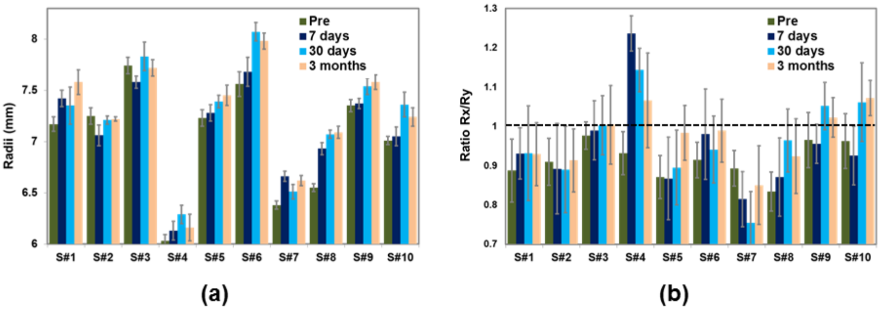

Figure 3.2. (a) Anterior cornea mean radius of curvature and (b) Rx to Ry ratio at various time points (pre- and 7, 30 and 90 days postoperatively).

Figure 3.3 shows the longitudinal variation of asphericity in the horizontal (Qx, Figure 3.3 (a)) and in the vertical (Qy, Figure 3.3 (b)). Pre-operatively, patients showed typically a highly prolate horizontal meridian (Qx=-1.64±0.91) and much lower vertical negative aphericity (or even positive asphericity values) in the vertical meridian (Qy=-0.11±0.72). In general, keratoconic patients showed higher magnitudes of asphericity (Q ranging from -3.65 to 0.72) in comparison with a normal population. The ICRS implant produced significant changes in Qx or Qy. On average, Qx shifted towards more negative values 7-days after the procedure (from -1.64 to -2.25), but typically decreased to values not significantly different from pre-operative values (Qx=-1.49±1.02) 90-days after the procedure. Qy did not follow a systematic pattern immediately after surgery or longitudinally.

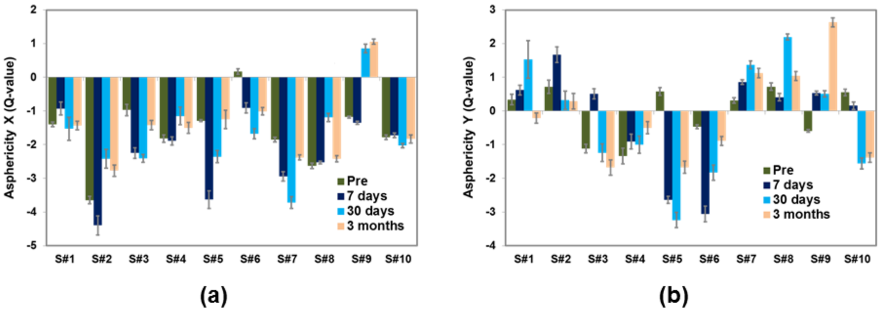

Figure 3.3. (a) Asphericity in the horizontal meridian (Qx) and (b) asphericity in the vertical meridian (Qy) pre- and 7, 30 and 90 days postoperatively

Figure 3.4 shows anterior corneal elevation maps from two patients (S#5 and S#8), for 4-mm diameters (i.e. within the optical zone defined by the ICRS), centered at the pupil center. The radii of curvature of the best fitting spheres and the corneal elevation RMS for asymmetric terms (excluding astigmatism) are also shown. These patients show corneal flattening after surgery and during the follow-up, as well as a reduction of the asymmetry of the corneal elevation map, with a decrease in the corneal elevation asymmetric RMS of 19.7% (S#5) and 14.6% (S#8), respectively.

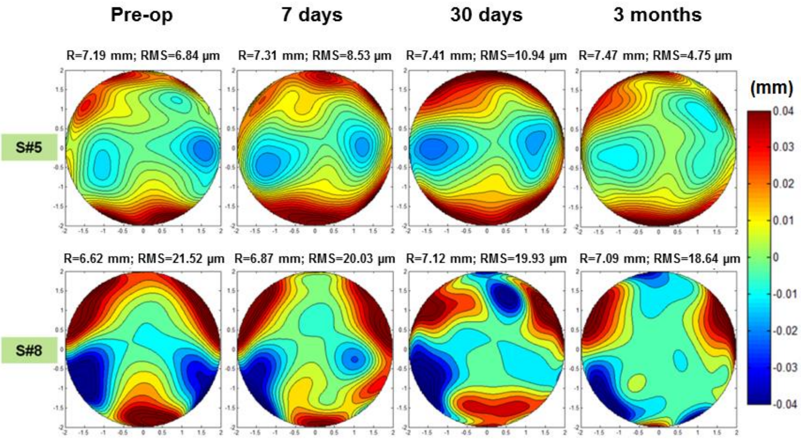

Figure 3.4. Anterior corneal elevation maps pre- and postoperatively in two patients of the study (S#5 and S#8). R stands for radius of curvature and RMS for RMS_asym.

Figure 3.5 shows the anterior cornea RMS_asym, including astigmatism (a) and excluding astigmatism (b). On average RMS_asym did not show significant differences between pre-op and post-op measurements, primarily due to the high intersubject variability of the corneal elevation asymmetry pre-operatively. S#5, S#6 and S#8 experienced a decrease in asymmetry (with and without astigmatism) from pre-op to 90-days post-operatively ($p<0.05$). S#3 and S#4 increased asymmetry significantly ($p=0.05$). Interestingly, the subject with highest amount of pre-operative RMS_asym (S#8) improved symmetry significantly (and progressively) both with and without astigmatism, whereas the subject with lowest pre-operative RMS_asym (S#3) increased asymmetry significantly. As expected, we found in the RMS_asym excluding astigmatism lower values ($p<0.001$) in comparison with RMS_asym with astigmatism. However, the RMS (with and without astigmatism) show similar trends during the follow-up.

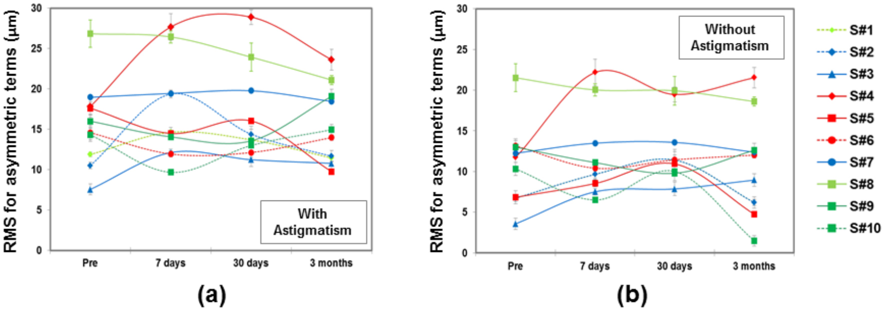

Figure 3.5. Anterior corneal elevation RMS for asymmetric Zernike coefficients (RMS_asym), (a) with astigmatism, and (b) without astigmatism.

3.2.1.2. Longitudinal changes of posterior corneal surface geometry and topography

The radius of curvature of the posterior corneal surface was obtained from sphere fitting, in a 4-mm optical ICRS zone. Intrasubject repeatability in the estimated anterior radius of curvature across repeated measurements is high, with average standard deviations of 0.08 mm (pre-op) and 0.09 mm (7, 30 and 90 days post-op). Figure 3.6 shows the longitudinal variations in radius of curvature of the posterior corneal surface with surgery. Unlike for the anterior surface, where most patients showed flattening, there was not a clear trend for the posterior surface. Only 3 patients (S#1, S#4 and S#9) showed flattening of the posterior cornea (average: 3.7% at 7 days, 6.4% at 30 days and 13.9% at 90 days), and S#2, S#5, S#6, S#8 and S#10 showed steepening (average: 8.8% at 7 days, 6.7% at 30 days and 6.9% at 90 days).

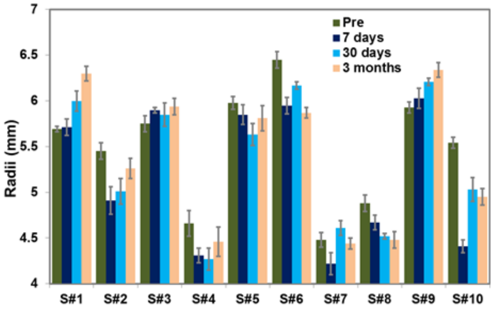

Figure 3.6. Posterior corneal mean radius of curvature (pre- and postoperatively 7-90 days).

Figure 3.7 shows posterior corneal elevation maps from two patients (S#1 and S#10), for 4-mm diameters (i.e. within the optical zone defined by the ICRS), centered at the pupil center. Maps are clearly dominated by astigmatism. Although the presence of ICRS induces marked changes in the topographic pattern with time, the posterior surface did not show significant decrease in astigmatism and asymmetric terms with surgery.

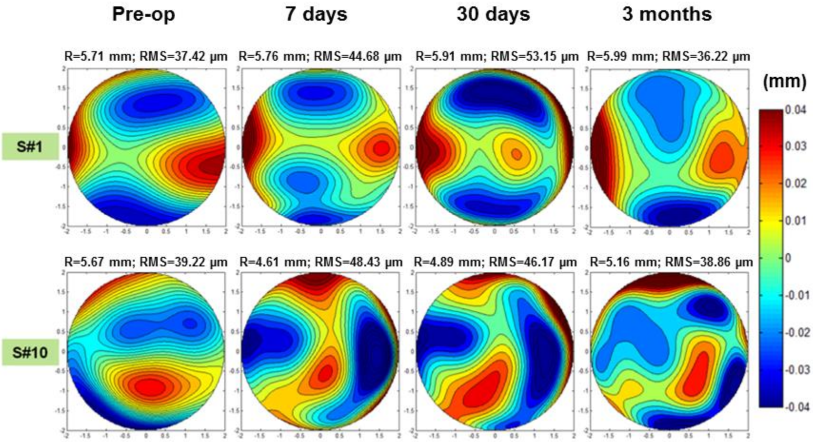

Figure 3.7. Posterior corneal elevation maps pre- and postoperatively in two patients of the study (S#1 and S#10). R stands for radius of curvature and RMS for RMS_asym.

Figure 3.8 shows the posterior cornea RMS_asym, including astigmatism (a) and excluding astigmatism (b). ICRS produced significant changes although the longitudinal trends show high intersubject variability. On average RMS_asym including astigmatism showed a slight but not significant ($p=0.4$) decrease (from 58.5±8.8 to 54.1±6.8 μm, pre-op to 90 days post-op). S#4, S#7 and S#8 experienced a decrease in RMS_asym (with and without astigmatism) from pre-op to 90 days post-op ($p<0.05$). S#1, S#5 and S#9 increased asymmetry significantly ($p<0.05$). Interestingly, the patients with highest amount of pre-operative asymmetric RMS (S#7 and S#8) improved symmetry significantly (and progressively).

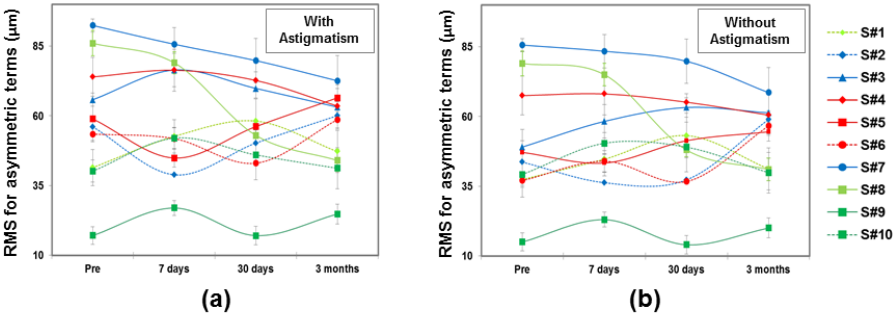

Figure 3.8. Posterior corneal elevation RMS for asymmetric Zernike coefficients (RMS_asym), (a) with astigmatism, and (b) without astigmatism.

3.2.1.3. Longitudinal variations of corneal power

Refractive changes are associated with changes in curvature of both the anterior and posterior corneal surfaces. Figure 3.9 shows the corneal power change during the follow-up (a), and the pre-op versus post-op (90 days) corneal power (b). Corneal refractive power changed significantly from a mean pre-op value of 46.2±3.2 D to a mean 90-day post-op value of 44.4±3.5 D ($p<0.05$). On average, corneal power decreased 1.71 D (between -5.1 D for S#8 to +1.1 D for S#4). Pre-op corneal power is highly correlated with post-operative power ($p<0.05$; Figure 3.10 (b)).

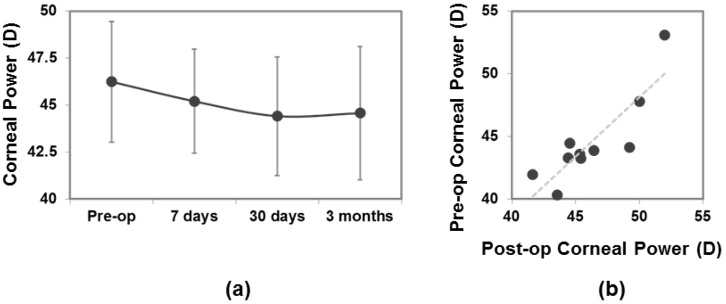

Figure 3.9. (a) Corneal power change during the follow-up; (b) preoperative *vs* postoperative (90 days) corneal power.

3.2.1.4. Corneal thickness: pre and post-ICRS implantation

Figure 3.10 (a) shows an example (S#2) of the corneal thickness map pre- and post-operatively. Minimum corneal thickness did not change significantly with surgery (384±60 µm pre-op to 396±46 µm post-operatively). However, both the distribution of corneal thickness and changes in the minimum thickness location did occur. Figure 3.10 (b) shows the longitudinal variation of the RMS of the corneal thickness map (RMS_thicknessmap) for all patients of the study as an estimation of the thickness distribution in the 4-mm optical ICRS zone. Corneal thickness redistribution occurred in most patients with time. RMS_thicknessmap decreased significantly (from pre-op to 90 days post-op, $p<0.05$) in 3 subjects (S#4, S#7 and S#9), and increased significantly ($p<0.05$) in 3 patients (S#2, S#8 and S#10). Figure 3.10 (c) shows the displacement of the minimum corneal thickness location across the optical zone, for all patients. Overall, there is an average displacement of the location of minimum thickness from inferior pre-operatively (centroid coordinates: -0.01 (x-axis) and -0.63 (y-axis)) towards more central post-operatively (centroid coordinates: -0.06 (x-axis) and -0.14 (y-axis) at 90-days). The largest shift occurred between pre-op and 7-days post-op, with little changes during the follow up.

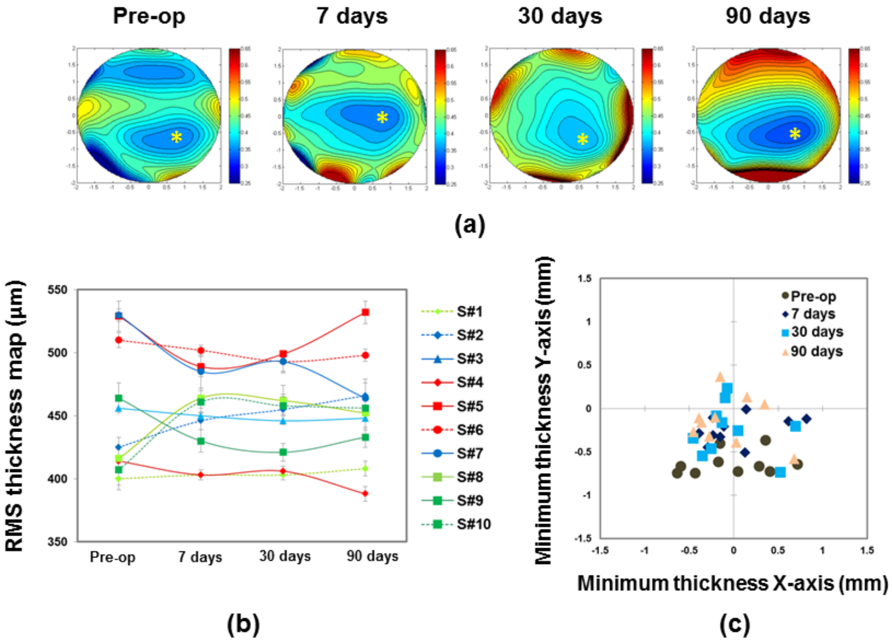

Figure 3.10. (a) Thickness map for S#2 preoperatively and 7, 30 and 90 days postoperatively (* denotes the minimum corneal thickness location); (b) RMS of the corneal thickness map. (c) Coordinates of the minimum corneal thickness location pre- and postoperatively (7, 30 and 90 days).

3.2.1.5. 3-D ICRS location

The location of the ICRS was analyzed in 3-D, both in terms of the implantation depth and tilt. Figure 3.11 (a) shows the ICRS depth (computed from the average distance from anterior corneal surface to the center of mass of the ICRS at every location along the ICRS) in all patients, at different times post-operatively. On average, there was a slight but progressive decrease of ICRS depth (by 10 µm, from 7 to 90 days post-operatively). Most patients showed longitudinal changes in ICRS depth. Patients S#2 (b), S#6 (a), S#9 and S#10 (b) showed a mean forward shift of the ICRS of 18±6 µm; and S#1 (a and b), S#6 (b), S#7, S#8 (b) showed a backward shift of the ICRS (41±17 µm) at 90 days. Figure 3.11 (b) shows the correlation between the ICRS planned depth and the measured ICRS depth at 7 days. The correspondence between the planned and the measured ICRS depth is higher for the femtosecond technique (15±20 µm between the planned and achieved depth) than for the manual technique (40±22 µm difference).

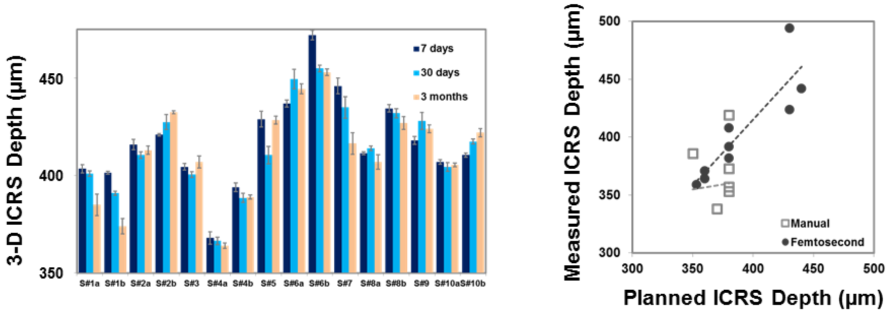

(a) (b)

Figure 3.11. (a) Average ICRS depth for all patients (7, 30 and 90 days postoperatively). (b) Planned depth *vs* OCT measured depth.

Figure 3.12 shows the ICRS tilt angles around X and Y-axes in all patients and post-operative time-points. The tilt angles of the left and right ICRS segments have been changed in sign for the nasal/temporal coordinates, to allow appropriate averaging. On average, there is a forward tilt of the temporal and superior part of the ring, with an overall tilt of -6.8±2.6 deg (temporal) and -2.1±0.8 deg (superior) at 7 days. Although there is intersubject variability, there is small (<1 deg) but systematic tilt of the ICRS between 7 and 90 days post-surgery.

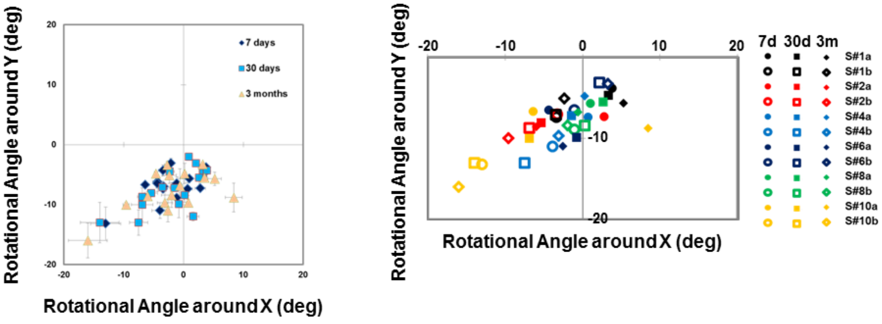

(a) (b)

Figure 3.12. (a) Average ICRS tilt for all patients at 7, 30 and 90 days. (b) ICRS tilt for patients with two segments at 7, 30 and 90 days ([a] left/superior segment and [b] right/inferior segment).

3.2.1.6. *Correlation between surgical parameters and corneal geometrical response*

The effect of ICRS implantation on corneal curvature was highly dependent on ICRS diameter. The ICRS with smaller diameters were more effective in flattening the anterior corneal surface than larger diameters: 0.33±0.18 mm (5 mm optical zone) *vs* 0.17±0.14 mm (6 mm optical zone), at 90-days post-op. As a result, the 5-mm ICRS produced the largest changes in corneal power. For example, S#8, with a 5-mm optical zone, experienced a decrease in total corneal power by 5.1 D (90-days post-op).

The optical zone diameter appeared also correlated, to a less extent, to the change of the posterior corneal surface radius of curvature. A 5-mm optical zone diameter produced an average posterior corneal flattening of 0.14±0.45 whereas a 6-mm optical zone diameter produced an average steepening of 0.31±0.25 mm (90 days post-op). In addition, the effect of ICRS on the posterior surface could be possibly associated to the ICRS arc length. Previously, we described steepening on the posterior corneal surface with a 90-deg arc length. A combination of 90-deg arc length ICRS and 160-deg arc-length (as in patients S#4, S#6, S#8 and S#10) produced a significant steepening of the posterior corneal surface (by 0.41±0.24 mm). However, a combination of 160-deg and 120-deg arc length ICRS (as in patients S#1, S#2, S#3 and S#9) tended to flatten the posterior corneal surface (by 0.15±0.35 mm). In addition, the ICRS arc length seems to be associated with the post-operative corneal symmetry. Patients implanted with 90-deg arc length ICRS showed a significant decrease of the corneal surface RMS for asymmetric terms of the posterior surface (from 63.4±8.8 µm pre-op to 51.8±6.0 µm 90-days post-op) and a slight increase in the RMS of the thickness map (from 436±8 µm pre-op to 448±9 µm 90 days post-op).

The position and rotation of the ICRS also seems to play a major role in the symmetry of the post-operative cornea. A strong direct correlation was found between the change in the ICRS tilt around X and change in anterior corneal RMS_assym, between 7 and 90-days (r=+0.83, $p<0.05$ with astigmatism; r=+0.76, $p<0.05$ without astigmatism). No significant correlations were noted among other parameters of the ICRS position and the corneal surface.

3.2.2. *OCT-based Corneal Aberrometry in Keratoconus & ICRS*

3.2.2.1. *LRT vs OCT-aberrometry*

Corneal and total aberrations were compared in 8 of the 19 eyes pre-operatively and 3-months post-ICRS implantation. Figure 3.13 shows the average coefficients describing the second and HOAs of the whole eye and of the cornea, as well as the corresponding wave aberration maps (excluding tilt, defocus and astigmatism). The corresponding simulated PSFs for all subjects (average) pre- and post-operatively are also shown. Both pre- and post-operatively, total and corneal aberrations are dominated by astigmatism (eliminated in the maps shown in Figure 3.13 to allow visualization of higher order aberrations), vertical coma (Z_3^{-1}), vertical trefoil (Z_3^{-3}) and secondary astigmatism (Z_4^4). Anterior corneal aberrations are slightly higher than those of the whole cornea aberrations (including both anterior and posterior surfaces), indicating a compensatory role of the posterior corneal surface. While total and corneal aberrations show quite similar aberration patterns, several total aberration terms tend to be lower than the corresponding corneal aberration terms.

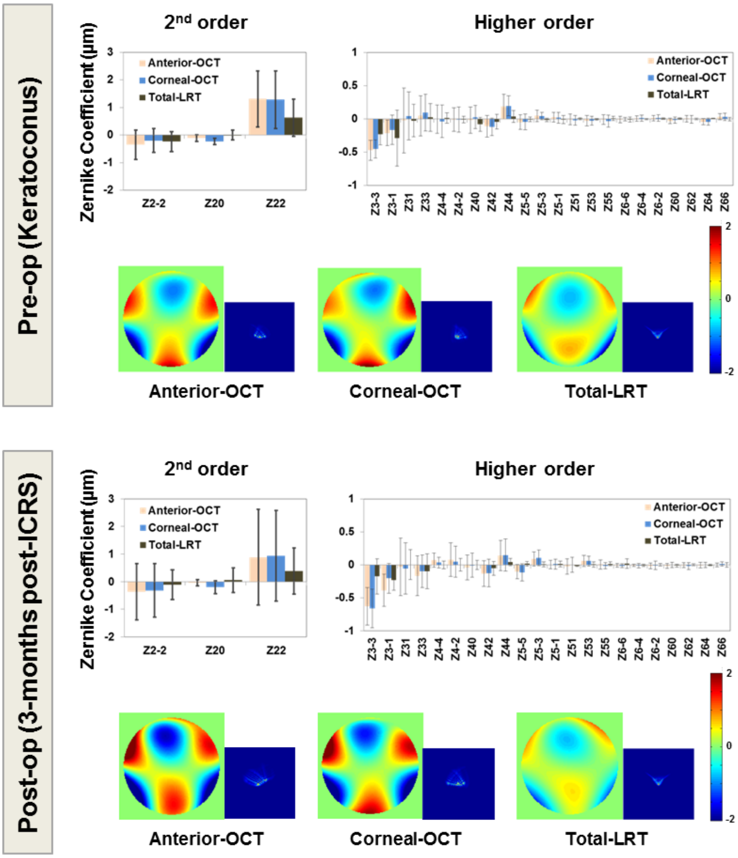

Figure 3.13. Total and corneal Zernike coefficient values (average across 8 eyes), wave aberration maps (calculated from average Zernike coefficients excluding tilt, defocus and astigmatism) and the simulated point-spread-functions (PSFs) from the wave aberrations (window size: 5 arc min) for keratoconic eyes pre-operatively and 3-months post-intracorneal ring segment (ICRS) implantation. Data are for 4-mm pupils and referred to the pupil center. (Top) pre-operative data, and (Bottom) post-operative data, 3 months post-intracorneal ring segment (ICRS) implantation in keratoconus. OCT: Optical coherence Tomography. LRT: Laser Ray Tracing.

Figure 3.14 shows individual corneal and total wave aberration maps (excluding tilt, defocus and astigmatism) for all eyes measured with OCT and with LRT, pre-operatively and 3-months post-ICRS implantation. In most eyes, the high-order wave aberration maps are dominated by coma and trefoil. Repeated measurements were highly reproducible within each subject, with average (across all patients and conditions) standard deviations of 0.13 µm (LRT), 0.17 µm (OCT anterior) and 0.19 µm (OCT corneal) for RMS astigmatism, and of

0.07 µm (LRT), 0.10 µm (OCT anterior) and 0.11 µm (OCT corneal) for RMS HOA. Total and corneal aberrations show in general a good correspondence (except for eye#5). In most cases total aberrations are lower than corneal aberrations, suggesting a compensatory effect of the crystalline lens. On average, the RMS HOAs was 0.78±0.35 µm (OCT) and 0.57±0.39 µm (LRT) pre-operatively and 0.88±0.36 µm (OCT) and 0.53±0.24 µm (LRT) post-operatively.

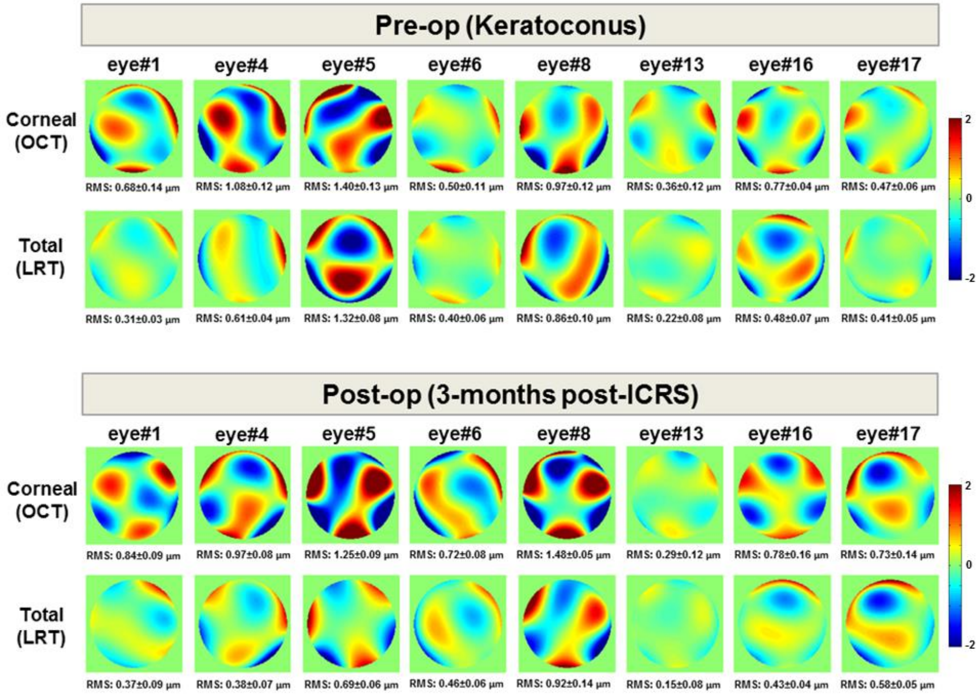

Figure 3.14. Total and corneal Zernike coefficient values (average across 8 eyes), wave aberration maps (calculated from average Zernike coefficients excluding tilt, defocus and astigmatism) and the simulated point-spread-functions (PSFs) from the wave aberrations (window size: 5 arc min) for keratoconic eyes pre-operatively and 3-months post-intracorneal ring segment (ICRS) implantation. Data are for 4-mm pupils and referred to the pupil center. (Top) pre-operative data, and (Bottom) post-operative data, 3 months post-intracorneal ring segment (ICRS) implantation in keratoconus. OCT: Optical coherence Tomography. LRT: Laser Ray Tracing.

Figure 3.15 shows the correlation between corneal and total Zernike coefficients (HOA, astigmatism, coma, trefoil and spherical aberration) for all patients and conditions.

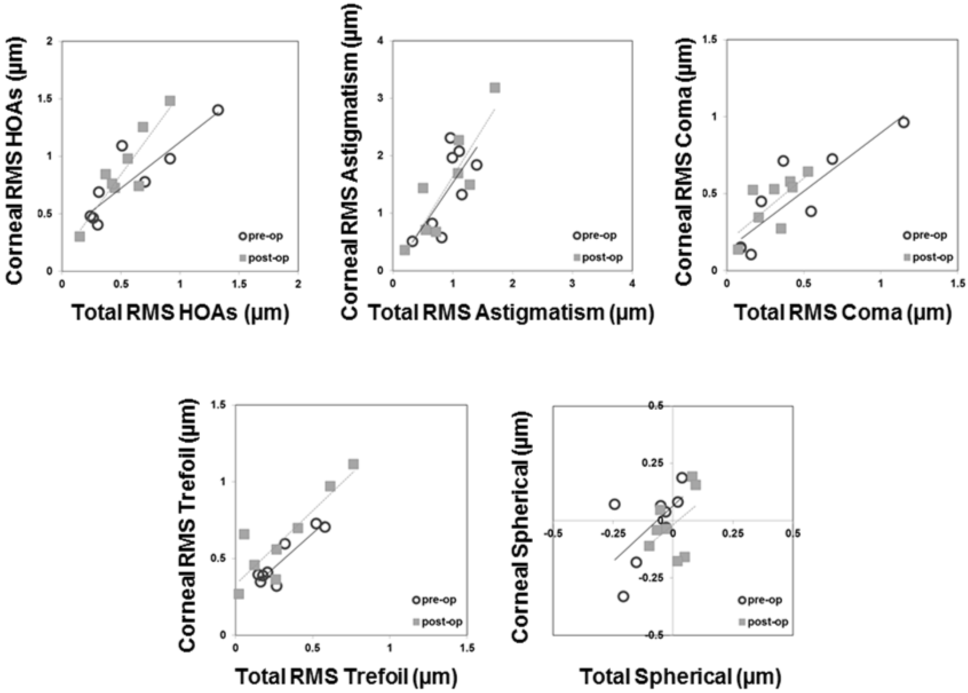

Figure 3.15. Correlation between corneal aberrations and total aberrations, in terms of root-mean-square (RMS) high-order aberrations (top left), astigmatism (top middle), coma (top right) and trefoil (bottom left), and spherical aberration (bottom right). Open circles stand for pre-operative data (keratoconus) and closed squares for post-operative data (3-months post-intracorneal ring segment (ICRS) implantation). Lines are linear regressions to the data.

Table 3.3 shows the corresponding correlation coefficients and slopes. Correlations between corneal and total data were statistically significant ($p<0.05$) for RMS HOAs (pre- and post-operatively), RMS Astigmatism (pre- and post-operatively), RMS Trefoil (pre- and post-operatively) and RMS Coma (post-operatively). The slopes ranged from 0.75 to 1.53 (1.07 on average). The highest dispersion (and least-significant correlation) was found for spherical aberration, indicative of a patient-dependent compensation of the corneal spherical aberration by the crystalline lens.

Table 3.3. Correlation parameters between corneal and total root-mean-square (RMS) for high-order aberrations (HOAs), astigmatism, coma and trefoil, and for spherical aberration pre-operatively (keratoconus) and post-operatively (3-months post-intracorneal ring segment (ICRS) implantation). r: Pearson product-moment correlation coefficient; slope: the slope of the regression line; p: p-value(*p<0.05).

		r	**slope**	**p**
HOAs	pre-op	0.87	0.80	0.012*
	post-op	0.90	1.40	0.001*
Astigmatism (Z_2^2 and Z_2^{-2})	pre-op	0.71	1.53	0.036*
	post-op	0.88	1.67	0.022*
Coma (Z_3^1 and Z_3^{-1})	pre-op	0.87	0.75	0.132
	post-op	0.64	0.83	0.023*
Trefoil (Z_3^3 and Z_3^{-3})	pre-op	0.91	0.90	0.001*
	post-op	0.88	0.96	0.003*
Spherical Aberration (Z_4^0)	pre-op	0.66	0.97	0.197
	post-op	0.44	0.86	0.691

3.2.2.2. Pre- and Post-ICRS aberrations

OCT-corneal aberrations were analyzed in 19 eyes pre-operatively and 3-months post-ICRS implantation. Figure 3.16 shows corneal (anterior+posterior) aberrations (RMS for HOAs, astigmatism, coma and trefoil terms) for all subjects. On average, ICRS implantation decreased corneal astigmatism (27%), and produced slight decrease of HOAs (2%) and coma (5%), and slight increase of trefoil (4%). We found slight but not significant correlations between pre- and post-operative astigmatism (r=0.54, p=0.07), HOAs (r=0.55, p=0.89), coma (r=0.36, p=0.84), trefoil (r=0.48, p=0.84). Besides astigmatism, Z_3^{-3}, Z_3^{-1}, Z_3^{1} and Z_4^{4} were the predominant corneal aberrations contributing 19%, 7%, 8%, 8% and 8% (pre-operatively) and 19%, 7%, 9%, 8% and 5% (post-operatively) respectively to the overall corneal HOAs.

At the individual level, astigmatism decreased significantly (p<0.006) 3-months post-ICRS implantation in 14/19 eyes (eye#2-#4, #6, #7, #9-#16, #18 and #19). Coma decreased significantly (p<0.03) in 11/19 eyes (eye#1, #3-#5, #9-#14, #16 and #19). Trefoil decreased (p<0.07) in 7/19 eyes (eye#2-#4, #9, #11, #13 and #19). HOAs decreased significantly (p<0.03) in 9/19 eyes (eye#2-#4, #9-#13 and #19). However, in 4/19 eyes (eye#1, #5, #8 and #17) astigmatism and HOA increased significantly 3-months post-ICRS implantation.

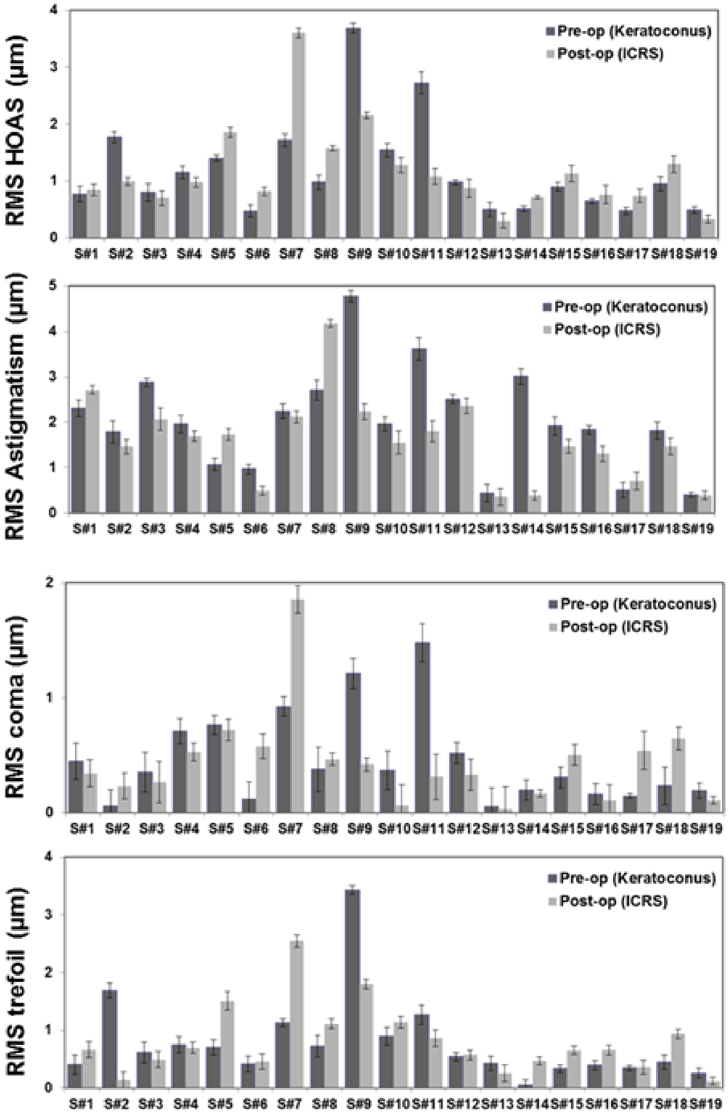

Figure 3.16. RMS for high-order aberrations (HOAs), astigmatism (Z_2^2 and Z_2^{-2}), coma (Z_3^1 and Z_3^{-1}) and trefoil (Z_3^3 and Z_3^{-3}). Data are for 4-mm pupils in keratoconic corneas pre-operatively and 3-months post-ICRS implantation.

3.2.2.3. Visual acuity versus optical quality

Figure 3.17 shows best-corrected visual acuity (BCVA) as a function of best Visual Strehl, for 4-mm pupil diameter. We found significant correlations between BVCA and Visual Strehl both pre-operatively (r=-0.51, p=0.02) and 3-month post-ICRS implantation (r=-0.68, p=0.001) values. On average, BCVA is slightly but significantly improved with ICRS treatment (pre-operative BCVA 0.38±0.19; post-operative BCVA 0.51±0.16; p=0.002). While there is a displacement of Visual Strehl towards higher post-operative values, the change did not reach statistical significance (pre-operative Visual Strehl: 0.059±0.03; post-operative Visual Strehl: 0.063±0.04; p=0.53).

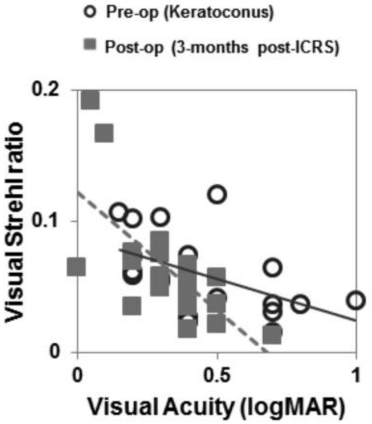

Figure 3.17. Correlation between best-corrected visual acuity (BCVA) and Visual Strehl ratio (computed from the visual Modulation Transfer Function for high order aberrations at best focus, i.e. maximum Visual Strehl, for 4-mm pupils). Open circles stand for pre-operative data (keratoconus) and closed squares for post-operative data (3-months post- ICRS implantation).

3.2.2.4. Posterior corneal surface contribution

The posterior corneal surface provides consistent partial compensation of the anterior corneal surface aberration. Figure 3.18 illustrates the contribution of the posterior corneal surface to the corneal aberrations. On average, the posterior corneal surface compensates 13.9% of astigmatism, 8.3% of HOAs, 16.1% of coma, and 7.7% of trefoil pre-operatively; and 9.1% of astigmatism, 4.1% of HOAs, 20.1% of coma, and 3.1% of trefoil 3-months post-ICRS implantation. The amount of compensation pre- or post-operatively did not differ significantly.

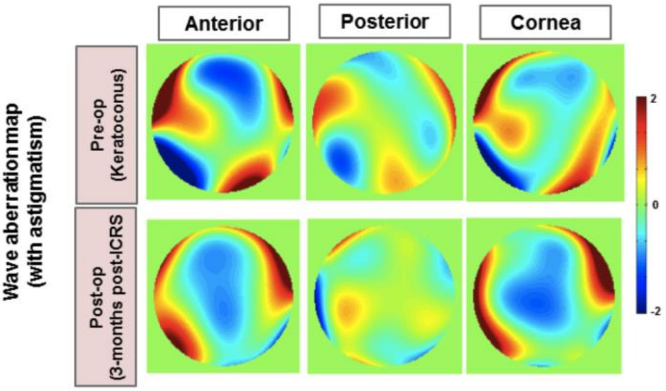

Figure 3.18. Examples of anterior, posterior and corneal wave aberration maps in a keratoconic eye (eye#19). Upper panels show pre-operative data (keratoconus), and lower panels post-operative data (3 months post- ICRS implantation).

3.2.3. OCT-based aberrometry vs OCT-based geometry

Table 3.4 shows the optical and geometrical changes after ICRS in the coincident subjects of Part 1 and Part 2 of the study.

Table 3.4. Geometry and aberrometry data from all subjects of Part 1 (geometry) and Part 2 (aberrometry). Data are the difference between the post-op measurement at 3 months and the pre-op measurement (-, means improvement).

		Geometry			**Aberrometry**		
Part 1 *(Geomet.)*	**Part 2** *(Aberrom.)*	*Corneal Power (D)*	*RMS Ant Cornea (μm)*	*RMS Post Cornea (μm)*	*RMS HOAs (μm)*	*RMS Astigm (μm)*	*RMS Coma (μm)*
S#1	S#4	-2.15	-0.43	5.76	-0.17	-0.26	-0.18
S#2	S#5	-0.05	1.14	4.03	0.45	0.66	-0.04
S#3	S#6	0.34	3.22	-2.65	0.34	-0.47	0.46
S#4	S#7	1.07	5.79	-10.43	1.88	-0.13	0.93
S#5	S#1	-1.73	-7.86	7.55	0.07	0.40	-0.10
S#7	S#8	-2.21	-0.51	-19.84	0.59	1.46	0.09
S#8	S#9	-5.1	-5.73	-42	-1.52	-2.54	-0.79
S#10	S#2	-2.56	0.64	1	-0.77	-0.32	0.17

Table 3.5 shows correlations of the ICRS effect (pre *vs* 3 months post-ICRS) in OCT-based aberrometry (RMS HOAs, RMS astigmatism, RMS coma and RMS trefoil; aberrometry data are from all cornea, anterior and posterior corneal surfaces) and OCT-based geometry (anterior corneal radius, posterior corneal radius, RMS anterior corneal surface including astigmatism, RMS posterior corneal surface including astigmatism and corneal power). A significant correlation indicates that the magnitudes of individuals Zernike coefficients are closely associated. We found strong positive correlation between the RMS HOAs and the posterior corneal radius and corneal power, between RMS coma and the RMS of the anterior corneal surface and corneal power, and between the RMS trefoil and corneal power. Interesingly, S#8 (Part 1-geometry, who corresponds to S#9 in part 2-aberrometry) showed

the highest geometrical improvement (-5.1 D of decrease in corneal power and -5.73 µm of decrease in the RMS of the anterior corneal surface) manifested the highest decrease in the RMS HOAs (-1.52 µm) and astigmatism (-2.54 µm); and S#2 (Part 1-geometry, who corresponds to S#5 in part 2-aberrometry) showed worsening in the RMS of the anterior and posterior surface, manifesting an increased in HOAs (+0.45 µm) and astigmatism (+0.66 µm).

Table 3.5. Pearson correlation coefficient and p-value between OCT-aberrometry and OCT-geometrical changes pre- and 3 months post-ICRS.

	R Anterior	*R Posterior*	*Corneal Power*	*RMS Anterior*	*RMS Posterior*
RMS HOAs	r=-0.63; p=0.08	r=0.75; p=0.03*	r=0.87; p=0.01*	r=0.65; p=0.08	r=0.32; p=0.43
RMS Astigmatism	r=-0.55; p=0.15	r=0.13; p=0.74	r=0.51; p=0.19	r=0.23; p=0.57	r=0.55; p=0.15
RMS Coma	r=-0.68; p=0.06	r=0.62; p=0.09	r=0.86; p=0.01*	r=0.8; p=0.01*	r=0.38; p=0.35
RMS Trefoil	r=-0.6; p=0.11	r=0.7; p=0.06	r=0.82; p=0.01*	r=0.45; p=0.25	r=0.37; p=0.36

3.3. Discussion

We have presented, to our knowledge, the first report of (1) full OCT-based quantification of geometrical, topographical and pachymetrical corneal changes following ICRS surgery, (2) 3-D ICRS accurate location and (3) corneal aberrations based on quantitative OCT measurements of corneal elevation maps of anterior and posterior surface.

(1) Full OCT-based corneal geometry, topography and pachymetry following ICRS surgery

Accurate measurements of anterior and posterior corneal topographies are essential to understand the corneal response to ICRS implants. The higher speed and resolution, axial and lateral, of OCT makes of this an ideal tool to evaluate the corneal geometry in keratoconus and its ICRS treatment. Most OCT studies of keratoconus address only the measurement of corneal thickness and corneal radii [Li et al., 2008; Tang et al., 2006], while few attempt quantification of corneal topography [Karnowski et al., 2011; Szalai et al., 2012]. In fact, reports comparing corneal shape (radii and pachymetry) measured with OCT and other techniques are conflicting, with some of the studies showing significant differences found across instruments [Szalai et al., 2012], and other reporting a good agreement between OCT and Scheimpflug [Karnowski et al., 2011].

Due to the scanning configuration and the refraction effects (particularly relevant in this case due to the ICRS inside the cornea with a higher index of refraction), fan and optical distortion affect significantly the acquisition of accurate quantitative 3-D data from OCT corneal surfaces. In a previous studies, Ortiz et al. [Ortiz et al., 2011] described the application of custom algorithms for reconstructing accurately 3-D corneal elevation maps after fan and optical distortion correction in a keratoconic cornea.

Previous studies after ICRS implantation reported a mean flattening of the anterior corneal surface by 2.5 D [Pinero et al., 2010; Shabayek & Alio, 2007]. In this study we found a mean decrease of corneal power (anterior + posterior corneal surfaces) of 1.71±1.83 D 90 days post-operatively. Despite the overall decrease of corneal power, the response varied across individuals (ranging from an increase of 1.07 D to a decrease of 5.10 D at 90 days). This intersubject variability is consistent with a previous study using videokeratography, who found an increase of 2.5% to a decrease of 18% in the topographic K-values, in 21 eyes 90-days post implantation of ICRS [Shabayek & Alio, 2007]. As predicted by a recently published Finite Element Model analysis of the corneal response to ICRS implants, we found that the change in anterior corneal radius was highly dependent on the optical zone diameter [Kling & Marcos, 2013].

Regarding the effect of ICRS on the posterior corneal surface, a previous study based on Scheimpflug imaging reported a significant flattening of approximately 0.25 mm after ICRS implantation [Sogutlu et al., 2012]. In the current study we found that the posterior corneal radii flattened in 4 eyes (by 0.59±0.41 mm) but steepened in 6 eyes (by 0.32±0.22 mm) 90-days post-operatively. This variable response appears to be associated with the arc length of the ICRS, with the combination of 90-deg and 160-deg arc lengths ICRS producing a significant steepening on the posterior corneal surface. The optical zone diameter appeared to play also some role in the posterior corneal changes, as we showed in the results.

The regularity of both anterior and posterior corneal surfaces was analyzed by means of RMS of the corneal elevation maps asymmetric terms. In agreement with Chen and Yoon [Chen & Yoon, 2008], who had reported that the posterior corneal surface profile is more irregular than that of the anterior corneal surface in keratoconus, we found much higher pre-op RMS_assym in the posterior corneal surface than in the anterior corneal surface (50.0±21.4 µm *vs* 10.6±5.3 µm). We found that the ICRS did not systematically reduced RMS_assym in either surface. The thickness redistribution after ICRS implantation has been suggested as a delay factor in keratoconus progression of the disease, since as cornea thickens in the weakest areas, the stress may be redistributed and the decompensatory biomechanical cycle might be delayed [Dauwe et al., 2009]. We did not find a systematic increase in the minimum thickness or in the corneal thickness regularity, although the location of minimum thickness tended to move more centrally post-surgery.

(2) 3-D ICRS location

Also, the automatic ICRS volume segmentation allowed a comprehensive characterization of the implanted ICRS. Migration, rotation or extrusion of the ICRS has been related to surgical complications. During the first month following ICRS, the wound healing response remains active, and the increase of myofibroblasts in the ICRS edges may result in slight variations in ICRS position with time [Perez-Merino et al., 2010]. Previous works have used OCT to characterize ICRS depth, but did not correct for optical distortion, and the depth quantification was typically done by analyzing only a few cross sectional OCT images [Gorgun et al., 2012; Lai et al., 2006; Naftali & Jabaly-Habib, 2013]. Naftali et al. [Naftali & Jabaly-Habib, 2013] reported significant differences between the planned and measured ICRS depth (~120 µm). In this study, we showed for the first time systematic measurements of the position of the ICRS in 3-D. Our measurements showed a very good agreement between the planned depth and the 3-D expected depth (~24 µm, on average across all patients of the study, 7-days post-op), with a higher difference for the manual than for the femtosecond tunnel technique. The quantification of the ICRS in 3-D also allowed a longitudinal analysis of the ICRS rotational angles. ICRS rotation appears to have a major impact on anterior corneal symmetry, given the correlation between the ICRS tilt around X and the change in RMS_assym for anterior cornea.

(3) OCT-based corneal aberrometry in keratoconus upon ICRS surgery

As in previous studies reporting the aberrations in keratoconic eyes [Barbero et al., 2002a; Maeda et al., 2002; Schlegel et al., 2009], we found that the astigmatism and coma were the dominant aberrations. We also found a high contribution of the trefoil vertical Z_3^{-3} (19%) and secondary astigmatism Z_4^4 (8%). In general, total and corneal aberrations showed a good correlation, with the corneal aberrations dominating the ocular wave aberration pattern. These results are in good correspondence with previous reports of corneal and total aberrations in keratoconic patients. Despite the high amount of corneal aberrations, total aberrations are consistently lower than corneal aberrations, likely due to compensatory effects of the crystalline lens, particularly for astigmatism and spherical aberration. Several studies in keratoconic eyes have shown that total HOAs are lower than corneal HOAs (by 27.6% [Schlegel et al., 2009] to 34.2% [Barbero et al., 2002a]), in consistency with the findings of the current study (33.3 %).

Several reports point to a compensatory role of the crystalline lens in astigmatism and coma, Dubbelman et al. reported an average compensation of 31% [Dubbelman et al., 2006a] of the anterior corneal astigmatism and 3.5% [Dubbelman et al., 2007a] of the anterior corneal coma by the posterior corneal surface in a normal population. In keratoconus, Chen and Yoon [Chen & Yoon, 2008] reported an average compensation of approximately 20% of the anterior corneal astigmatism and coma by the posterior corneal surface. In this study, we found a larger compensation of coma (16.1% pre-op and 20.1% post-op), but smaller compensation of astigmatism (13.9% pre-op and 9.1% post-op). In addition some compensation occurred for trefoil-terms (7.7% pre-op and 3.1% post-op). Overall, the posterior cornea compensated, on average, 8.3% (pre-op) and 4.1% (post-op) of the aberrations of the anterior cornea, with no significant differences in the amount of compensation pre- and post-operatively. Differences with respect to the anterior/posterior corneal balances reported in the literature on normal subjects may arise from the large topographic differences (in anterior and posterior corneal surfaces) of keratoconic (both pre- and post-operatively) with respect to normal eyes.

While the literature reporting clinical visual performance outcomes is relatively extensive following ICRS treatment, few studies evaluate aberrations. Piñero et al. [Pinero et al., 2010] reported a significant improvement in anterior corneal astigmatism (3.21±2.16 µm (pre-op), 2.50±1.73 µm (post-ICRS), a reduction of coma-like anterior corneal aberrations (3.46±1.86 µm (pre-op), 2.94±1.45 µm (post-ICRS), and of anterior corneal HOAs (3.73±1.97 µm (pre-op), 3.24±1.44 µm (post-ICRS) 3-months post-ICRS implantation, for 6-mm pupils. In contrast, Chalita and Krueger [Chalita & Krueger, 2004] reported an increase in ocular HOA in the ICRS-implanted eye, when compared to the non-treated fellow eye. On average, 3-months post-ICRS implantation we found very small changes (average values not statistically significant) in HOAs (mean decrease of 2%), coma (mean decrease of 5%) and trefoil (mean increase of 4%) after ICRS surgery. Furthermore, we found a larger decrease (although it did not reach statistical significance, on average) of astigmatism (27%). At the individual level, we have found a reduction of asymmetric aberration term and an overall significant decrease of aberrations in several patients (up to a decrease of 2.63 µm in astigmatism, 1.17 µm in coma or 1.63 µm for trefoil). Intersubject variability in the optical response to ICRS may arise from differences in the corneal biomechanical properties across patients, and from the difficulty of the treatment to control simultaneously the topographical and refractive outcomes. In general, the aims of reducing astigmatism, reducing coma or flattening the cornea (to improve contact lens fitting) were met, at least partially, in most patients, although a full simultaneous reduction of both overall astigmatism and HOA was not generally achieved.

The optical findings were in good agreement with visual performance measurements in this group of patients. As found in previous studies in normal subjects [Cheng et al., 2004; Schoneveld et al., 2009], we also found significant correlations between optical quality for HOAs (described by the Visual Strehl optical quality metric at best focus) and visual quality (Best Corrected Visual Acuity), supporting the value of aberration measurements in predicting visual performance. The small overall improvement in visual acuity is consistent with the small improvement in optical quality.

To sum up, this chapter presents:

(1) The first report of comprehensive longitudinal quantification of ICRS surgery based on OCT, including anterior and posterior corneal geometrical, topographical and pachymetric analysis, and 3-D location (depth and rotation) of the ICRS. We have shown that ICRS produced a significant flattening of the anterior corneal surface, particularly with a 5-mm optical zone diameter. There was a not a systematic improvement in corneal symmetry, which was influenced by the arc length of the ICRS, and by the ICRS rotation inside the cornea.

(2) The first report of 3-D OCT-based corneal aberrometry. The high correlation between the measured corneal and total aberrations indicates that OCT alone could be used to describe, to a large extent, the optical quality of keratoconic eyes pre- and post-ICRS treatment, as a result of the predominance of the corneal optics in the overall optical quality of these eyes. ICRS implantation produced a decrease in astigmatism, but on average did not produce a consistent decrease of higher order aberrations, which is consistent with the small increase of visual acuity following treatment. The effect of the ICRS implantation on optical quality varied across patients.

Chapter IV. ***ACCOMMODATION***

OCT-based Crystalline Lens Topography in Accommodating Eyes

This chapter is based on the following publication:

> ***OCT-based Crystalline Lens Topography in Accommodating Eyes***, by P. Pérez-Merino, M. Velasco-Ocana, E. Martinez-Enriquez, S. Marcos in Biomedical Optics Express (2015).

The contribution of Pablo Pérez-Merino to the study, in collaboration with other coauthors, was the literature search, the design of the experiments, the data acquisition (in collaboration with Miriam Velasco-Ocana), the development of specific routines (in collaboration with Eduardo Martínez-Enriquez) and the analysis and processing of the data (in collaboration with Miriam Velasco-Ocana and Eduardo Martínez-Enriquez).

The young crystalline lens is a unique transparent and biconvex lens with aspheric surfaces and it shows the ability of focusing objects at different distances [Atchison, 1995; Glasser & Campbell, 1998b]. However, due to its inaccessibility, knowledge of *in vivo* geometrical or optical parameters of the crystalline lens (relaxed or accommodated) is limited. Information on the crystalline lens provided by commercial or custom-developed instruments is generally limited to axial properties (e.g., crystalline lens thickness). In particular, most of the data of the anterior and posterior lens surfaces come from single cross-sections, not revealing topographic features of the lens.

Different aberrometry studies have also reported the change in the optics of the crystalline lens with accommodation, describing changes in spherical aberration (towards more negative values), and an increase in astigmatism and coma [Gambra et al., 2010; He et al., 2000a; Liang & Williams, 1997b; Lopez-Gil et al., 1998]. Lens aberrations have been measured either *ex vivo* (using laser ray tracing [Birkenfeld et al., 2013] or Hartmann-Shack [Roorda & Glasser, 2004]), or *in vivo* by subtracting corneal aberrations from total aberrations [Artal et al., 2001a; Kelly et al., 2004b]. However, although aberrometers allow measuring the optics of the eye, the relative contribution of the lens surfaces themselves to aberrations is still poorly understood.

Due to its higher speed, depth range and resolution, OCT has been positioned as a promising technique for imaging in 3-D the whole anterior segment of the eye [Grulkowski et al., 2009; Grulkowski et al., 2013; Shen et al., 2010]. However, as we described in previous chapters OCT images are subject to distortions; so, need to be corrected [Ortiz et al., 2010; Ortiz et al., 2011; Ortiz et al., 2009a]. Using distortion-corrected OCT, Ortiz et al. [Ortiz et al., 2012b], reported the first 3-D *in vivo* surface elevation maps of the human crystalline lens, Gambra et al. [Gambra et al., 2013] analyzed static and dynamic changes of the crystalline lens with accommodation, and Sun et al. [Sun et al., 2014] evaluated the surface elevation maps of donor crystalline lenses of different ages.

In this chapter, we present, for the first time to our knowledge, 3-D surface elevation crystalline lens changes with accommodation *in vivo*, and we specifically explored the role of astigmatism and high-order irregularities of all anterior segment surfaces (cornea and lens) and their relationship.

4.1. Material and methods

4.1.1. Subjects

Nine eyes from seven young subjects (mean age: 31±3.1 y.o) were studied. Refractive errors ranged between -5.25 to +0.75 D sphere and -1.25 to 0 D cylinder (Table 4.1). Subjects signed a consent form approved by the Institutional Review Boards after they had been informed on the nature and possible consequences of the study, in accordance to the tenets of the Declaration of Helsinki.

Table 4.1. Individual refractive profile (age and refractive error)

	Age (y.o)	Sphere (D)	Cylinder (D) / axis (deg)
S#1 (OS)	29	-0.5	-0.5 / 20
S#2 (OD)	32	-1.5	-0.5 / 80
S#2 (OS)	32	-1.5	-0.25 / 110
S#3 (OD)	26	-2.5	-0.75 / 150
S#4 (OS)	30	-1.5	-0.25 / 50
S#5 (OS)	36	-5.25	-1.00 / 170
S#6 (OD)	31	-4.25	-1.25 / 175
S#6 (OS)	31	-4.25	-1.25 / 180
S#7 (OS)	33	+0.75	-0.5 / 80

4.1.2. OCT system

The SD-OCT instrument, image processing algorithms, and distortion correction (fan and optical) to obtain anterior and posterior corneal and crystalline lens topographies from OCT images was described in chapter II.

For the purposes of this study, an external accommodative channel was incorporated to the OCT. A Badal system mounted on a motorized stage (VXM-1, Velmex) was used for compensating defocus and for inducing accommodation. The fixation stimulus consists of a 20/25 white Snellen E-letter presented in a black background on a Digital-Light-Processing (DLP) picoprojector (854x480 pixels, Philips NV, Amsterdam, Netherlands; 55 lum) subtending a 5-arcmin visual angle. Two neutral filters (ND 16) were placed after the picoprojector to produce an average luminance of ~30cd/m^2 in an otherwise dark environment. The OCT axis was aligned with the pupilary axis by moving the fixation stimulus in 5 pixels-steps horizontally and vertically until the iris appeared flat in the preview OCT horizontal and vertical cross-sections, so all measurements were acquired when both OCT and pupilary axis were aligned (Figure 2.7 in Chapter II).

4.1.3. OCT: Experimental Procedure

The subjects viewed the stimulus monocularly, with the contralateral eye covered with a patch during the measurements. Measurements were collected in 11x11 mm area and consisted of a collection of 50 B-scans composed by 300 A-scans. The total acquisition time of a 3-D data set was 0.6 seconds. These parameters showed a good balance between time acquisition and resolution for further Zernike fit of the surfaces. The anterior segment of the eye was imaged while stimulating accommodation from 0 to 6 D, in 1.5-D steps. Images containing artifacts (i.e., eyelids) which precluded corneal and lens surface analysis within the optical zone were excluded. Five repeated measurements were collected in each condition after inducing mydriasis with one drop of phenylephrine, which allowed larger pupils without paralyzing the ciliary muscle.

The specifications of the spectrometer and light source do not allow sufficient axial range to capture all anterior segment surfaces in a single acquisition. To solve that, three sets of 3-D images were captured sequentially at 5 seconds after blinking: (1) cornea, (2) anterior lens and (3) posterior lens, rapidly shifting axially the plane of focus; all 3-D sets of data contained the iris.

4.1.4. OCT: Image Processing

In previous studies, we described image-processing tools for distortion correction, denoising, segmentation and merging of volumes [de Castro et al., 2010; Gambra et al., 2013; Ortiz et al., 2013; Ortiz et al., 2012b; Ortiz et al., 2010; Ortiz et al., 2011; Ortiz et al., 2009a; Perez-Merino et al., 2013]. The quantification capabilities of the OCT have been validated *ex vivo* with artificial model eyes with known dimensions, and *in vivo* comparing with other imaging techniques (videokeratography, Scheimpflug and non-contact profilometry). In this chapter we incorporated improved signal processing algorithms, including a simpler and more robust approach to automatic surface segmentation. For every B-scan, simple uni-modal thresholding and morphological operations on the resulting binary image were used to generate masks, which allowed identification of signal of interest in the different eye structures. Segmentation algorithms use properties of these masks (i.e. centroid positions) and *a-priori* knowledge on the measurements (i.e. relative position of iris and cornea). Finally, an AND operation between labeled masks and edges (obtained using a Canny detector) is performed in order to obtain the layers of interest.

The pupil center (obtained from the automatically identified iris volume) was used as fixed reference for anterior segment images collected at different depths. Images of the cornea, anterior lens and posterior lens were merged using this fixed reference for further registration: (1) the corneal image was inverted (since, for efficiency in the focus range shift, the cornea was acquired in the opposite side of the Fourier transform) and then (2) the 3-D volumes of the anterior cornea/iris and posterior lens/iris were shifted to the fixed reference in order to superimpose these volumes to the anterior lens/iris volume (Figure 2.12 in Chapter II).

Distortion correction (fan and optical) algorithms were applied on the merged volumes for quantification by using 3-D ray tracing routines [Ortiz et al., 2010; Ortiz et al., 2011; Ortiz et al., 2009a, 2009b]. The corneal refractive index was taken as 1.376, the aqueous humor refractive index as 1.336, and the crystalline lens refractive index was obtained from the age-dependent average refractive index expression derived by Uhlhorn et al. [Uhlhorn et al., 2008].

Figure 4.1 illustrates the change in anterior segment biometric and geometrical parameters following transformation of optical paths to distances and distortion corrections. For example, distortions produced errors of 38%-17% in the estimates of anterior and posterior lens radii of curvature.

The beam diameter reduced across surfaces due to refraction. The mean diameters in the different surfaces were 6.32±0.07 mm at the anterior cornea, 6.17±0.06 mm at the posterior cornea, 5.47±0.11 mm at the anterior cornea, and 4.74±0.12 mm at the anterior cornea in the relaxed state (mean±SD for all eyes). For comparison of the surface elevation maps, the analysis was performed for a constant pupil diameter of 4-mm diameter (common to all subjects and surfaces, and free of edge artifacts).

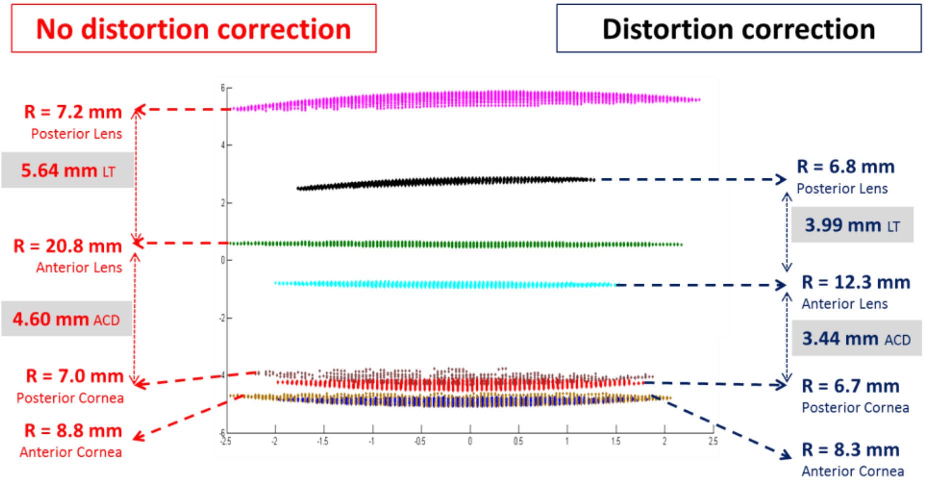

Figure 4.1. Illustration of the effect of distortion correction on the anterior segment surfaces in S#1 (OS). Left data: from optical paths, without distortion correction; right data: distortion correction.

All signal-processing algorithms run completely automatically with no need of user interaction. Full computational processing time per eye was 14.6 s (Intel Xeon CPU@3.5 GHz processor, 8GB RAM).

4.1.5. OCT: Spatial Resolution and Accuracy Considerations

The effective actual resolution, the effect of lateral sampling, and the robustness of the merging algorithm were investigated, as they all play a role in the accuracy of the lens surface elevation estimates. A simulation on virtual surfaces with added white noise of standard deviation equal to nominal axial resolution (1000 realizations), revealed differences between the original-correct-surface and the noisy surfaces of 2.4 µm (RMS surface elevation) and 0.28 µm (RMS of the Zernike coefficients). Therefore the error caused by the axial resolution limit is around half to that given by the nominal OCT axial resolution. Also, a simulation using 500 random realistic surfaces of 300 A-Scans x 300 B-Scans in a 5x5 mm which were then subsampled by a sampling factor of 6 in the y-coordinate (as in our measurement configuration, 50 B-Scans) showed that the RMS error between the generated and the subsampled surfaces was below 0.3 µm, demonstrating a low impact of sampling in the lateral resolution of our measurements. Finally, we evaluated the accuracy and robustness of the merging methodology by removing a percentage of points of the iris (randomly taken from a uniform distribution) and we compared the estimated center point of the complete and the subsampled iris. The mean estimation error was below 2 µm for x_0, y_0 and z_0 if we removed 80% of the iris points.

4.1.6. Biometric, geometric and surface elevation changes with accommodation

The geometrical distances between ocular elements in the anterior segment were taken from the apex positions: (1) anterior chamber depth (ACD), distance between the posterior corneal apex and the anterior lens surface apex, and (2) lens thickness (LT), distance between the anterior and posterior lens apex (Figure 4.2).

Corneal and lens segmented surfaces were first fitted by spheres, and their radii of curvature estimated. Corneal and lens surface elevations were obtained by subtraction of the best fitting spheres from the segmented surfaces. Both, corneal and lens surfaces were fitted by Zernike polynomial expansions (6th order; note that these Zernike coefficients describe surface elevations, and not wave aberrations).

Descriptive parameters of the surface elevation maps include individual surface Zernike coefficients, the Root Mean Square (RMS) for all high order coefficients (excluding tilt, defocus and astigmatism) and the RMS of the combination of some terms (RMS astigmatism, RMS trefoil and RMS coma).

For all computations, the central 4-mm area (with respect to the pupil center) of the cornea and lens was evaluated, since after ray convergence (optical distortion compensation) this area is common and free of edge artifacts in all surfaces and conditions, including the posterior lens surface.

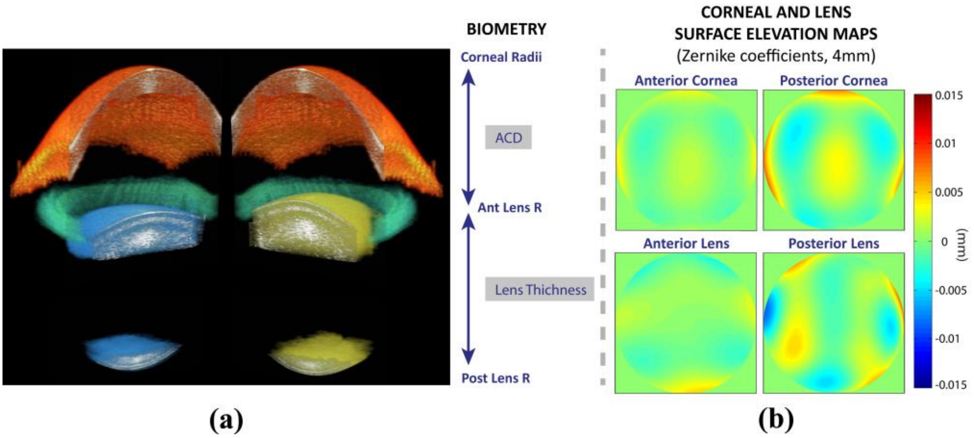

Figure 4.2. (a) Examples of 3-D images in S#2 relaxed (left) and for 6 D of accommodative demand (right). (b) Corneal (up) and crystalline lens (down), anterior (left) and posterior (right) surface elevation maps in S#2 (OD) relaxed accommodation. Data are for 4 mm.

4.1.7. Accommodative response

The accommodative response was estimated from the changes in the anterior segment biometry data (radii, ACD and LT) with accommodation. A schematic eye model in paraxial approximation (considering all refractive indices of the eye) was used to analyze the refractive change of the eye.

Equation 4.1: $\mathrm{P_C} = \frac{\mathrm{n_h}-1}{\mathrm{R_c}}$; $\mathrm{P_L} = (n_l - n_h)\left(\frac{1}{\mathrm{R_a}} - \frac{1}{\mathrm{R_p}}\right) + \frac{(\mathrm{n_l} - \mathrm{n_h})^2\ \mathrm{LT}}{\mathrm{n_l}\ \mathrm{R_a R_p}}$

Equation 4.2: $\mathrm{P} = \mathrm{P_C} + \mathrm{P_L} - \frac{\mathrm{ACD}*\mathrm{P_c}*\mathrm{P_L}}{\mathrm{n_h}} + \frac{(\mathrm{n_l} - \mathrm{n_h})*\ \mathrm{LT}*\mathrm{P_c}}{\mathrm{n_l}*\mathrm{R_p}}$

where P, P_C and P_L are the power of the eye, cornea and lens, nh and nl are the refractive indexes of the aqueous humor and the lens, and Rc, Ra and Rp are the radii of curvature of the cornea, anterior lens and posterior lens

4.1.8. Corneal and lens surface astigmatism axis

The corneal and lens surfaces astigmatism (C) and angle (α) were obtained from the surface elevation astigmatism Zernike coefficients using equation 4.3:

Equation 4.3: $\mathrm{J_0} = \frac{-2\sqrt{6}\mathrm{C}_2^2}{\mathrm{R}^2}$; $\mathrm{J_{45}} = \frac{-2\sqrt{6}\mathrm{C}_2^{-2}}{\mathrm{R}^2}$; $\mathrm{C} = -2\sqrt{\mathrm{J}_0^2 + \mathrm{J}_{45}^2}$; $\alpha = \frac{1}{2}\arctan\frac{\mathrm{J_{45}}}{\mathrm{J_0}}$

If $J_0 < 0$, then meridian = axis + 90 degrees
If $J_0 = 0$, and if $J_{45} < 0$, then meridian = 135 degrees
If $J_0 = 0$, and if $J_{45} > 0$, then meridian = 45 degrees
If $J_0 > 0$, and if $J_{45} \leq 0$, then meridian = axis + 180 degrees
If $J_0 > 0$, and if $J_{45} > 0$, then meridian = axis [Salmon et al., 2003].

We represent anterior and posterior corneal and lens surface astigmatism data in a power vector graph. The length of the vectors represents the calculated magnitude of surface astigmatism (in diopters) and the direction of the vectors allows estimating the relative angle between anterior and posterior corneal and lens astigmatism axis. All vectors were represented in a polar coordinate system.

4.1.9. Statistics

The changes in lens surfaces with accommodation were analyzed using an analysis of variance (ANOVA; general linear model for repeated measurements). Significant levels (ANOVA and pair-wise two tailed comparison t-test) were set at $p<0.05$. The statistical significant levels were adjusted by a Bonferroni correction. The statistical tests were performed using SPSS software (SPSS, Inc., Chicago, Illinois).

4.2. Results

4.2.1. Anterior and posterior lens surface elevation (relaxed state)

Figure 4.3 shows anterior and posterior surface elevation maps (3rd and higher-order terms) and figure 4.4. the Zernike terms (also including astigmatism), in all eyes in the relaxed state. The posterior lens shape generally shows higher magnitude than the anterior lens in some higher order terms.

On average, for the unaccommodated state, the individual dominant high-order irregularities of the anterior lens surface were horizontal/vertical (H/V) astigmatism (Z_2^2), oblique trefoil (Z_3^{-3}), and spherical (Z_4^0), accounting for 15%, 11% and 21% of the variance, respectively. For the posterior lens surface, the individual dominant high-order irregularities were oblique astigmatism (Z_2^{-2}) and vertical quadrafoil (Z_4^4), accounting for 48% and 32% of the variance, respectively.

The RMS of high-order irregularities and astigmatism of the posterior lens surface was statistically significantly higher than that of the anterior lens surface (high-order irregularities: x2.02, p<0.0001; astigmatism: x1.58, p=0.01).

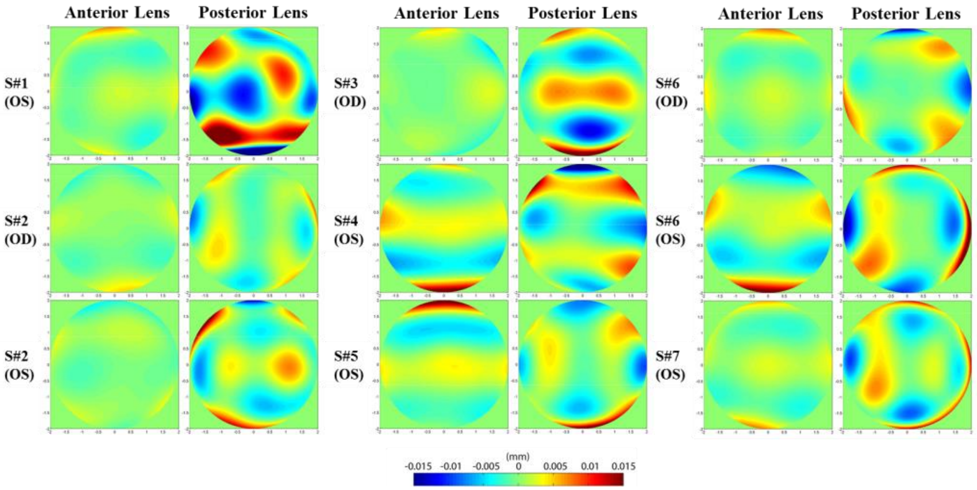

Figure 4.3. Anterior and posterior crystalline lens elevation surface maps in the unaccommodated state (maps exclude tilt, defocus and astigmatism).

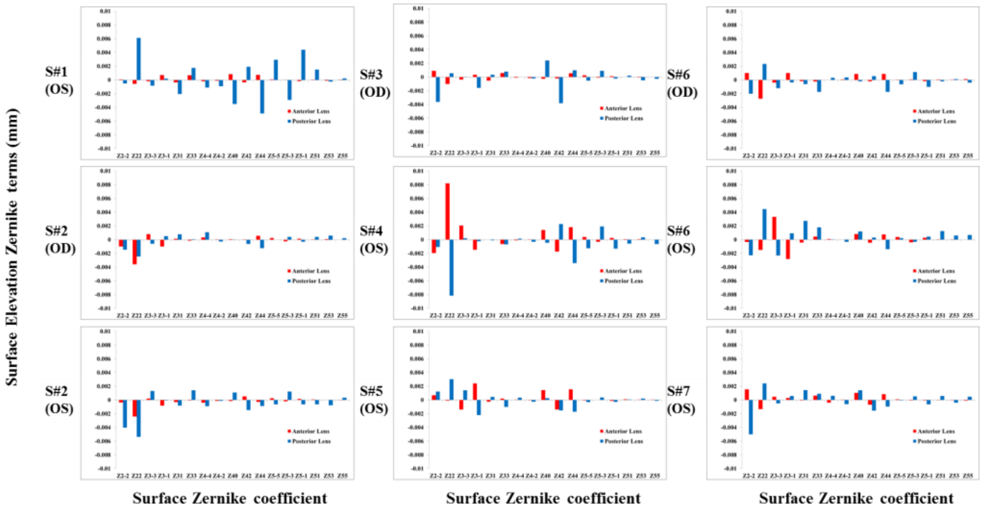

Figure 4.4. Anterior and posterior crystalline lens surface Zernike coefficient (plots include astigmatism and high-order terms; pupil diameter is 4-mm).

4.2.2. Comparison of Zernike coefficients of ocular surfaces (cornea and crystalline lens)

An analysis of repeatability showed highly reproducible Zernike coefficient across repetitive measurements (average SD for all high-order Zernike coefficients) within each surface: 0.33 µm (anterior cornea), 0.57 µm (posterior cornea), 0.29 µm (anterior lens), 0.59 µm (posterior lens), in the relaxed state.

Table 4.2 shows correlations of anterior and posterior corneal and anterior and posterior crystalline lens Zernike coefficients in the relaxed state. A significant correlation indicates that the magnitudes of individuals Zernike coefficients are closely associated. We found strong positive correlation in H/V astigmatism (Z_2^{2}), spherical (Z_4^{0}), vertical coma (Z_3^{-1}) and secondary astigmatism (Z_4^{-2} and Z_4^{2}) between corneal surfaces, and strong negative correlation in vertical coma (Z_3^{-1}) and oblique trefoil (Z_3^{-3}) between lens surfaces. We further investigated the relationship between corneal and lens surfaces. There is significant positive correlation in the spherical aberration (Z_4^{0}) between anterior corneal and anterior lens surfaces and significant negative correlation in lateral coma (Z_3^{1}) and positive correlation in vertical trefoil (Z_3^{-3}) between anterior corneal and posterior lens surfaces.

Table 4.2. Pearson correlation coefficient and p-value for individual Zernike coefficients in corneal and lens surfaces in the relaxed state.

		Cornea	***Lens***	***Cornea & Lens***	
		Ant vs Post	*Ant vs Post*	*Ant Cornea vs Ant Lens*	*Ant Cornea vs Post Lens*
Astigmatism	Z_2^{-2}	r=0.55; p=0.15	r=-0.25; p=0.5	r=-0.57; p=0.1	r=-0.35; p=0.3
	Z_2^{2}	r=0.79; p=0.01*	r=0.63; p=0.08	r=-0.37; p=0.3	r=-0.37; p=0.3
Spherical	Z_4^{0}	r=0.79; p=0.02*	r=-0.34; p=0.41	r=0.83; p=0.01*	r=-0.19; p=0.6
Coma	Z_3^{-1}	r=0.69; p=0.05*	r=-0.74; p=0.03*	r=-0.39; p=0.3	r=0.53; p=0.16
	Z_3^{1}	r=0.39; p=0.33	r=0.06; p=0.87	r=-0.03; p=0.9	r=-0.73; p=0.03*
Trefoil	Z_3^{-3}	r=0.42; p=0.28	r=-0.71; p=0.04*	r=-0.33; p=0.4	r=0.82; p=0.01*
	Z_3^{3}	r=0.33; p=0.41	r=0.62; p=0.09	r=0.15; p=0.7	r=-0.26; p=0.5
Secondary	Z_4^{-2}	r=0.83; p=0.01*	r=0.28; p=0.49	r=-0.25; p=0.5	r=-0.35; p=0.3
Astigmatism	Z_4^{2}	r=0.97; p=0.001*	r=-0.33; p=0.38	r=0.42; p=0.3	r=-0.15; p=0.7

Figure 4.5 shows the average Zernike coefficients of all subjects (astigmatism and high-order terms) of the corneal and lens surface elevation maps in the relaxed state. The higher corneal coefficients were the horizontal astigmatic terms Z_2^{-2}, followed by the spherical term Z_4^0. Corneal surface astigmatism was significantly higher in the posterior than in the anterior cornea ($p<0.001$). The sign of the average Zernike surface coefficients in the anterior and posterior crystalline lens surfaces is opposite in some coefficients (i.e. Z_2^2, Z_3^{-1}, Z_3^{-3} and Z_4^4). As shown in Figure 4.5, on average (all subjects) anterior and posterior corneal surfaces Zernike terms are positively correlated ($r=0.97$, $p<0.0001$), while anterior and posterior lens surfaces Zernike terms are negatively correlated ($r=-0.43$, $p=0.04$).

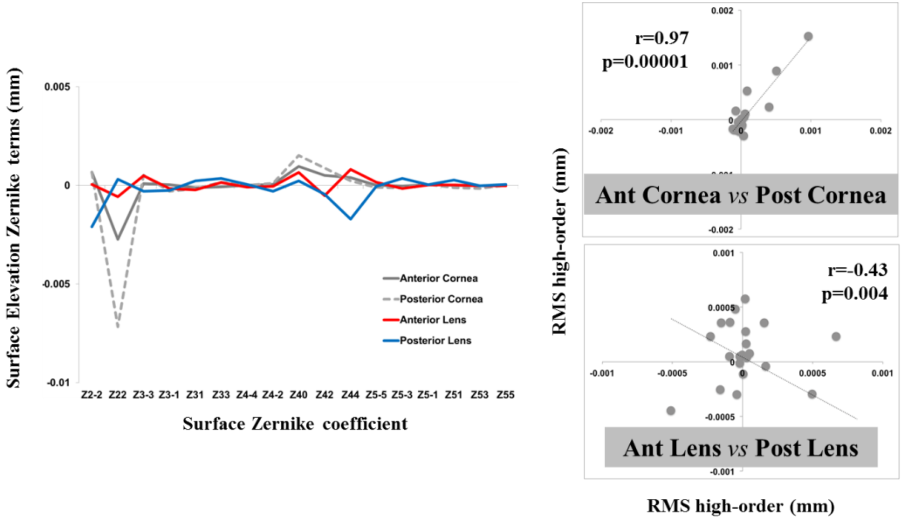

Figure 4.5. (a) Cornea and crystalline lens surface elevation Zernike terms (astigmatism and high-order) in the relaxed state (average over all subjects). (b) Cornea and crystalline lens individual Zernike coefficients (high-order) in the relaxed state.

4.2.3. Phenylephrine vs natural anterior lens surface topography

Figure 4.6 compares the Zernike coefficients of the anterior crystalline lens surface between phenylephrine and natural conditions, for different levels of accommodation. RMS differences range between 0.41 µm and 0.81 µm. The correlation between Zernike coefficients of the lens surface elevation in both conditions were high (r=0.85-0.97, p<0.0001).

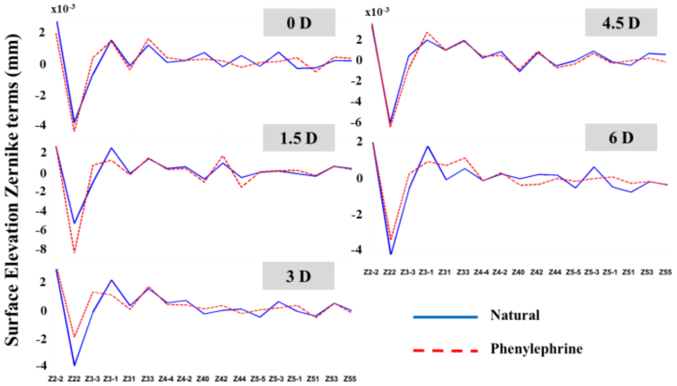

Fig. 4.6. Natural *vs* phenylephrine conditions in the anterior crystalline lens surface (Zernike coefficients) for all accommodative demands.

4.2.4. Changes in anterior segment geometry and biometry with accommodation

For the relaxed state, the average ACD was 3.43±0.21 mm, central lens thickness was 3.88±0.19 mm, and the average anterior and posterior lens radii of curvature were 13.07±1.28 mm and -6.48±0.51 mm respectively. ACD decreased at a rate of 0.04±0.01 mm/D (Figure 4.7a) and lens thickness increased at 0.04±0.01 mm/D (Figure 4.7b) with accommodative demand. Both anterior and posterior lens surfaces became steeper with accommodation (particularly the anterior lens surface): anterior and posterior lens radii of curvature changed at rates of 0.78±0.18 and 0.13±0.07 mm/D (Figure 4.7c and 4.7d). The ranges of radii of curvature, ACD and lens thickness in the accommodated state, as well as their change with accommodative demand, are consistent with those reported in the literature [Gambra et al., 2013]. On average, the standard deviation across subjects and accommodative states in axial distances were 0.028 mm in ACD and 0.027 mm in lens thickness. The optical power of the lens was estimated for all subjects at all accommodative demands (Figure 4.7e). It ranges from 17.5 to 22.7 D in the relaxed state and from 21.5 to 25.9 D for 6 D of accommodative demand. The average change was 0.81±0.19 D per D of accommodative demand.

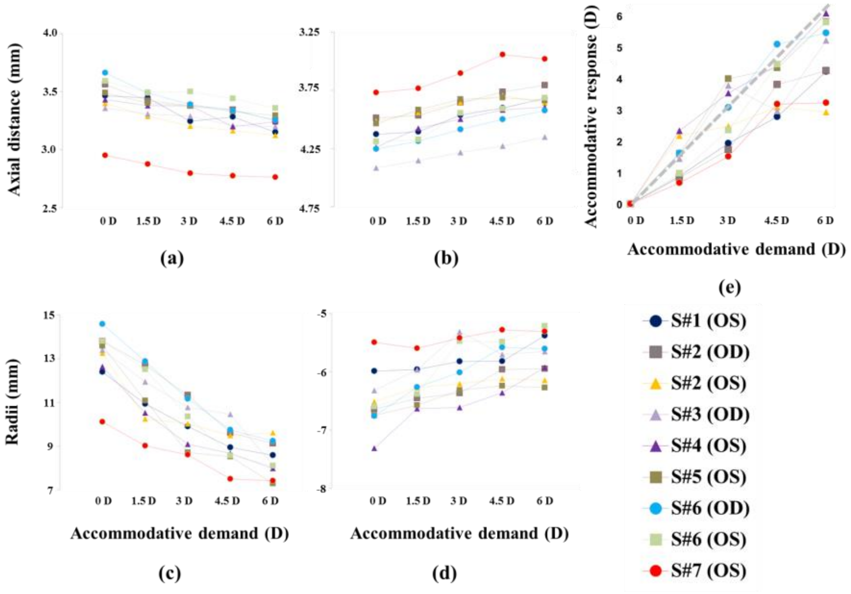

Figure 4.7. Biometric and geometrical changes with accommodation: (a) Anterior Chamber Depth, (b) Lens Thickness, (c) Anterior Lens Radius and (d) Posterior Lens Radius (e) Accommodative response vs Accommodative demand in all subjects.

4.2.5. Changes in anterior and posterior lens surface elevation with accommodation

Figure 4.8 shows an example (S#2, OS) of the corneal and lens segmented surfaces from the OCT image (left) and the corresponding anterior and posterior lens surface elevation maps for different accommodative states (right).

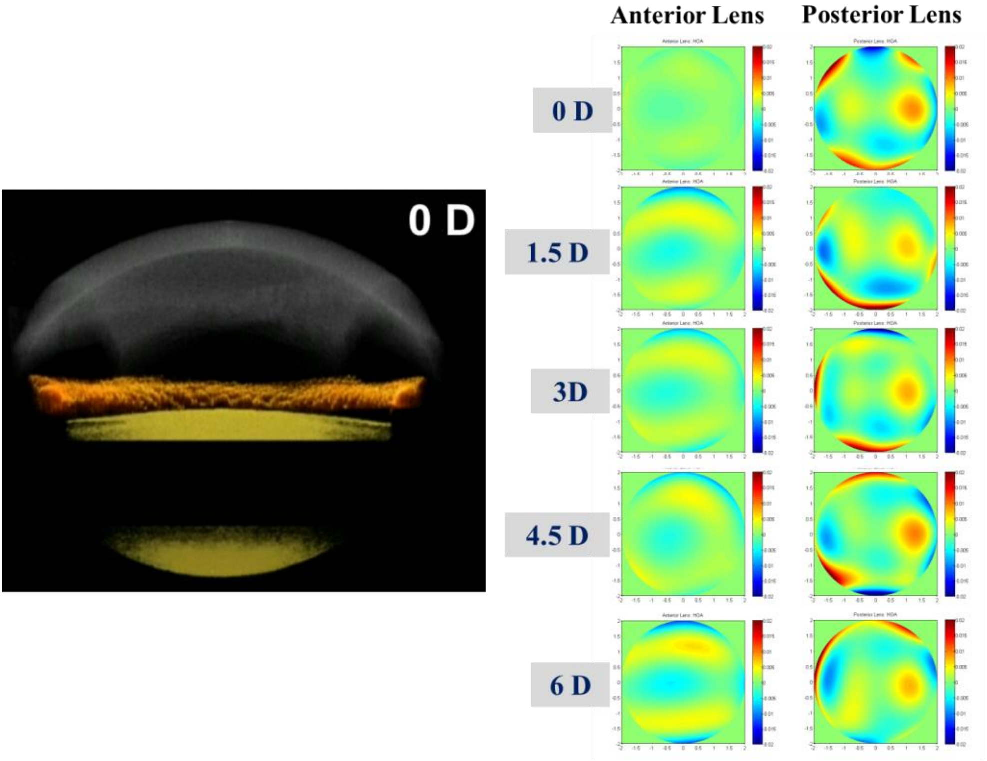

Figure 4.8. Example of the anterior segment segmented surfaces (corneal and lens) with accommodation (left) and the corresponding lens surface elevation maps for different accommodative demands (right). Data are for subject S#3. Pupil diameter in maps is 4-mm.

Figure 4.9 shows changes in RMS of high-order irregularities, astigmatism, coma, trefoil and spherical as a function of accommodative demands. High-order irregularities, astigmatism, coma and trefoil increased with accommodation by a factor of x1.44 ($p<0.05$), x1.95 ($p<0.05$), x1.95 and x1.28 in the anterior lens surface (between 0 and 6 D), respectively, and changed by a factor of x1.04, x1.10, x1.39 and x1.33 in the posterior lens surface (between 0 and 6 D), respectively. Interestingly, we found a notch at 3 D for the RMS high-order irregularities, RMS coma and RMS trefoil in 7/9 subjects in the posterior lens surface, but this was not found to be statistically significant. As in previous studies reporting the wave aberrations, we found that the spherical term changed towards negative values with accommodation in the anterior lens surface but this tendency is not observed in the posterior lens surface.

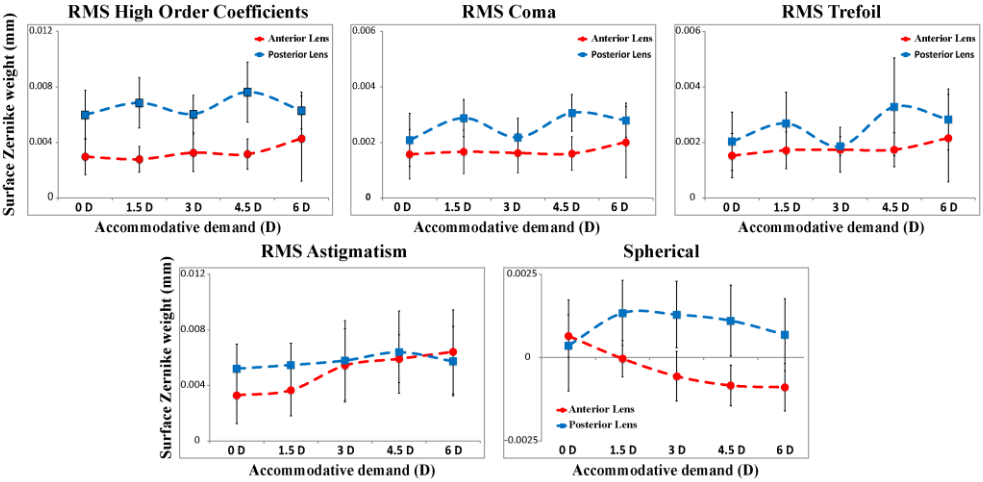

Figure 4.9. Average RMS of high-order irregularities, astigmatism, coma, trefoil and spherical for different accommodative demands. Data are for 4-mm pupils.

Table 4.3 shows the average relative contribution (in terms of variance, RMS^2) of the lower and higher order Zernike terms (astigmatism, coma, trefoil, spherical term, 4th order and of 5th and higher-order coefficients). In the relaxed state, the spherical term accounts for most of the surface irregularity in the anterior lens (47%). However, with accommodation, the astigmatism is the predominant surface irregularity (accounting for 90% of the variance). In contrast, the posterior lens surface astigmatism accounts for 70% of the variance in the relaxed state, but with accommodation its contribution decreased.

Table 4.3. Relative contribution (in terms of %) of different Zernike terms to the overall surface elevation maps (for 4-mm pupils).

	Anterior Lens Surface					**Posterior Lens Surface**				
	0 D	*1.5 D*	*3 D*	*4.5 D*	*6 D*	*0D*	*1.5 D*	*3 D*	*4.5 D*	*6 D*
Astigmatism	17.05	93.16	91.03	94.05	94.52	70.06	48.13	21.20	3.33	68.67
Coma	3.12	5.35	2.76	0.46	0.53	1.33	0.10	7.47	3.59	13.10
Trefoil	13.13	0.67	1.96	0.06	0.06	2.45	6.85	14.88	0.31	3.07
Spherical	47.32	0.03	2.87	4.44	4.44	1.73	26.17	34.21	54.87	6.24
4th order	19.06	0.74	1.34	0.97	0.97	23.31	18.14	21.69	36.36	7.98
Others	0.30	0.03	0.01	0.01	0.01	1.11	0.58	0.53	1.51	0.91

4.2.6. Corneal and lens surface astigmatism magnitude and axes with accommodation

On average, the astigmatic axis of the anterior and posterior corneal surfaces tends to be aligned (6.2±2.1 deg). In the relaxed state of accommodation, the astigmatic axis of the anterior lens surface is moderately rotated with respect to the anterior cornea (27±25 deg, on average). Furthermore, the anterior and posterior lens astigmatism axes differed by 80±42 deg.

Figure 4.10 shows a power vector analysis of surface astigmatism in anterior and posterior lens surface in all eyes, for all accommodative demands. Individually, the relative angle between corneal astigmatic axis and anterior lens astigmatic axis was <20 deg in 5/9 eyes (S#1 (OS), S#2 (OS), S#3 (OD), S#6 (OD) and S#6 (OS)), >20 and <50 deg in 3/9 eyes (S#2, S#6 and S#9) and > 80 deg in 1/9 eyes (S#4 (OS)). In contrast, the relative angle between the anterior and posterior lens was around 90 deg in 7/9 eyes (S#1 (OS), S#3 (OS), S#4 (OS), S#5 (OS), S#6 (OD), S#6 (OS) and S#7 (OS)), while was <10deg in 2/9 eyes (S#2 and S#3). At the maximum accommodative demand the relative angle between anterior and posterior lens was on average 90±43 deg, around 40 deg in 3/9 eyes (S#2 (OD), S#2 (OS) and S#4 (OS)), around 90 deg in 3/9 eyes (S#1 (OS), S#6 (OS) and S#6 (OS)) and >120 deg in 3/9 eyes (S#3 (OD), S#5 (OS) and S#7 (OS)). The average change of the astigmatism angle with accommodation was 15±11 deg and 21±18 deg in the anterior and in the posterior lens surface, respectively.

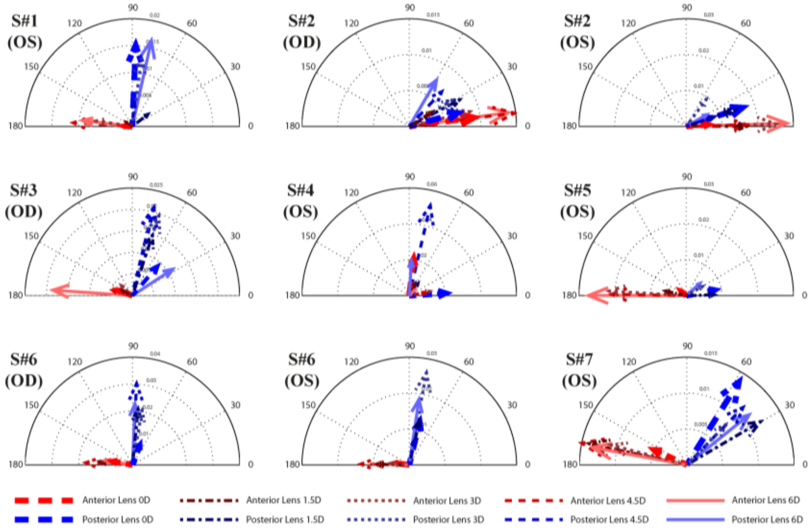

Figure 4.10. Power vector polar plot of astigmatism in anterior and posterior crystalline lens surfaces, for different accommodative demands. Each panel represents a different eye. Red lines stand for anterior lens and blue lines for posterior lens astigmatism. Each line type represents a different accommodative demand. The angle represents the axis of astigmatism and the length of the vectors represents the magnitude of the corresponding surface astigmatism.

Figure 4.11 shows the change in the magnitude of astigmatism with accommodative demand. In the relaxed state, the magnitude of astigmatism was higher in the posterior lens surface but this tendency reversed in most subjects with accommodation.

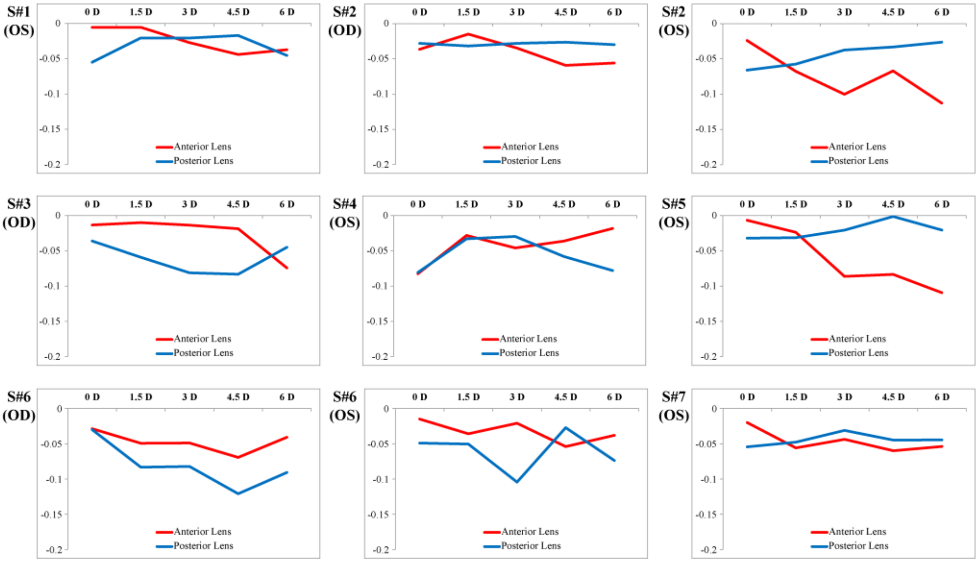

Figure 4.11. Astigmatism surface magnitude in all eyes for different accommodative demands.

4.3. Discussion

The higher speed and axial and lateral resolution of OCT makes it an ideal tool to evaluate the anterior segment of the eye (cornea and lens) in 3-D. Most previous studies quantifying lens geometry *in vivo* using different imaging modalities were limited to only one or two central cross-sections (2-D information) and generally report only central thickness and radii of curvature [He & Wang, 2014; Leng et al., 2014; Neri et al., 2015]. However, the cornea and the crystalline lens surfaces are non-rotationally symmetric, therefore 3-D measurements are required. Recently, OCT combined with dedicated image processing algorithms provide accurate 3-D corneal [Karnowski et al., 2011; Ortiz et al., 2011; Perez-Merino et al., 2014; Zhao et al., 2010] and lens [Ortiz et al., 2012b] surface reconstructions after distortion correction.

This study represents, to our knowledge, the first *in vivo* study reporting the cornea and the crystalline lens shapes in 3-D as a function of accommodation, allowing studying relationships across the surfaces elevation maps, and the 3-D changes of the anterior and posterior crystalline lens surfaces with accommodation.

Knowledge of corneal and lens astigmatism and surface irregularities is critical for understanding the underlying optical causes for astigmatism, and the relative contribution of the different optical elements. To date, the contribution of the crystalline lens astigmatism to total astigmatism comes from indirect comparison of ocular astigmatism (measured by refraction or aberrometry), and corneal astigmatism (measured by keratometry or corneal topography) [Artal et al., 2001a; Dunne et al., 1996; Keller et al., 1996; Kelly et al., 2004b]. Javal postulated a relationship between corneal and refractive astigmatism, proposing a compensation of -0.5 D of against-the-rule corneal astigmatism by the internal optics. However, the Javal rule has been adjusted over time, either based on theoretical considerations or clinical data [Dunne et al., 1996; Grosvenor et al., 1988; Keller et al., 1996]. Artal et al. [Artal et al., 2001a] and Kelly et al. [Kelly et al., 2004b] found significant negative correlation for anterior corneal horizontal/vertical total and internal astigmatism of the internal optics, suggesting at least a partial compensation for corneal astigmatism by the lens in a relaxed state.

Our results suggest that compensation of astigmatism does not only happen between the cornea and the crystalline lens but also between the lens surfaces of the ocular components. In agreement with prior work by Dubbelman et al. [Dubbelman et al., 2006a; Dubbelman et al., 2007a] we found that on average the posterior corneal surface compensated part of the irregularities of the anterior cornea, in particular astigmatism (31% [Dubbelman et al., 2006a] / 18% in the current study) and coma (from 3.5% [Dubbelman et al., 2007a] / 12% in the current study). As in the cornea, our study also revealed a high correlation between the magnitude of the irregularities of the anterior and posterior lens surfaces in coma and trefoil terms, indicating coordinated development. Although we did not find correlations between the magnitude of astigmatism of the anterior and posterior crystalline lens surfaces, the tendency in many subjects for orthogonal astigmatic axis in anterior and posterior lens (which we had also shown *in vivo* in a preliminary study on three young subjects) also indicates compensatory processes accounted by lens geometry. Interestingly, this tendency was also reported in some *ex vivo* eyes by Sun et al. [Sun et al., 2014] on isolated crystalline lenses, more frequently in younger than older lenses.

Our study did not directly address the presence of Gradient Index (GRIN) distribution in the lens, and its potential role in our findings. Siedlecki et al. [Siedlecki et al., 2012] found that a homogeneous index could overestimate the posterior lens asphericity but not the posterior lens radius of curvature. Previous work on isolated lenses shows that GRIN plays in fact a major compensatory role for the spherical aberration in the young eye [Birkenfeld et al., 2014; de Castro et al., 2013], by shifting lens spherical aberration towards more negative values, and therefore compensating the spherical aberration of the cornea. With accommodation, de Castro et al. [de Castro et al., 2012] found more negative aberration and a larger shift toward more negative values. However, although posterior lens surface shape estimation could have a benefit by increasing knowledge of the lens GRIN (especially in the spherical Zernike terms), it should be noted that *ex vivo* GRIN distribution represent more closely values the GRIN in a maximally accommodated state and it is unlikely that GRIN plays a major role in non-rotationally symmetric aberrations. In fact, in a recent study on the impact of shape and GRIN on the astigmatism of isolated lenses, Birkenfeld et al. [Birkenfeld et al., 2013] found little influence of GRIN on the magnitude and axis of lens astigmatism.

Overall, our results of the crystalline lens surface elevation *in vivo* hold similarities with those that we recently reported on *ex vivo* human donor lenses [Sun et al., 2014]. As in this study, we found significant correlations between anterior and posterior vertical coma and vertical trefoil (*ex vivo* data showed correlations also in several other high order terms). However, we found *in vivo* significantly higher astigmatism and high-order irregularities in with the posterior lens surface than in the anterior lens surface, which was not reported *ex* *vivo*. Differences between results *in vivo* and *ex vivo* may be associated to the lack of zonular tension in the isolated lenses, which may be responsible for some of the irregularities in the posterior lens *in vivo*. In fact isolated lenses adopt its more accommodated form, and therefore, lens surface elevations from *ex vivo* data are more representative of accommodating lenses.

As the lens accommodates, many studies have demonstrated accommodation-induced changes in aberrations of the eye, which include changes in spherical aberrations, and to a lesser extent in astigmatism, coma, and trefoil [Gambra et al., 2010; He et al., 2000a; Lopez-Gil et al., 1998; Roorda & Glasser, 2004]. The most relevant high order aberration change in the lens with accommodation is the negative shift of spherical aberration (due to changes in radii of curvature and asphericity, and to a lesser extent GRIN). Although some of these changes may be associated to some changes in lens tilt with accommodation [Rosales et al., 2008], our results show that changes in lens surface astigmatism (including relative anterior/posterior astigmatic angle shifts between 10 and 20 deg) can also occur. We also found some systematic (not monotonic) changes in high order surface terms, coma and trefoil in particular, with accommodation, both for anterior and posterior lens surfaces.

In summary, quantitative OCT imaging in accommodating eyes has allowed us to evaluate changes in the anterior segment of the eye with accommodation, including 3-D corneal and lens surface elevation maps, allowing us to gain insights on the geometrical changes undergone by the eye with accommodation, and the relative contribution of the different lens surfaces to the optics of the eye, including astigmatism and high-order aberrations. Further studies on a larger population of different age and/or refractive profiles will allow gaining insights on the role of the crystalline lens on the age-dependent changes of the eye's optics.

Chapter V. ***PRESBYOPIA-CATARACT AND IOL***

OCT-based Geometrical Evaluation and Aberrometry of Patients Implanted with Accommodative IOLs

This chapter is based on the following publications:

1. ***Three-Dimensional Evaluation of Accommodating Intraocular Lens Shift and Alignment In Vivo***, by S. Marcos, S. Ortiz, P. Pérez-Merino, J. Birkenfeld, S. Durán, I. Jimenez-Alfaro, in Ophthalmology (2014).
2. ***Aberrometry in Patients Implanted with Accommodative Intraocular Lenses***, by P. Pérez-Merino, J. Birkenfeld, C. Dorronsoro, S. Ortiz, S. Durán, I. Jimenez-Alfaro and S. Marcos, in American Journal of Ophthalmology (2014).

The contribution of Pablo Pérez-Merino to the study, in collaboration with other coauthors, was the literature search, the design of the experiments, the customization of the measuring instruments (in collaboration with Sergio Ortiz), the data acquisition, the development of specific routines (in collaboration with Sergio Ortiz) and the analysis of the data (in collaboration with Sergio Ortiz).

With aging, the crystalline lens first loses its capability to accommodate to near and far objects (presbyopia), and later it loses transparency (cataract). An emerging solution for presbyopia and cataract correction are accommodative intraocular lenses (A-IOLs), artificial lenses that would replace the aged crystalline lens of the eye, ideally mimicking the dynamic focusing capability of the young human crystalline lens in response to the ciliary muscle contraction, and which would restore both lens transparency and accommodation [Glasser, 2008].

In the last years, A-IOLs have been proposed that aim at restoring accommodation, ranging from FDA-approved A-IOLs to conceptual proposals, and relying on various principles of operation (axial shifts, lateral shifts or curvature-changing surfaces) [Cumming et al., 2006; McLeod et al., 2007]. Most studies on A-IOLs primarily report visual functional outcomes based on the patient's visual function, showing than the subjective accommodative response after A-IOL implantation was close to the magnitude of standard monofocal IOLs [Beiko, 2013; Tahir et al., 2010]. Whereas subjective tests assess visual performance at different distances, the results provided cannot generally conclude whether the A-IOLs are actually working according to their functional mechanism [Leydolt et al., 2009; Macsai et al., 2006; Tucker & Rabie, 1980].

Alternatively, aberrometry and biometry to evaluate whether A-IOLs are operating as expected appear as highly suitable objective techniques to evaluate the optical performance and to visualize the movement of A-IOLs with accommodation. With aberrometry, Dick and Kaiser [Dick & Kaiser, 2002] found small changes in defocus in patients implanted with the Crystalens AT-45 (Bausch&Lomb, Rochester, NY) and 1CU (HumanOptics AG, Erlangen, Germany) A-IOLs; and Wolffsohn et al. [Wolffsohn et al., 2010] reported some changes in ocular aberrations (defocus, astigmatism, coma and trefoil) with increased accommodative demand in eyes implanted with the Tetraflex A-IOL (model KH-3500; Lenstec, St. Petersburg, FL) [Wolffsohn et al., 2010]. Using high-frequency ultrasound biomicroscopy (UBM) and partial coherence interferometry (PCI), Marchini et al. [Marchini et al., 2004] reported a forward mean shift of 0.32 mm at 1-month after A-IOL implantation (with several eyes showing backward shifts), Stachs et al. [Stachs et al., 2006] described a forward a mean shift of 0.24 mm under pilocarpine treatment, and Koeppl et al. [Koeppl et al., 2005] detected only negligible counterproductive backward movement of the AT-45 with pilocarpine-induced accommodation. While there have been attempts for 3-D imaging with UBM technology, most studies solely report the ACD based on cross-sectional images.

Apart from slight axial shifts of the Crystalens in the axial direction, observational studies have also reported asymmetric vaulting in the IOL associated to IOL tilt (caused by capsular contraction or by asymmetric fibrosis in the haptic region), known as Z syndrome [Yuen et al., 2008]. So, measurement of tilt with this IOL is particularly relevant because the hinged design of the haptic and the effect of accommodative forces onto the lens likely play a role in IOL alignment.

Recently, Ortiz et al. [Ortiz et al., 2013] quantified full 3-D anterior segment geometry and biometry in patients implanted with IOL with distortion-corrected OCT, reporting also IOL tilt. While quantification of the 3-D position of the A-IOL with accommodation by using

OCT will assess whether the mechanism of operation of the A-IOL complies with the expected design, aberrometry will be essential to understand the causes why eyes appear to gain near vision functionality with these A-IOLs. In fact, a future link between geometrical factors and optical outcomes may be established by means of customized eye models.

In this chapter we measured 3-D biometry (with distortion-corrected OCT) and ocular aberrations (with LRT) and for different accommodative demands in 22 eyes implanted with Crystalens AO A-IOL. These measurements will allow evaluating the objective accommodative response, aberrations, depth-of-focus and 3-D the changes in IOL position in Crystalens A-IOL eyes at different accommodative states.

5.1. Methods

5.1.1. Patients, surgery and A-IOLs

Twenty-two eyes from eleven patients were measured (age: 75±4 years old, ranging from 67 to 81 years old; spherical equivalent: -0.5±0.4 D, ranging from -1.25 D to 0.75 D) in this prospective observational study. Consecutive patients scheduled for cataract surgery with good general health and meeting the inclusion criteria (age > 50 years old; manifest astigmatism < 1.5 D; and bilateral cataract considered as the sole cause of visual acuity decrease) were invited to participate. All enrolled patients provided informed consent after they have been informed on the nature and consequences of the study. The protocols had been approved by the Institutional Review Boards (IRB) of the Fundación Jiménez-Díaz (Madrid, Spain), and met the tenets of the Declaration of Helsinki.

Patients were implanted with the Crystalens AO A-IOL. This lens has a biconvex single-optic design, with aspheric anterior and posterior surfaces (nominally aiming at zero IOL aberration, according to the manufacturer). The IOL power (selected using the SRK/T and/or the Holladay II formula) of the implanted IOLs ranged from 19.50 to 24.50 D.

All procedures were performed by the same surgeon (Dr. Sonia Durán) using standard phacoemulsification under local anesthesia The IOLs were implanted using a purpose-designed injector through a clear suture-less corneal incision created in superior/temporal and superior/nasal locations in the right and left eyes respectively, and enlarged to approximately 2.8 mm. Anterior curvilinear capsulorhexis (6.5-mm intended diameter) was created manually. All surgeries were uneventful, and all IOLs were successfully implanted intracapsulary.

5.1.2. Control groups: young control group and monofocal IOL group

In addition to the patients implanted with A-IOLs, we also measured wave aberrations in young eyes (n=17; age: 28±4 years old, ranging from 21 to 34 years old; spherical equivalent: -0.2±0.6 D, ranging from -1.0 D to +1.25 D) under natural conditions and similar accommodative demands than in Crystalens patients. Subjects were recruited specifically for this study among normal volunteers, following a standard ophthalmological exam, and signed IRB-approved informed consents before undertaking the study.

An additional control group includes an aged-matched group of pseudophakic patients implanted with monofocal IOLs (n=17; age: 74±9; patients implanted with Tecnis and Acrysof aspheric IOLs).

5.1.3. OCT: measurements

The OCT images were acquired using a custom developed SD-OCT system (from a collaborative effort with Copernicus University, Torun, Poland) previously described in chapter II.

For the purposes of this study, a motorized Badal system to stimulate accommodation was incorporated in the fixation channel. Fixation is provided by a mini-display, which allows projection of accommodating targets. The desired accommodative demand was produced by changing the distance between the two lenses of the Badal system, which allowed a change in vergence while keeping constant retinal and pupil magnification. The motor was moved in synchronization with the image acquisition program in the OCT system.

Images were acquired pre- and post-operatively (at 3 months). Pre-operative measurements were conducted under natural conditions, for relaxed accommodation. Post-operative measurements were typically conducted in two sessions. In a first session, measurements were obtained under instillation of phenylephrine. In a second session, measurements were obtained under natural conditions (which allowed monitoring of the natural pupil diameter), and then 30 min after instillation of 1% pilocarpine, to pharmacologically stimulate accommodation.

Patients were stabilized by means of a bite bar and ask to fixate text (20/25 Snellen E-letters) in the fixation channel minidisplay (SVGA OLED LE400, LiteEye Systems). The position of the fixating letters was moved across the display until the cornea was aligned with the optical axis of the instrument. To achieve a full 3-D anterior segment image three images (50 B-scans, composed by a collection for A-scans in a 7x15 mm lateral area), with the OCT beam focused in the cornea, anterior and posterior lens were obtained sequentially. Three accommodative demands (0, 1.25, and 2.5 D) were produced with the Badal optometer, and the patient requested to focus the text on the display. Three full anterior segment images were obtained per accommodation condition. Each image was obtained in 0.72 seconds. Image collection protocols were similar in the natural viewing and phenylephrine conditions. Collection of all images for each condition typically took around 30 minutes. The pilocarpine condition only involved acquisition of one series of images, for a fixed position of the Badal optometer.

5.1.4. OCT: data analysis

3-D Reconstructions of Full Anterior Segment

Full anterior segment images (from the anterior corneal surface to the posterior lens surface) were obtained pre- and post- operatively. Automatic clustering analysis allowed automatic identification of the cornea, iris and lens. The iris plane and 3-D coordinates of the pupil center were used to register pre- and post-operative anterior segment images in the same eye, as well post-operative anterior segment images in the same eye for different accommodative demands. Due to the high accuracy of image registration, cornea and iris appear merged across conditions.

Anterior Chamber Depth (ACD)

ACD was obtained from the OCT data as the distance between the posterior corneal apex and the anterior lens surface apex. In contrast to ACD obtained from a single A-scan (as in PCI), ACD is consistently measured along the same axis, independently on the fixation stability of the subject.

Natural Lens Thickness

The crystalline lens thickness was obtained from OCT data as the distance between the anterior and posterior lens vertex.

IOL tilt

Crystalline lens/IOL tilt was obtained from OCT data as the angle between the axis of the lens and the pupillary axis. The Lens/IOL axis is defined as the vector that joins the apexes of the anterior and posterior lens surfaces apexes. The pupillary axis is defined as the vector that joins the center of curvature of the anterior cornea and the pupil center. Crystalline lens/IOL tilt were computed for pre-operative and post-operative (all accommodative demands) measurements under phenylephrine.

Capsulorhexis and haptic axis.

The margins of the capsulorhexis and the locations of the haptics were identified from *en face* OCT images obtained under phenylephrine pupil dilation. The diameter and centration (with respect to the lens optical zone) of the capsulorhexis were estimated, by circumference fitting. Also the polar coordinates of the haptics were obtained by estimating the axes of the visualized haptics (0º indicating a horizontal axis, 90º vertical axis, and 135º temporal/superior and nasal/superior in the right and left eye, respectively).

5.1.5. *Laser Ray Tracing: measurements*

Total wave aberrations were measured in Crystalens AO A-IOL implanted patients 3 months after surgery using a custom-developed LRT (described in Chapter II), for three different accommodation stimuli.

Measurements were conducted in two sessions. In a first session, measurements were performed under natural conditions. In a second session, measurements were obtained under instillation of phenylephrine, which allowed larger pupils without paralyzing the ciliary muscle.

The same instrument was used to measure aberrations under natural conditions and three different accommodation stimuli in the young eyes, and under dilated pupils (tropicamide 1%) and relaxed accommodation in monofocal IOL eyes.

In Crystalens eyes, the pupil ranged from 4 to 6 mm after inducing mydriasis (phenylephrine) and from 2 to 4 mm in natural conditions. In young control eyes, the natural pupil ranged from 4 to 6.5 mm (natural conditions), and in the monofocal IOL eyes from the pupil ranged from 4 to 6 mm (tropicamide 1%).

For the purposes of this study (static measurements of aberrations under steady accommodation), an open-field external fixation channel was incorporated in the LRT setup to stimulate accommodation. The subjects viewed the stimulus monocularly (the contralateral eye was covered with a patch during the measurement). The desired accommodative demand was produced by changing the fixation distance. The far fixation target (4 m) was the middle letter in the last line seen by each patient in an ETDRS chart (typically corresponding to a 20/25 visual acuity). The intermediate and near fixation targets were the middle word of the last line read by each patient in ETDRS test intermediate vision (80 cm, equivalent to 1.25 D) and near vision (40 cm, equivalent to 2.5 D) charts, respectively. The size of the stimulus was therefore adjusted to the visual acuity of each patient and condition. Each set of measurements consisted of 5 runs under the same conditions for every fixation target (far, intermediate and near), and the results presented are the average of 5 repeated measurements.

5.1.6. *Laser Ray Tracing: data analysis*

Wave aberrations were fitted by Zernike polynomials expansions up to the 6th order. The change of defocus (Z_2^0), astigmatism (Z_2^2 and Z_2^{-2}), coma (Z_3^1 and Z_3^{-1}), trefoil (Z_3^3 and Z_3^{-3}) and spherical aberration (Z_4^0) with accommodative demand were specifically analyzed. Root mean square (RMS) was also used to report the magnitude of high order aberrations (excluding tilt, defocus and astigmatism) and of certain characteristic aberrations (astigmatism, coma and trefoil). When averaging individual Zernike coefficients across eyes, the mirror symmetry terms were flipped in right eyes to account for the enantiomorphism of the right and left eyes.

The accommodative response was obtained as the difference between the accommodative demand and the measured effective defocus. The effective defocus takes into account potential interactions between 2nd order Zernike defocus term and the 4th order Zernike spherical aberration, as well as potential changes in pupil diameter with accommodation, and was defined as:

Equation 5.1: $$M = \frac{-4\sqrt{3}C_2^0+12\sqrt{5}C_4^0-24\sqrt{7}C_6^0}{R^2}$$

Previous studies have shown that the spherical error computed using eq. 5.1 agrees well with that computed from the best focus using retinal plane image quality metrics.

Unless otherwise noted, the analysis was done for a 4-mm pupil diameter for all eyes (under dilated pupils) and for the natural pupil diameter in each eye and condition (under natural viewing conditions).

Additionally, the astigmatism (C) and its angle (α) was analyzed from Zernike polynomials expansion by using equation 2:

Equation 5.2: $$J_0 = \frac{-2\sqrt{6}C_2^2}{R^2}\ ; J_{45} = \frac{-2\sqrt{6}C_2^{-2}}{R^2}\ ; C = -2\sqrt{J_0^2+J_{45}^2}\ ; \alpha = arctan\frac{\frac{J_{45}}{J_0}}{2}$$

The point-spread-function (PSF), the modulation transfer function (MTF) and the Optical Transfer Function (OTF) were computed using Fourier optics from Zernike coefficients using routines written in Matlab (MathWorks, Natick, MA).

Depth of focus (DoF) was estimated from through-focus objective optical quality. The optical quality metric used in the computations was Visual Strehl. Visual Strehl was computed as the volume under the Visual MTF (MTF weighted by a general Neural Transfer Function) normalized to diffraction limit. Visual Strehl was evaluated through-focus in 0.125 D defocus steps. All computations considered high-order aberrations (HOAs) up to 6th order, and cancelling the astigmatism terms. Computations were done for the natural pupil size, as well as for a fixed 3-mm pupil diameter for comparison across subjects. Two standard definitions of DoF were used, one based on a relative metric, and the other on an absolute metric. DoF was defined as the dioptric range for which Visual Strehl was at least 50% the maximum Visual Strehl value in the through-focus Strehl curve (relative definition) and as the dioptric range for which Visual Strehl was above 0.12 (absolute definition).

5.1.7. Statistical analysis

Univariate analysis (independent samples Student´s t-test) was used to evaluate the differences in the evaluated parameters across different accommodative demands. Differences between aberrations and DoF in eyes implanted with A-IOLs, young subjects and eyes implanted with monofocal IOLs were analyzed with one-way ANOVA.

5.2. Results

5.2.1. Anterior Chamber Depth (ACD)

Average ACD was 2.64±0.24 mm pre-operatively, and 3.65±0.35 mm post-operatively (relaxed accommodation). Measurements of ACD were highly reproducible (average standard deviation of repeated measurements of 0.015 mm pre-operatively and 0.035 mm post-operatively). Independent measurements of ACD post-operatively with dilated pupils under phenylephrine, and under natural conditions were not statistically significantly different. There was a high statistical correlation of ACD between right and left eye pre-operatively (Figure 5.1.A, $r=0.9342$, $p=0.0001$). The correlation was still significant post-operatively (Figure 5.1.B, $r=0.9276$, $p=0.0032$ for measurements with phenylephrine; $r=0.8397$, $p=0.0123$ for measurements under natural conditions), excluding S#3, which very consistently showed high ACD post-operative values (4.46 mm) in the left eye. There was a statistically significant correlation between pre-operative and post-operative ACD (Figure 5.1.C, $r=0.438$, $p<0.0001$ for measurements with phenylephrine; and $r=0.399$; $p<0.0001$ for measurements under natural conditions). We found a highly significant correlation between post-operative ACD and post-operative spherical equivalent ($r=0.655$; $p=0.0017$). Interocular (right/left eye) differences in ACD are also significantly correlated with interocular differences in spherical equivalent ($r=0.713$; $p=0.02$).

Figure 5.1.D shows the post-operative ACD measured (for all accommodative stimuli) under phenylephrine versus natural accommodation. There is a highly statistical significant correlation ($r=0.99$; $p<0.0001$) between the two types of data (obtained in different sessions). Compared to intersubject differences, the relative shift of the A-IOL with stimulated accommodation is almost negligible. We did not find significant correlations between the A-IOL shifts under phenylephrine or natural accommodation. Similarly, we did not find overall significant correlations between A-IOL shift under natural (or phenylephrine) accommodation and pilocarpine-induced accommodation, very likely due to the small amount of effective A-IOL shifts. In five eyes however, we found consistent shift signs in both natural and pilocarpine-induced accommodation.

Figure 5.1.E represents a merged pre- and postoperative 3-D image showing both the crystalline lens and the implanted A-IOL (relaxed accommodation) with phenylephrine in patient S#8-OD. The relative position of the IOL with respect to the natural lens can be observed. The anterior surface of the IOL sits 0.71 mm behind the anterior surface of the preoperative natural crystalline lens and is more tilted superiorly.

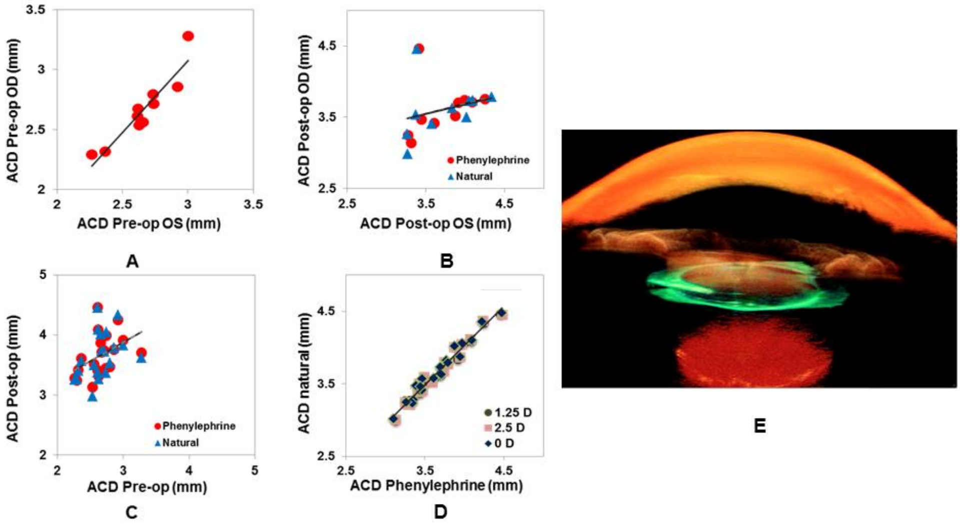

Figure 5.1. (A) Pre-operative ACD in left versus right eye; (B) Post-operative ACD in left versus right eye (both under natural and phenylephrine conditions); (C) Pre-operative versus post-operative ACD (both under natural and phenylephrine conditions); (D) Post-operative ACD under natural conditions (for different accommodative demands) versus Post-operative ACD under phenylephrine stimulation. (E) Three-dimensional (3-D) view of merged full anterior segment 3-D OCT images in a same patient before and after Crystalens A-IOL implantation. ACD stands for Anterior Chamber Depth. OD: right eye; OS: left eye.

5.2.2. Changes in ACD with Accommodative Effort

There was not a consistent shift of the A-IOL with accommodative effort. A-IOLs shifted on average by +0.005±0.025 mm for an accommodative effort of 1.25 D and +0.008±0.03 mm for an accommodative effort of 2.5 D, under phenylephrine, and -0.006±0.036 mm and +0.01±0.02 mm respectively under natural conditions. The average A-IOL shift under stimulated accommodation with pilocarpine was -0.02±0.20 mm. The measured A-IOL shift values are above the accuracy of the technique, but clinically not significant. Figure 5.10 shows the relative shifts of the A-IOL as a function of accommodative effort in right (solid lines, solid diamonds) and left eyes (dashed lines, open circles) of all patients, both under phenylephrine (Figure 5.2.A) and natural conditions (Figure 5.2.B). The post-operative ACD measured under pilocarpine accommodation is also shown for reference (solid squares). Some eyes (8 under phenylephrine and 9 under natural conditions) experienced a forward move of the A-IOL with accommodative effort (1.25 D of accommodative stimulus), as expected from design, while others moved backward. In general a larger shift (in absolute values) was elicited by the 1.25 D accommodative stimulus than by a 2.5 D accommodative stimulus (thus the V or inverted V-shape of the shift vs accommodative stimulus functions in Figure 5.2). With pilocarpine, 8 A-IOLs moved forward (-0.19±0.22 mm, on average) and 12 moved backward (+0.09±0.22 mm, on average). We did not find a significant correlation between the A-IOL shift in the right eye and left eye (under phenylephrine or under natural conditions). The correlation between the pilocarpine-induced A-IOL shift in right and left eye was statistically significant (r=0.843, p=0.0023). However, only in S#6 the A-IOL shift was relevant in both eyes (-0.49 and -0.52 mm, in right and left eye respectively). Figure 5.2.C represents a merged postoperative 3-D image showing the implanted IOL for 3 accommodative demands (0, 1.25 D and 2.5 D) in patient S#11 (under natural conditions), with the IOL volume depicted in different colors for each accommodation. The IOL moved backward (opposed as expected) with accommodation (by 700 µm from 0 to 2.5 D of accommodation).

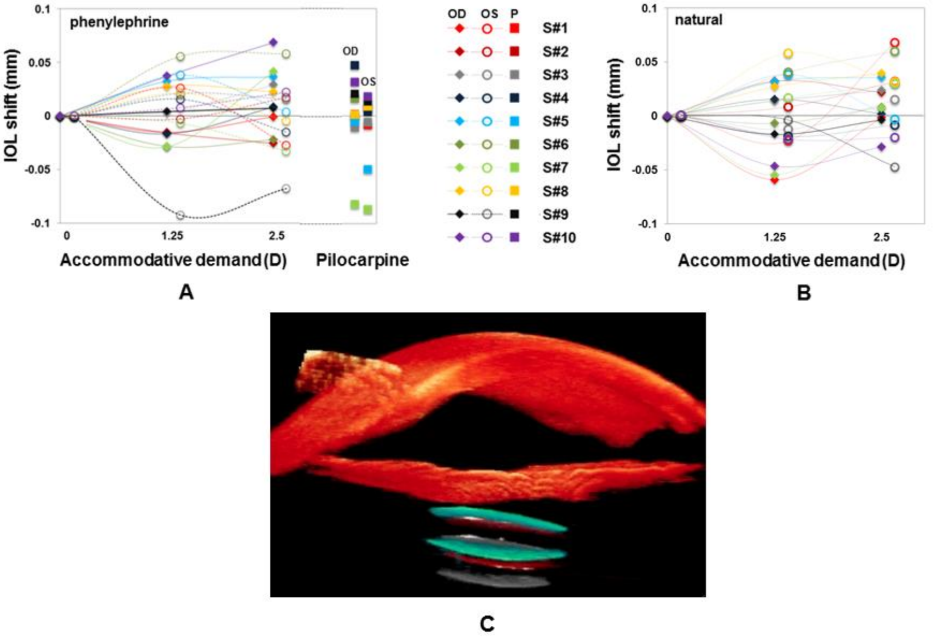

Figure 5.2. Relative shift of the A-IOL as a function of accommodative demand (solid diamonds, OD; open circles, OS) and pilocarpine stimulation (solid squares; P in the legend). Positive shifts indicate backward A-IOL movement, and negative shift forward lens movement. (A) Phenylephrine; (B) natural; (C) 3-D view of the anterior segment.

5.2.3. Lens thickness

Average pre-operative crystalline lens thickness was 4.53±0.22 mm. The standard deviation of repeated lens thickness measurements was 0.030 mm (averaged across eyes). Pre-operative lens thickness was highly correlated between right and left eyes (Figure 5.3, r=0.79; p=0.006). However, we did not find an association between pre-operative lens thickness and A-IOL shift (in any of the conditions under test). Also pre-operative lens thickness was not statistically correlated with the difference of pre-operative and post-operative ACD.

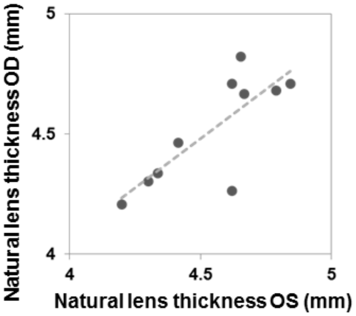

Figure 5.3. Lens central thickness preoperatively, OS *vs* OD.

5.2.4. IOL tilt

Lens tilt was measured with reproducibility of 0.79 deg around the x-axis, and of 0.44 deg around the y-axis. There were no differences in the measurement reproducibility between the crystalline lens, A-IOL and across different accommodative efforts. The lens average tilt magnitude was 5.71 deg pre-operatively (crystalline lens) and 5.01 deg post-operatively (A-IOL, relaxed accommodation). The intersubject variability in lens tilt was lowest for the natural lens (standard deviation=1.30 deg) and highest for the A-IOLs with increasing accommodative effort (2.46, 3.02 and 3.19 deg, for A-IOL at 0, 1.25 and 2.5 D of accommodative effort, respectively). Figure 5.4 shows the horizontal and vertical coordinates of tilt in right (A and C) and left (B and D) eye, both pre-operatively (A and B) and post-operatively (phenylephrine, all accommodative efforts, C and D). Pre-operatively the crystalline lens was systematically tilted around the vertical axis by 5.1 deg on average with the nasal side of the lens forward (positive OD). Also, the lens tends to tilt around the horizontal axis (by 1.96 deg on average) with the superior side of the lens moved forward. There is a high mirror symmetry in natural lens tilt between left and right eyes (r=0.847; p=0.0019). Post-operatively (relaxed accommodation), the nasal/temporal symmetry between left and right eye IOL tilt is lost (r=0.237; p=0.5): in 2 eyes the nasal side of the lens IOLs tilted further backward, and in 8 eyes tilted forward. There is a slight trend for the lens to superior side of the lens to move further backward. Two eyes (S#9-OD and S#10-OS experienced large shifts in IOL alignment with respect to the natural lens), showing tilts around y of more than 9 deg for the relaxed state of accommodation.

Figure 5.4 shows A-IOL tilt around x (E) and around y (F) as a function of accommodative effort, in all eyes (right eyes indicated by diamonds/solid lines and left eyes by circles/dashed lines). While the tilt around y (nasal/temporal tilt) remained fairly constant with accommodative effort the tilt around x (superior/inferior) varied significantly with accommodative effort in most eyes showing the characteristic V/inverted V-patterns found in other parameters (A-IOL shift and pupil diameter) with accommodative effort. In 12 eyes the superior side of the IOL moved backward and in 8 eyes forward with accommodative effort. On average, the IOL tilted around the x-axis 1.65 deg for 1.25 D, and 1.53 deg for 2.5 D of accommodative effort. The largest A-IOL tilt change (9.5 deg) during accommodative effort occurred for S#1-OS. There was no correlation between the relative tilt of the implanted A-IOL (relaxed state) with respect to the natural lens and its change with accommodation.

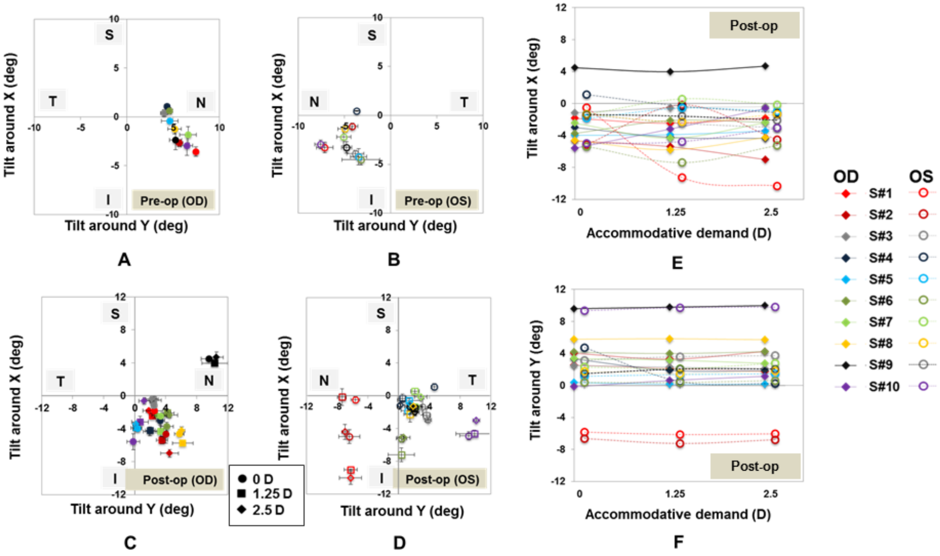

Figure 5.4. Pre-operative (A, B) and Post-operative (C, D) lens tilt coordinates on right (A, C) and left (B, D) eyes. (E) A-IOL Tilt around x (superior/inferior); (F) A-IOL tilt around y (nasal/temporal). Tilts around x represent superior/inferior tilts. Tilts around y represent nasal/temporal tilts. OD: Right eye; OS: Left eye; D: diopters.

5.2.5. Capsulorhexis and haptic axis

The average measured capsulorhexis diameter was 4.88±0.72 mm (3-months post-operatively). The capsulorhexis was generally elliptical in shape, and slightly smaller than the intended diameter, likely due to fibrosis-induced shrinkage. The magnitude of the capsulorhexis shifts with respect to the IOL center was 0.34±0.30 mm on average. Horizontal shifts ranged from 0.22 temporal to 0.63 mm nasal in the right eye, and were consistently temporal in the left eye; vertical shifts ranged from 1.33 superior to -0.63 mm inferior. In the left eye, the largest tilts tended to occur for the largest capsulorhexis diameters and largest capsulorhexis shifts. No significant correlation was found between the direction of capsulorhexis shift and the tilt orientation.

The average haptic polar orientation was 129.95±20.38 deg, consistent with the 120 deg (11 o’clock) incision location, in both left and right eyes. We did not find significant correlations between horizontal and vertical components of the haptic polar orientations and the measured tilts around horizontal and vertical axes. Tilt changes with accommodation tended to correlate with slight polar rotations in the lens (up to 6.9 deg).

5.2.6. Individual aberrations: unaccommodated state

Figure 5.5 shows astigmatism and relevant high order Zernike terms/orders in Crystalens and control groups (monofocal IOL and young) for the un-accommodated state, averaged across eyes in each group (for 4-mm pupils). We found significant differences ($p<0.005$) in astigmatism, HOA RMS and vertical trefoil (Z_3^{-3}) between IOLs groups (Crystalens accommodative IOL and monofocal IOL) and young control group. The average HOA RMS wavefront error was 0.18±0.05 µm (ranging from 0.06 µm to 0.28 µm) in Crystalens eyes, 0.20±0.08 µm (ranging from 0.11 µm to 0.47 µm) in monofocal IOL eyes and 0.09±0.04 µm (ranging from 0.03 µm to 0.17 µm) in young eyes, for 4-mm pupil diameters. Repeated wave aberration measurements were highly reproducible within each subject: average HOA RMS standard deviations for repeated measurements were 0.05, 0.04 and 0.03 µm, for Crystalens, monofocal IOL and young control eyes respectively.

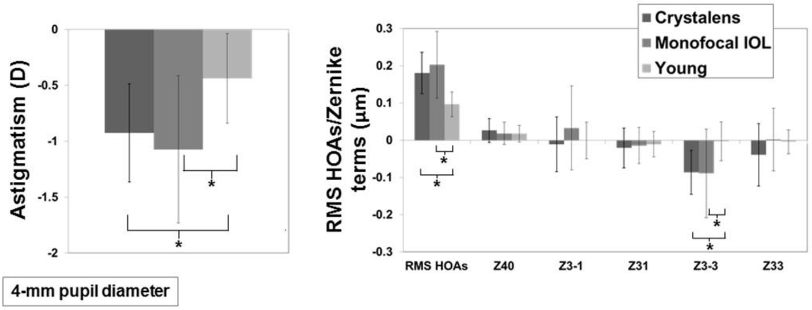

Figure 5.5. Astigmatism (left) and high order Zernike terms/orders (right) in A-IOLs (Crystalens) and control (monofocal IOLs and young) groups for the un-accommodated state, averaged across eyes. Data are for 4-mm pupils. D stands for diopters and µm stands for microns; * stands for statistical significance at a level of $p<0.005$).

Table 5.1 shows the contribution of selected high order aberrations (Z_4^0, coma (Z_3^{-1}, Z_3^1) and trefoil (Z_3^{-3}, Z_3^3)) to total RMS. Vertical trefoil (Z_3^{-3}) was the predominant high order aberration in the Crystalens group (-0.08 µm, 33.15% of the total RMS) and in the monofocal IOL control group (-0.09 µm, 35.73% of the total RMS), and significantly higher ($p<0.0001$) than in the young control group (-0.003 µm, 3.39% of the total RMS). Individual coma Zernike coefficients were not statistically significantly different between Crystalens and control groups (monofocal IOL and young). The coma RMS was significantly higher ($p<0.005$) in Crystalens (0.08±0.04 µm) and in monofocal IOL group (0.10 ± 0.07 µm) than in the young control group (0.05±0.02 µm). Spherical aberration was not statistically significantly different across the three groups (0.02±0.03 µm in the Crystalens group; 0.02 ± 0.03 µm in the monofocal IOL group, 0.02±0.02 µm in the young group), indicating that, on average, aspheric designs correct for corneal spherical aberration in a similar proportion than the crystalline lens in young subjects. Nevertheless, due to the lower amount of other aberrations, the contribution of spherical aberration to HOA is much higher in the young control group (21.20% of the total RMS).

Table 5.1. Percentage of some relevant high order aberration terms (Z_4^0, Z_3^{-1}, Z_3^1, Z_3^{-3} and Z_3^3) to total high-order aberrations root-mean-square in the unaccommodated state for the Crystalens (Accommodative Intraocular Lenses), monofocal Intraocular Lenses and young groups.

	Crystalens (%)	*Monofocal IOL (%)*	*Young (%)*
Z_4^0	*10.13*	*7.35*	*21.20*
Z_3^{-1}	*4.17*	*13.15*	*0.78*
Z_3^1	*7.87*	*0.74*	*12.75*
Z_3^{-3}	*33.15*	*35.72*	*3.39*
Z_3^3	*14.98*	*20.21*	*5.08*

5.2.7. Individual aberrations: changes with accommodative stimulus

Figure 5.6 shows average ocular 2nd and higher-order Zernike coefficients, and the corresponding wave aberration maps (excluding tilt, but including defocus, astigmatism and HOAs; and excluding tilt, defocus and astigmatism, but including HOAs) for Crystalens eyes (top: A, B, C) and for young eyes (bottom: D, E, F) for far, intermediate (1.25 D) and near (2.5 D) vision respectively for 4-mm pupil diameters, under phenylephrine (Crystalens) and natural condition (young control). In the Crystalens group wave aberrations maps are similar across accommodative demands, whereas in the young control group the wave aberration maps show drastic changes (in defocus, but also, to a lesser extent, in HOA). On average, the defocus term (Z_2^0), astigmatism or high order aberrations did not change systematically with accommodative demand in Crystalens eyes. On the other hand, as expected, young eyes showed highly statistically significant changes in the defocus term ($p<0.001$), and in the spherical aberration (Z_4^0) which shifted towards less positive values with accommodation ($p<0.005$). Additionally, vertical trefoil (Z_3^{-3}, $p=0.09$), vertical coma (Z_3^{-1}, $p=0.02$) and secondary vertical astigmatism (Z_4^{-4}, $p=0.05$) showed changes with accommodation in the young control group.

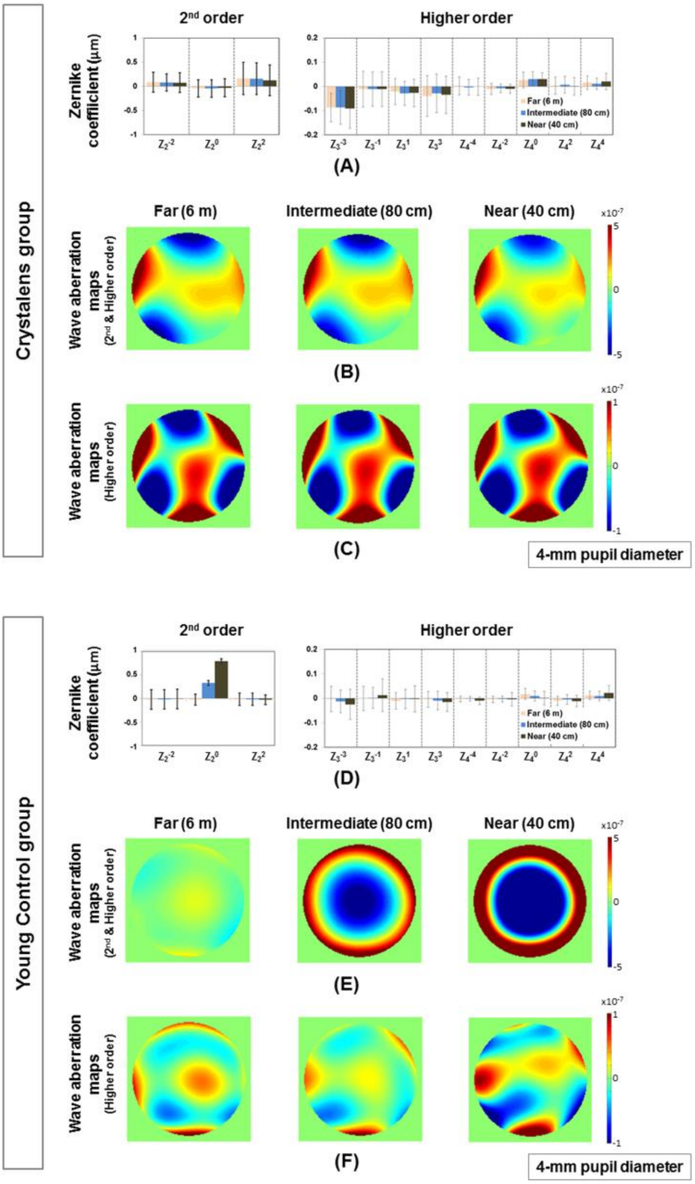

Figure 5.6. Average Zernike coefficients and wave aberration maps for different accommodative demands in A-IOLs (Crystalens) and young control groups. Data are for phenylephrine (Crystalens) and natural (young) conditions, and for 4-mm pupils. Zernike coefficients are shown up to the 4th order. Wave aberration maps are calculated from average Zernike coefficients up to the 5th order excluding piston and tilt and (B, E), and excluding piston, tilt, defocus and astigmatism (C, F).

Figure 5.7 shows the accommodative change of defocus (left) and astigmatism (right), expressed in diopters, in all Crystalens eyes under phenylephrine. Some Crystalens eyes (24%) experienced significant changes in defocus with accommodative demand (S#1 (OS), S#2 (OD), S#2 (OS), S#3 (OD), and S#3 (OS)), although the direction for the change differed across subjects. While an accommodative response consistent with effective near accommodation should show a negative shift in the Zernike defocus term (as seen in the control group), seven Crystalens eyes (S#2 (OS), S#3 (OS), S#4 (OS), S#5 (OS), S#7 (OS), S#10 (OD) and S#11 (OD)) actually changed defocus in the opposite direction. The largest change in defocus with accommodative demand (approximately 0.4 D) occurred for S#2 (OD). Additionally, some subjects (14%) showed significant changes in astigmatism with different accommodative demands (S#1 (OS), S#10 (OS), and S#11 (OD) for intermediate). A larger change in defocus and astigmatism was generally observed for the 1.25 D than for a 2.5 D accommodative demand. The absolute average defocus shift across accommodative demands was 0.11 D between intermediate-far, and 0.10 D between near and far. The absolute average difference in astigmatism was 0.09 D between intermediate and far, and 0.10 D between near and far.

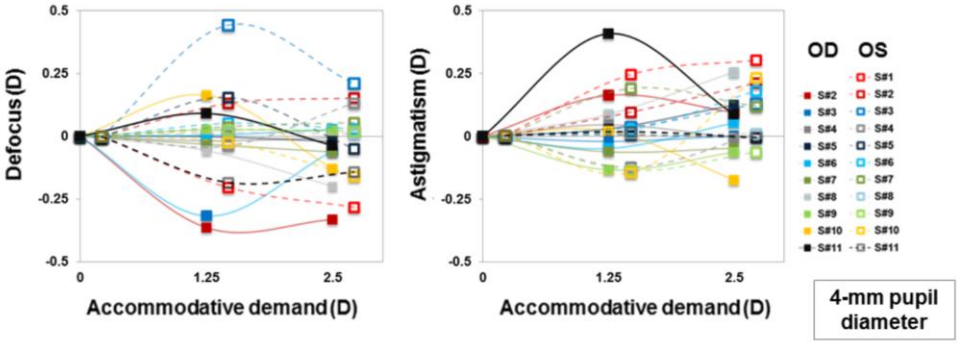

Figure 5.7. Relative change in defocus (left) and astigmatism (right), in diopters, in all Crystalens (A-IOLs) eyes as a function of accommodative demand. Data are for measurements under phenylephrine and 4-mm pupil diameters. OD: solid symbols; OS: open symbols.

Figure 5.8 shows the change of the HOA RMS, spherical aberration (Z_4^0), coma-like terms (Z_3^1 and Z_3^{-1}), and trefoil-like terms (Z_3^3 and Z_3^{-3}) with accommodative demand in all Crystalens subjects, for 4-mm pupil diameters and under phenylephrine. Most eyes experienced slight changes in aberrations with accommodative demand. In many cases, the largest change occurred for 1.25 D of accommodative demand, and decreased for 2.5 D. S#11 (OD) showed the largest change in HOA RMS (approximately 0.05 µm), for 1.25 D of accommodative demand. This eye showed significant increase in coma, trefoil and spherical aberration ($p<0.05$). Conversely, other eyes (e.g., S#1 OD) also showed significant changes ($p<0.05$) in coma, trefoil and spherical aberration, but towards more negative values.

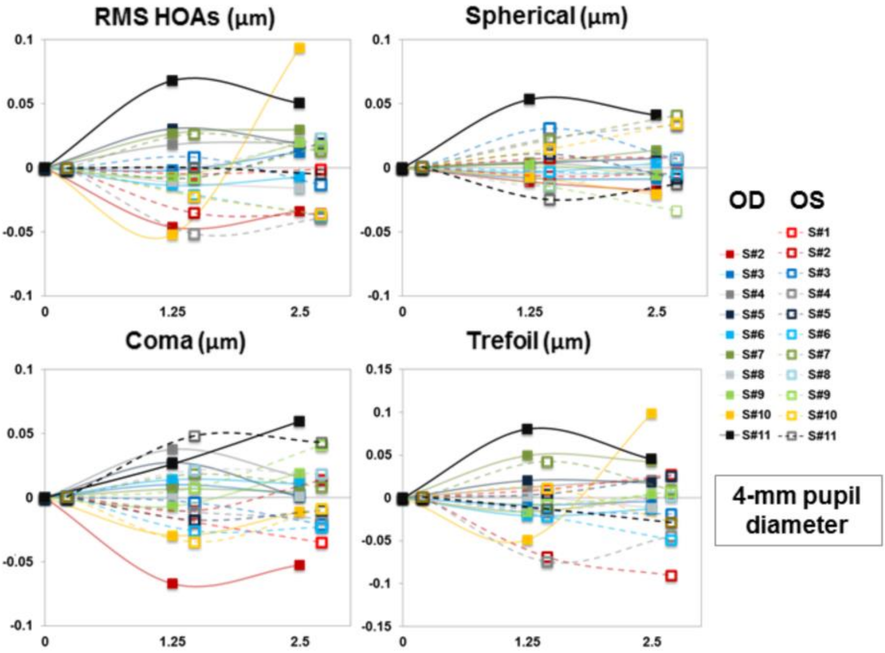

Figure 5.8. Relative change in root-mean-square high-order aberrations (top left), spherical (top right), coma (bottom left) and trefoil (bottom right) of all Crystalens (A-IOLs) subjects as a function of accommodative demand. Data are for measurements under phenylephrine and 4-mm pupil diameters. OD: solid symbols; OS: open symbols.

5.2.8. Wave aberrations with phenylephrine and natural viewing conditions

Measurements of defocus and astigmatism (and its angle) measured in different sessions and conditions (phenylephrine and natural viewing) in Crystalens eyes did not show significant differences between conditions (Figure 5.9). The average deviations were less than 0.01 D in defocus (mean defocus 0.037 D and 0.047 D for phenylephrine and natural conditions, respectively), less than 0.037 D in astigmatism (mean astigmatism -0.95 D and -0.91 D for phenylephrine and natural conditions, respectively), and less than 8.3 deg in astigmatic angle (-4 and 4.3 deg with phenylephrine and natural conditions, respectively).

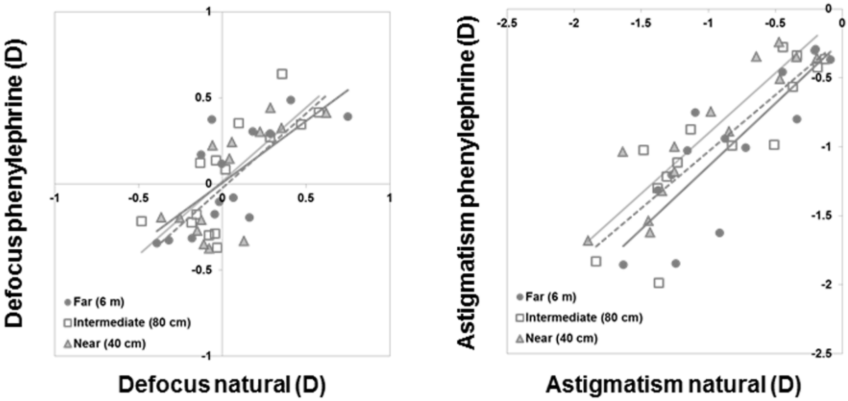

Figure 5.9. Defocus for natural conditions versus defocus with phenylephrine in A-IOLs (Crystalens group) (left). Astigmatism for natural conditions *vs* astigmatism with phenylephrine in A-IOLs (Crystalens group) (right). Lines are linear regressions of the data.

5.2.9. Change in accommodative response with accommodative demand

Figure 5.10 shows the accommodative response in Crystalens eyes (left) and young control eyes (right) estimated for natural viewing conditions using equation 5.1. For Crystalens eyes, on average, the effective defocus (M) did not show significant differences between conditions: 0.03±0.33 D (intermediate-far) and 0.03±0.32 D (near-far). Mean pupil diameter (Crystalens group) was 3.90±0.64 mm for far, 3.72±0.47 mm for intermediate and 3.59±0.64 mm for near. As found for paraxial defocus, most Crystalens eyes did not show significant accommodative responses. In addition, while some Crystalens eyes (14%) showed significant accommodative responses in the expected direction (S#1 (OS), S#2 (OD), S#7 (OD)), other eyes (14%) respond in the opposite direction (S#3 (OS), S#7 (OS) and S#11(OD)). Figure 5.10 (right) shows for comparison the effective defocus changes in the young control group. The accommodative response in young eyes was on average -0.79±0.25 D (intermediate-far) and -1.67±0.30 D (near-far). The accommodative lag varied across subjects and was on average 0.46±0.25 D (ranging from 0 to 0.7 D) and 0.82±0.30 D (ranging from 0 to 1.03 D) D for 1.25 and 2.5 D stimuli, respectively. Mean pupil diameter in the young control group was 5.62±0.83 mm for far, 5.45±0.76 mm for intermediate and 5.17±0.69 mm for near.

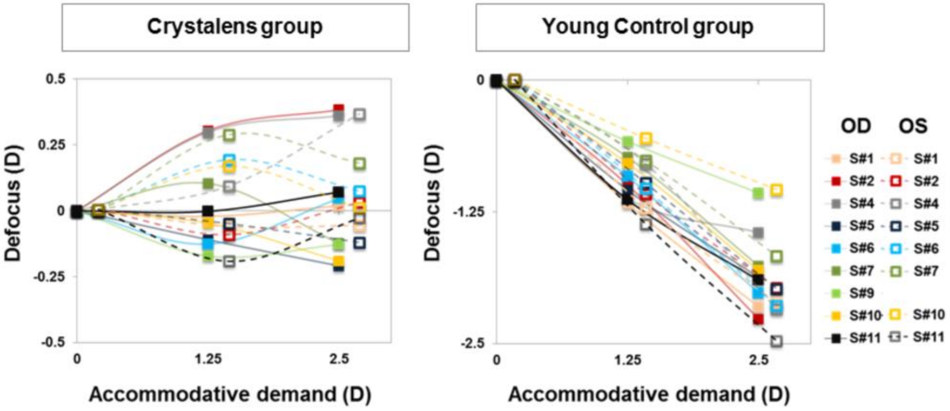

Figure 5.10. Accommodative response as a function of accommodative demand, relative to 0, computed from the corresponding changes in defocus, spherical aberration and pupil diameter, under natural conditions. Crystalens (A-IOL) group (left); Young control group (right). OD: solid symbols; OS: open symbols.

5.2.10. Depth-of-focus

Figure 5.11 shows the through-focus Visual Strehl in Crystalens (top left, 3-mm pupil; bottom left, natural pupil), monofocal IOL control (top middle, 3-mm pupil), and young control (top right, 3-mm pupil; bottom middle, natural pupil) groups, as well as the average through-focus Strehl ratio for all groups and conditions (bottom right). Maximum Visual Strehl in the Crystalens group (0.42±0.15 for natural pupil diameter, and 0.61±0.11 for 3-mm pupils) was significantly lower ($p=0.05$ and $p<0.0005$, for natural pupil and 3-mm pupil diameters, respectively) than in the young control group (0.56±0.21 for natural pupil diameter and 0.88±0.08 for 3-mm pupils) and marginally lower ($p=0.09$) than in the monofocal IOL group. Despite the large intersubject variability (arising from differences in the subjects' HOA and pupil dynamics), the differences in optical quality between the Crystalens and young control groups are attenuated with natural pupils, mostly as a result of the age-related smaller pupil size of Crystalens eyes (3.90±0.64 mm, un-accommodated state) in comparison to the young eyes (5.62±0.83 mm, un-accommodated state).

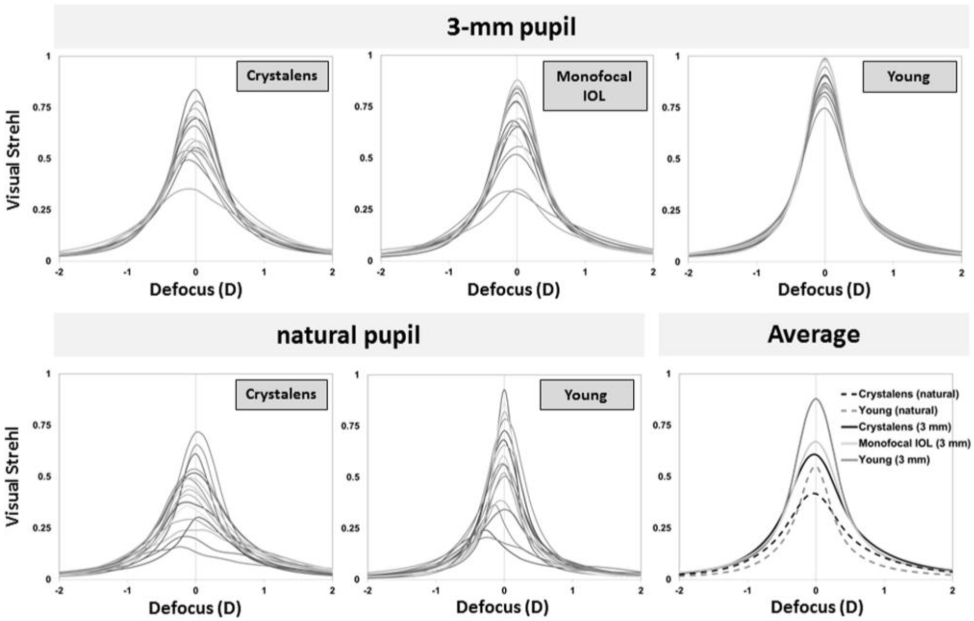

Figure 5.11. Through-focus Visual Strehl for the Crystalens (A-IOLs) group (top left, 3-mm pupil diameter; bottom left, natural pupil diameter), monofocal IOL group (top middle, 3-mm pupil diameter), and young group (top right, 3-mm pupil diameter; bottom middle, natural pupil diameter). (Bottom right) Average through-focus groups for the Crystalens (A-IOL) group (black lines) and for the control groups (gray lines, monofocal IOL and young), for 3-mm (solid) and natural (dashed) pupil diameters.

Depth-of-focus (DoF) was estimated from the Visual Strehl through-focus curve for each eye. Figure 5.12 shows the DoF for relative and absolute definitions (3-mm pupil, top; natural pupil, bottom). The Crystalens group shows the largest DoF in all conditions compared to the control groups. For 3-mm pupil, the relative DoF definition yields a value of 1.02±0.15 D for the Crystalens group, and 0.77±0.12 D for the young control group. DoF of the Crystalens group is statistically significantly higher than the DoF of the monofocal IOL group ($p=0.04$, relative definition, 3-mm pupil) and than the DoF of the young control group ($p<0.0005$, relative definition, 3-mm pupil, $p<0.005$; absolute definition, natural pupil, $p<0.0005$).

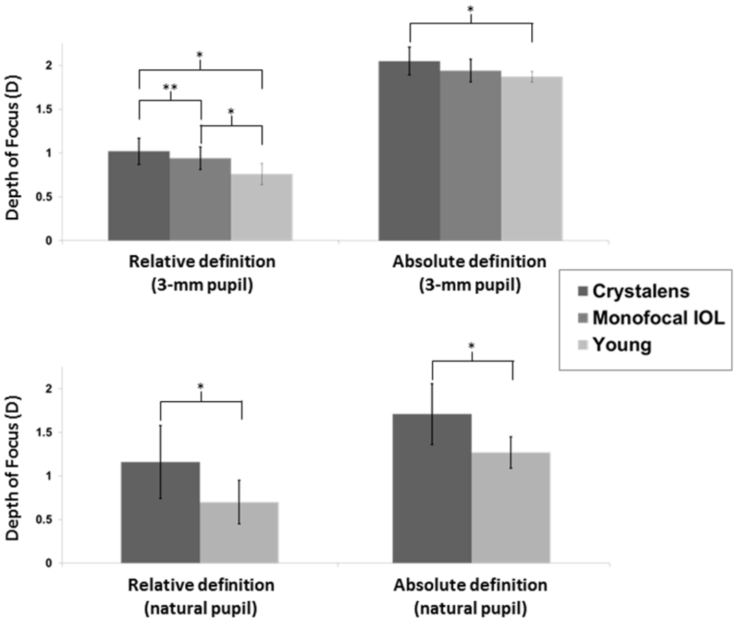

Figure 5.12. Depth of focus for relative (50%) and absolute (Visual Strehl threshold: 0.12) definitions, for the Crystalens (A-IOL), monofocal IOL and young groups (3-mm pupil, top; natural pupil, bottom).* stands for statistical significance at the p<0.005 level; ** stands for statistical significance at the p<0.05 level.

5.3. Discussion

Using the OCT, we quantified three-dimensionally the anterior segment geometry pre- and post-operatively in these group of patients. And, using LRT aberrometry, we measured the accommodative response, monochromatic aberrations, optical performance and depth-of-focus (DoF) in patients implanted with the Crystalens A-IOL for different accommodative demands.

To our knowledge, this the first time that OCT and LRT has been used in a series of patients to assess corneal geometry, biometry, lens tilt of A-IOLs and optical aberrations, particularly under the natural response to an accommodative stimulus.

Using 3-D OCT biometry, we did not find axial shifts of the A-IOL with either natural or stimulated accommodation. The average displacement was negligible in all cases. Several subjects showed a forward movement of the A-IOL (the largest forward shift was close to 0.5 mm in both eyes in one subject, with pilocarpine, and also under natural accommodation). The average forward shift with pilocarpine-induced accommodation was 0.28 mm, and the average backward shift was 0.09 mm. These values are close to previous reports of pilocarpine-induced A-IOL shifts from Koeppl et al. [Koeppl et al., 2005] in 28 eyes implanted with the Crystalens AT-45, using Partial Coherence Interferometry (who reported an average backward shift of 0.136 mm), and from Stachs et al. [Stachs et al., 2006] in 4 patients implanted with the Crystalens AT-45, using custom-developed 3-D UBM (who reported an average forward shift of 0.13 mm). Those A-IOL axial shifts are too small to produce a clinically relevant dioptric shift.

The correlation of the biometric measurements pre- and post-operatively gives also some interesting insights on the mechanism of the A-IOL. As expected, anterior chamber depth (ACD) and lens thickness (LT) are highly correlated in right and left eyes, pre-operatively. The right-left correlation of ACD post-operatively indicates that the overall axial position of the A-IOL is driven by anatomical parameters, primarily the size of the anterior segment, as previously suggested in monofocal IOLs [Olsen, 2006]. However, we did not find a fine-tuning of the IOL location (in relaxed accommodation) within the capsular bag. Olsen et al. [Olsen, 2006] found in patients implanted with monofocal IOLs that the post-operative ACD is linearly related with the pre-operative ACD as well as with LT, and used this finding as a predictor for the estimated lens position, through the C-constant, which would account for the role of haptic angulation and biomechanical features of the IOL platform in the actual axial location of the IOL. The fact that we could not determine a C-constant for this lenses (due to the high dispersion of the correlation of ACDpre-ACDpost *vs* lens thickness) suggests that the lens does not sit on a well-defined location within the lens capsule, very likely as the result of the hinged haptic design, and therefore its axial position in a relaxed accommodation state cannot be finely defined. In addition, the fact that we could not establish a correlation between lens thickness and A-IOL shift suggests that other factors beyond the lens anatomy (e.g., capsular fibrosis) play a role in the A-IOL ability to move within the eye and in the direction of displacement.

Quantitative 3-D OCT also allowed accurate measurements of the A-IOL tilt, both pre-operatively and post-operatively at different accommodative demands. Knowledge of the relative location of the implanted A-IOL within the capsular bag, and potential changes with accommodation provides additional insights into the mechanism of the A-IOL. As previously reported we found a nasal-temporal tilt of the natural lens (close to 5 deg on average), highly symmetric across left and right eyes. While the left-right symmetry of lens tilt and decentration occurs in some eyes (as previously reported in pseudophakic eyes implanted with monofocal IOLs), the lack of a general symmetric pattern, changes in orientation of the lens tilt, and the presence of large relative lens tilts (with respect to the pre-operative lens orientation) indicate a certain degree of instability in the A-IOL alignment, likely due to the hinged nature of the haptics in this lens.

Cases of very large IOL tilts in patients implanted with the Crystalens have been reported in the literature, known as “Z syndrome” [Yuen et al., 2008]. We also found significant increase in lens tilt with accommodative effort. Very interestingly this tilt happens primarily around the x axis (superior/inferior tilt), closer to the orientation of the hinged IOL haptics. However, we did not find a significant correlation between the haptic axis coordinates and tilt coordinates, nor between the size or decentration of the capsulorhexis and the coordinates of tilt. Remarkably, in the left eye trends were found between the capsulorhexis diameter and decentration magnitude and the magnitude of IOL tilt. Asymmetric fibrosis is likely to play a role on this effect.

Incidentally, the location of the incision (and therefore the haptic axis) seems to play a critical role in the tilt outcomes. The non-mirror symmetric location of the incision (temporal in the right eye and nasal in the left eye) may be related to the disrupture of the right/left eye lens tilt symmetry that was found in the natural lens. Whereas in the right eye the nasal-inferior of the natural lens tends to be preserved post-operatively, in the left eye, the variability in tilt around y is largely increased, perhaps reflecting tensions between the capsular bag natural orientation and the lens axis location.

The biometric findings in the eyes implanted with the Crystalens can be correlated with optical findings obtained with the LRT, both in terms of magnitude and direction of the A-IOL shifts. With OCT we found that Crystalens axial shifts with accommodative demand ranged from 0.07 to -0.1 mm, being consistent with the defocus shifts ranging from 0.43 to -0.36 D found with LRT.

The positive shifts are opposite to the expected A-IOL shift/defocus change, and the overall magnitudes are below clinical relevance. Our data therefore confirm that this A-IOL does not produce a relevant change in eye optical power by axial shifts of its position. Also, in keeping with the observation that the 1.25 D stimulus elicited relatively larger accommodative A-IOL shifts, we also found larger changes in defocus (and aberrations) for the 1.25 D intermediate accommodation demand, in most subjects.

While spherical aberration changed significantly in young accommodating eyes, we did not find, on average, significant changes in spherical aberration with accommodation in Crystalens eyes. Individually, most eyes did not show significant changes in spherical aberration with accommodative demand, although some showed significant shifts towards more positive values, and others towards more negative values, indicating that, even if modifications in the A-IOL surface might occur leading to optical changes, these are not systematic nor can reliably produce the desired accommodative response. In fact, our estimates of accommodative response, integrating changes in defocus, spherical aberration and pupil diameter, do not show functional accommodation in any of the eyes.

Crystalens and monofocal IOL eyes show significantly higher amounts of astigmatism and higher-order aberrations than young eyes. The increased trefoil found both in Crystalens and monofocal IOL eyes may be associated with incision-induced corneal aberrations, as shown by a prior study [Guirao et al., 2004]. However, the fact that trefoil increased with accommodative demand in some eyes suggests also some lenticular involvement.

Increased astigmatism may be related to the incision, but also to tilt of the IOL. Very interestingly, in general, eyes with the higher amount of post-operative astigmatism, coma and trefoil are those for which larger amounts of tilt: e.g., S#10 (OS) showed the largest amount of astigmatism (0.75 ± 0.05 µm) and also large tilts around x and y (tilt x = -4.86 ± 1.15 deg; tilt y = 9.10 ± 1.15 deg).

Hence, we found correlations between RMS HOAs (r=-0.48; p=0.038), RMS astigmatism (r=-0.47; p=0.041) and RMS trefoil (r=-0.61; p=0.005) and the tilt around x, for the un-accommodated state. Although not significant, we observed slight correlations between the

RMS coma and the magnitude of tilt (r=0.37; p=0.12). In addition, we observed some trend between changes in aberrations and in tilt with accommodative demand: e.g., astigmatism *vs* tilt around x for near vision (r=0.47; p=0.04); coma *vs* tilt around x for near vision (r=0.38; p=0.09)). Some differences in the accommodative response may occur since 3-D biometry and aberrometry were measured in different instruments (OCT and LRT, respectively), influenced by differences in the accommodation target (single letter vs word) and stimulus (Badal vs proximity), ambient illumination (0.2 vs 3.4 cd/m^2), and alignment of the subject. The high intersubject variability in the high order aberrations and their change with accommodation agrees with reports by Wolffsohn et al. [Wolffsohn et al., 2010] in eyes implanted with another axial-shift based A-IOL (Tetraflex).

The high “amplitudes of accommodation” measured by push-up test, defocus curves or reading performance in Crystalens eyes reported by some previous studies (i.e. 2.42 D and 1.74 D respectively) [Alio et al., 2004; Macsai et al., 2006] may be confounded by multiple factors. It has been speculated that the functional visual performance in Crystalens eyes may be in fact achieved by pseudo-accommodation, rather than true optical power changes [Beiko, 2013]. Increased aberrations (such as those produced by increased A-IOL tilt and corneal aberrations, as shown here) result in increased depth-of-focus. Using Visual Strehl as optical quality metric, we found that the DoF was expanded on average approximately 0.2 D over normal young eyes and 0.1 D over monofocal IOL, with the differences being systematic and statistically significant. While this amount may not represent a clinically relevant increase in depth-of-focus, the contrast achieved out-of-focus may produce additional functional near vision in these patients.

Several Crystalens eyes showed changes in astigmatism, spherical aberration, trefoil and coma with accommodation, which must arise from geometrical and alignment changes in the lens with accommodative demand. These changes are highly variable across subjects in both magnitude and sign. However, the higher amount of aberrations in Crystalens eyes in comparison with young eyes, likely arising from A-IOL tilt and increased corneal aberrations, results in increased depth-of-focus, which may explain some functional near vision performance in these eyes (by pseudo-accommodation, rather than by true accommodative changes in optical power).

To sum up, OCT and LRT allowed characterization of the anterior segment geometry pre- and post-operatively (anterior and posterior corneal surface geometry, ACD, lens geometry and alignment, and IOL geometry and alignment) and aberration measurements. These measurements therefore shed light into the mechanisms of operation of the Crystalens A-IOL.

(1) The axial shifts of the A-IOL were very small, and in many cases the lens shifted backwards (opposite to the expected movements) upon accommodative effort. This indicates that the claimed working mechanism of the Crystalens AO A-IOL is not by an axially shift. Significant IOL tilts occurred (particularly around the horizontal axis), consistent with the orientation of the hinged haptics.

(2) LRT measurements confirm OCT measurements. LRT aberration measurements in eyes implanted with the Crystalens AO A-IOLs showed changes in objective accommodative response below 0.4 D, and negative accommodative responses in 14% of the eyes.

Chapter VI. ***CATARACT AND IOL***

Chromatic Aberration with IOLs

This chapter is based on the following publication:

> ***In Vivo Chromatic Aberration in Eyes Implanted with Intraocular Lenses***, by P. Pérez-Merino, C. Dorronsoro, L. Llorente, S. Durán, I. Jimenez-Alfaro, S. Marcos in Investigative Ophthalmology and Visual Science (2013).

The contribution of Pablo Pérez-Merino to the study, in collaboration with other coauthors, was the literature search, the design of the experiments, the adaptation of the Laser Ray Tracing setup (in collaboration with Carlos Dorronsoro) and the analysis routines, and the data collection, analysis and processing.

Retinal image quality is determined by the combined optical aberrations of the cornea and crystalline lens, pupil size, and intraocular scattering. In eyes with cataract, scattering by the opacified lens causes a major decrease in image quality. Upon replacement of the crystalline lens by an artificial lens, the source of scattering is eliminated and refractive errors are generally well corrected. State-of-the art aspheric designs also aim at compensating the spherical aberration of the cornea [Barbero, 2003; Holladay et al., 2002; Marcos et al., 2005a; Piers et al., 2007; Tabernero et al., 2006]. In natural conditions, both monochromatic and chromatic aberrations play a role in determining retinal image quality [Charman & Jennings, 1976; Howarth & Bradley, 1986; Llorente et al., 2003; Marcos et al., 1999; Marcos et al., 2001; McLellan et al., 2002; Ravikumar et al., 2008; Rynders et al., 1995; Thibos et al., 1990; Thibos et al., 1991; Yoon & Williams, 2002]. In fact, it has been shown that interactions between monochromatic and chromatic aberrations occur, and that the presence of monochromatic aberrations partly attenuates the optical degradation produced by the Longitudinal Chromatic Aberration (LCA), or *viceversa* [McLellan et al., 2002; Ravikumar et al., 2008]. Modifications in either the monochromatic or chromatic aberration component may alter this compensatory effect found in the natural eye.

LCA in the eye is determined by dispersion of light in the intraocular media and in the crystalline lens [Charman & Jennings, 1976; Howarth & Bradley, 1986]. Unlike Transverse Chromatic Aberration (TCA), which shows a high intersubject variability, LCA is less variable across subjects, and seems to remain fairly constant with age [Charman & Jennings, 1976; Howarth & Bradley, 1986; Marcos et al., 1999; Marcos et al., 2001; McLellan et al., 2002; Ravikumar et al., 2008; Thibos et al., 1990].

The replacement of the crystalline lens by an intraocular lens (IOL) modifies the chromatic dispersion properties of the eye, according to the dispersion properties of the IOL material (defined by the Abbe number). Reports of the Abbe number of different IOL materials range between 35 to 60 (37, for the Alcon acrylic; 55, for the Tecnis Acrylic) [Nagata et al., 1999]. In principle, the higher the Abbe number the lower the LCA. This role of the IOL material on the chromatic difference of focus of the pseudophakic eye has been already acknowledged [Negishi et al., 2001; Zhao & Mainster, 2007], and it has led to proposals for IOLs designs aiming at correcting the chromatic aberration of the eye [Artal et al., 2010; Weeber & Piers, 2012]. This has also prompted studies on the expected performance of eyes corrected for LCA both computationally from real aberration measurements [Llorente et al., 2003; Marcos et al., 1999] or psychophysically [Yoon & Williams, 2002].

The chromatic aberrations of the phakic eye have been studied widely, and numerous studies report experimental measurements (psychophysical or objective) of the LCA in normal phakic eyes [Charman & Jennings, 1976; Howarth & Bradley, 1986; Llorente et al., 2003; Thibos et al., 1991]. However, most estimates of the LCA in pseudophakic eyes are based on computer simulations, using data for the Abbe number of the lens material [Zhao & Mainster, 2007] or on bench measurements of the isolated IOLs [Siedlecki & Ginis, 2007]. To our knowledge, only one study measured the LCA *in vivo* (between 500 and 650 nm) in pseudophakic eyes implanted with PMMA and Acrylic IOLs [Nagata et al., 1999], using a modified chromoretinoscopy system [Bobier & Sivak, 1978b].

In a previous study, we reported the measurement of chromatic difference of focus based on aberrometry at two different wavelengths [Llorente et al., 2003]. In particular, the use of Laser Ray Tracing (LRT) or Hartmann-Shack aberrometry using different illumination might allow us rapid and reliable measurement of LCA in phakic subjects. Aberrometry provides, in addition, monochromatic high-order aberrations (HOA) measurements. This allows testing the correction/induction of HOA for a given IOL design, and ultimately, estimating the polychromatic image quality in the pseudophakic eye [Marcos et al., 2001].

In the present chapter, we measured monochromatic aberrations in both 532 nm (green) and 785 nm (IR) wavelengths in patients implanted with Alcon Acrysof and with AMO Tecnis Acrylic aspheric IOLs. We estimated the LCA as the chromatic difference of focus between the equivalent spherical error corresponding to each wavelength, by using a previously described and validated aberrometry-based methodology.

To our knowledge, this is the first report of both monochromatic and chromatic aberrations in pseudophakic patients, as well as the first report *in vivo* of the chromatic difference of focus of two of the most widespread IOL materials.

6.1. Methods

6.1.1. Patients, Surgery and IOLs

Eighteen eyes from eighteen patients participated in the study, 9 implanted with the Tecnis ZCB00 1-Piece (Abbot Medical Optics Inc., Santa Ana, CA, USA), and 9 implanted with the Acrysof IQ SN60WF (Alcon Inc., Fort Worth, TX, USA). Both IOLs are monofocal, acrylic and aspheric, but they differ in the specific optical design and material. Table 6.1 shows the age and refractive profiles of the two groups of patients.

Table 6.1. Age and refractive profiles of the Tecnis and Acrysof groups.

	Tecnis Group (n=9)	**Acrysof Group (n=9)**
Age (mean ± std)	73.4±10.9	74.3±7.2
IOL power (mean ± std)	21.2±0.8	22.0±1.6

Selection criteria of the patients included good general health, no ocular pathology, and no complications during surgery. All enrolled patients provided informed consent. The protocols had been approved by the Institutional Review Board, and met the tenets of the Declaration of Helsinki. Patients received a comprehensive ophthalmic evaluation at the hospital (Fundación Jiménez Díaz, Madrid, Spain) prior to enrollment to the study and surgery. The examination included uncorrected and best-corrected visual acuity, biomicroscopy, keratometry, corneal topography, tonometry and indirect ophthalmoscopy. Axial length and anterior chamber depth were measured with optical biometry (IOL Master 500, Carl Zeiss Meditec AG, Jena, Germany). The IOL power was calculated with the SRK-T formula, always selecting the closest value to emmetropia.

Postoperative evaluations at the hospital were conducted at 1 day, 1 week, 1 month and 3 months after surgery, and included uncorrected and best-corrected VA, autorefractometry, manifest refraction, biomicroscopy, keratometry, tonometry, and indirect ophthalmoscopy.

All procedures were performed by the same surgeon (Dr. Sonia Durán) on an outpatient basis under topical anaesthesia. A 2.2-mm corneal incision and a paracentesis were performed with a surgical knife. A 6.0-mm continuous curvilinear capsulorhexis was made under viscoelastic material. Phacoemulsification of the lens was performed with the Millenium Venturi system (Bausch & Lomb, Rochester, NY, USA). After removing cortical material, the surgeon proceeded to clean the anterior and posterior capsules with the automatic I-A straight tip. Both foldable posterior chamber lenses were implanted using the Monarch III injector through the 2.2 mm incision. Once the viscoelastic material was removed, the incision was closed by hydration without sutures. Postoperatively, patients were treated with a combination of antibiotic and corticosteroid drops (dexametasone plus tobramicyn) for 4 weeks.

6.1.2. Laser Ray Tracing: Total Aberration Analysis

Total wave aberrations were measured using custom laser ray tracing, which has been described in detail in previous studies and in chapter II.

Illumination was provided by two collinear laser diodes (laser-diode pumped green He-Ne laser at 532 nm (Brimrose, Baltimore, USA), and an IR laser diode at 785 nm (Schäfter + Kirchhoff, Hamburg, Germany).

Measurements were done under mydriasis (1 drop 1% tropicamide) for a 4-6 mm pupil diameter at three months after cataract surgery. Each set of measurements consisted of 5 runs for green and 5 for IR wavelengths under the same conditions, and the results presented are the average of the corresponding 5 repeated measurements.

6.1.3. Data Analysis

Ray aberrations were estimated from the deviations of the centroids of the retinal images corresponding to each entry pupil location from the reference (chief ray), using Matlab (MathWorks, Inc.) custom software. These deviations are proportional to the local derivatives of the monochromatic wave aberrations. The monochromatic wave aberration was described with Zernike polynomials up to 7th order. The spherical error for each wavelength was estimated considering different definitions for spherical equivalent error (M) [Thibos et al., 2004b; Thibos & Horner, 2001].

Equation 6.1: $M = \frac{-4\sqrt{3}Z_2^0}{R^2}$

Equation 6.2: $M = \frac{-4\sqrt{3}Z_2^0+12\sqrt{5}Z_4^0-24\sqrt{7}Z_6^0}{R^2}$

Equation 6.3: $J_0 = \frac{-2\sqrt{6}Z_2^2}{R^2}\,;\ J_{45} = \frac{-2\sqrt{6}Z_2^{-2}}{R^2}\,;\ C = -2\sqrt{J_0^2+J_{45}^2};\ M = (\frac{-4\sqrt{3}Z_2^0}{R^2} - C)/2$

The LCA was then estimated as the difference between the spherical equivalent error obtained for green and IR wavelengths, as described in an earlier study from our laboratory on phakic subjects [Llorente et al., 2003]. The analysis was done for a 4-mm effective pupil diameter for all subjects.

Point Spread Functions (PSF) were also computed using standard Fourier Optics for the same pupil diameter. Image quality was analyzed in terms of Strehl Ratio, defined as the maximum of the PSF relative to the maximum of the diffraction-limited PSF. Strehl ratio is an appropriate optical quality metric in non-highly aberrated optical systems, and in the absence of large amounts of defocus, as in this study [Cheng et al., 2004]. Besides, through focus analysis of Strehl Ratio have been shown to allow accurate estimates of the best subjective focus [Guirao & Williams, 2003]. PSFs in green were computed at best focus (that maximizing Strehl ratio); PSFs in IR were computed assuming the chromatic difference of focus in the defocus term. The effect of the chromatic difference of focus was evaluated on average PSFs for each group (Tecnis or Acrysof). Average PSFs in focus and defocused by the chromatic difference of focus were computed by averaging individual PSFs in each condition, assuming no aberrations (diffraction-limited ideal case), the measured HOA only, and HOA and astigmatism (from IR aberration data). All computations were performed for 4-mm pupils. Univariate analysis (independent samples Student´s t-test) was used to evaluate the differences in chromatic difference of focus between green and IR, as well as in monochromatic aberrations and optical quality between the two groups implanted with the IOLs.

6.2. Results

6.2.1. Monochromatic Aberrations

Figure 6.1 shows the Zernike coefficients, and the corresponding wave aberration maps (excluding tilt, defocus and astigmatism), for two representative subjects from the Tecnis and Acrysof groups respectively. Repeated wave aberration measurements were highly reproducible within each subject. The RMS standard deviation for HOA for repeated measurements was 0.04 µm (averaged across subjects). The standard deviation for the defocus Zernike term for repeated measurements was 0.06 µm (averaged across subjects).

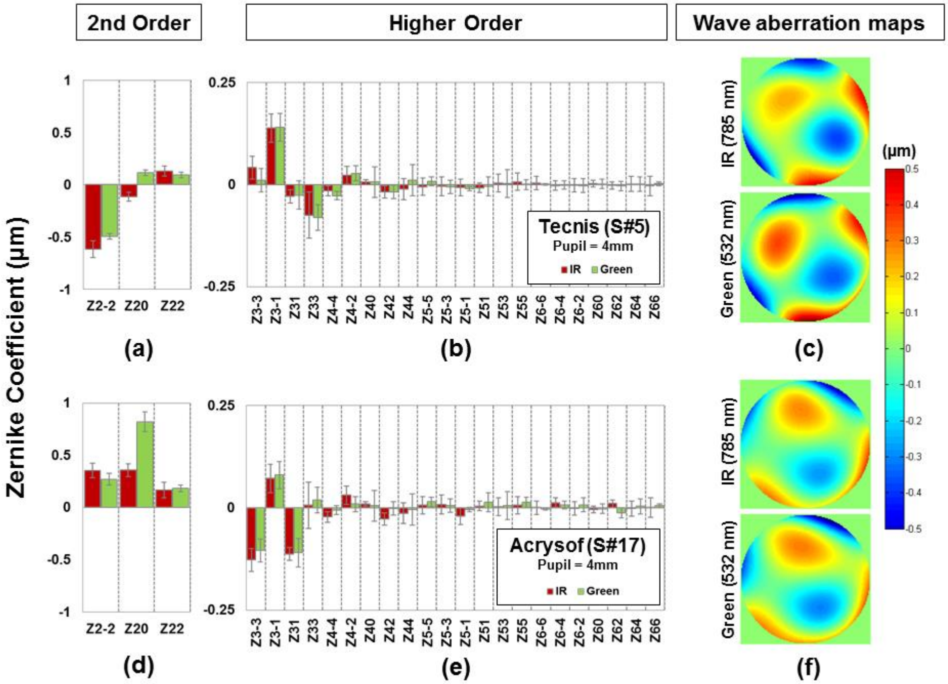

Figure 6.1. a) Second-order and b) Higher-order Zernike coefficients (averaged across 5 repeated measurements) for a representative eye implanted with Tecnis (S#5), for IR (785 nm, red column) and green (532 nm, green column) illumination. c) Wave aberration maps (calculated from average Zernike coefficients excluding tilt, defocus and astigmatism) for IR (785 nm, upper) and green (532 nm, lower) (Tecnis (S#5)). d) Second-order and e) Higher-order Zernike coefficients (averaged across 5 repeated measurements) for a representative eye implated with Acrysof (S#17), for IR (785 nm, red column) and green (532 nm, green column). f) Wave aberration maps (calculated from average Zernike coefficients excluding tilt, defocus and astigmatism) for IR (785 nm, upper) and green (532 nm, lower) respectively (Acrysof (S#17)).

The average value for defocus (Z_2^0), astigmatism-term (Z_2^2 and Z_2^{-2}), spherical aberration (Z_4^0), coma-like term (Z_3^1 and Z_3^{-1}), and the RMS for HOAs for the Tecnis as well as for the Acrysof group are summarized in Table 2, for both green and IR wavelengths. For both IOL groups, the defocus term shows significant differences across wavelengths ($p<0.05$). However, the levels of astigmatism, coma, spherical aberration and total HOAs are very similar between Tecnis and Acrysof IOLs.

6.2.2. Chromatic Difference of Focus

As expected, the defocus term was significantly different across wavelengths in both Tecnis and Acrysof groups (see Table 6.2).

Table 6.2. Effective Defocus (D), and RMS (µm) for defocus (Z_2^0), spherical (Z_4^0), astigmatism (Z_2^2 and Z_2^{-2}), coma (Z_3^1 and Z_3^{-1}), and total HOAs (mean ± SD) in Tecnis and Acrysof groups for 532 nm and 785 nm. Data are shown as mean ± standard deviation.

		Defocus (D)	**Astigmatism (µm)**	**Spherical (µm)**	**Coma (µm)**	**Total HOAs (µm)**
532 nm	***Tecnis***	-0.14±0.15	0.36±0.26	0.01±0.03	0.14±0.07	0.21±0.08
	Acrysof	-0.28±0.27	0.46±0.24	0.02±0.03	0.09±0.03	0.17±0.04
785 nm	***Tecnis***	0.30±0.17	0.39±0.30	0.01±0.03	0.13±0.09	0.22±0.11
	Acrysof	0.41±0.24	0.49±0.18	0.02±0.02	0.09±0.03	0.18±0.04

Figure 6.2 shows the chromatic difference of focus (estimating LCA) expressed in diopters (D) between green and IR wavelengths in both groups, using the different definitions for spherical equivalent error (M). The average chromatic difference of focus (from Eq. 6.1) in patients implanted with Tecnis was 0.46 ± 0.15 D and in patients implanted with Acrysof was 0.76 ± 0.12 D, between 532 (green) and 785 nm (IR). The chromatic difference of focus of a phakic population (0.78 ± 0.16 D) from an earlier study using the same instrument is also used for comparison with our results. The difference in LCA between the Tecnis and the phakic population of our previous study (9 subjects) was statistically significant different ($p<0.05$), whereas there was no statistically significant differences between the Acrysof and phakic groups.

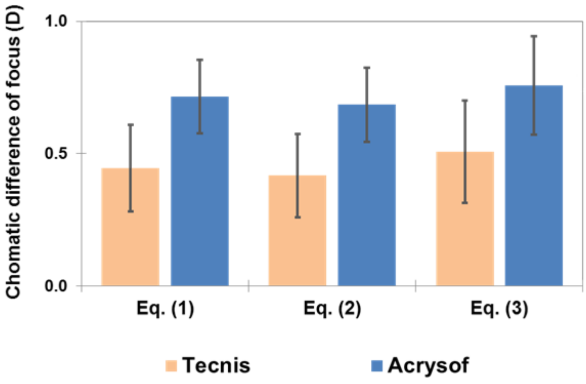

Figure 6.2. Chromatic difference of focus for Tecnis and Acrysof between 532 and 785 nm wavelengths. Eq. (1), Eq. (2) and Eq. (3) correspond to different definitions for spherical equivalent error: equation 6.1, equation 6.2 and equation 6.3, respectively.

6.2.3. Effect of Chromatic Difference of Focus on Retinal Image Quality

Figure 6.3 shows simulated PSFs from monochromatic aberration measurements at green and IR wavelengths for all subjects, including astigmatism and HOAs. PSFs varied significantly across subjects for both the Acrysof IOLs and Tecnis IOLs, with some subjects showing markedly asymmetric PSFs (dominated by coma and/or astigmatism) while others showing closer to diffraction-limited intensity distribution. The effect of the defocus produced by the chromatic difference of focus on the IR PSF appears more dependent on the amount of present astigmatism and HOA than on the lens type defocus produced a larger degradation on the highest quality PSFs (more so in eyes implanted with the Acrysof IOL). For example Strehl ratio changed from 0.16 (G) to 0.007 (IR) in S#2, and from 0.14 (G) to 0.007 (IR) in S#13, in the presence of chromatic defocus. On the other hand, the chromatic defocus produced a relatively lower degradation in higher aberrated eyes, i.e. Strehl ratios from 0.021 (G) to 0.020 (IR) in S#9, and from 0.018 (G) to 0.010 (IR) in S#10. In eyes with astigmatism, chromatic defocus moved the best focus (i.e. the focus that maximized Strehl ratio) along the Sturm interval.

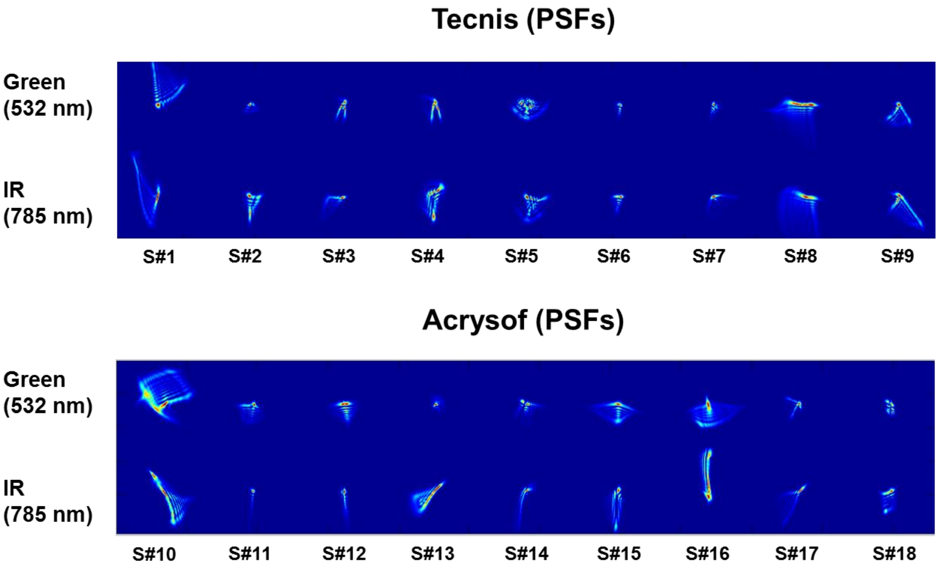

Figure 6.3. Simulated PSFs from the wave aberrations corresponding to all subjects of the study (pupil size = 4 mm), implanted with Tecnis and Acrysof) for all eyes in green (at the best focus) and IR (defocused by the chromatic difference of focus) wavelengths.

Figure 6.4 illustrates the effective impact of the chromatic difference of focus on the image quality for both IOLs, in terms of PSFs (a-c) and Strehl ratios (d-f), averaged across subjects in each group, and for 4-mm diameter pupils. The PSFs (all based on IR measurements) are shown in best focus (upper panels) and defocused by the corresponding chromatic difference of focus (lower panels), for both Tecnis and Acrysof. Three conditions were tested: (a) assuming diffraction-limited optics, i.e. full correction of astigmatism and HOAs; (b) considering the measured HOA aberrations present (excluding astigmatism); (c) considering both measured HOA and astigmatism. In the absence of HOA (Figure 6.4.d), Strehl ratio decreased from 1 (in focus) to 0.08 (defocused) in eyes implanted with Tecnis, and to 0.01 in eyes implanted with Acrysof. However, the presence of real HOA and astigmatism diminished dramatically the impact of chromatic difference of focus on retinal image quality. HOA decrease image quality at best focus with respect to diffraction-limit (Strehl ratio of 0.15 in both Tecnis and Acrysof groups), but attenuate to a much lesser extent than in the diffraction-limited case the chromatic defocused image, resulting in a Strehl ratio of 0.09±0.05 for Tecnis and 0.05±0.03 for Acrysof (Figure 6.4.e). Including the subjects' astigmatism (Figure 6.4.f) further degraded image quality in focus (Strehl ratio of 0.08, both for Tecnis and Acrysof) and further attenuated the impact of chromatic defocus (Strehl ratios of 0.03±0.02 for Tecnis and 0.02±0.01 for Acrysof).

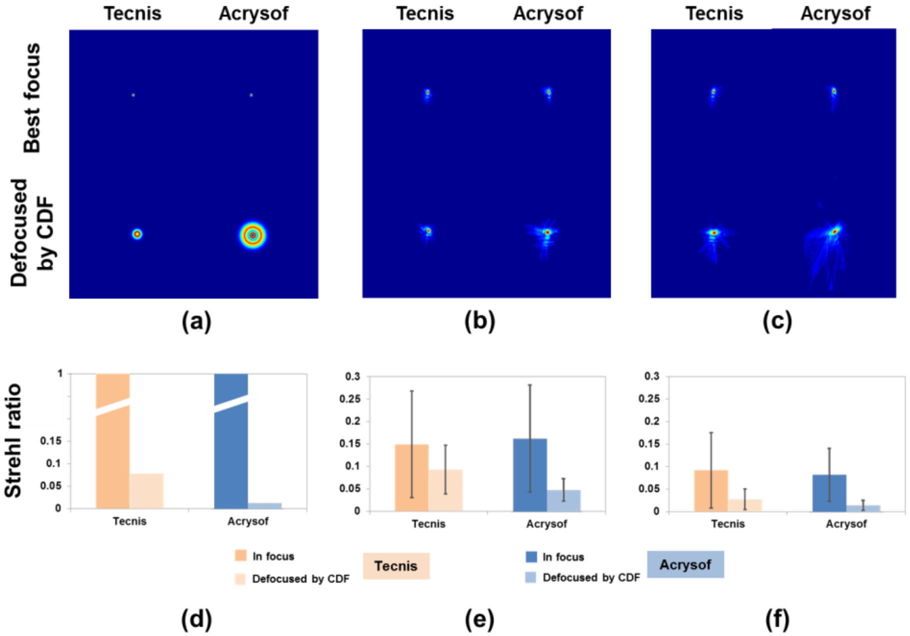

Figure 6.4. (a) Average PSF excluding astigmatism and HOAs at best focus, i.e. diffraction-limited (top) and defocused by the measured chromatic difference of focus G-IR (bottom) of the Tecnis (left) and Acrysof (right) IOLs. (b) Average PSF with HOAs, excluding astigmatism at best focus (top) and defocused by the chromatic difference of focus (bottom) for both groups. (c) Average PSF with HOAs and astigmatism at best focus (top) and defocused by the chromatic difference of focus (button) for both groups. Average Strehl ratios in eyes implanted with Tecnis and Acrysof, in focus and defocused by the chromatic difference of focus (d) for a theoretical diffraction-limited eye, (e) for HOAs without astigmatism, and (f) for HOAs and astigmatism. CDF=Chromatic difference of focus.

When evaluated in terms of retinal image quality metrics (Strehl), we did not find statistical differences between in focus image quality of eyes implanted with Tecnis or Acrysof (HOA only, and HOA and astigmatism; $p>0.5$). Also, we did not find differences in the chromatic defocused conditions between the two lenses (HOA only, $p=0.08$; HOA and astigmatism $p>0.5$). Optical quality in focus and with chromatic defocus were statistically significant different with astigmatism ($p<0.05$) in both IOLs, and without considering astigmatism in Acrysof ($p<0.05$) but not in Tecnis.

6.3. Discussion

We have shown that LRT aberrometry using different wavelengths is a reproducible technique to measure monochromatic aberrations, as well as chromatic difference of focus *in vivo* in eyes implanted with different IOLs. Intra-subject repeatability in chromatic difference of focus estimates was high, and the intersubject variability in LCA (0.15 D and 0.12 D, for Tecnis and Acrysof respectively) was similar or even smaller to that values reported in previous studies in phackic eyes using both objective (0.29 D) [Llorente et al., 2003] and psychophysical techniques (0.16 D) [Marcos et al., 1999] or those from the only report in pseudophakic eyes (0.18 D and 0.22 D, for PMMA and Acrysof respectively) [Nagata et al., 1999].

Our *in vivo* measurements of chromatic difference of focus (0.46 D and 0.76 D in eyes implanted with Tecnis and Acrysof IOLS, respectively), are in general, consistent with theoretical predictions using computer eye models and the nominal/measured material Abbe numbers in our range of wavelengths (0.35 D and 0.65 D, for Tecnis and Acrysof respectively) [Zhao & Mainster, 2007]. The reported Chromatic Difference of Focus is lower than the Longitudinal Chromatic Aberration for the entire visible wavelength range. Our measurements are restricted to the longer wavelength part of the spectrum, although the impact of the short wavelength range on vision is relatively minor, due to the reduced density of blue cones, and the important absorption of light in the macular pigment and in the IOL yellow filters (Acrysof). In addition, double-pass based measurements of LCA tend to be lower than psychophysical measurements of LCA [Charman & Jennings, 1976; Rynders et al., 1995]. In contrast, chromoretinoscopy measurements performed on patients implanted with PMMA and Acrysof IOLs (the only previous report of LCA measured *in vivo* on pseudophakic patients) [Nagata et al., 1999] overestimate LCA with respect to theoretical computations. In comparison with chromoretinoscopy experimental measurements, theoretical estimates of LCA (between 500 and 640 nm) in eyes implanted with Acrysof IOLs were on average 0.22 D lower (modeling by Nagata et al. [Nagata et al., 1999]) or 0.4 D (modeling by Zhao et al. [Zhao & Mainster, 2007]). As expected, we found a consistently lower LCA in eyes implanted with Tecnis IOLs (reported Abbe number=55) than in eyes implanted with Acrysof (reported Abbe number=37). A comparison with the LCA of a group of phakic patients [Llorente et al., 2003] measured with the same instrument revealed that the Tecnis group had a significantly lower LCA than the natural crystalline lens, but the differences between the Acrysof and the phakic subjects were not statistically significant.

The correction of the LCA in the eye has been long been debated and proposals of LCA-correcting IOLs have been made, mostly in the form of diffractive elements [Artal et al., 2010; Weeber & Piers, 2012]. While the monochromatic MTF of the eye clearly exceeds the polychromatic MTF [Marcos et al., 1999; McLellan et al., 2002], and there is evidence that, in the absence of both chromatic and monochromatic aberrations, visual performance exceeds that with non-corrected chromatic aberrations [Ravikumar et al., 2008; Yoon & Williams, 2002], correction of LCA alone has not yielded remarkable vision correction [Zhang et al., 1991]. Reasons for this relatively low benefit of correcting LCA include the presence of TCA, and the fact that monochromatic aberrations and LCA interact favorably in eyes with physiological amounts of aberrations [Marcos et al., 1999; Marcos et al., 2001; McLellan et al., 2002; Ravikumar et al., 2008]. McLellan et al. [McLellan et al., 2002] and Ravikumar et al. [Ravikumar et al., 2008] reported that, in fact, the presence of monochromatic aberrations attenuated the degrading effect of the chromatic aberration, particularly for shorter wavelengths, in contrast with a diffraction-limited eye where chromatic defocus produced large differences in the MTF across wavelengths. As the IOLs become more sophisticated in design (ultimately aiming at correcting the HOA of the individual eye) [Artal et al., 2010; Holladay et al., 2002; Piers et al., 2007; Tabernero et al., 2006; Weeber & Piers, 2012], the correction of LCA may become more relevant. Both IOLs of the study had aspheric surfaces, and aimed by design at correcting (or at least reducing) the positive spherical aberration of the average cornea [Marcos et al., 2005b; Piers et al., 2007], similarly to the corneal/internal balance of spherical aberration in the young eye [Artal & Guirao, 1998; Barbero et al., 2002b]. The measured HOA in the pseudophakic patients of the study (average RMS_HOA= 0.21±0.08 µm (Tecnis) and 0.17±0.04 µm (Acrysof), green light, 4-mm pupil) were of the order of magnitude of those found in a young population (average RMS_HOA=0.70±0.11 µm, green light, 6.51-mm pupil) [Llorente et al., 2003]. Our simulations of the PSFs reveal the image quality degradation produced by the HOAs in the tested pseudophakic patients, which changed in shape and magnitude across eyes. According to the mentioned prior literature, physiological amounts of LCA are not greatly detrimental to retinal image quality, as a result of the positive interaction with the existing natural HOA. In fact, in most eyes, the interactions of HOA and astigmatism with chromatic defocus attenuated the impact of the chromatic difference of focus on the PSF, very much like the effect of pure defocus, having a lesser relative impact on image degradation in the presence of HOA and astigmatism than in a diffraction-limited eye. As seen in Figures 6.3 and 6.4, the relative impact of the chromatic difference of focus in eyes with HOAs (with or without astigmatism), is much lower than that expected in a diffraction limited eye (Figure 6.4.a and 6.4.d), with no significant differences in the degradation of the PSF with LCA between groups. Other functions that have been suggested to be helped by the presence of LCA include emmetropization and accommodation [Kruger et al., 1993; Kruger & Pola, 1986].

Epilogue: CONCLUSIONS AND FUTURE WORK

This thesis addressed physical quantitative evaluations of geometry (OCT-based) and aberrations (OCT and LRT-based) in normal eyes and eyes with keratoconus, presbyopia and cataract pre- and post-treatment. In particular, this thesis has focused on better understanding of the ICRS as a keratoconus treatment (quantitative geometrical and optical corneal changes and 3-D ICRS positioning), the mechanism of accommodation (*in vivo* crystalline lens topographies) and the potential of accommodative IOLs for the treatment of presbyopia and cataract (*in vivo* 3-D positioning and aberrations while stimulating accommodation). We have studied the changes induced in the geometry of the optical surfaces (cornea and crystalline lens/IOL), and also the optical outcomes in terms of optical monochromatic and chromatic aberrations. Measurements on real patients have allowed us to assess the individual ocular properties in the visual performance of different anterior segment conditions (keratoconus, accommodation, presbyopia and cataract).

Achievements

1. We have developed different instrument implementations in OCT and Laser Ray Tracing (LRT), measurement procedures and image processing algorithms for the accurate study of the 3-D geometry, biometry and aberrometry of the optical surfaces of the eye (cornea and corneal implants; crystalline lens and IOL). The technology has demonstrated precise measurements on patients with different anterior segment physiological and clinical conditions: keratoconus, accommodation, presbyopia and cataract and their corresponding treatments (ICRS, IOLs and A-IOLs).
2. We have designed two external fixation/accommodation channels for compensating refractive errors and estimulating accommodation in LRT and OCT.
3. We have developed a ray-tracing multi-surface methodology based on OCT for simulating corneal and ocular aberrations. The procedure includes the description of the surface shape with Zernike coefficients and wavefront analysis. OCT-Corneal aberrometry was validated against LRT ocular aberrations in keratoconic eyes (eyes with cornea-dominated wave aberrations).
4. We have studied, for the first time, with 3-D quantitative distortion-corrected OCT, the surface shape, thickness, geometrical and optical (aberrations) of the keratoconic cornea before and after ICRS surgery. We have also analyzed the 3-D positioning (depth and tilt) of the ICRS and we have defined analitical metrics for determining the regulariry of the corneal surfaces.
5. We have explored, for the first time *in vivo*, the cornea and crystalline lens surface topography as a function of accommodation, allowing studying relationships across corneal and crystalline lens surfaces.
6. We have measured, for the first time and objectively with OCT and LRT, the accommodative response, aberrations, depth of focus and 3-D axial changes in patients implanted with an accommodative-IOL.

7. We have analyzed *in vivo* the longitudinal chromatic aberration (LCA) in patients implanted with different IOLs.

Conclusions

1. ICRS produced a significant flattening of the anterior corneal surface (by 1.71±1.83 D), particularly with a 5-mm optical zone diameter segment. The benefit for corneal surface regularization and thickness redistribution varied across patients, which was influenced by the arc-length of the ICRS and by the rotation inside the cornea.

The 3-D ICRS depth measured with OCT matched the planned femtosecond ICRS depth well (within 15±15 µm). On average, ICRS showed an overall tilt of -6.8±2.6 deg (temporal) and -2.1±0.8 deg (superior).

ICRS produced a significant decrease in astigmatism (27%), but on average did not produce a consistent decrease of HOAs, which is consistent with the small increase of visual acuity following treatment. The effect of the ICRS implantation on optical quality varied across patients.

2. In young eyes, corneal anterior and posterior surface astigmatism tend to be aligned. The anterior lens astigmatism is on average rotated 27 deg with respect to corneal astigmatism. The anterior and posterior lens astigmatism axes are close to orthogonal (80 deg, on average).

On average, we found that the posterior corneal surface compensated part of the anterior cornea (18% astigmatism, 12% coma). The astigmatism and the high-order irregularities were statistically significant higher in the posterior crystalline lens surface than in the anterior crystalline lens surface in the relaxed state. Coma and trefoil were correlated in the anterior and posterior lens surfaces, suggesting coordinated development.

In the relaxed state, the spherical term accounted for most of the surface irregularity in the anterior lens (47%) and astigmatism in the posterior lens (70%). However, in accommodated lenses astigmatism was the predominant surface irregularity in the anterior lens (90%).

As the crystalline lens accommodated, astigmatism changed both in magnitude (increased in the anterior lens surface) and angle (relative shift 10-20 deg), spherical term changed from positive to negative values in the anterior lens surface.

3. OCT measurements of the A-IOL (Crystalens AO) 3-D positioning revealed small A-IOL axial shifts with accommodative effort (and in many patients backward, opposite to the expected movements), ranging from 0.07 to -0.1 mm. Significant IOL tilts occurred particularly around the horizontal axis, consistent with the orientation of the hinged haptics.

LRT measurements showed that the accommodative response of eyes implanted with the Crystalens AO A-IOL was lower than 0.4 D in all eyes (consistent with the reported small axial shifts). Several subjects showed changes in astigmatism, spherical aberration, trefoil and coma with accommodation, which arise from geometrical and alignment changes in the lens with accommodative demand. These changes are highly variable across subjects in both magnitude and sign. Pseudoaccommodation from increased depth-of-focus may contribute to near vision functionality in Crystalens AO-implanted patients.

4. Replacement of the crystalline lens by the IOL did not increase chromatic difference of focus above that of phakic eyes implanted with two commercially available IOLs (0.46 D and 0.76 D, respectivley). The group implanted with IOLs with low Abbe number showed values of chromatic difference of focus very similar to physiological values in young eyes (0.78 D).

The interactions of HOAs and astigmatism with chromatic defocus attenuated the impact of the longitudinal chromatic aberration (LCA) on the PSF. The relative impact of the LCA in eyes with HOAs is much lower than that expected in a diffraction-limited eye, with no significant differences in the degradation of the PSF with the LCA between IOL groups.

Clinical impact

The results of this thesis have a number of clinical implications, which may change paradigments in diagnosis, clinical management and treatment evaluation in different anterior segment conditions, such as in keratoconus (new nomograms based on OCT to increase the predictability of ICRS surgery in keratoconus) and cataract (full 3-D biometry prior to cataract surgery based on OCT).

Future work

LINKING ABERRATIONS and ANTERIOR SEGMENT GEOMETRY. Modeling the optics of an individual patient´s eye and predicting the resulting optical performance addresses a current unmet need in visual optics. Combined measurements of wavefront aberrations and 3-D corneal and crystalline lens/IOL surface shape provided a deeper understanding of the relative contributions corneal and lens surfaces themselves to the aberrations and allowed realistic individual simulations of the ocular properties such as ocular aberrations by incorporating patient´s based eye biometry. These measurements will allow to evaluate the contribution of the individual optical components (corneal and lens surfaces) and their alignment to optical degradation.

KERATOCONUS and ICRS TREATMENT. OCT-based corneal aberrometry, topography and 3-D ICRS positioning provided a better approach for the improvement of ICRS surgery. Further studies on a larger population using similar keratoconus patterns, similar surgical parameters and similar ICRS combination may give further insights on the mechanism of action and help in improving surgical nomograms.

CRYSTALLINE LENS. *In vivo* crystalline lens topography allows investigating the role of crystalline lens in visual processes. Further studies on a larger population of different age and/or refractive profiles will allow gaining insights on the role of the crystalline lens on the age-dependent changes of the eye´s optics, myopia development, ocular astigmatism and accommodation.

CHROMATIC ABERRATION. Aberrometry-based measurements provide both high-order aberrations and longitudinal chromatic aberration. A full estimation of retinal image quality *in vivo* would require measurements at a higher number of wavelengths (covering the visible spectrum) and individual estimates of transverse chromatic aberration. Which can be achieved by adding multiple laser of different wavelengths or a supercontinuum laser source.

ACCOMMODATING IOLs. Application of OCT (direct visualization) and LRT aberrometry (objective accommodative response) in the study of patients implanted with accommodative IOLs (A-IOL) will be essential to evaluate the mechanism of action of the A-IOL and its final positioning in different accommodative demands.

MULTIFOCAL CONTACT LENSES. The adaptation of multifocal contact lenses is still challenging for patients and practitioners. An *in vivo* 3-D objective evaluation of the optical and fitting effects will be helpful for providing the best contact lens design.

CUSTOMIZING IOLs. OCT-based anterior segment geometry can be used to generate customized eye models both preoperatively (for ray tracing calculations of the IOL power) and custom selection of IOLs.

SWEPT-SOURCE OCT and 3-D QUANTITATIVE IMAGE PROCESSING ALGORITHMS. The long imaging depth range, high resolution and ultrahigh speed of new swept-source generation enables unprecendent 3-D measurements of the entire eye (from the cornea to the retina). The high performance of swept-source, the integration of quantitative image processing tools and an external aberrometer channel in a single instrument will enable new applications, being particularly relevant in cataract surgery and presbyopia.

RESUMEN EN ESPAÑOL

El ojo es un sistema óptico extraordinariamente simple, tiene dos lentes transparentes, la córnea y el cristalino, que de manera combinada forman las imágenes del mundo en la retina, iniciando el proceso visual. La córnea proporciona la mayor parte de la potencia refractiva del ojo, ya que contribuye aproximadamente con 2/3 de la potencia total del ojo en estado relajado (aproximadamente 42 D). Este gran aporte se debe a la forma de la superficie corneal y a la diferencia de índice de refracción entre la córnea (1.37) y el aire (1.0). El cristalino aporta el tercio restante y tiene la capacidad de autoenfoque en personas jóvenes, es decir, permite cambiar el estado refractivo del ojo, acomodar, para proporcionar una imagen nítida de los objetos a distintas distancias.

Sin embargo, alteraciones o irregularidades que se presenten en la córnea o el cristalino, o descentramientos respectivos, suponen un claro deterioro en la calidad óptica y, en consecuencia, de la visión. Estas imperfecciones del sistema visual son conocidas como aberraciones ópticas, donde la imagen de la retina de un punto objeto no es otro punto sino una distribución extensa de la luz, y se caracterizan por su degradación del contraste y su limitación en el contenido de las frecuencias espaciales de las imágenes proyectadas. Al menos en sujetos jóvenes se ha demostrado que una parte de las aberraciones corneales se compensa por las aberraciones del cristalino pero, existen patologías y/o condiciones oculares en las que este equilibrio se rompe, ya que, en la adolescencia, el queratocono degrada progresivamente la córnea, mientras que la presbicia y las cataratas son condiciones asociadas al envejecimiento que afectan al cristalino.

Por un lado, un análisis de las aberraciones en condiciones patológicas y, por otro, una precisa cuantificación tridimensional de las superficies de la córnea y el cristalino (y sus posibles tratamientos) es esencial en la exploración ocular, ya que de esta forma se podrá proporcionar una evaluación exacta del ojo estudiado, analizar qué superficie es la que altera la calidad visual, y decidir qué tratamiento es el más adecuado, abordando, en definitiva, la deseada solución personalizada para queratocono, presbicia y cataratas.

La interacción entre óptica y geometría es clave para entender el mecanismo de la función visual. Por ello, en este trabajo se ha llevado a cabo el desarrollo de un OCT para visualizar en alta resolución y cuantificar tridimensionalmente el segmento anterior del ojo y hemos adaptado el aberrómetro Trazado de rayos laser (LRT) para medir las aberraciones oculares de forma precisa en distintas condiciones oculares: queratocono y su tratamiento con ICRS, estimulando la acomodación y en pacientes con lentes intraoculares (IOL) monofocales y acomodativas.

En particular, se presenta (1) una serie de estudios longitudinales en los que analizamos tridimensionalmente la geometría de la córnea y la posición de los anillos intracorneales, las aberraciones corneales con OCT y, también, las propiedades ópticas con LRT en pacientes con queratocono antes y después de la implantación de ICRS; (2) se evalúa por primera vez *in vivo* la topografía del cristalino con la acomodación; (3) se analiza por primera vez la posición tridimensional y el impacto visual de las lentes intraoculares acomodativas después de la cirugía de cataratas; y (4) se analiza *in vivo* la aberración cromática longitudinal en pacientes con lentes intraoculares.

Capítulo I. **INTRODUCCIÓN**

En resumen, el capítulo de introducción describe los antecedentes más relevantes en los campos de la óptica, fisiología, oftalmología y optometría que han sido relevantes para el desarrollo de esta tesis. Se presentan las bases fundamentales de las técnicas de imagen del segmento anterior, entre ellas el OCT, y se describen los métodos de medida aberrometría, incluyendo la terminología del campo de la óptica utilizada, como frente de onda, aberraciones y las métricas de análisis de calidad óptica. Y, por último, se presentan las patologías y condiciones del segmento anterior (queratocono, acomodación, presbicia y cataratas) y las aplicaciones clínicas estudiadas en esta tesis (anillos intracorneales y lentes intraoculares monofocales y acomodativas).

En el ojo, la calidad visual está prácticamente determinada por la relación entre sus elementos ópticos, córnea y cristalino. Durante el crecimiento del ojo, existe una alta correlación entre la potencia de la córnea, del cristalino y la longitud axial, es decir, la distancia focal se va ajustando para proporcionar la mejor calidad óptica. La calidad óptica depende de ese acople, por lo que el papel del cristalino ha de considerarse en conjunción al de la córnea. Artal y cols. y Kelly y cols., mostraron una correlación significativa en astigmatismo horizontal/vertical, coma lateral y aberración esférica entre la córnea y el cristalino, demostrando un ajuste activo entre ambos elementos. Sin embargo, hay condiciones oculares (por ejemplo, queratocono, presbicia y cataratas) que producen imperfecciones en las superficies ópticas, rompen el ajuste córnea/cristalino y degradan la calidad óptica del ojo, aumentando las aberraciones y provocando un emborronamiento de la imagen.

Las aberraciones oculares se han medido en los últimos años gracias al desarrollo de sensores de frente de onda y su apertura a la clínica, contando con Hartmann-Shack y Trazado de rayos laser (LRT) como aberrómetros más comunes.

Por su parte, la forma tridimensional de la córnea se ha descrito mediante sistemas de topografía corneal computerizada, como el disco de Plácido o la cámara de Scheimpflug, y el estudio de la óptica de la córnea (aberraciones corneales) se ha desarrollado a partir de su geometría. Sin embargo, los resultados ópticos sobre el cristalino *in vivo* siempre han sido indirectos (restando las aberraciones corneales de las totales) y los geométricos están generalmente limitados a propiedades axiales.

Por su carácter no invasivo, su mayor resolución (2 μm), velocidad de adquisición (150000 AScans/s) y profundidad de evaluación en el ojo (hasta 30 mm), la tomografía de coherencia óptica (OCT) se ha convertido en la técnica de imagen más prometedora para el análisis tridimensional de todo el segmento anterior (córnea, cristalino y sus posibles tratamientos). En este aspecto, en nuestro grupo se han desarrollado algoritmos de cuantificación tridimensional compensando la distorsión de las imágenes de OCT.

Siendo clave el OCT y sus programas de procesado para el desarrollo de lo modelos de ojo personalizados en distintas patologías oculares, como queratocono, presbicia y cataratas, y una correcta evaluación de sus tratamientos (anillos intracorneales (ICRS) en queratocono y las lentes intraoculares acomodativas (A-IOLs) en presbicia y cataratas).

En este contexto, las grandes líneas de investigación en esta tesis doctoral se han orientado a estudiar la relación entre la forma tridimensional de las superficies del ojo (OCT) y la calidad óptica (LRT) en distintas condiciones clínicas del segmento anterior.

(1) **Queratocono y anillos intracorneales (ICRS)**. La implantación de ICRS es un tratamiento aceptado para el tratamiento del queratocono, ya que, por un lado, aplana la córnea y, por otro, ofrece en la mayoría de los casos una mejora a largo plazo en la agudeza visual. Sin embargo, en la actualidad, la implantación de los anillos se basa en un nomograma con pocos parámetros de entrada. Además, es difícil estimar la mejora en calidad visual, su mecanismo de acción dentro de la córnea y su efecto en las superficies anterior y posterior de la córnea. Por ello, las nuevas técnicas de imagen pueden proporcionar la información necesaria para mejorar el resultado final de esta técnica quirúrgica.

Algunas preguntas por resolver son: ¿Cuál es el efecto real de los anillos en las superficies corneales? ¿Qué estabilidad tienen los anillos en la córnea? ¿Existe una redistribución del espesor corneal al implantar los anillos? ¿Los anillos frenan la progresión del queratocono? ¿Aumentan las aberraciones de alto orden?

(2) **Acomodación**. La mayoría de los estudios *in vivo* del cristalino con la acomodación describen cambios axiales o de curvatura en la zona central pero no de las superficies del cristalino en 3-D. Por ello, un análisis exhaustivo de la forma del cristalino y su geometría es crítico para entender (1) sus propiedades ópticas , (2) el papel de las superficies del cristalino en la compensación de las aberraciones corneales (en particular, astigmatismo y aberración esférica), (3) la implicación del cristalino en el desarrollo de errores refractivos (por ej., miopía), (4) los cambios en la óptica del ojo con la edad, y por último, (5) podrá mejorar la predicción en el cálculo de la potencia de IOLs.

(3) **Presbicia/Cataratas y lentes intraoculares (IOLs)**. El aumento de la esperanza de vida y el incremento de la demanda visual para visión cercana ha llevado en los últimos años al desarrollo de IOLs que imiten en cierta medida las propiedades naturales del cristalino joven. Las IOL monofocales son diseños esféricos que proporcionan una excelente visión funcional; sin embargo, limitan la profundidad de foco y no abordan la compensación de las aberraciones corneales. Hoy en día, existen muchas más posibilidades para mejorar la calidad visual de estos pacientes. Así, se han propuesto lentes que corrijan el astigmatismo, que compensen la aberración esférica de la córnea, que disminuyan la aberración cromática, que proporcionen multifocalidad o acomodación. Como consecuencia, ahora es posible elegir una IOL específica para cada paciente en función de sus necesidades. En este contexto, una medida precisa de las aberraciones oculares y la biometría en 3-D pre- y post-operatoria es crítico para el diseño personalizado de IOLs y su planificación quirúrgica.

Sin embargo, quedan todavía preguntas sin respuesta: ¿Cuál es la calidad óptica de los pacientes operados con IOL? ¿Funcionan las IOL acomodativas como se esperaba? ¿Proporcionan un rango acomodativo objetivo? ¿Qué consecuencias visuales de las aberraciones monocromáticas y cromáticas ? ¿Aumentan las aberraciones de alto orden?

Capítulo II. MATERIAL Y MÉTODOS

En este capítulo se presentan las técnicas experimentales utilizadas en el transcurso de esta tesis doctoral.

En primer lugar, se utilizó un aberrómetro de *Trazado de Rayos Laser (LRT)* desarrollado en el Instituto de Óptica. Este sistema cuantifica la aberración transversal en función de la posición de la pupila. En el LRT la pupila se muestrea secuencialmente mediante un escáner que barre la pupila y proyecta un haz de luz en la retina. Las imágenes del haz de luz en la retina en las distintas posiciones de entrada son grabadas por una cámara.

El LRT consta esencialmente de (1) Canal de iluminación, con dos posibles fuentes de luz: laser infrarrojo (785 nm) y láser verde (532 nm); (2) Escáner, el escáner distribuye el haz de luz por la pupila; (3) Sistema de Badal, compuesto por dos espejos y dos lentes que compensan los errores refractivos del sujeto; (4) Cámara de pupila y retina, la cámara de pupila graba las imágenes correspondientes a la posición de entrada del haz de luz en la pupila y la cámara de retina recoge la luz reflejada de la retina para cada haz de entrada y (5) Sistema externo de Fijación/Acomodación.

En la sección de LRT se describen los protocolos de control de medida, calibración y análisis.

En segundo lugar, se utilizó un sistema de *Tomografía de Coherencia Óptica (OCT)* de dominio espectral desarrollado en el Instituto de Óptica en colaboración con la Copernicus University de Torun, Polonia. Este sistema permite la obtención *in vivo* de imágenes tridimensionales del segmento anterior con resolución de micras y a gran velocidad. Un OCT es esencialmente (1) luz monocromática de baja coherencia, (2) un interferómetro Michelson en configuración de fibra óptica y (3) un escáner óptico. El interferómetro consta de una fuente de luz, un divisor de haz y dos espejos. Y en OCT el desarrollo es el siguiente: la luz de baja coherencia que sale del diodo superluminiscente (SLD, 840 nm) se divide en un divisor de haz. Los haces que van a cada brazo se reflejan, uno en el espejo de referencia y el otro en la muestra (ojo), y vuelven a juntarse en el divisor de haz. De ahí van al detector. Cuando los caminos ópticos de los dos haces coinciden exactamente (o están dentro del margen de la longitud de coherencia de la luz), las interferencias entre ellos son constructivas, y la señal captada es alta.

Los sistemas de OCT obtienen la imagen punto a punto. Por tanto, el sistema de iluminación enfoca el haz de luz en un solo punto de la muestra. Gracias a la utilización de luz de baja coherencia, no hay luz proveniente de otros puntos situados en el mismo plano que el punto de interés. En OCT de dominio espectral la longitud del brazo de referencia se fija y la luz de salida del interferómetro se analiza con un espectrómetro. Debido a la longitud de onda y el ancho espectral del SLD, la interferencia de banda ancha se registra con detectores espectralmente separados, en nuestro caso codificando la frecuencia óptica en el espacio con un detector dispersivo (en nuestro caso con una red de dispersión y una cámara CMOS lineal). Y, por la relación de Fourier y el teorema de Wiener-Khintchine, relacionado con la autocorrelación y la densidad de potencia espectral, el barrido en profundidad puede ser calculado de forma inmediata mediante la transformada de Fourier del espectro registrado, sin necesidad de modificar la longitud de camino del brazo de muestreo. Esta característica hace que se incremente la velocidad del proceso de manera importante, a la vez que reduce las pérdidas durante un registro puntual en profundidad y mejore la razón señal/ruido.

En la sección de OCT se describe también el brazo de fijación/acomodación, los programas de corrección de distorsión, procesado de imagen y cuantificación del segmento anterior del ojo, con especial dedicación a la metodología desarrollada para el análisis de las aberraciones corneales basada en trazado de rayos virtual a través de las elevaciones corneales con la ayuda de un programa de diseño óptico (ZEMAX).

En este capítulo también se definen las métricas de calidad óptica obtenidas a partir de la aberración de onda, en foco y a través de foco. La PSF designa la distribución de intensidades de la imagen de una fuente tras su paso por un sistema óptico. La MTF nos ofrece el grado de detalle, esto es, la reducción del contraste en función de frecuencia espacial de la imagen a su paso por un sistema óptico. En particular, Visual Sthrel es la métrica más utilizada por su alta correlación con la Agudeza Visual medida en la clínica.

Y, por último, se explica el protocolo de medidas realizado en los pacientes estudiados en esta tesis.

Capítulo III. **QUERATOCONO & ICRS**

Este capítulo está basado en los artículos *“Quantitative OCT-based longitudinal evaluation of intracorneal ring segment implantation in keratoconus, Invest Ophthalmol Vis Sci 2013”* y *“Ocular and Optical Coherence Tomography-based corneal aberrometry in keratoconic eyes treated by intracorneal ring segments, Am J Ophthalmol 2014”* de Pérez-Merino y cols.

Los coautores son Sergio Ortiz, Nicolás Alejandre, Alberto de Castro, Ignacio Jimenez-Alfaro y Susana Marcos.

Propósito. Caracterizar las propiedades geométricas de la córnea y analizar las aberraciones corneales explorando las posibilidades del OCT como una nueva herramienta para el análisis completo (geométrico y óptico) del queratocono y su tratamiento quirúrgico con anillos intracorneales (ICRS).

Métodos. El primer apartado está basado en el análisis longitudinal de la geometría corneal con OCT y se evalúa la topografía corneal, paquimetría y la posición tridimensional de los anillos en pacientes de queratocono operados con ICRS; las medidas se realizan en 10 pacientes antes y después de la operación (7, 30 y 90 días). El segundo apartado está basado en la propuesta del OCT como aberrómetro corneal, donde se midieron 19 ojos antes y 3-meses después de la implantación de anillos intracorneales y se compararon los resultados con las aberraciones totales (LRT) en 8 ojos. A partir de los datos de elevación de la córnea (superficie anterior y posterior) se puede calcular la deformación de un frente de ondas que la atraviese por medio del programa de diseño óptico ZEMAX. El análisis geométrico y aberrométrico se realizó para 4-mm de diámetro (centro pupilar).

Resultados. En promedio, el radio de curvatura de la córnea fue de 7.02±0.54 mm (anterior), 5.40±0.77 mm (posterior) y el mínimo espesor corneal 384±60 μm antes de la implantación de ICRS. Después de la cirugía de ICRS (90 días), el radio de curvatura de la córnea fue de 7.26±0.53 mm (anterior), 5.44±0.71 mm (posterior) y el mínimo espesor corneal 396±46 μm. La implantación de los ICRS aplanó la superficie anterior de la córnea y disminuyó su potencia (1.71±1.83 D). Las irregularidades de la córnea (definidas por los términos de Zernike de alto orden de las superficies corneales) y la distribución del espesor (definida como la variación de RMS del espesor) disminuyó en algunos pacientes y aumentó en otros. La profundidad tridimensional de los ICRS fue muy similar a la planificada con laser de femtosegundo (diferencias en promedio de 15±20 μm) y mostraron una inclinación de -6.8±2.6 grados (temporal) y -2.1±0.8 grados (superior) 7 días después de la implantación de los ICRS. En promedio, hubo una ligera y progresiva disminución de la profundidad de los ICRS (10 μm, del día 7 al 90 post-op) y una pequeña variación de la inclinación (1 grado). Comparando los datos de aberraciones corneales (OCT) y totales (LRT) antes y después de la implantación de los ICRS (90 días), se encontró una alta correlación en la mayoría de los sujetos. Los valores de RMS HOAs con OCT fueron 0.78±0.35 μm (pre-op) y 0.88±0.36 μm (post-op) y con LRT 0.57±0.39 μm (pre-op) y 0.53±0.24 μm (post-op), para 4-mm de pupila. La superficie posterior de la córnea compensó parcialmente las aberraciones de la superficie anterior (8.3%, pre-op; 4.1%, post-op). Individualmente, las aberraciones predominantes fueron coma vertical (Z_3^{-1}), trefoil vertical (Z_3^{-3}) y astigmatismo secundario (Z_4^{4}). La implantación de ICRS disminuyó el astigmatismo corneal en un 27% y el coma un 5%. Sin embargo, no se encontró una disminución estadísticamente significativa en las aberraciones de alto orden después de la cirugía de ICRS.

Conclusiones. Comprender el acople entre la óptica y la geometría corneal es esencial para mejorar la planificación quirúrgica en pacientes con queratocono. El OCT es una herramienta útil ya que nos permite analizar de forma precisa (1) los cambios topográficos de la superficie anterior y posterior de la córnea, (2) la redistribución del espesor corneal, (3) la posición tridimensional (profundidad e inclinación) de los ICRS, y (4) evaluar las aberraciones de la córnea. ICRS es una alternativa quirúrgica que aplana la superficie anterior de la córnea y disminuye el astigmatismo corneal. Sin embargo, la respuesta en regularización de las superficies corneales y cambios en las aberraciones de alto orden presenta una variabilidad alta entre sujetos.

Capítulo IV. ACOMODACIÓN

Este capítulo está basado en el artículo *"Crystalline lens topography in accommodating eyes, Biomed Opt Express 2015"* de Pérez-Merino y cols.

Los coautores son Miriam Velasco-Ocana, Eduardo Martinez-Enriquez y Susana Marcos.

Propósito. Analizar por primera vez *in vivo* los cambios topográficos de las superficies anterior y posterior del cristalino con la acomodación para entender (1) sus propiedades ópticas, (2) el papel de las superficies del cristalino en la compensación de las aberraciones corneales (en particular, astigmatismo y aberración esférica), y (3) la relación entre las superficies anterior y posterior del cristalino.

Métodos. Con OCT medimos 9 cristalinos de 7 sujetos no présbitas (33±2 años de edad) en 5 estados acomodativos, de 0 a 6 D (en pasos de 1.5 D). Se obtuvieron imágenes 3-D del segmento anterior (1) Córnea+Iris, (2) Cristalino anterior+Iris y (3) Cristalino posterior+Iris con una densidad de 300 AScans x 50 BScans (11 x 11 mm), y se caracterizaron las superficies de la córnea y el cristalino restando la mejor esfera de referencia y mediante el ajuste de polinomios de Zernike de sexto orden (analizando la RMS de las irregularidades de alto orden, astigmatismo, coma y trefoil). La relación entre los ángulos y magnitud de astigmatismo de córnea (anterior y posterior) y cristalino (anterior y posterior) se estudió en el estado desacomodado y para cada demanda acomodativa. Por último, se analizó la biometría del segmento anterior con la acomodación: profundidad de cámara anterior (ACD), espesor del cristalino y radios de todas las superficies.

Resultados. Los radios de curvatura del cristalino disminuyeron 0.78±0.18 mm/D (anterior) y 0.13±0.07 mm/D (posterior), ACD disminuyó 0.04±0.01 mm/D y el espesor del cristalino aumentó 0.04±0.01 mm/D con la acomodación. En el estado relajado, el término de esférica (47%) aporta la mayor parte de irregularidad de superficie en la superficie anterior del cristalino y el término de astigmatismo (70%) en la superficie posterior del cristalino. Sin embargo, con acomodación astigmatismo fue la irregularidad de superficie predominante (90%). La RMS de las irregularidades de alto orden de la superficie posterior del cristalino es estadísticamente significativa mayor que la de la superficie anterior del cristalino (x2.02, $p<0.0001$). Encontramos una correlación negativa significativa en el coma vertical (Z_3^{-1}) y el trefoil oblicuo (Z_3^{-3}) entre las superficies del cristalino. El ángulo de astigmatismo presentó un alto grado de alineamiento entre las superficies de la córnea, moderado entre las superficies de la córnea y la superficie anterior del cristalino (~27 grados), y un ángulo perpendicular entre las superficies anterior y posterior del cristalino (~80 grados).

Conclusiones. El OCT con programas específicos dedicados al procesado de imagen, corrección de las distorsiones y cuantificación es una herramienta única en la evaluación de los cambios de forma en la superficie del cristalino con la acomodación. Una precisa descripción de la forma del cristalino es crítica para estudiar la implicación del cristalino en la óptica del ojo en estado desacomodado y acomodado, incluyendo el astigmatismo y las irregularidades de alto orden. Nuestros resultados demuestran que la compensación de astigmatismo no solo sucede entre la córnea y el cristalino, sino también entre las propias superficies. Con acomodación el cambio más representativo aparece en el término de esférica que pasa de valores positivos a negativos, aunque también se producen cambios en astigmatismo y en irregularidades de alto orden.

Capítulo VI. PRESBICIA/CATARATAS & A-IOL

Este capítulo está basado en los artículos *"Aberrometry in patients implanted with accommodative introcular lenses, Am J Ophthalmol 2014"* de Pérez-Merino y cols y *"Three-dimensional evaluation of accommodating intraocular lens shift and alignment in vivo, Ophthalmology 2014"* de Marcos y cols.

Los coautores son Sergio Ortiz, Judith Birkenfeld, Carlos Dorronsoro, Sonia Durán, Ignacio Jimenez-Alfaro y Susana Marcos.

Propósito. Evaluar de forma objetiva la respuesta acomodativa, cambio de aberraciones, profundidad de foco y cambios biométricos en 3-D en ojos implantados con la IOL acomodativa (A-IOL) Crystalens-AO.

Métodos. Se examinaron 11 pacientes (22 ojos) con cataratas después de la implantación de la Crystalens-AO A-IOL. También se incluyeron en el estudio dos grupos controles (sujetos jóvenes y sujetos implantados con IOL monofocal) de 17 ojos cada uno. En la primera parte del estudio se analizaron los cambios ópticos por medio del estudio de las aberraciones oculares con el LRT: (1) aberraciones oculares, (2) respuesta acomodativa paraxial (asociada con cambios en el desenfoque), (3) respuesta acomodativa efectiva (asociada con cambios en el desenfoque, aberraciones esféricas y diámetro de pupila), (4) profundidad de foco, estimada a partir de VSMTF a través de foco. En el segundo apartado se analizan los cambios biométricos del segmento anterior (cornea+A-IOL) mediante cuantificación tridimensional con OCT: (5) ACD, (6) espesor del cristalino, (7) inclinación de A-IOL. Todas las medidas se realizaron para demandas acomodativas de 0, 1.25 y 2.5 D.

Resultados. Trefoil vertical (Z_3^{-3}) y coma (Z_3^{1}, Z_3^{-1}) fueron las aberraciones individuales de alto orden predominantes en el grupo Crystalens y control de IOL monofocal, y fueron más altas que en el grupo control de sujetos jóvenes ($p<0.0001$). La profundidad de foco fue estadísticamente significativa mayor en el grupo de Crystalens que en los grupos controles. En promedio, en el grupo de Crystalens el término de desenfoque (Z_2^{0}), astigmatismo o las aberraciones de alto orden no cambiaron con la demanda acomodativa. Tampoco se observaron cambios en el desenfoque efectivo entre las distintas condiciones acomodativas: 0.34±0.48 D (visión lejos), 0.32±0.50 D (visión intermedia), 0.34±0.44 D (visión cercana). Con OCT, la visualización directa de la A-IOL nos permitió cuantificar las distancias de ACD pre-op (2.64±0.24 mm) y post-op (3.65±0.35 mm, en el estado relajado), encontrando una significativa correlación ($r=0.93$; $p<0.05$). La posición de la A-IOL no cambió axialmente con la demanda acomodativa, presentando únicamente cambios en la inclinación vertical (siendo mayor de 9 grados en dos de los sujetos). El mayor cambio en inclinación tuvo lugar en la demanda acomodativa de 1.25 D. Los sujetos con mayor cantidad de astigmatismo ($r=-0.47$, $p=0.04$), HOAs ($r=-0.48$, $p=0.03$) y trefoil ($r=-0.61$, $p=0.05$) fueron los que mayor cantidad de inclinación en la A-IOL presentaron.

Conclusiones. La respuesta acomodativa de los ojos implantados con Crystalens A-IOL, medida objetivamente con LRT y OCT, fue menor de 0.4 D y menor de 0.07 mm en todos los sujetos. Varios sujetos presentaron cambios en astigmatismo, aberración esférica, trefoil y coma con la acomodación, que se asocian con los cambios geométricos y de alineamiento en la A-IOL con la demanda acomodativa.

Capítulo VII. CATARATAS & IOL

Este capítulo está basado en los artículos *"In vivo chromatic aberration in eyes implanted with Intraocular lenses, Invest Ophthalmol Vis Sci 2013"* de Pérez-Merino y cols.

Los coautores son Carlos Dorronsoro, Lourdes Llorente, Sonia Durán, Ignacio Jimenez-Alfaro y Susana Marcos.

Propósito. Medir *in vivo* y objetivamente las aberraciones monocromáticas a diferentes longitudes de ondas y determinar la aberración cromática longitudinal (LCA) entre verde e IR en ojos implantados con dos modelos de IOL.

Métodos. Se midieron 18 ojos (9 implantados con Tecnis ZB99 1-Piece acrylic IOL y 9 implantados con AcrySof SN60WF IOL) con LRT en dos longitudes de onda, 532 nm (verde) y 785 (IR). Se analizaron las aberraciones monocromáticas para ambas longitudes de onda y la diferencia cromática de foco se estimó como la diferencia entre el error equivalente esférico para cada longitud de onda.

Resultados. Las medidas de las aberraciones fueron altamente reproducibles para las dos longitudes de onda. Excepto para el término de desenfoque (Z_2^0) no se encontraron diferencias significativas en las aberraciones de alto orden. En promedio, la diferencia cromática de foco fue de 0.46±0.15 D en el grupo Tecnis y 0.75±0.12 D en el grupo AcrySof ($p<0.05$). La diferencia cromática de foco en el grupo de AcrySof no fue estadísticamente significativa en comparación con LCA descrita anteriormente en ojos jóvenes (0.78±0.16 D). El impacto de la LCA en la calidad de imagen retiniana (medida en términos de Strehl ratio) disminuyó drásticamente cuando se incluyó el astigmatismo y las aberraciones de alto orden, en este caso no se apreciaron diferencias estadísticamente significativas en la calidad de imagen retiniana entre los grupos Tecnis y AcrySof.

Conclusiones. LRT con diferentes longitudes de onda es una excelente técnica para evaluar objetivamente la LCA en ojos con IOLs. La implantación de estos modelos de IOL no aumentó la LCA en comparación con ojos fáquicos, siendo el grupo de AcrySof el que presentó valores similares a los fisiológicos de sujetos jóvenes. Las aberraciones juegan un importante papel en los resultados visuales en pacientes con IOL.

Epílogo. CONCLUSIONES Y TRABAJO FUTURO

En este estudio, por primera vez, se ha analizado la contribución geométrica y óptica de los componentes oculares individuales en diversas patologías, condiciones oculares y procedimientos quirúrgicos, y se presentan técnicas basadas en LRT y OCT para su uso sistemático en el estudio de las propiedades ópticas del ojo en las aplicaciones clínicas más comunes de córnea y cristalino.

Las principales aportaciones de este trabajo son las siguientes:

1. Hemos desarrollado diferentes implementaciones de sistemas ópticos, protocolos de medida y algoritmos de procesado para el estudio preciso de geometría y las aberraciones de las superficies ópticas (córnea+tratamiento y cristalino/tratamiento). Estas técnicas son Tomografía de Coherencia Óptica (OCT) y Trazado de Rayos Laser (LRT), y han demostrado ser útiles en la medida de pacientes con distintas patologías o condiciones clínicas del segmento anterior del ojo como: queratocono, acomodación, presbicia y cataratas y sus distintos tratamientos (anillos intracorneales, ICRS; lentes intraoculares monofocales, IOL; lentes intraoculares acomodativas, A-IOL).

2. Hemos desarrollado una metodología computacional con OCT para estimar las aberraciones de las superficies anterior y posterior de la córnea basado en un trazado de rayos virtual. El procedimiento incluye la descripción de la forma de la córnea en polinomios de Zernike y el cálculo de la aberración de onda. El procedimiento completo se validó *in vivo* en sujetos con queratocono (donde las aberraciones de la córnea aportan la totalidad de las aberraciones oculares) y los resultados se compararon con los obtenidos en aberrometría LRT (sistema estándar en aberrometría ocular).

3. Hemos estudiado, por primera vez con OCT, la forma tridimensional, espesor, geometría y óptica (aberraciones de cada superficie) de la córnea de sujetos con queratocono (antes y después del tratamiento con ICRS). También se ha analizado de forma tridimensional la posición, profundidad e inclinación de los ICRS y, por último, se definieron métricas para el análisis de la regularidad de superficie y distribución del espesor.
   En este estudio encontramos que algunos pacientes presentan unas superficies más regulares y, en consecuencia, una disminución de las aberraciones corneales, y en otros pacientes se observa una mayor irregularidad superficial y un aumento en las aberraciones. Su fracaso en algunos pacientes en aplanar y regularizar la superficies corneales y proponer una calidad visual adecuada *a priori* parece determinada por la elección quirúrgica. De este estudio se extrae que el cambio en el radio corneal anterior está asociado con el diámetro de la zona óptica, y la longitud del arco del ICRS con el efecto sobre el radio en la superficie posterior. Asimismo, hemos demostrado que la rotación de los ICRS con el tiempo modifica la regularidad de la superficie anterior de la córnea.

4. Hemos diseñado dos canales de fijación/acomodación externos para estimular la acomodación en los sistemas de OCT y LRT.

5. Hemos estudiado, por primera vez, la topografía del cristalino *in vivo* y sus cambios con la acomodación, analizando en detalle la contribución de los componentes individuales de la córnea (superficie anterior y posterior) y cristalino (superficie anterior y posterior) y sus distancias relativas. La relación entre todas las superficies ópticas aporta una información clave para entender el mecanismo de la acomodación y contribuye de forma significativa al conocimiento de los cambios ópticos producidos.

En promedio, encontramos que la superficie posterior de la córnea compensa un 18% del astigmatismo y un 12% del coma de la superficie anterior. El astigmatismo y las irregularidades de alto orden de la superficie posterior del cristalino es significativamente mayor que en la superficie anterior y en la mayoría de sujetos sus ejes muestran diferencia de 90 grados. En el estado relajado, las dos superficies del cristalino muestran una alta correlación en las irregularidades de sus superficies, en particular coma y trefoil, indicando un desarrollo coordinado.

Con acomodación, se producen cambios en magnitud (aumenta el astigmatismo en la superficie anterior del cristalino, siendo en la mayoría de sujetos mayor que el de la superficie posterior) y eje (entre 10 y 20 grados) en las dos superficies del cristalino. También, se produce un cambio de valores positivos a negativos en el coeficiente esférico en la superficie anterior del cristalino y cambios en coma y trefoil (alcanzando un mínimo la demanda acomodativa de 3 D).

6. Por primera vez, se ha medido de forma objetiva *in vivo* la respuesta acomodativa (aberraciones, LRT; biometría tridimensional, OCT) de la lente intraocular Crystalens-AO (única lente intraocular acomodativa aprobada por la FDA). El cambio en desenfoque estimulando acomodación con LRT varió de 0.43 a -0.36 D, siendo consistente con el cambio axial de 0.07 a -0.01 mm. Los resultados de LRT demuestran que los cambios en la respuesta acomodativa con Crystalens AO A-IOL están por debajo de 0.5 D y que un 14% de los pacientes presentan respuestas acomodativas negativas. Los resultados de OCT confirman las medidas de LRT, ya que los cambios axiales con acomodación son muy pequeños y, en algunos caso, opuestos al esperado. Estas evidencias indican que el mecanismo de funcionamiento de la Crystalens AO A-IOL no produjo los cambios en potencia o axiales esperados.

En este estudio también hemos observado una mayor inclinación en la posición de la A-IOL, indicando un cierto grado de inestabilidad en el alineamiento, y siendo mayor con el esfuerzo acomodativo (principalmente alrededor del eje X, inclinación superior/inferior). Curiosamente, los ojos con mayor astigmatismo, coma y trefoil presentaron la mayor cantidad de inclinación. Esta mayor cantidad de aberraciones en los pacientes de Crystalens resultó en un ligero aumento en la profundidad de foco, pudiendo ofrecer un mayor rango funcional en visión de cerca.

7. Hemos medido, por primera vez, la aberración cromática longitudinal (LCA) *in vivo* en pacientes con IOLs. En este estudio, hemos analizado dos modelos de lentes intraoculares asféricas con distinto número de Abbe (Tecnis, número de Abbe = 55; AcrySof, número de Abbe = 37. La compensación de la LCA ha sido objeto de debate en los últimos años, ya que el beneficio de su corrección tan solo ha sido estudiado por medio de simulaciones ópticas. Nuestras medidas de LCA se ajustan a las medidas teóricas (0.46 D, Tecnis; 0.76 D, AcrySof), ya que la IOL con mayor número de Abbe presenta una menor LCA. Sin embargo, el relativo impacto de la LCA con las aberraciones de alto orden (con y sin astigmatismo) es menor del esperado, ya que no se observan diferencias significativas en la degradación de la PSF entre ambas IOLs.

Uno de los avances tecnológicos más espectaculares de los últimos años en oftalmología es la aparición de técnicas y diagnóstico de imagen. La utilización independiente o combinada de sistemas ópticos, imagen de alta resolución y algoritmos de cuantificación precisos, OCT y aberrometría LRT en esta tesis, aportan la información necesaria para cualquier exploración del segmento anterior del ojo y cualquier planteamiento quirúrgico. Las posibilidades de explorar *in vivo* la topografía del cristalino no sólo abre una nueva línea de investigación y ofrece nuevos conocimientos sobre el mecanismo de acomodación, si no que también determina la contribución de cada superficie óptica (córnea y cristalino) a la calidad óptica del ojo y establece el grado de relación/compensación entre superficies, por lo que podrá aportar avances sobre el desarrollo de errores refractivos (por ejemplo, miopía) y analizar en detalle los cambios del cristalino relacionados con la edad. Además, las capacidades cuantitativas del OCT se pueden ampliar para analizar en detalle la córnea y el cristalino antes de abordar una cirugía y determinar el cambio postoperatorio (incluyendo la posición tridimensional de los tratamientos, ICRS en queratocono y IOLs en cataratas), y en un futuro próximo desarrollar en un único instrumento (en particular, con los nuevos desarrollos swept-source) toda la exploración ocular. Esto abre nuevas posibilidades en el análisis y tratamiento del queratocono y, en exclusiva, en la cirugía de cataratas, ya que, este desarrollo propondrá perspectivas novedosas y únicas en el modelo de ojos personalizados, en el cálculo de la potencia de la lente basada en trazado de rayos y en la determinación de la posición final de la lente, ofreciendo, en definitiva, un paso definitivo en el abordaje de la personalización de los tratamientos del segmento anterior del ojo.

List of PUBLICATIONS

Publications included in this thesis

1. P. Pérez-Merino, M. Velasco-Ocana, E. Martínez-Enríquez, & S. Marcos. "OCT-based crystalline lens topography in accommodating eyes". *Biomed Opt Express*; 2015.

2. S. Marcos, S. Ortiz, P. Pérez-Merino, J. Birkenfeld, S. Durán & I. Jiménez-Alfaro. "Three-dimensional evaluation of accommodating intraocular lens shift and alignment *in vivo*". *Ophthalmology*; 121(1):45-55. 2014.

3. P. Pérez-Merino, J. Birkenfeld, C. Dorronsoro, S. Ortiz, S. Durán, I. Jiménez-Alfaro & S. Marcos. "Aberrometry in patients with accommodative intraocular lenses". *Am J Ophthalmol*; 157(5):1077-89. 2014.

4. P. Pérez-Merino, S. Ortiz, N. Alejandre, A. de Castro, I. Jiménez-Alfaro & S. Marcos. "Ocular and optical coherence tomography-based corneal aberrometry in keratoconic eyes treated by intracorneal ring segments". *Am J Ophthalmol*; 157(1):116-27. 2014.

5. P. Pérez-Merino, S. Ortiz, N. Alejandre, I. Jiménez-Alfaro & S. Marcos. "Quantitative OCT-based longitudinal evaluation of intracorneal ring segment implantation in keratoconus". *Invest Ophthalmol Vis Sci*; 54(9):6040-51. 2013

6. P. Pérez-Merino, C. Dorronsoro, L. Llorente, S. Durán, I. Jiménez-Alfaro & S. Marcos. "*In vivo* chromatic aberration in eyes implanted with intraocular lenses". *Invest Ophthalmol Vis Sci*; 54(4):2654-61. 2013.

Other Publications

1. M. Sun, A. de Castro, P. Pérez-Merino, E. Martínez-Enriquez, M. Velasco-Ocana & S. Marcos. "Intraocular lens alignment from an *en face* optical coherence image Purkinje-like method". Submitted to *Biomed Opt Express*; 2015.

2. M. Sun, A. de Castro, S. Ortiz, P. Pérez-Merino, J. Birkenfeld & S. Marcos. "Intraocular lens alignment from an *en face* optical coherence image Purkinje-like method". *Optical Engineering*; 53(6):06174. 2014.

3. E. Gambra, S. Ortiz, P. Pérez-Merino, M. Gora, M. Wojtkowski & S. Marcos. "Static and dynamic crystalline lens accommodation evaluated using quantitative 3-D OCT". *Biomed Opt Express*; 4(9):1595-609. 2013.

4. S. Ortiz, P. Pérez-Merino, S. Durán, M. Velasco-Ocana, J. Birkenfeld, A. de Castro, I. Jiménez-Alfaro & S. Marcos. "*In vivo* human crystalline lens topography". *Biomed Opt Express*; 4(3):387-96. 2013.

5. C. Dorronsoro, D. Pascual, P. Pérez-Merino, S. Kling & S. Marcos. "Dynamic OCT measurement of corneal deformation by an air puff in normal and cross-linked corneas". *Biomed Opt Express*; 3(3):473-87. 2012.

6. S. Ortiz, P. Pérez-Merino, N. Alejandre, E. Gambra, I. Jimenez-Alfaro & S. Marcos. "Quantitative OCT-based corneal topography in keratoconus with intracorneal ring segments". *Biomed Opt Express*; 3(5):814-24. 2012.

7. P. Gallego, C. Martínez-García, P. Pérez-Merino, L. Ibares-Frías, A. Mayo-Iscar & J. Merayo-Lloves. “Scleral changes induced by atropine in chicks as an experimental model of myopia”. *Ophthalmic Physiol Opt*; 32(6):478-84. 2012.

8. S. Ortiz, P. Pérez-Merino, E. Gambra, A. de Castro & S. Marcos. “*In vivo* human crystalline lens topography”. *Biomed Opt Express*; 3(10):2471-88. 2012.

9. S. Marcos, J. Requejo-Isidro, J. Merayo-Lloves, A.U. Acuña, V. Hornillos, E. Carrillo, P. Pérez-Merino, S. del Olmo-Aguado, C. del Aguila, F. Amat-Guerri & L. Rivas. “Fluorescent labeling of *acanthamoeba* assessed *in situ* from corneal sectioned microscopy”. *Biomed Opt Express*; 3(10):2489-99. 2012.

10. J.M. Bueno, E.J. Gualda, A. Giakoumaki, P. Pérez-Merino, S. Marcos & P. Artal. “Multiphoton microscopy of *ex vivo* corneas after collagen cross-linking”. *Invest Ophthalmol Vis Sci*; 52(8):5325-31. 2011.

11. S. Ortiz, D. Siedlecki, P. Pérez-Merino, N. Chia, A. de Castro, M. Szkulmowski, M. Wojtkowski & S. Marcos. “Corneal topography from *spectral optical coherence tomography (sOCT)”. Biomed Opt Express;* 2(12):3232-47. 2011.

12. C. Dorronsoro, S. Schumacher, P. Pérez-Merino, J. Siegel, M. Mrochen & S. Marcos. “Effect of air-flow on the evaluation of refractive surgery ablation patterns”. *Opt Express*; 19(5):4653-66. 2011.

13. P. Pérez-Merino, M.C. Martínez-García, S. Mar-Sardaña, A. Pérez-Escudero, T. Blanco-Mezquita, A. Mayo-Iscar & J. Merayo-Lloves. “Corneal light transmission and roughness after refractive surgery”. *Optom Vis Sci*; 87(7):469-74. 2010.

14. P. Pérez-Merino, F. Parra, L. Ibares-Frías, P. Gallego, B. Vázquez-Lasa, L. Benito, J. San Román, C. Martínez-García & J. Merayo-Lloves. “Clinical and pathological effects of different acrylic intracorneal ring segments in corneal additive surgery”. *Acta Biomater*; 6(7):2572-9. 2010.

International Congress Contributions

Personally presented

1. P. Pérez-Merino, M. Velasco-Ocana, E. Martinez-Enriquez, S. Marcos. “OCT-based crystalline lens topography in accommodating eyes”. Association for Research in Vision and Ophtalmology (ARVO). Denver, CO. 2015. *Oral communication.*

2. P. Pérez-Merino, C. Dorronsoro, L. Llorente, S. Duran, I. Jimenez-Alfaro, S. Marcos. "*in vivo* chromatic aberration of intraocular lenses”. IONS 2013. Zurich, Switzerland. 2013. *Oral communication.*

3. P. Perez-Merino, S. Ortiz, N. Alejandre, A. de Castro, I. Jimenez-Alfaro, S. Marcos. “OCT-based topography and corneal aberrations and ray tracing total aberrations in keratoconus before and after ICRS treatment”. Association for Research in Vision and Ophtalmology (ARVO). Fort Lauderdale, FL. 2012. *Poster.*

4. P. Perez-Merino, S. Ortiz, N. Alejandre, A. de Castro, I. Jimenez-Alfaro, S. Marcos. “Assesing corneal geometrical and optical changes on ICRS-treated corneas with quantitative OCT”. Eurokeratoconus. Bordeaux, France. 2011. *Poster.*

5. P. Perez-Merino, S. Ortiz, N. Alejandre, A. de Castro, I. Jimenez-Alfaro, S. Marcos. “Full OCT Corneal Topography and Aberrations in Keratoconic Patients and Their Change After Intrastromal Corneal Ring Segments (ICRS) Implantation”. Association for Research in Vision and Ophtalmology (ARVO). Fort Lauderdale, FL. 2011. *Poster.*

6. C. Dorronsoro, S. Schumacher, P. Perez-Merino, J. Siegel, M. Mrochen, S. Marcos. "Effect of Aspiration Air-Flow Speed on the Effective Refractive Surgery Ablation Patterns". Association for Research in Vision and Ophtalmology (ARVO). Fort Lauderdale, FL. 2011. *Poster.*
7. P. Perez-Merino, S. Ortiz, N. Alejandre, E. Gambra, I. Jimenez-Alfaro, S. Marcos. "Pre- and Post-operative quantitative 3-D OCT imaging of keratoconic eyes implanted with intracorneal ring segments". V European Meeting on Visual and Physiological Optics. Stockholm, Sweden. 2010. *Poster.*
8. P. Pérez-Merino, F. Parra, L. Ibares-Frías, P. Gallego, B. Vázquez-Lasa, L. Benito, J. San Román, C. Martinez-Garcia, J. Merayo-Lloves. "Biomaterials and Intracorneal Ring Segments: Acrylic Copolymers". Jornadas de Jóvenes Investigadores en Óptica Visual 2010: de la ciencia básica a la transferencia tecnológica. Madrid, Spain. 2010. *Oral communication.*
9. P. Perez-Merino, L. Ibares-Frías, P. Gallego, S. Del Olmo, F. Parra, M.R. Aguilar, B. Vazquez-Lasa, J. San Román, E. Larra, J. Merayo-Lloves. "Effect of different intracorneal ring composites shift on clinical and optical outcome". Association for Research in Vision and Ophtalmology (ARVO). Fort Lauderdale, FL. 2009. *Poster.*
10. P. Perez-Merino, M.C. Martinez-Garcia, S. Mar-Sardaña, A. Perez- Escudero T. Blanco-Mezquita, J. Merayo-Lloves. "Relationship between the roughness of corneal epithelium and the transmission of light". Association for Research in Vision and Ophtalmology (ARVO). Fort Lauderdale, FL. 2008. *Poster.*

Presented by collaborators

1. N. Alejandre-Alba, P. Pérez-Merino, S. Quintana, P. Pascual, I. Jimenez-Alfaro, S. Marcos. "Scheimpflug-based derived aberrometry before and after implantation of different combinations of ICRS in keratoconus". Association for Research in Vision and Ophtalmology (ARVO). Denver, CO. 2015. *Poster.*
2. C. Dorronsoro, J.R: Alonso-Sanz, D. Pascual, A. Radhakrishnan, M. Velasco-Ocana, P. Pérez-Merino, S. Marcos. "Visual performance and perception with bifocal and trifocal presbyopia corrections simulated using a hand-held simultaneous vision device". Association for Research in Vision and Ophtalmology (ARVO). Denver, CO. 2015. *Poster.*
3. N. Bekesi, P. Pérez-Merino, L. Ibares-Frías, C. Martínez-Garcia, I.E. Kochevar, S. Marcos, "Corneal deformation imaging of Rose-Bengal-green light cross-linked rabbit corneas: *in vivo vs ex vivo* treatments and measurements". Association for Research in Vision and Ophtalmology (ARVO). Denver, CO. 2015. *Poster.*
4. M. Sun, P. Pérez-Merino, S. Duran, I. Jimenez-Alfaro, S. Marcos, "OCT-based ray tracing on pseudophakic eyes to identify optimal IOL centration". Association for Research in Vision and Ophtalmology (ARVO). Denver, CO. 2015. *Poster.*
5. M. Sun, P. Pérez-Merino, A. de Castro, J. Birkenfeld, S. Ortiz, S. Marcos, "Full OCT-based pseudophakic custom computer eye model". Association for Research in Vision and Ophtalmology (ARVO). Orlando, FL. 2014. *Poster.*
6. S. Marcos, S. Ortiz, P. Pérez-Merino, M. Velasco, M. Sun, J. Birkenfeld, S. Durán, I.

Jimenez-Alfaro. “Three-dimensional biometry and alignment in eyes implanted with accommodative-IOLs as a function of accommodative demand”. Association for Research in Vision and Ophtalmology (ARVO). Seattle, WA. 2013. *Oral communication.*

7. S. Ortiz, P. Pérez-Merino, E. Gambra, S. Marcos. “Image analysis and quantification in anterior segment OCT: techniques and applications”. Biomedical Optics. Miami, FL. 2012. *Oral communication.*

8. S. Marcos, S. Ortiz, P. Pérez-Merino. “Quantitative Three-Dimensional anterior segment imaging optical coherence tomography: development and its applications”. 30th European Society of Cataract and Refractive Surgery Meeting. Milan, Italy. 2012. *Oral communication.*

9. S. Marcos, P. Pérez-Merino, C. dorronsoro, L. Llorente, S. Durán, I. Jiménez-Alfaro. “Effect of tilt and decentration of IOL”. 30th European Society of Cataract and Refractive Surgery Meeting. Milan, Italy. 2012. *Oral communication.*

10. S. Marcos, E. Gambra, S. Ortiz, P. Pérez-Merino. “Aberrations of the optical system”. 30th European Society of Cataract and Refractive Surgery Meeting. Milan, Italy. 2012. *Oral communication.*

11. S. Marcos, E. Gambra, S. Ortiz, P. Pérez-Merino. “Accommodation dynamics using high-speed optical coherence tomography”. 7th Accommodation Club. Miami, FL. 2012. *Oral communication.*

12. J. Birkenfeld, A. de Castro, S. Ortiz, P. Pérez-Merino, E. Gambra, S. Marcos. “Three-dimensional reconstrution of the isolated human crystalline lens gradient index distribution”. Association for Research in Vision and Ophtalmology (ARVO). Fort Lauderdale, FL. 2011. *Oral communication.*

13. C. Dorronsoro, D. Pascual, P. Pérez-Merino, S. Kling, S. Marcos. “Medida de la deformación producida por un pulso de aire en corneas normales y en corneas tratadas con cross-linking mediante imagen OCT”. X Reunión Nacional de Óptica. Zaragoza, Spain. 2012. *Oral communication.*

14. S. Ortiz, D. Siedlecki, P. Pérez-Merino, S. Marcos. “Anterior Segment Optical Coherence Tomography (OCT): From Nice Images to Accurate Topography”. Association for Research in Vision and Ophtalmology (ARVO). Fort Lauderdale, FL. 2011. *Oral communication.*

15. J. Birkenfeld, A. de Castro, S. Ortiz, P. Pérez-Merino, E. Gambra, S. Marcos. “Quantitative 3D Imaging of the *in vivo* Crystalline Lens During Accommodation”. Association for Research in Vision and Ophtalmology (ARVO). Fort Lauderdale, FL. 2011. *Oral communication*.

16. S. Ortiz, P. Perez-Merino, E. Gambra, S. Kling, A. de Castro, D. Pascual, I. Grulkwoski, M. Gora, M. Wojtkowski. “Quantitative three-dimensional anterior segment imaging optical coherence tomography: developments and applications”. V European Meeting on Visual and Physiological Optics. Stockholm, Sweden. 2010. *Oral communication.*

17. E. Gambra, S. Ortiz, P. Pérez-Merino, M. Gora, M. Wojtkowski, S. Marcos. “Quantitative 3D Imaging of the *in vivo* Crystalline Lens During Accommodation”. Association for Research in Vision and Ophtalmology (ARVO). Fort Lauderdale, FL. 2010. *Oral communication.*

18. S. Kling, P. Perez-Merino, S. Ortiz, D. Pascual, S. Marcos. “Biomechanical Response to Intraocular Pressure Changes From Scheimpflug and Anterior Segment OCT". Association for Research in Vision and Ophtalmology (ARVO). Fort Lauderdale, FL. 2010. *Oral communication.*

19. J. M. Bueno, E. J. Gualda, A. Giakoumaki, P. Perez-Merino, S. Kling, S. Marcos, P. Artal. "Second Harmonic Imaging of Corneas After Collagen Cross-Linking". Association for Research in Vision and Ophtalmology (ARVO). Fort Lauderdale, FL. 2010. *Poster.*

20. L. Ibares-Frias, P. Perez-Merino, P. Gallego, S. del Olmo, B. Vázquez-Lasa, J. San Román, N. Garagorri, E. Larra, J. Merayo-Lloves, E. Hernandez-Galilea. "Clinical and pathological outcome of new materials for corneal additive surgery". Association for Research in Vision and Ophtalmology (ARVO). Fort Lauderdale, FL. 2009. *Poster.*

21. J. Merayo-Lloves, T. Blanco, J. Hincapié, R. Cantalapiedra, P. Perez-Merino, I. Alcalde, P. Gallego, S. del Olmo-Aguado, L. Ibares-Frias, S. Mar. "Long-term light scattering measurements after corneal collagen cross-linking using riboflavin/UVA treatment (CXL)". Association for Research in Vision and Ophtalmology (ARVO). Fort Lauderdale, FL. 2009. *Poster.*

Invited talks

P. Perez-Merino. "From corneal topography to ZEMAX: Odd cases". IOL Power Club, 11th Scientific Session Agenda. San Sebastian, Spain. 2015.

P. Perez-Merino. "Topografía y aberraciones del segment anterior del ojo: aplicaciones en queratocono y cataratas". Instituto Oftalmológico Fernández Vega. Oviedo, Spain. 2014.

P. Perez-Merino. "Topografía de queratocono por OCT". I Reunión de la Sociedad Gallega de Optometría Clínica. Santiago, Spain. 2012.

P. Perez-Merino. "Fundamentos de OCT". I Reunión de la Sociedad Gallega de Optometría Clínica. Santiago, Spain. 2012.

P. Perez-Merino, "Keratoconus roundtable disccussion group". Association for Research in Vision and Ophtalmology (ARVO). Fort Lauderdale, FL. 2012.

P. Perez-Merino, S. Ortiz, N. Alejandre, I. Jimenez-Alfaro, S. Marcos. "Evaluación del queratocono con OCT cuantitativo". III Congreso Fundacional de la Asociación Española de Tecnología y Cirugía de Implantes, Refractiva y Cornea. Madrid, Spain. 2012.

P. Perez-Merino, T. Blanco-Mezquita, R. Rodriguez-Cantalapiedra, P. Gallego, I. Alcalde, S. del Olmo, M.C. Martinez-Garcia, S. Mar-Sardaña, J. Merayo-Lloves. "Transparencia Corneal tras Cross-Linking en modelo de gallina". I Congreso Fundacional de la Asociación Española de Tecnología y Cirugía de Implantes, Refractiva y Cornea. Madrid, Spain. 2010.

Other information that might be relevant

Panel reviewer 2015 IDEA^2 Madrid-MIT M+Vision Consortium.

S. Ortiz, P. Pérez-Merino, S. Marcos. "Eye biometry using quantitative 3-D OCT", *Optics and Photonics News*; 24(12):31-31.

Book Chapters:

- "Monochromatic aberrations". *Authors:* Susana Marcos, Pablo Pérez-Merino, Carlos Dorronsoro. *Book:* Handbook of visual optics. *Year:* 2015.
- "Biomecánica de la córnea". *Authors:* Jesús Merayo-Lloves, Pablo Pérez-Merino, Nestor Cortes, David Galarreta. *Book:* Técnicas de modelado corneal desde la ortoqueratología hasta el cross-linking. Dr. Julian Cezón. *Editor:* Sociedad Española de Cirugía Ocular Implanto-Refractiva. *Year:* 2009. ISBN: 8493314471, 9788493314477.
- "Transparencia y cicatrización tras cross-linking del colágeno corneal". *Authors:* Jesús Merayo-Lloves, Pablo Pérez-Merino, Tomás Blanco, Janeth Hincapie, Lucía Ibares, Nestor Cortes, David Galarreta, Susana del Olmo, Patricia Gallego, Roberto Cantalapiedra, Carmen Martínez, Santiago Mar. *Book:* Técnicas de modelado corneal desde la ortoqueratología hasta el cross-linking. Dr. Julian Cezón. *Editor:* Sociedad Española de Cirugía Ocular Implanto-Refractiva. *Year:* 2009. ISBN: 8493314471, 9788493314477.

Reviewer in different scientific journals: PLOS One, Biomedical Optics Express, Journal of Cataract and Refractive Surgery, Optometry and Vision Science, European Journal of Ophthalmology, Journal of Optometry.

IOSA (Instituto de Óptica-OSA Student Chapter). Outreach activities.

Honors

Awardee of IDEA^2 Madrid-MIT M+Vision Consortium. NiCO project: smartphone-based corneal topographer (http://mvisionconsortium.mit.edu/2014-idea²-madrid-awardees-announced). 2014.

Awardee in innoSmart European Competition (http://www.innosmart.eu/). 2015.

Bibliography

Ahmad, B. U., Shah, G. K., & Hardten, D. R. (2014). Presbyopia-correcting intraocular lenses and corneal refractive procedures: a review for retinal surgeons. *Retina, 34*(6), 1046-1054.doi: 10.1097/IAE.0000000000000237

Alio, J. L., Pinero, D. P., Aleson, A., Teus, M. A., Barraquer, R. I., Murta, J., . . . Uceda-Montanes, A. (2011). Keratoconus-integrated characterization considering anterior corneal aberrations, internal astigmatism, and corneal biomechanics. *J Cataract Refract Surg, 37*(3), 552-568.doi: 10.1016/j.jcrs.2010.10.046

Alio, J. L., & Shabayek, M. H. (2006). Corneal higher order aberrations: a method to grade keratoconus. *J Refract Surg, 22*(6), 539-545

Alio, J. L., Tavolato, M., De la Hoz, F., Claramonte, P., Rodriguez-Prats, J. L., & Galal, A. (2004). Near vision restoration with refractive lens exchange and pseudoaccommodating and multifocal refractive and diffractive intraocular lenses: comparative clinical study. *J Cataract Refract Surg, 30*(12), 2494-2503.doi: 10.1016/j.jcrs.2004.04.052

Alio, J. L., Vega-Estrada, A., Esperanza, S., Barraquer, R. I., Teus, M. A., & Murta, J. (2014). Intrastromal corneal ring segments: how successful is the surgical treatment of keratoconus? *Middle East Afr J Ophthalmol*, *21*(1), 3-9.doi: 10.4103/0974-9233.124076

Allison, M., & Brennan, N. (1997). The Axis of Astigmatism in Right and Left Eye Pairs. *Optometry and Vision Science, 74*, 668-675

Applegate, R. A., Ballentine, C., Gross, H., Sarver, E. J., & Sarver, C. A. (2003a). Visual acuity as a function of Zernike mode and level of root mean square error. *Optometry and Vision Science*, *80*(2), 97-105

Applegate, R. A., Hilmante, l. G., Howland, H. C., Tu, E. Y., Starck, T., & Zayac, E. J. (2000). Corneal first surface optical aberrations and visual performance. *Journal of Refractive surgery, 16*, 507-514

Applegate, R. A., Marsack, J. D., Ramos, R., & Sarver, E. J. (2003b). Interaction between aberrations to improve or reduce visual performance. *Journal of Cataract and Refractive Surgery*, *29*(8), 1487-1495

Applegate, R. A., Marsack, J. D., & Thibos, L. N. (2006). Metrics of retinal image quality predict visual performance in eyes with 20/17 or better visual acuity. *Optometry and Vision Science*, *83*(9), 635-640

Aramberri, J. (2003). Intraocular lens power calculation after corneal refractive surgery: double-K method. *J Cataract Refract Surg, 29*(11), 2063-2068

Arnulf, A., & Dupuy, O. (1956). Méthode objective pour l'etude des défauts du systéme optique de l'oeil *Problems in contemporary optics* (pp. 330-335): Inst. Naz. Ottica, Arcetri-Firenze.

Artal, P., & Guirao, A. (1998). Contributions of the cornea and the lens to the aberrations of the human eye. *Optics Letters, 23*(21), 1713-1715

Artal, P., Guirao, A., Berrio, E., & Williams, D. R. (2001a). Compensation of corneal aberrations by the internal optics in the human eye. *J Vis, 1*(1), 1-8.doi: 10.1167/1.1.1

Artal, P., Guirao, A., Berrio, E., & Williams, D. R. (2001b). Compensation of corneal aberrations by the internal optics in the human eye. *Journal of Vision., 1*, 1-8. http://journalofvision.org/1/1/1, DOI 10.1167/1161.1161.1161.

Artal, P., Manzanera, S., Piers, P., & Weeber, H. (2010). Visual effect of the combined correction of spherical and longitudinal chromatic aberrations. *Opt Express, 18*(2), 1637-1648.doi: 10.1364/OE.18.001637

Artal, P., & Tabernero, J. (2010). Optics of human eye: 400 years of exploration from Galileo's time. *Appl Opt, 49*(16), D123-130.doi: 10.1364/AO.49.00D123

Atchison, D. A. (1989). Optical design of intraocular lenses .1. On-axis performance. *Optometry and Vision Science*, *66*(8), 492-506

Atchison, D. A. (1991). Design of aspheric intraocular lenses. *Ophthalmic Physiology Optics, 11*(2), 137-146

Atchison, D. A. (1995). Accommodation and presbyopia. *Ophthalmic Physiol Opt, 15*(4), 255-272

Atchison, D. A., & Smith, G. (1995). Continuous gradient index and shell models of the human lens. *Journal of the Optical Society of America A, 14*, 1684-1695

Atchison, D. A., & Smith, G. (2000). *Optics of the Human Eye*. Oxford: Butterworth-Heinemann.

Baldwin, W. R., & Mills, D. (1981). A longitudinal study of corneal astigmatism and total astigmatism. *Am J Optom Physiol Opt, 58*(3), 206-211

Barbero, S., & Marcos, S. (2007). Analytical tools for customized design of monofocal intraocular lenses. http://www.opticsinfobase.org/abstract.cfm?URI=oe-15-14-8576 *Opt Express, 15*, 8576-8591

Barbero, S., Marcos, S., Merayo-Lloves, J., & Moreno-Barriuso, E. (2002a). Validation of the estimation of corneal aberrations from videokeratography in keratoconus. *Journal of Refractive surgery, 18*, 263-270

Barbero, S., Marcos, S., & Merayo-Lloves, J. M. (2002b). Total and corneal aberrations in an unilateral aphakic subject. *Journal of Cataract and Refractive Surgery., 28*, 1594-1600

Barbero, S., Marcos, S., Montejo, J., & Dorronsoro, C. (2011). Design of isoplanatic aspheric monofocal intraocular lenses. *Opt Express, 19*(7), 6215-6230.doi: 10.1364/OE.19.006215

Barbero, S., Marcos, S., & Jimenez-Alfaro, I. (2003). Optical aberrations of intraocular lenses measured in vivo and in vitro. *Journal of the Optical Society of America A., 20*, 1841-1851

Bassnett, S., Shi, Y., & Vrensen, G. F. (2011). Biological glass: structural determinants of eye lens transparency. *Philos Trans R Soc Lond B Biol Sci, 366*(1568), 1250-1264.doi: 10.1098/rstb.2010.0302

Bedford, R. E., & Wyszecki, G. (1957). Axial chromatic aberration of the human eye. *Journal of the Optical Society of America A, 47*, 564-565

Beebe, D. C. (2003). The Lens In: Kaufman PL,Alm A, eds. *Adler´s Physiology of the Eye*. 3 ed. *St. Louis: Mosby*, 117-158

Beems, E. M., & Van Best, J. A. (1990). Light transmission of the cornea in whole human eyes. *Exp Eye Res, 50*(4), 393-395

Beiko, G. (2007). Status of accommodative intraocular lenses. *Curr Opin Ophthalmol, 18*(1), 74-79.doi: 10.1097/ICU.0b013e328011fbab

Beiko, G. H. (2013). Comparison of visual results with accommodating intraocular lenses versus mini-monovision with a monofocal intraocular lens. *J Cataract Refract Surg, 39*(1), 48-55.doi: 10.1016/j.jcrs.2012.08.059

Benedek, G. B. (1971). Theory of transparency of the eye. *Appl Opt, 10*(3), 459-473.doi: 10.1364/AO.10.000459

Bennett, E. S. (2008). Contact lens correction of presbyopia. *Clin Exp Optom, 91*(3), 265-278.doi: 10.1111/j.1444-0938.2007.00242.x

Berrio, E., Tabernero, J., & Artal, P. (2010). Optical aberrations and alignment of the eye with age. *J Vis, 10*(14).doi: 10.1167/10.14.34

Birkenfeld, J., de Castro, A., & Marcos, S. (2014). Contribution of shape and gradient refractive index to the spherical aberration of isolated human lenses. *Invest Ophthalmol Vis Sci, 55*(4), 2599-2607.doi: 10.1167/iovs.14-14201

Birkenfeld, J., de Castro, A., Ortiz, S., Pascual, D., & Marcos, S. (2013). Contribution of the gradient refractive index and shape to the crystalline lens spherical aberration and astigmatism. *Vision Res, 86*, 27-34.doi: 10.1016/j.visres.2013.04.004

Bobier, C. W., & Sivak, J. G. (1978a). Chromoretinoscopy. *Vision research, 18*, 247-250

Bobier, C. W., & Sivak, J. G. (1978b). Chromoretinoscopy. *Vision Res, 18*(3), 247-250

Bolz, M., Prinz, A., Drexler, W., & Findl, O. (2007). Linear relationship of refractive and biometric lenticular changes during accommodation in emmetropic and myopic eyes. *British Journal of Ophthalmology, 91*(3), 360-365

Boote, C., Dennis, S., Huang, Y., Quantock, A. J., & Meek, K. M. (2005). Lamellar orientation in human cornea in relation to mechanical properties. *J Struct Biol, 149*(1), 1-6.doi: 10.1016/j.jsb.2004.08.009

Born, M., & Wolf, E. (1993). *Principles of Optics* (6th ed.). Oxford, U.K.: Pergamon Press.

Bradley, A. (1992). Perceptual Manifestations of Imperfect Optics in the Human Eye: Attempts to Corrects for Ocular Chromatic Aberration. *Optometry and Vision Science, 69*(7), 515-521

Brown, B., Bowman, K. J., & Collins, M. J. (1987). Visual Performance with Multifocal Contact Lenses and Spectacles.

Burns, S., & Marcos, S. (2001). Measurement of image quality with the spatilly resolved refractometer. In S. McRae, R. Krueger & R. Applegate (Eds.), *Customized corneal ablation: The quest for super vision* (pp. 203-209): Stack publising.

Campbell, F. W., & Gubisch, R. W. (1966). Optical quality of the human eye. *Journal of Physiology (London), 186*, 558-578

Canovas, C., & Artal, P. (2011). Customized eye models for determining optimized intraocular lenses power. *Biomed Opt Express, 2*(6), 1649-1662.doi: 10.1364/BOE.2.001649

Colin, J., Cochener, B., Savary, G., & Malet, F. (2000). Correcting keratoconus with intracorneal rings. *J Cataract Refract Surg, 26*(8), 1117-1122

Cumming, J. S., Colvard, D. M., Dell, S. J., Doane, J., Fine, I. H., Hoffman, R. S., . . . Slade, S. G. (2006). Clinical evaluation of the Crystalens AT-45 accommodating intraocular lens: results of the U.S. Food and Drug Administration clinical trial. *J Cataract Refract Surg, 32*(5), 812-825.doi: 10.1016/j.jcrs.2006.02.007

Chalita, M. R., & Krueger, R. R. (2004). Wavefront aberrations associated with the Ferrara intrastromal corneal ring in a keratoconic eye. *J Refract Surg, 20*(6), 823-830

Charman, W. N. (2008). The eye in focus: accommodation and presbyopia. *Clinical and Experimental Optometry, 91*(3), 207-225.doi: 10.1111/j.1444-0938.2008.00256.x

Charman, W. N. (2009). Physiological optics in 2008: standing on Helmholtz's shoulders. *Ophthalmic Physiol Opt, 29*(3), 209-210.doi: 10.1111/j.1475-1313.2009.00668.x

Charman, W. N., & Jennings, J. A. (1976). Objective measurements of the longitudinal chromatic aberration of the human eye. *Vision Res, 16*(9), 999-1005

Chen, L., Kruger, P. B., Hofer, H., Singer, B., & Williams, D. R. (2006). Accommodation with higher-order monochromatic aberrations corrected with adaptive optics. *Journal of the Optical Society of America a-Optics Image Science and Vision, 23*(1), 1-8

Chen, M., & Yoon, G. (2008). Posterior corneal aberrations and their compensation effects on anterior corneal aberrations in keratoconic eyes. *Invest Ophthalmol Vis Sci, 49*(12), 5645-5652.doi: 10.1167/iovs.08-1874

Cheng, X., Bradley, A., Hong, X., & Thibos, L. (2003a). Relationship between refractive error and monochromatic aberrations of the eye. *Optom Vis Sci., 80*, 43-49

Cheng, X., Bradley, A., & Thibos, L. N. (2004). Predicting subjective judgment of best focus with objective image quality metrics. *Journal of Vision, 4*(4), 310-321

Cheng, X., Thibos, L., & Bradley, A. (2003b). Estimating visual quality from wavefront aberration measurements. *J Refract Surg., 19*, 579-584

Chinn, S. R., Swanson, E. A., & Fujimoto, J. G. (1997). Optical coherence tomography using a frequency-tunable optical source. *Opt Lett, 22*(5), 340-342

Choi, M., Weiss, S., Schaeffel, F., Seidemann, A., Howland, H. C., Wilhelm, B., & Wilhelm, H. (2000). Laboratory, clinical, and kindergarten test of a new eccentric infrared photorefractor (PowerRefractor). *Optom Vis Sci, 77*(10), 537-548

Choma, M., Sarunic, M., Yang, C., & Izatt, J. (2003). Sensitivity advantage of swept source and Fourier domain optical coherence tomography. *Opt Express, 11*(18), 2183-2189

Dauwe, C., Touboul, D., Roberts, C. J., Mahmoud, A. M., Kerautret, J., Fournier, P., . . . Colin, J. (2009). Biomechanical and morphological corneal response to placement of intrastromal corneal ring segments for keratoconus. *J Cataract Refract Surg, 35*(10), 1761-1767.doi: 10.1016/j.jcrs.2009.05.033

Daza de Valdés, B. (1623). *Uso de los anteojos*.

de Castro, A., Birkenfeld, J., Maceo, B., Manns, F., Arrieta, E., Parel, J. M., & Marcos, S. (2013). Influence of shape and gradient refractive index in the accommodative changes of spherical aberration in nonhuman primate crystalline lenses. *Invest Ophthalmol Vis Sci, 54*(9), 6197-6207.doi: 10.1167/iovs.13-11996

de Castro, A., Ortiz, S., Gambra, E., Siedlecki, D., & Marcos, S. (2010). Three-dimensional reconstruction of the crystalline lens gradient index distribution from OCT imaging. *Opt Express, 18*(21), 21905-21917.doi: 10.1364/OE.18.021905

de Castro, A., Siedlecki, D., Borja, D., Uhlhorn, S., Parel, J. M., Manns, F., & Marcos, S. (2011). Age-dependent variation of the Gradient Index profile in human crystalline lenses. *J Mod Opt, 58*(19-20), 1781-1787.doi: 10.1080/09500340.2011.565888

Dick, H. B., & Kaiser, S. (2002). [Dynamic aberrometry during accommodation of phakic eyes and eyes with potentially accommodative intraocular lenses]. *Ophthalmologe, 99*(11), 825-834.doi: 10.1007/s00347-002-0737-3

Drexler, W., Baumgartner, A., Findl , O., Hitzenberger, C., & Fercher, A. (1997). Biometric investigation of changes in the anterior eye segment during accomodation. *Vision research, 37*(19), 2789-2800

Drexler, W., Findl, O., Menapace, R., Rainer, G., Vass, C., Hitzenberger, C., & Fercher, A. (1998). Partial coherence interferometry: a novel approach to biometry in cataract surgery. *american journal of ophtalmology, 126*(4), 524-534

Dubbelman, M., & Heijde, V. (2001). The shape of the aging human lens: curvature, equivalent refractive index and the lens paradox. *Vision research, 41*, 1867-1877

Dubbelman, M., Sicam, V. A., & Van der Heijde, G. L. (2006a). The shape of the anterior and posterior surface of the aging human cornea. *Vision Res, 46*(6-7), 993-1001.doi: 10.1016/j.visres.2005.09.021

Dubbelman, M., Sicam, V. A., & van der Heijde, R. G. (2007a). The contribution of the posterior surface to the coma aberration of the human cornea. *J Vis, 7*(7), 10 11-18.doi: 10.1167/7.7.10

Dubbelman, M., Sicam, V. A. D. P., & van der Heijde, R. G. L. (2007b). The contribution of the posterior surface to the coma aberration of the human cornea, http://journalofvision.org/7/7/10/, doi:10.1167/7.7.10. *Journal of Vision, 7*, 1-8

Dubbelman, M., Sicarn, V., & Van der Heijde, G. L. (2006b). The shape of the anterior and posterior surface of the aging human cornea. *Vision research, 46*(6-7), 993-1001

Dubbelman, M., Van der Heijde, G. L., & Weeber, H. A. (2005). Change in shape of the aging human crystalline lens with accommodation. *Vision research, 45*(1), 117-132.doi: 10.1016/j.visres.2004.07.032

Dunne, M. C., Elawad, M. E., & Barnes, D. A. (1996). Measurement of astigmatism arising from the internal ocular surfaces. *Acta Ophthalmol Scand, 74*(1), 14-20

Dupps Jr, W. J., & Wilson, S. E. (2006). Biomechanics and wound healing in the cornea. *Exp Eye Res, 83*(4), 709-720

Einighammer, J., Oltrup, T., Feudner, E., Bende, T., & Jean, B. (2009). Customized aspheric intraocular lenses calculated with real ray tracing. *J Cataract Refract Surg, 35*(11), 1984-1994.doi: 10.1016/j.jcrs.2009.05.053

Elsheikh, A., Alhasso, D., & Rama, P. (2008). Biomechanical properties of human and porcine corneas. *Exp Eye Res, 86*(5), 783-790

Fercher, A. F., Hitzenberger, C. K., Drexler, W., Kamp, G., & Sattmann, H. (1993). In vivo optical coherence tomography. *Am J Ophthalmol, 116*(1), 113-114

Fercher, A. F., Mengedoht, K., & Werner, W. (1988). Eye-length measurement by interferometry with partially coherent light. *Opt Lett, 13*(3), 186-188

Fyodorov, S. N., Galin, M. A., & Linksz, A. (1975). Calculation of the optical power of intraocular lenses. *Invest Ophthalmol, 14*(8), 625-628

Gambra, E., Ortiz, S., Perez-Merino, P., Gora, M., Wojtkowski, M., & Marcos, S. (2013). Static and dynamic crystalline lens accommodation evaluated using quantitative 3-D OCT. *Biomed Opt Express, 4*(9), 1595-1609.doi: 10.1364/BOE.4.001595

Gambra, E., Sawides, L., Dorronsoro, C., & Marcos, S. (2009). Accommodative lag and fluctuations when optical aberrations are manipulated. *J Vis, 9*(6), 4 1-15.doi: 10.1167/9.6.4

Gambra, E., Wang, Y., Yuan, J., Kruger, P. B., & Marcos, S. (2010). Dynamic accommodation with simulated targets blurred with high order aberrations. *Vision Res, 50*(19), 1922-1927.doi: 10.1016/j.visres.2010.06.015

Garner, L. F., & Smith, G. (1997). Changes in equivalent and gradient refractive index of the crystalline lens with accommodation. *Optom Vis Sci, 74*(2), 114-119

Glasser, A. (2008). Restoration of accommodation: surgical options for correction of presbyopia. *Clin Exp Optom, 91*(3), 279-295.doi: 10.1111/j.1444-0938.2008.00260.x

Glasser, A., & Campbell, M. (1998a). Presbyopia and the optical changes in the human crystalline lens with age. *Vision research, 38*(2), 209-229

Glasser, A., & Campbell, M. C. (1998b). Presbyopia and the optical changes in the human crystalline lens with age. *Vision Res, 38*(2), 209-229

Gokhale, N. S. (2013). Epidemiology of keratoconus. *Indian J Ophthalmol, 61*(8), 382-383.doi: 10.4103/0301-4738.116054

Goncharov, A. V., & Dainty, C. (2007). Wide-field schematic eye models with gradient-index lens. *Journal of the Optical Society of America a-Optics Image Science and Vision, 24*(8), 2157-2174

Gorgun, E., Kucumen, R. B., Yenerel, N. M., & Ciftci, F. (2012). Assessment of intrastromal corneal ring segment position with anterior segment optical coherence tomography. *Ophthalmic Surg Lasers Imaging, 43*(3), 214-221.doi: 10.3928/15428877-20120301-01

Grosvenor, T., Quintero, S., & Perrigin, D. M. (1988). Predicting refractive astigmatism: a suggested simplification of Javal's rule. *Am J Optom Physiol Opt, 65*(4), 292-297

Grulkowski, I., Gora, M., Szkulmowski, M., Gorczynska, I., Szlag, D., Marcos, S., . . . Wojtkowski, M. (2009). Anterior segment imaging with Spectral OCT system using a high-speed CMOS camera. *Opt Express, 17*(6), 4842-4858

Grulkowski, I., Liu, J. J., Potsaid, B., Jayaraman, V., Jiang, J., Fujimoto, J. G., & Cable, A. E. (2013). High-precision, high-accuracy ultralong-range swept-source optical coherence tomography using vertical cavity surface emitting laser light source. *Opt Lett, 38*(5), 673-675.doi: 10.1364/OL.38.000673

Grulkowski, I., Liu, J. J., Potsaid, B., Jayaraman, V., Lu, C. D., Jiang, J., . . . Fujimoto, J. G. (2012). Retinal, anterior segment and full eye imaging using ultrahigh speed swept source OCT with vertical-cavity surface emitting lasers. *Biomed Opt Express, 3*(11), 2733-2751.doi: 10.1364/BOE.3.002733

Guirao, A., & Artal, P. (1999a). Corneal aberrations as a function of age. *Investigative Ophthalmology & Visual Science, 40*(4), S535-S535

Guirao, A., & Artal, P. (1999b). Off-axis monochomatic aberrations estimated from double pass measurements in the human eye. *Vision research, 39*(2), 207-217

Guirao, A., Redondo, M., Geraghty, E., Piers, P., Norrby, S., & Artal, P. (2002). Corneal optical aberrations and retinal image quality in patients in whom monofocal intraocular lenses were implanted. *Arch Ophthalmol, 120*, 1143-1151

Guirao, A., Tejedor, J., & Artal, P. (2004). Corneal aberrations before and after small-incision cataract surgery. *Invest Ophthalmol Vis Sci, 45*(12), 4312-4319.doi: 10.1167/iovs.04-0693

Guirao, A., & Williams, D. (2003). A method to predict refractive errors from wave aberration data. *Optom Vis Sci., 80*, 36-42

Gullstrand, A. (1909). Appendix II in: H. von Helmholtz ‘Handbuch der Physiologischen Optik’, 3rd edition, part I.

. 350-358

Hart, R. W., & Farrell, R. A. (1968). Light scattering in the cornea. *Journal of the Optical Society of America A, 59*, 766-775

Hartmann, J. (1900). Bemerkungen über den Bau und die Justierung von Spektrgraphen. *Z Instumentenkd, 20*, 47-58

Hartmann, J. (1904). Objektivuntersuchungen. *Z Instrumentenkd, 24*, 1-32

He, J. C., Burns, S. A., & Marcos, S. (2000a). Monochromatic aberrations in the accommodated human eye. *Vision Res, 40*(1), 41-48

He, J. C., Burns, S. A., & Marcos, S. (2000b). Monochromatic aberrations in the accommodated human eye. *Vision research, 40*, 41-48

He, J. C., & Wang, J. (2014). Measurement of wavefront aberrations and lens deformation in the accommodated eye with optical coherence tomography-equipped wavefront system. *Opt Express, 22*(8), 9764-9773.doi: 10.1364/OE.22.009764

Ho, A., Manns, F., Therese, & Parel, J. M. (2006). Predicting the performance of accommodating intraocular lenses using ray tracing. *J Cataract Refract Surg, 32*(1), 129-136.doi: 10.1016/j.jcrs.2005.07.047

Hofer, H., Artal, P., Singer, B., Aragon, J., & Williams, D. (2001). Dynamics of the eye´s wave aberration. *Journal Optical Society of America A, 18*(3), 497-506

Hoffer, K. J. (1993). The Hoffer Q formula: a comparison of theoretic and regression formulas. *J Cataract Refract Surg, 19*(6), 700-712

Hoffer, K. J., Aramberri, J., Haigis, W., Olsen, T., Savini, G., Shammas, H. J., & Bentow, S. (2015). Protocols for Studies of Intraocular Lens Formula Accuracy. *Am J Ophthalmol*.doi: 10.1016/j.ajo.2015.05.029

Holladay, J., Piers, P., Koranyi, G., van der Mooren, M., & Norrby, N. (2002). A new intraocular lens design to reduce spherical aberration of pseudophakic eyes. *Journal Refractive Surgery, 18*, 683-691

Holladay, J. T., Prager, T. C., Chandler, T. Y., Musgrove, K. H., Lewis, J. W., & Ruiz, R. S. (1988). A three-part system for refining intraocular lens power calculations. *J Cataract Refract Surg, 14*(1), 17-24

Howarth, P. A. (1984). The lateral chromatic aberration of the eye. *Ophthalmology and Physiological Optics, 4*(3), 223-226

Howarth, P. A., & Bradley, A. (1986). The longitudinal chromatic aberration of the human eye, and its correction. *Vision research, 26*, 361-366

Howland, H. C. (2000, Feb 12). *The history and methods of ophthalmic wavefront sensing.* Paper presented at the 1st International Congress of Wavefront Sensing and Aberration-free Refractive Correction, Santa Fe, New Mexico.

Howland, H. C., & Howland, B. (1977). A subjective method for the measurement of the monochromatic aberrations of the eye. *Journal of the Optical Society of America A, 67*, 1508-1518

Huang, D., Swanson, E. A., Lin, C. P., Schuman, J. S., Stinson, W. G., Chang, W., . . . et al. (1991). Optical coherence tomography. *Science, 254*(5035), 1178-1181

Ibn al-Haytham, A. (1028-1038). Kitab al-Manazir (Book of Optics).

Izatt, J. A., Hee, M. R., Swanson, E. A., Lin, C. P., Huang, D., Schuman, J. S., . . . Fujimoto, J. G. (1994). Micrometer-scale resolution imaging of the anterior eye in vivo with optical coherence tomography. *Arch Ophthalmol, 112*(12), 1584-1589

Jakus, M. A. (1962). Further observations on the fine structure of the cornea. *Invest Ophthalmol, 1,* 202-225

Jester, J. V. (2008). Corneal crystallins and the development of cellular transparency. *Seminars in Cell & Developmental Biology, 19*(2), 82-93

Jones, C. E., Atchison, D. A., & Pope, J. M. (2007). Changes in lens dimensions and refractive index with age and accommodation. *Optometry and Vision Science, 84*(10), 990-995

Karnowski, K., Kaluzny, B. J., Szkulmowski, M., Gora, M., & Wojtkowski, M. (2011). Corneal topography with high-speed swept source OCT in clinical examination. *Biomed Opt Express, 2*(9), 2709-2720.doi: 10.1364/BOE.2.002709

Kasthurirangan, S., Markwell, E. L., Atchison, D. A., & Pope, J. M. (2011). MRI study of the changes in crystalline lens shape with accommodation and aging in humans. *J Vis, 11*(3).doi: 10.1167/11.3.19

Keller, P. R., Collins, M. J., Carney, L. G., Davis, B. A., & van Saarloos, P. P. (1996). The relation between corneal and total astigmatism. *Optom Vis Sci, 73*(2), 86-91

Kelly, J. E., Mihashi, T., & Howland, H. C. (2004a). Compensation of corneal horizontal/vertical astigmatism, lateral coma, and spherical aberration by internal optics of the eye. *Journal of Vision, 4*(4), 262-271

Kelly, J. E., Mihashi, T., & Howland, H. C. (2004b). Compensation of corneal horizontal/vertical astigmatism, lateral coma, and spherical aberration by internal optics of the eye. *J Vis, 4*(4), 262-271.doi: 10:1167/4.4.2

Kepler, J. (1604). Ad Vitellionem paralipomena.

Kim, M. J., Zheleznyak, L., Macrae, S., Tchah, H., & Yoon, G. (2011). Objective evaluation of through-focus optical performance of presbyopia-correcting intraocular lenses using an optical bench system. *J Cataract Refract Surg, 37*(7), 1305-1312.doi: 10.1016/j.jcrs.2011.03.033

Klein, S. A. (1997). Axial curvature and the skew ray error in corneal topography. *Optom Vis Sci, 74*(11), 931-944

Kling, S., & Marcos, S. (2013). Finite-element modeling of intrastromal ring segment implantation into a hyperelastic cornea. *Invest Ophthalmol Vis Sci, 54*(1), 881-889.doi: 10.1167/iovs.12-10852

Kling, S., Remon, L., Perez-Escudero, A., Merayo-Lloves, J., & Marcos, S. (2009). *Biomechanical Response of Normal and Cross-linked Porcine Corneas*. Paper presented at the IOVS 2009: ARVO E-Abstract: 5477.

Knupp, C., Pinali, C., Lewis, P. N., Parfitt, G. J., Young, R. D., Meek, K. M., & Quantock, A. J. (2009). The architecture of the cornea and structural basis of its transparency. *Adv Protein Chem Struct Biol, 78*, 25-49.doi: 10.1016/S1876-1623(08)78002-7

Koeppl, C., Findl, O., Menapace, R., Kriechbaum, K., Wirtitsch, M., Buehl, W., . . . Drexler, W. (2005). Pilocarpine-induced shift of an accommodating intraocular lens: AT-45 Crystalens. *J Cataract Refract Surg, 31*(7), 1290-1297.doi: 10.1016/j.jcrs.2005.03.055

Koretz, J., Cook, C., & Kaufman, P. (1997). Accommodation and presbyopia in the human eye. Changes in the anterior segment and crystalline lens with focus. *Invest Ophthalmol Vis Sci., 38*, 569-578.

Kruger, P. B., Mathews, S., Aggarwala, K. R., & Sanchez, N. (1993). Chromatic aberration and ocular focus: Fincham revisited. *Vision Res, 33*(10), 1397-1411

Kruger, P. B., & Pola, J. (1986). Stimuli for accommodation: blur, chromatic aberration and size. *Vision Res, 26*(6), 957-971

Lai, M. M., Tang, M., Andrade, E. M., Li, Y., Khurana, R. N., Song, J. C., & Huang, D. (2006). Optical coherence tomography to assess intrastromal corneal ring segment depth in keratoconic eyes. *J Cataract Refract Surg, 32*(11), 1860-1865.doi: 10.1016/j.jcrs.2006.05.030

Langenbucher, A., Huber, S., Nguyen, N. X., Seitz, B., Gusek-Schneider, G. C., & Kuchle, M. (2003). Measurement of accommodation after implantation of an accommodating posterior chamber intraocular lens. *J Cataract Refract Surg, 29*(4), 677-685

Le Grand, Y. (1956). *Optique Physiologique (Vol. 3); L'espace Visuel* (1 ed. Vol. 3). Paris: Éditions de la Revue d'Optique.

Leng, L., Yuan, Y., Chen, Q., Shen, M., Ma, Q., Lin, B., . . . Lu, F. (2014). Biometry of anterior segment of human eye on both horizontal and vertical meridians during accommodation imaged with extended scan depth optical coherence tomography. *PLoS One, 9*(8), e104775.doi: 10.1371/journal.pone.0104775

Leydolt, C., Neumayer, T., Prinz, A., & Findl, O. (2009). Effect of patient motivation on near vision in pseudophakic patients. *Am J Ophthalmol, 147*(3), 398-405 e393.doi: 10.1016/j.ajo.2008.09.002

Li, X., Yang, H., & Rabinowitz, Y. S. (2009). Keratoconus: classification scheme based on videokeratography and clinical signs. *J Cataract Refract Surg, 35*(9), 1597-1603.doi: 10.1016/j.jcrs.2009.03.050

Li, Y., Meisler, D. M., Tang, M., Lu, A. T., Thakrar, V., Reiser, B. J., & Huang, D. (2008). Keratoconus diagnosis with optical coherence tomography pachymetry mapping. *Ophthalmology, 115*(12), 2159-2166.doi: 10.1016/j.ophtha.2008.08.004

Li, Y., Shekhar, R., & Huang, D. (2006). Corneal pachymetry mapping with high-speed optical coherence tomography. *Ophthalmology, 113*(5), 792-799 e792.doi: 10.1016/j.ophtha.2006.01.048

Li, Y., Tan, O., Brass, R., Weiss, J. L., & Huang, D. (2012). Corneal epithelial thickness mapping by Fourier-domain optical coherence tomography in normal and keratoconic eyes. *Ophthalmology, 119*(12), 2425-2433.doi: 10.1016/j.ophtha.2012.06.023

Liang, J., Grimm, B., Goelz, S., & Bille, J. F. (1994). Objective measurement of wave aberrations of the human eye with the use of a Hartmann-Shack wave-front sensor. *Journal of the Optical Society of America A, 11*, 1949-1957

Liang, J., & Williams, D. R. (1997a). Aberrations and retinal image quality of the normal human eye. *Journal of the Optical Society of America A, 14*, 2873-2883

Liang, J., & Williams, D. R. (1997b). Aberrations and retinal image quality of the normal human eye. *J Opt Soc Am A Opt Image Sci Vis, 14*(11), 2873-2883

Lopez-Gil, N., Iglesias, I., & Artal, P. (1998). Retinal image quality in the human eye as a function of the accommodation. *Vision Res, 38*(19), 2897-2907

Lopez-Gil, N., Rucker, F. J., Stark, L. R., Badar, M., Borgovan, T., Burke, S., & Kruger, P. B. (2007). Effect of third-order aberrations on dynamic accommodation. *Vision research, 47*(6), 755-765

Losada, M. A., & Navarro, R. (1998). Point spread function of the human eye obtained by a dual double-pass method. *Appl Opt, 7*, L7-L13

Loyd, T. L., & Gills, J. P. (1986). Linear regression software for intraocular lens implant power calculation. *Am J Ophthalmol, 102*(3), 405-406

Lyle, W. (1971). Changes in corneal astigmatism with age. *Am J Optom Arch Am Acad Optom, 48*, 467-478

Llorente, L., Diaz-Santana, L., Lara-Saucedo, D., & Marcos, S. (2003). Aberrations of the human eye in visible and near infrared illumination. *Optometry and Vision Science, 80*, 26-35

Macsai, M. S., Padnick-Silver, L., & Fontes, B. M. (2006). Visual outcomes after accommodating intraocular lens implantation. *J Cataract Refract Surg, 32*(4), 628-633.doi: 10.1016/j.jcrs.2006.01.027

Maeda, N., Fujikado, T., Kuroda, T., Mihashi, T., Hirohara, Y., Nishida, K., . . . Tano, Y. (2002). Wavefront aberrations measured with Hartmann-Shack sensor in patients with keratoconus. *Ophthalmology, 109*(11), 1996-2003

Maeda, N., Klyce, S. D., Smolek, M. K., & Thompson, H. W. (1994). Automated keratoconus screening with corneal topography analysis. *Invest Ophthalmol Vis Sci, 35*(6), 2749-2757

Mahajan, V. N. (1994). Zernike circle polynomials and optical aberrations of systems with circular pupil. *Appl Opt, 33*, 8121-8124

Malacara, D., Martin, J., & Sánchez-Mondragón, J. J. (1990). Wavefront fitting with discrete orthogonal polynomials in a unit radius circle. *Optical Engineering, 29*(6), 672-675

Marcos, S., Barbero, S., & Jimenez-Alfaro, I. (2005a). Optical quality and depth-of-field of eyes implanted with spherical and aspheric intraocular lenses. *J Refract Surg, 21*(3), 223-235

Marcos, S., Barbero, S., & Jiménez-Alfaro, I. (2005b). Optical quality and depth-of-field of eyes implanted with spherical and aspheric intraocular lenses. *Journal of Refractive surgery, 21*, 223-235

Marcos, S., Burns, S. A., Moreno-Barriusop, E., & Navarro, R. (1999). A new approach to the study of ocular chromatic aberrations. *Vision Res, 39*(26), 4309-4323

Marcos, S., Burns, S. A., Prieto, P. M., Navarro, R., & Baraibar, B. (2001). Investigating sources of variability of monochromatic and transverse chromatic aberrations across eyes. *Vision research, 41*, 3861-3871

Marcos, S., Díaz-Santana, L., Llorente, L., & Dainty, C. (2002). Ocular aberrations with ray tracing and Shack-Hartmann wavefront sensors: does polarization play a role? *Journal of the Optical Society of America A., 19*, 1063-1072

Marcos, S., Rosales, P., Llorente, L., Barbero, S., & Jiménez-Alfaro, I. (2008). Balance of corneal horizontal coma by internal optics in eyes with intraocular artificial lenses: evidence of a passive mechanism. *Vision Res., 48*, 70-79

Marcos, S., Velasco-Ocana, M., Dorronsoro, C., Sawides, L., Hernandez, M., & Marin, G. (2015). Impact of astigmatism and high-order aberrations on subjective best focus. *J Vis, 15*(11), 4.doi: 10.1167/15.11.4

Marchini, G., Pedrotti, E., Sartori, P., & Tosi, R. (2004). Ultrasound biomicroscopic changes during accommodation in eyes with accommodating intraocular lenses: pilot study and hypothesis for the mechanism of accommodation. *J Cataract Refract Surg, 30*(12), 2476-2482.doi: 10.1016/j.jcrs.2004.04.053

Massig, J. H., Lingelbach, E., & Lingelbach, B. (2005). Videokeratoscope for accurate and detailed measurement of the cornea surface. *Appl Opt, 44*(12), 2281-2287

Mathias, R. T., Rae, J. L., & Baldo, G. J. (1997). Physiological properties of the normal lens. *Physiol Rev, 77*(1), 21-50

Maurice, D. M. (1957). The structure and transparency of the cornea. *J Physiol, 136*(2), 263-286

Mclellan, J., Marcos, S., & Burns, S. (2001). Age-related changes in monochromatic wave aberrations in the human eye. *Investigative Ophthalmology and Visual Science*, 1390-1395

McLellan, J. S., Marcos, S., & Burns, S. A. (1999). The change of the aberrations of the eye with age. *Investigative Opthalmology and Visual Science (Suppl.), 40*, 36

McLellan, J. S., Marcos, S., Prieto, P. M., & Burns, S. A. (2002). Imperfect optics may be the eye's defence against chromatic blur. *Nature, 417*(6885), 174-176.doi: 10.1038/417174a

McLeod, S. D., Vargas, L. G., Portney, V., & Ting, A. (2007). Synchrony dual-optic accommodating intraocular lens. Part 1: optical and biomechanical principles and design considerations. *J Cataract Refract Surg, 33*(1), 37-46.doi: 10.1016/j.jcrs.2006.09.020

Meek, K. M., & Knupp, C. (2015). Corneal structure and transparency. *Prog Retin Eye Res*.doi: 10.1016/j.preteyeres.2015.07.001

Meek, K. M., & Newton, R. H. (1999). Organization of collgen fibrils in the corneal stroma in relation to mechanical properties and surgical practice. *Refractive Surgery, 15*, 695-699

Meek, K. M., Tuft, S. J., Huang, Y., Gill, P. S., Hayes, S., Newton, R. H., & Bron, A. J. (2005). Changes in collagen orientation and distribution in keratoconus corneas. *Invest Ophthalmol Vis Sci, 46*(6), 1948-1956.doi: 10.1167/iovs.04-1253

Mejia-Barbosa, Y., & Malacara-Hernandez, D. (2001). A review of methods for measuring corneal topography. *Optom Vis Sci, 78*(4), 240-253

Michael, R., & Bron, A. J. (2011). The ageing lens and cataract: a model of normal and pathological ageing. *Philos Trans R Soc Lond B Biol Sci, 366*(1568), 1278-1292.doi: 10.1098/rstb.2010.0300

Molebny, V. V., Pallikaris, I. G., Naoumidis, L. P., Chyzh, I. H., Molebny, S. V., & Sokurenko, V. M. (1997). Retina Ray-Tracing technique for eye-refraction mapping. *Proceedings of the SPIE, 2971*, 175-183

Moreno-Barriuso, E., & Navarro, R. (2000). Laser Ray Tracing versus Hartmann-Shack Sensor for Measuring Optical Aberrations in the Human Eye. *Journal of the Optical Society of America A, 17*, 974-985

Morishige, N., Takagi, Y., Chikama, T., Takahara, A., & Nishida, T. (2011). Three-dimensional analysis of collagen lamellae in the anterior stroma of the human cornea visualized by second harmonic generation imaging microscopy. *Invest Ophthalmol Vis Sci, 52*(2), 911-915.doi: 10.1167/iovs.10-5657

Morishige, N., Wahlert, A. J., Kenney, M. C., Brown, D. J., Kawamoto, K., Chikama, T., . . . Jester, J. V. (2007). Second-harmonic imaging microscopy of normal human and keratoconus cornea. *Investigative Ophthalmology & Visual Science, 48*(3), 1087-1094

Morrell, A., Whitefoot, H., & Charman, W. (1991). Ocular chromatic aberration and age. *Ophthalmic Physiol Opt, 11*, 385-390

Naftali, M., & Jabaly-Habib, H. (2013). Depth of intrastromal corneal ring segments by OCT. *Eur J Ophthalmol, 23*(2), 171-176.doi: 10.5301/ejo.5000212

Nagata, T., Kubota, S., Watanabe, I., & Aoshima, S. (1999). [Chromatic aberration in pseudophakic eyes]. *Nihon Ganka Gakkai Zasshi, 103*(3), 237-242

Nakagawa, T., Maeda, N., Higashiura, R., Hori, Y., Inoue, T., & Nishida, K. (2011). Corneal topographic analysis in patients with keratoconus using 3-dimensional anterior segment optical coherence tomography. *J Cataract Refract Surg, 37*(10), 1871-1878.doi: 10.1016/j.jcrs.2011.05.027

Navarro, R., & Losada, M. A. (1997). Aberrations and relative efficiency of light pencils in the living human eye. *Optometry and Vision Science, 74*, 540-547

Navarro, R., Moreno, E., & Dorronsoro, C. (1998). Monochromatic aberrations and point-spread functions of the human eye across the visual field. *Journal of the Optical Society of America A, 15*, 2522-2529

Navarro, R., Rozema, J. J., & Tassignon, M. J. (2013). Optical changes of the human cornea as a function of age. *Optom Vis Sci, 90*(6), 587-598.doi: 10.1097/OPX.0b013e3182928bc6

Negishi, K., Ohnuma, K., Hirayama, N., Noda, T., Policy-Based Medical Services Network Study Group for Intraocular, L., & Refractive, S. (2001). Effect of chromatic aberration on contrast sensitivity in pseudophakic eyes. *Arch Ophthalmol, 119*(8), 1154-1158

Neri, A., Ruggeri, M., Protti, A., Leaci, R., Gandolfi, S. A., & Macaluso, C. (2015). Dynamic imaging of accommodation by swept-source anterior segment optical coherence tomography. *J Cataract Refract Surg, 41*(3), 501-510.doi: 10.1016/j.jcrs.2014.09.034

Nishi, Y., Mireskandari, K., Khaw, P., & Findl, O. (2009). Lens refilling to restore accommodation. *Journal of Cataract and Refractive Surgery, 35*(2), 374-382.doi: 10.1016/j.jcrs.2008.10.054

Nordan, L. T. (1997). Keratoconus: diagnosis and treatment. *Int Ophthalmol Clin, 37*(1), 51-63

Norrby, S., Piers, P., Campbell, C., & van der Mooren, M. (2007). Model eyes for evaluation of intraocular lenses. *Appl Opt, 46*(26), 6595-6605

Novis, C. (2000). Astigmatism and toric intraocular lenses. *Curr Opin Ophthalmol, 11*(1), 47-50

Olsen, T. (2006). Prediction of the effective postoperative (intraocular lens) anterior chamber depth. *J Cataract Refract Surg, 32*(3), 419-424.doi: 10.1016/j.jcrs.2005.12.139

Ortiz, S., Perez-Merino, P., Alejandre, N., Gambra, E., Jimenez-Alfaro, I., & Marcos, S. (2012a). Quantitative OCT-based corneal topography in keratoconus with intracorneal ring segments. *Biomed Opt Express, 3*(5), 814-824.doi: 10.1364/BOE.3.000814

Ortiz, S., Perez-Merino, P., Duran, S., Velasco-Ocana, M., Birkenfeld, J., de Castro, A., . . . Marcos, S. (2013). Full OCT anterior segment biometry: an application in cataract surgery. *Biomed Opt Express, 4*(3), 387-396.doi: 10.1364/BOE.4.000387

Ortiz, S., Perez-Merino, P., Gambra, E., de Castro, A., & Marcos, S. (2012b). In vivo human crystalline lens topography. *Biomed Opt Express, 3*(10), 2471-2488.doi: 10.1364/BOE.3.002471

Ortiz, S., Siedlecki, D., Grulkowski, I., Remon, L., Pascual, D., Wojtkowski, M., & Marcos, S. (2010). Optical distortion correction in optical coherence tomography for quantitative ocular anterior segment by three-dimensional imaging. *Opt Express, 18*(3), 2782-2796.doi: 10.1364/OE.18.002782

Ortiz, S., Siedlecki, D., Perez-Merino, P., Chia, N., de Castro, A., Szkulmowski, M., . . . Marcos, S. (2011). Corneal topography from spectral optical coherence tomography (sOCT). *Biomed Opt Express, 2*(12), 3232-3247.doi: 10.1364/BOE.2.003232

Ortiz, S., Siedlecki, D., Remon, L., & Marcos, S. (2009a). Optical coherence tomography for quantitative surface topography. *Appl Opt, 48*(35), 6708-6715.doi: 10.1364/AO.48.006708

Ortiz, S., Siedlecki, D., Remon, L., & Marcos, S. (2009b). Three-dimensional ray tracing on Delaunay-based reconstructed surfaces. *Appl Opt, 48*(20), 3886-3893

Ostrin, L. A., & Glasser, A. (2004). Accommodation measurements in a prepresbyopic and presbyopic population. *Journal of Cataract and Refractive Surgery, 30*(7), 1435-1444

Pepose, J. S., Wang, D., & Altmann, G. E. (2012). Comparison of through-focus image sharpness across five presbyopia-correcting intraocular lenses. *Am J Ophthalmol, 154*(1), 20-28 e21.doi: 10.1016/j.ajo.2012.01.013

Perez-Escudero, A., Dorronsoro, C., & Marcos, S. (2010). Correlation between radius and asphericity in surfaces fitted by conics. *J Opt Soc Am A Opt Image Sci Vis, 27*(7), 1541-1548.doi: 10.1364/JOSAA.27.001541

Perez-Merino, P., Ortiz, S., Alejandre, N., de Castro, A., Jimenez-Alfaro, I., & Marcos, S. (2014). Ocular and optical coherence tomography-based corneal aberrometry in keratoconic eyes treated by intracorneal ring segments. *Am J Ophthalmol, 157*(1), 116-127 e111.doi: 10.1016/j.ajo.2013.08.017

Perez-Merino, P., Ortiz, S., Alejandre, N., Jimenez-Alfaro, I., & Marcos, S. (2013). Quantitative OCT-based longitudinal evaluation of intracorneal ring segment implantation in keratoconus. *Invest Ophthalmol Vis Sci, 54*(9), 6040-6051.doi: 10.1167/iovs.13-12401

Perez-Merino, P., Parra, F., Ibares-Frias, L., Gallego, P., Vazquez-Lasa, B., Benito, L., . . . Merayo-Lloves, J. (2010). Clinical and pathological effects of different acrylic intracorneal ring segments in corneal additive surgery. *Acta Biomater, 6*(7), 2572-2579.doi: 10.1016/j.actbio.2010.01.014

Phillips, P., Perez-Emmanuelli, J., Rosskothen, H. D., & Koester, C. J. (1988). Measurement of intraocular lens decentration and tilt in vivo. *Journal of Cataract and Refractive Surgery, 14*, 129-135

Piers, P. (2002). Contribution of the cornea and internal surfaces to the change of ocular aberrations with age. *Journal of the opt society america A, 19*(1), 137-143

Piers, P. A., Norrby, N. E., & Mester, U. (2004). Eye models for the prediction of contrast vision in patients with new intraocular lens designs. *Opt Lett, 29*(7), 733-735

Piers, P. A., Weeber, H. A., Artal, P., & Norrby, S. (2007). Theoretical comparison of aberration-correcting customized and aspheric intraocular lenses. *J Refract Surg, 23*(4), 374-384

Pierscionek, B. K. (1996). Aging changes in the optical elements of the eye. *J. Biomed. Opt., 1*, 147-157

Pinero, D. P., Alio, J. L., Aleson, A., Escaf, M., & Miranda, M. (2009a). Pentacam posterior and anterior corneal aberrations in normal and keratoconic eyes. *Clin Exp Optom, 92*(3), 297-303.doi: 10.1111/j.1444-0938.2009.00357.x

Pinero, D. P., Alio, J. L., El Kady, B., Coskunseven, E., Morbelli, H., Uceda-Montanes, A., . . . Pascual, I. (2009b). Refractive and aberrometric outcomes of intracorneal ring segments for keratoconus: mechanical versus femtosecond-assisted procedures. *Ophthalmology, 116*(9), 1675-1687.doi: 10.1016/j.ophtha.2009.05.016

Pinero, D. P., Alio, J. L., Teus, M. A., Barraquer, R. I., & Uceda-Montanes, A. (2010). Modeling the intracorneal ring segment effect in keratoconus using refractive, keratometric, and corneal aberrometric data. *Invest Ophthalmol Vis Sci, 51*(11), 5583-5591.doi: 10.1167/iovs.09-5017

Pinsky, P. M., van der Heide, D., & Chernyak, D. (2005). Computational modeling of mechanical anisotropy in the cornea and sclera. *J Cataract Refract Surg, 31*(1), 136-145.doi: 10.1016/j.jcrs.2004.10.048

Plainis, S., & Pallikaris, I. G. (2006, Sep 07-09). *Ocular monochromatic aberration statistics in a large emmetropic population.* Paper presented at the 3rd European Meeting in Physiological Optics, London, ENGLAND.

Polack, F. M. (1961). Morphology of the cornea. I. Study with silver stains. *Am J Ophthalmol, 51*, 1051-1056

Porter, J., Guirao , A., Cox , I., & Williams, D. (2001). Monochromatic aberrations of the human eye in a large population. *J Opt Soc Am A, 18*(8), 1793-1803

Qin, B., Chen, S., Brass, R., Li, Y., Tang, M., Zhang, X., . . . Huang, D. (2013). Keratoconus diagnosis with optical coherence tomography-based pachymetric scoring system. *J Cataract Refract Surg, 39*(12), 1864-1871

Rabinowitz, Y. S. (1995). Videokeratographic indices to aid in screening for keratoconus. *J Refract Surg, 11*(5), 371-379

Rabinowitz, Y. S. (1998). Keratoconus. *Surv Ophthalmol, 42*(4), 297-319

Rabinowitz, Y. S., Rasheed, K., Yang, H., & Elashoff, J. (1998). Accuracy of ultrasonic pachymetry and videokeratography in detecting keratoconus. *J Cataract Refract Surg, 24*(2), 196-201

Radhakrishnan, H., & Charman, W. N. (2007). Age-related changes in ocular aberrations with accommodation. *J Vis, 7*(7), 11.11-21

Ramasubramanian, V., & Glasser, A. (2015). Can ultrasound biomicroscopy be used to predict accommodation accurately? *J Refract Surg, 31*(4), 266-273.doi: 10.3928/1081597X-20150319-06

Rand, R. H., Howland, H. C., & Applegate, R. A. (1997). Mathematical model of a Placido disk keratometer and its implications for recovery of corneal topography. *Optom Vis Sci, 74*(11), 926-930

Ravikumar, S., Thibos, L. N., & Bradley, A. (2008). Calculation of retinal image quality for polychromatic light. *J Opt Soc Am A Opt Image Sci Vis, 25*(10), 2395-2407

Read, S. A., Collins, M. J., Iskander, D. R., & Davis, B. A. (2009). Corneal topography with Scheimpflug imaging and videokeratography: comparative study of normal eyes. *J Cataract Refract Surg, 35*(6), 1072-1081.doi: 10.1016/j.jcrs.2009.01.020

Reinstein, D. Z., Gobbe, M., Archer, T. J., Silverman, R. H., & Coleman, D. J. (2010). Epithelial, stromal, and total corneal thickness in keratoconus: three-dimensional display with artemis very-high frequency digital ultrasound. *J Refract Surg, 26*(4), 259-271.doi: 10.3928/1081597X-20100218-01

Reinstein, D. Z., Srivannaboon, S., & Holland, S. P. (2001). Epithelial and stromal changes induced by intacs examined by three-dimensional very high-frequency digital ultrasound. *J Refract Surg, 17*(3), 310-318

Ridley, H. (1952). Intra-ocular acrylic lenses; a recent development in the surgery of cataract. *Br J Ophthalmol, 36*(3), 113-122

Roberts, C. (2000). The cornea is not a piece of plastic. *Journal of Refractive surgery, 16*, 407-413

Roorda, A., & Glasser, A. (2004). Wave aberrations of the isolated crystalline lens. *J Vis, 4*(4), 250-261.doi: 10:1167/4.4.1

Rosales, P., Dubbelman, M., Marcos, S., & van der Heijde, R. (2006). Crystalline lens radii of curvature from Purkinje and Scheimpflug imaging. *J Vis, 6*(10), 1057-1067.doi: 10.1167/6.10.5

Rosales, P., & Marcos, S. (2006). Phakometry and lens tilt and decentration using a custom-developed Purkinje imaging apparatus: validation and measurements. *J Opt Soc Am A Opt Image Sci Vis, 23*(3), 509-520

Rosales, P., & Marcos, S. (2007). Customized computer models of eyes with intraocular lenses. *Opt Express, 15*(5), 2204-2218

Rosales, P., & Marcos, S. (2009). Pentacam Scheimpflug quantitative imaging of the crystalline lens and intraocular lens. *J Refract Surg, 25*(5), 421-428

Rosales, P., Wendt, M., Marcos, S., & Glasser, A. (2008). Changes in crystalline lens radii of curvature and lens tilt and decentration during dynamic accommodation in rhesus monkeys. *J Vis, 8*(1), 18 11-12.doi: 10.1167/8.1.18

Ruggeri, M., Uhlhorn, S. R., De Freitas, C., Ho, A., Manns, F., & Parel, J. M. (2012). Imaging and full-length biometry of the eye during accommodation using spectral domain OCT with an optical switch. *Biomed Opt Express, 3*(7), 1506-1520.doi: 10.1364/BOE.3.001506

Rynders, M., Lidkea, B., Chisholm, W., & Thibos, L. N. (1995). Statistical distribution of foveal transverse chromatic aberration, pupil centration, and angle psi in a population of young adult eyes. *J Opt Soc Am A Opt Image Sci Vis, 12*(10), 2348-2357

Saad, A., & Gatinel, D. (2010). Topographic and tomographic properties of forme fruste keratoconus corneas. *Invest Ophthalmol Vis Sci, 51*(11), 5546-5555.doi: 10.1167/iovs.10-5369

Salmon, T. O., West, R. W., Gasser, W., & Kenmore, T. (2003). Measurement of refractive errors in young myopes using the COAS Shack-Hartmann aberrometer. *Optom Vis Sci, 80*(1), 6-14

Sanders, D., Retzlaff, J., Kraff, M., Kratz, R., Gills, J., Levine, R., . . . Loyd, T. (1981). Comparison of the accuracy of the Binkhorst, Colenbrander, and SRK implant power prediction formulas. *J Am Intraocul Implant Soc, 7*(4), 337-340

Sanders, D. R., Retzlaff, J., & Kraff, M. C. (1988). Comparison of the SRK II formula and other second generation formulas. *J Cataract Refract Surg, 14*(2), 136-141

Sanders, D. R., Retzlaff, J. A., Kraff, M. C., Gimbel, H. V., & Raanan, M. G. (1990). Comparison of the SRK/T formula and other theoretical and regression formulas. *J Cataract Refract Surg, 16*(3), 341-346

Savini, G., & Hoffer, K. J. (2011). IOL power after excimer laser surgery. *Ophthalmology, 118*(8), 1691-1692.doi: 10.1016/j.ophtha.2011.04.004

Schlegel, Z., Lteif, Y., Bains, H. S., & Gatinel, D. (2009). Total, corneal, and internal ocular optical aberrations in patients with keratoconus. *J Refract Surg, 25*(10 Suppl), S951-957.doi: 10.3928/1081597X-20090915-10

Schoneveld, P., Pesudovs, K., & Coster, D. J. (2009). Predicting visual performance from optical quality metrics in keratoconus. *Clin Exp Optom, 92*(3), 289-296.doi: 10.1111/j.1444-0938.2009.00372.x

Shabayek, M. H., & Alio, J. L. (2007). Intrastromal corneal ring segment implantation by femtosecond laser for keratoconus correction. *Ophthalmology, 114*(9), 1643-1652.doi: 10.1016/j.ophtha.2006.11.033

Shack, R., Platt, B. (1971). Production and use of a lenticular Hartmann screen. *J. Opt. Soc. Am., 61*, 656

Shankar, H., Taranath, D., Santhirathelagan, C. T., & Pesudovs, K. (2008). Repeatability of corneal first-surface wavefront aberrations measured with Pentacam corneal topography. *J Cataract Refract Surg, 34*(5), 727-734.doi: 10.1016/j.jcrs.2007.11.056

Shao, Y., Tao, A., Jiang, H., Mao, X., Zhong, J., Shen, M., . . . Wang, J. (2015). Age-related changes in the anterior segment biometry during accommodation. *Invest Ophthalmol Vis Sci, 56*(6), 3522-3530.doi: 10.1167/iovs.15-16825

Shen, M., Wang, M. R., Yuan, Y., Chen, F., Karp, C. L., Yoo, S. H., & Wang, J. (2010). SD-OCT with prolonged scan depth for imaging the anterior segment of the eye. *Ophthalmic Surg Lasers Imaging, 41 Suppl*, S65-69.doi: 10.3928/15428877-20101031-18

Sicam, V., Dubbelman, M., & van der Heijde, R. G. L. (2006). Spherical aberration of the anterior and posterior surface of the human cornea. *Journal of the Optical Society of America a-Optics Image Science and Vision, 23*(3), 544-549

Sicam, V., & Van der Heijde, R. G. L. (2006). Topographer reconstruction of the nonrotation-symmetric anterior corneal surface features. *Optometry and Vision Science, 83*(12), 910-918

Siedlecki, D., de Castro, A., Gambra, E., Ortiz, S., Borja, D., Uhlhorn, S., . . . Parel, J. M. (2012). Distortion correction of OCT images of the crystalline lens: gradient index approach. *Optom Vis Sci, 89*(5), E709-718.doi: 10.1097/OPX.0b013e3182508344

Siedlecki, D., & Ginis, H. S. (2007). On the longitudinal chromatic aberration of the intraocular lenses. *Optom Vis Sci, 84*(10), 984-989.doi: 10.1097/OPX.0b013e318157ac82

Simonet, P., & Campbell, M. C. W. (1990). The optical transverse chromatic aberration on the fovea of the human eye. *Vision research, 30*(2), 187-206

Smirnov, M. S. (1961). Measurement of the wave aberration of the human eye. *Biofizika, 6*, 687-703

Smith, G., & Atchison, D. (2001). The gradient index and spherical aberration of the lens of the human eye. *Ophthalmology physiology optics, 21*(4), 317-326

Sogutlu, E., Pinero, D. P., Kubaloglu, A., Alio, J. L., & Cinar, Y. (2012). Elevation changes of central posterior corneal surface after intracorneal ring segment implantation in keratoconus. *Cornea, 31*(4), 387-395.doi: 10.1097/ICO.0b013e31822481df

Spoerl, E., Huhle, M., & Seiler, T. (1998). Induction of Cross-links in Corneal Tissue. *Exp Eye Res, 66*(1), 97-103

Stachs, O., Schneider, H., Beck, R., & Guthoff, R. (2006). Pharmacological-induced haptic changes and the accommodative performance in patients with the AT-45 accommodative IOL. *J Refract Surg, 22*(2), 145-150

Sun, M., Birkenfeld, J., de Castro, A., Ortiz, S., & Marcos, S. (2014). OCT 3-D surface topography of isolated human crystalline lenses. *Biomed Opt Express, 5*(10), 3547-3561.doi: 10.1364/BOE.5.003547

Swanson, E. A., Izatt, J. A., Hee, M. R., Huang, D., Lin, C. P., Schuman, J. S., . . . Fujimoto, J. G. (1993). In vivo retinal imaging by optical coherence tomography. *Opt Lett, 18*(21), 1864-1866

Szalai, E., Berta, A., Hassan, Z., & Modis, L., Jr. (2012). Reliability and repeatability of swept-source Fourier-domain optical coherence tomography and Scheimpflug imaging in keratoconus. *J Cataract Refract Surg, 38*(3), 485-494.doi: 10.1016/j.jcrs.2011.10.027

Tabernero, J., Benito, A., Alcon, E., & Artal, P. (2007). Mechanism of compensation of aberrations in the human eye. *Journal of the Optical Society of America a-Optics Image Science and Vision, 24*(10), 3274-3283

Tabernero, J., Piers, P., Benito, A., Redondo, M., & Artal, P. (2006). Predicting the optical performance of eyes implanted with IOLs to correct spherical aberration. *Invest Ophthalmol Vis Sci, 47*(10), 4651-4658.doi: 10.1167/iovs.06-0444

Tahir, H. J., Tong, J. L., Geissler, S., Vedamurthy, I., & Schor, C. M. (2010). Effects of accommodation training on accommodation and depth of focus in an eye implanted with a crystalens intraocular lens. *J Refract Surg, 26*(10), 772-779.doi: 10.3928/1081597X-20100921-02

Tang, M., Li, Y., Avila, M., & Huang, D. (2006). Measuring total corneal power before and after laser in situ keratomileusis with high-speed optical coherence tomography. *Journal of Cataract and Refractive Surgery, 32*, 1843-1850

Thibos, L., & Hong, X. (1999). *Comparison of monochromatic aberrations of the human eye measured with the Howland crossed-cylinder aberroscope and the Shack-Hartmann aberrometer.* Paper presented at the Technical Digest Optical Society of America Annual Meeting, Santa Clara, California (USA).

Thibos, L. N., Bradley, A., Still, D. L., Zhang, X., & Howarth, P. A. (1990). Theory and measurement of ocular chromatic aberration. *Vision Res, 30*(1), 33-49

Thibos, L. N., Bradley, A., & Zhang, X. X. (1991). Effect of ocular chromatic aberration on monocular visual performance. *Optom Vis Sci, 68*(8), 599-607

Thibos, L. N., Faao, P., & Xin Hong, M. (1999). Clinical applications of the Shack-Hartmann aberrometer. *Optometry and Vision Science, 76*, 817-825

Thibos, L. N., Hong, X., Bradley, A., & Applegate, R. A. (2004a). Accuracy and precision of objective refraction from wavefront aberrations. *Journal of Vision, 4*(4), 329-351

Thibos, L. N., Hong, X., Bradley, A., & Applegate, R. A. (2004b). Accuracy and precision of objective refraction from wavefront aberrations. *J Vis, 4*(4), 329-351.doi: 10.1167/4.4.9

Thibos, L. N., & Horner, D. (2001). Power vector analysis of the optical outcome of refractive surgery. *J Cataract Refract Surg, 27*(1), 80-85

Tomidokoro, A., Oshika, T., Amano, S., Higaki, S., Maeda, N., & Miyata, K. (2000). Changes in anterior and posterior corneal curvatures in keratoconus. *Ophthalmology, 107*(7), 1328-1332

Torquetti, L., Ferrara, G., Almeida, F., Cunha, L., Araujo, L. P., Machado, A., . . . Ferrara, P. (2014). Intrastromal corneal ring segments implantation in patients with keratoconus: 10-year follow-up. *J Refract Surg, 30*(1), 22-26

Torquetti, L., & Ferrara, P. (2010). Intrastromal corneal ring segment implantation for ectasia after refractive surgery. *J Cataract Refract Surg, 36*(6), 986-990.doi: 10.1016/j.jcrs.2009.12.034

Trokel, S. (1962). The physical basis for transparency of the crystalline lens. *Invest Ophthalmol, 1*, 493-501

Truscott, R. J., & Zhu, X. (2010). Presbyopia and cataract: a question of heat and time. *Prog Retin Eye Res, 29*(6), 487-499.doi: 10.1016/j.preteyeres.2010.05.002

Tucker, J., & Rabie, E. P. (1980). Depth-of-focus of the pseudophakic eye. *Br J Physiol Opt, 34*, 12-21

Uhlhorn, S. R., Borja, D., Manns, F., & Parel, J. M. (2008). Refractive index measurement of the isolated crystalline lens using optical coherence tomography. *Vision Res, 48*(27), 2732-2738.doi: 10.1016/j.visres.2008.09.010

van der Mooren, M., Steinert, R., Tyson, F., Langeslag, M. J., & Piers, P. A. (2015). Explanted multifocal intraocular lenses. *J Cataract Refract Surg, 41*(4), 873-877.doi: 10.1016/j.jcrs.2015.02.005

Vega-Estrada, A., Alio, J. L., Brenner, L. F., & Burguera, N. (2013). Outcomes of intrastromal corneal ring segments for treatment of keratoconus: five-year follow-up analysis. *J Cataract Refract Surg, 39*(8), 1234-1240.doi: 10.1016/j.jcrs.2013.03.019

Vega-Estrada, A., Alio, J. L., & Plaza-Puche, A. B. (2015). Keratoconus progression after intrastromal corneal ring segment implantation in young patients: Five-year follow-up. *J Cataract Refract Surg, 41*(6), 1145-1152.doi: 10.1016/j.jcrs.2014.08.045

Vinas, M., Dorronsoro, C., Cortes, D., Pascual, D., & Marcos, S. (2015). Longitudinal chromatic aberration of the human eye in the visible and near infrared from wavefront sensing, double-pass and psychophysics. *Biomed Opt Express, 6*(3), 948-962.doi: 10.1364/BOE.6.000948

Von Helmholtz, H. (1909). *Helmholtz's Treatise on Physiological Optics*. New York: Optical Society of America.

Wang, L., Canovas, C., Weeber, H. A., Piers, P. A., & Koch, D. D. (2012). Aspheric intraocular lenses. *Ophthalmology, 119*(6), 1284; author reply 1285.doi: 10.1016/j.ophtha.2012.02.020

Wardrop, J. (1808). Essays on the Morbid Anatomy of the Human Eye.

Weeber, H. A., & Piers, P. A. (2012). Theoretical performance of intraocular lenses correcting both spherical and chromatic aberration. *J Refract Surg, 28*(1), 48-52.doi: 10.3928/1081597X-20111103-01

Wojtkowski, M., Bajraszewski, T., Targowski, P., & Kowalczyk, A. (2003). Real-time in vivo imaging by high-speed spectral optical coherence tomography. *Opt Lett, 28*(19), 1745-1747

Wojtkowski, M., Leitgeb, R., Kowalczyk, A., Bajraszewski, T., & Fercher, A. F. (2002). In vivo human retinal imaging by Fourier domain optical coherence tomography. *J Biomed Opt, 7*(3), 457-463.doi: 10.1117/1.1482379

Wolffsohn, J. S., Davies, L. N., Gupta, N., Naroo, S. A., Gibson, G. A., Mihashi, T., & Shah, S. (2010). Mechanism of action of the tetraflex accommodative intraocular lens. *J Refract Surg, 26*(11), 858-862.doi: 10.3928/1081597X-20100114-04

Wride, M. A. (2011). Lens fibre cell differentiation and organelle loss: many paths lead to clarity. *Philos Trans R Soc Lond B Biol Sci, 366*(1568), 1219-1233.doi: 10.1098/rstb.2010.0324

Yoon, G. Y., & Williams, D. R. (2002). Visual performance after correcting the monochromatic and chromatic aberrations of the eye. *J Opt Soc Am A Opt Image Sci Vis, 19*(2), 266-275

Young, T. (1801). On the mechanisms of the eye. *Phil. Trans. Royal Society, 19,* 23-88

Yuen, L., Trattler, W., & Boxer Wachler, B. S. (2008). Two cases of Z syndrome with the Crystalens after uneventful cataract surgery. *J Cataract Refract Surg, 34*(11), 1986-1989.doi: 10.1016/j.jcrs.2008.05.061

Yun, S., Tearney, G., de Boer, J., Iftimia, N., & Bouma, B. (2003). High-speed optical frequency-domain imaging. *Opt Express, 11*(22), 2953-2963

Zamora-Alejo, K. V., Moore, S. P., Parker, D. G., Ullrich, K., Esterman, A., & Goggin, M. (2013). Objective accommodation measurement of the Crystalens HD compared to monofocal intraocular lenses. *J Refract Surg, 29*(2), 133-139.doi: 10.3928/1081597X-20130117-09

Zernike, F. (1934). Beugungstheorie des schneidenverfahrens und seiner verbesserten form, des phasenkontrastmethode. *Physica, 1*, 689-704

Zhang, X. X., Bradley, A., & Thibos, L. N. (1991). Achromatizing the human eye: the problem of chromatic parallax. *J Opt Soc Am A, 8*(4), 686-691

Zhao, H., & Mainster, M. A. (2007). The effect of chromatic dispersion on pseudophakic optical performance. *Br J Ophthalmol, 91*(9), 1225-1229.doi: 10.1136/bjo.2007.118745

Zhao, M., Kuo, A. N., & Izatt, J. A. (2010). 3D refraction correction and extraction of clinical parameters from spectral domain optical coherence tomography of the cornea. *Opt Express, 18*(9), 8923-8936.doi: 10.1364/OE.18.008923

Zheleznyak, L., Kim, M. J., MacRae, S., & Yoon, G. (2012). Impact of corneal aberrations on through-focus image quality of presbyopia-correcting intraocular lenses using an adaptive optics bench system. *J Cataract Refract Surg, 38*(10), 1724-1733.doi: 10.1016/j.jcrs.2012.05.032

Zhu, Z., Janunts, E., Eppig, T., Sauer, T., & Langenbucher, A. (2011). Tomography-based customized IOL calculation model. *Curr Eye Res, 36*(6), 579-589.doi: 10.3109/02713683.2011.566978

Acknowledgements

"Cuando yo salí del pueblo, hace ya la friolera de cuarenta y ocho años, me topé con el Aniano, el Corsario, bajo el chopo del Elicio, frente al palomar de la Tía Zenona, ya en el camino de Pozal de la Culebra. Y el Aniano se vino a mí y me dijo: ¿Dónde va el estudiante? Y yo le dije, ¡Qué sé yo! Lejos. ¿Por tiempo? Dijo él. Y yo le dije: Ni lo sé.

Miguel Delibes, Viejas historias de Castilla la Vieja

Bien podría ser la historia de cualquiera que sale de casa y empieza su camino. Yo no es que me fuera muy lejos, de hecho, en los tiempos que corren, Madrid podría considerarse un barrio de la periferia, todo es cuestión de desplazar el centro (y ya lo hicieron a lo largo de la historia poniendo otra esfera de referencia). El caso es que después de unos cuantos años por Valladolid, salí (la friolera fue de veintitantos) y Susana me acogió en su laboratorio, en su familia del VioBio (Visual Optics and Biophotonics) Lab. Y aquí empieza esta parte del camino hacia Ítaca, el de la tesis, donde he conocido a la gente más especial de mi vida. Sin ellos, y sin los que ya estaban, claro, esto no podría ser.

Susana (S. Marcos), muchas gracias, muchas gracias de todo corazón. Aún recuerdo tu llamada un día de mayo de 2009, estaba en el coche y paré donde pude, al volver a arrancar puse a todo volumen *"ring the bells"* y de lo contento que estaba me canté toda la canción con la ventanilla bajada. Me iba a trabajar a tu laboratorio. Para mí, tu laboratorio, el Instituto de Óptica, el CSIC, era un sueño. En realidad, cada paso dado desde que crucé la puerta del IO ha estado acompañado por pequeños sueños. Así que muchas gracias por confiar en mí, abrir esa puerta y dejarla abierta. El grupo es referencia mundial en Óptica Visual, en Ciencia, y en Ciencia nadie te pone, te haces. La Ciencia no son científicos que se equivocan y aciertan. La Ciencia es trabajo, pasión, valentía, ingenio, constancia, inteligencia, educación, aprendizaje, confianza y también curiosidad. Es lo que es. Y yo, he tenido la suerte cada día de ver, tocar y sentir Ciencia en el Instituto de Óptica. Te debo mucho a ti. Gracias, Susana, por dejar que aprenda cada día a tu lado.

Jesús (J. Merayo). Más que un guía, un mentor, un gran científico (mira que es grande lo que estás haciendo en la Fundación Fernández-Vega), un viticultor incluso y un excelente oftalmólogo, es un gran amigo. Contigo compartí las primeras discusiones científicas y disfruté de los primeros ARVO. Confiaste en mí desde el principio y gracias a ti puedo escribir estas líneas en el Instituto de Óptica. Sabes que no tengo palabras suficientes para agradecerte todos estos años y sabes, también, que con los ojos cerrados te seguiría donde fuera. Este trabajo también es tuyo. Muchas gracias, Jesús.

Carmen (C. Martínez) y Santiago (S. Mar). Los dos profesores de este camino, Carmen en Medicina, Santiago en Físicas. Una perfecta conjunción. Mis padres científicos. Mi primer paper fue fruto de aquel trabajo de fin de master. A ti, Carmen, qué te puedo decir, que eres como una madre y una amiga. ¡Muchas gracias!

Carlos (C. Dorronsoro). Desde que me abrieron la puerta del IO soy incapaz de cerrarla y desde que me abriste la del despacho no soy capaz de salir, y, lo cierto, es que no dejo de asombrarme ni un solo momento con tu trabajo y sacrificio. También, aunque esto ya no es sorpresa, admiro como buscas nuevos desafíos y nuevas metas implicando a todos. No sé de dónde sacas las fuerzas y las ideas, pero me encanta. Las cenas, cervezas, conciertos (Smashing, Muse, Subterfuge, Vistillas y, como no, Nada Surf), excursiones nocturnas (la mítica Peñalara y el paseo por las Rocky), carreras (la del CSIC y la de Central Park) quedan grabadas. Gracias por compartir tanto en este despacho, en el labo y fuera del CSIC.

Enrique (E. Gambra), Alfonso (A. Pérez-Escudero), Sam (S. Arba-Mosquera). La inquietud y curiosidad por descubrir el maravilloso mundo de la Investigación tuvo un brote esplendoroso con vosotros vagando por distintas ciudades. Sí, sí, con vosotros, ¡qué tres físicos!. Enrique, tú, que fuiste como un hermano mayor en mi primer día de colegio, como una madre en Santa Juliana (cenas, intermedios, conversaciones, qué a gustito estábamos en el sofá rojo…) y como un padre en el laboratorio. Tú, que serás un gran compañero en todo momento. Muchas gracias.

María (M. Vinas). Porque me encanta como eres. Porque la vida hay que vivirla como lo haces tú. Porque afrontas los contratiempos y los resuelves. Porque te puedo preguntar cualquier duda. Porque tienes una capacidad de trabajo tremenda. Porque has desarrollado un setup increíble. Porque eres espectacular y divina. Porque eres luchadora y comprometida. Porque quiero salir a la calle y brindar contigo. Porque escribiendo esto me veo en Chueca, Malasaña, NY, Denver, Zurich y Miami Beach. Porque estés donde estés. Porque ahora mismo te daría un abrazo. Futura Dra. Viñas para mí eres el ejemplo de lo que es trabajo en Investigación.

Dani (D. Cortés). Dani no es negociable. Nos guardamos unos cuantos secretos, unos cuantos vídeos, muchas vivencias y los días más importantes de nuestras vidas con un mes de diferencia. Contigo he compartido Madrid. Sé que compartiremos muchos momentos en uno y otro lado del charco (ahí tienes tu sueño). Sé que lo esencial es invisible a los ojos. Sé que eres especial y amarillo.

Alberto (A. de Castro) y Lucie (L. Sawides). Ay, Alber y Lucie. Recuerdo como con envidia espiaba vuestros pasos subiendo López de Hoyos, Alberto gesticulando y Lucie sonriendo. Los dos llenasteis de unión el grupo y de planes los días. Alberto, las palabras que escuché a Fabrice Manns decir sobre ti me parecieron las más bonitas que he escuchado sobre un doctorando. Tú has tenido una paciencia increíble enseñando a un zote algo de Zemax y Matlab, entre muchísimas otras cosas. Dr. de Castro, muchas gracias. Dra. Sawides, mi boca se abre sola al ver la alegría y seguridad que tienes al dar las charlas, nunca quites tu sonrisa. Menudo tándem.

Lourdes (L. Llorente). No coincidimos todo lo que me hubiera gustado en el IO, pero sí lo suficiente como para saber que hubiera trabajado a tu lado muy a gusto. Menos mal que siempre hay buenas excusas para un mensaje, un wasap y un buen encuentro, seguro que pronto llegarán muchos más encuentros.

Dani (D. Pascual). Tío, tú estás por encima del bien, tú has hecho la mili, tú has echado el cuerpo a tierra y te has partido un piño. Si me garantizan que haciéndola podría llegar a una mínima parte de todo lo que sabes mañana mismo iría a filas. Lástima que no sea así. Verte trabajar y ver como con tanta paciencia nos explicas lo que no sabemos bien merece la pena el día. Dani, eres un gran ejemplo para todos, para todo.

Sergio (S. Barbero). Además de ser un Científico como la copa de un pino eres una persona increíble. Cuando discutimos algo sobre óptica, algo a lo que no llegamos, siempre decimos, vamos a preguntar a Sergio, que lo sabe todo. Muchas gracias por tener siempre la puerta abierta y la respuesta. Muchas gracias por el primer EMVPO de Estocolmo y por todas las excursiones. Estar contigo es como observar al atardecer el rayo verde en el horizonte en cualquier pico de la sierra madrileña, un placer infinito.

Pablo (P. de Gracia). No puedo olvidar tus historias, tu carácter, tu originalidad, pabladas y lazos sorianos. Personaje único, si ya lo dice “*el mundo*”.

Judith (J. Birkenfeld). Estoy seguro que sigues bailando y riendo por los lab del MIT. En los del IO nunca sabías lo que había al otro lado de la puerta.

Jorge (J. Lamela). Qué alegría de tío, solo te veo con una sonrisa en estos momentos. Que sea siempre así.

Damian (D. Siedlecki). Great Damian! What can I possibly say?!? I am glad you stood in my way. Dzięki! Thanks for being the first reviewer of this manuscript (OCT team). You are a great friend.

Sabine (S. Kling), Danke!. Mengchan (M. Sun), Xièyi! 謝意. Aishu (A. Radhakrishnan), Nanri! धन्यवाद. Nandor (N. Bekesi), Köszönet!. Andrés (A. de la Hoz), ¡Gracias!. James, Vyas, Hrebesh. Thanks to all of you for the great opportunity to work with you in an incredible international atmosphere and my sincere gratitude for all the time spent (site/non site). Enrique (E. Bustos), Belén, muchas gracias por todo. Contigo, Enrique, seguiré pateando el asfalto.

Sonia (S. Durán), Iñigo (I. Jiménez-Alfaro). Tener tan cerca y tan accesibles a tan grandes oftalmólogos es fantástico. Muchas gracias por todo. Sonia, vente al IO cuando quieras, aún recuerdo con una sonrisa la historia del saxo.

Miriam (M. Velasco-Ocana). Nos hemos ido juntando poco a poco y a día de hoy agradezco esa proximidad y confianza. Miriam, tú completas lo que falta, organizas el caos y uno se encuentra cómodo, como en casa. Eres una gran compañera, una buena amiga y tienes una valía increíble. Has hecho especial estos años. ¡Qué de cosas están por venir!

Edu (-ez^2, E. Martínez-Enríquez). Si es que contigo me quedaría hablando toda una vida, aunque no siempre te mire a los ojos. Haces accesible lo incomprensible, cercano el procesado de imágenes, surrealistas las conversaciones y mágico el día. Qué fácil es trabajar contigo. Qué fácil es estar contigo.

Nico (N. Alejandre). Lo cierto es que cada semana estoy esperando que llegue el miércoles para poder verte y charlar un rato, ya sea de ojos, política, educación, ciclismo, basket, sueños, ideas, el NiCO. Ojalá, algún día llevemos a cabo todas las ideas imaginadas. Eres prota en este doc y en todo este tiempo. Eres un gran amigo, esta tesis también es tuya. ¡Muchas gracias!

Sergio (S. Ortiz). Compañero de labo, de OCT, de faena, de vida. El procesado de las medidas de OCT ha sido posible gracias a tu gran trabajo. Hace poco escuché a Santamaría contar como él y Bescós, compañeros en el labo y muy distintos en carácter, fraguaron una amistad que aún les dura (y ya van años). Tanto en el labo como fuera hemos contado el uno con el otro, hace poco más de dos años y a esta misma hora estábamos por Valladolid mano a mano y hasta aquí puedo escribir. Ay, maño, por este camino todavía nos quedan muchos paseos, confesiones, canciones, charlas y mucho camino. Gracias de todo corazón, Sergio.

Llegado aquí, solo puedo escribir, muchas gracias VioBio Lab. ¡Qué de momentos vividos!

No me puedo olvidar de todos los pacientes de la Fundación Jiménez-Díaz que desinteresadamente aguantaron unas cuantas horas de medidas en los distintos estudios. Sin ellos, este trabajo no hubiera sido posible.

Los del GPL, los silenciosos, los del ondiñas. Antonio, no sé que tienes que tanto atraes, majo, contigo las horas uno las echa muy tranquilamente. Giorgio, todavía me duele el cuello de las veces que he mirado para arriba para hablar contigo (percheroooo). Andrés, algún día me encantaría explicar mi trabajo con la pasión que tú pones. Puerto, a ojos cerrados te votaría. Jan, para cuándo la próxima. Mario, ilacixem, la alegría del otro lado del pasillo. También me acuerdo de aquellos amigos y compañeros del primer año en el IO. Elena Gil, Rafa (Vali), Jose Rodrigo. Aquel despacho que con tanta curiosidad miraba al cruzar el pasillo. Aquellos días culturales. Aquellas largas conversaciones.

Eloy, Chari, Encarnita, Jose Luis. ¡Qué buen equipo!

Patricia (P. Gallego), Lucía (L. Ibares), Rober (R. Cantalapiedra), Nacho (I. Alcalde), Susana (S. del Olmo), Tomás (T. Blanco), Iván (I. Fernández). Parte de los sueños que comenzamos hace ya unos años hacen parada con la tesis. Mi sincero agradecimiento y enhorabuena a todos vosotros.

Como no, el IOBA, institución ejemplar que ha puesto a Valladolid en un lugar de referencia en Oftalmología. Es de admirar la fuerza, ilusión y creatividad de su director (J.C. Pastor) y su equipo. Yolanda (Y. Diebold), recuerdo ahora la conversación que tuvimos al terminar el máster, ya ves. Maria Jesús y Raúl (M.J. González y R. Martin), con vosotros he conversado mucho de óptica, profesión, dudas, no sé, de todo, buenos profes, buenos ejemplos. Y, mi Lurdes y su sonrisa, qué decir.

No me olvido de Leti (y su family), Mikel (M. Aldaba), Victoria (V. de Juan), Anita (Cis), Cristina, Gema, Henar, MJ, Paco y Jorge, María (Niño, mi niña y su pequeño Mateo), Elena (Alonso), Lauri (Herrero, ¿una de Catan?), Saad (paga Antonio), Antonio (el que paga), entre otros tantos amigos de clase y profesión. Aurori, Karen, Javi, Alfonso. Mis compañeritos de piso, os quiero mucho. A los Mena, ellos siempre se han preocupado y con ellos he aprendido (Itzi, Iratxe, Jon, Arrieta, Toño, Yolanda, Ana, Carmen).

Los de toda una vida. Nelson, Juan, Agus, Óscar, Diego, JL, Ra, Rober, Sergio, Samu, Sino, Cucu, Nano, Api, Pableras y Jorge. A todos, a vuestras parejas, familias y peques que están y que vienen, tengo la gran suerte de decir que tengo unos amigos estupendos, que yo no soy sin ellos, que sin ellos mi vida hubiera sido tremendamente aburrida y que con ellos soy feliz.

Mi familia (Cipriano, Adriana, Victoria, Resu, Leandro, Marta y Luís, Panin, Jesús, Olga, Jose, Miluca, Jesús, Ana, Olgui, Miguel, Joel y Keko, Bea, Tino, Álvaro y Adriana, Jesús y Balta). Olgui, aunque todo esté perdido siempre nos queda molestar. A mis estupendos suegros, cuñados y sobrinos, Rodolfo e Isa, Josemi, Laura, Álvar y Carla, Javi que me abrieron las puertas de su casa y juntos hemos formado un nuevo hogar y una vida.

Mi hermanito, David. Tú me llamas, así, hermanito, pero, aunque no lo parezca en realidad, soy el mayor. Me da pena que ya no seamos tan pequeños, que ya no juguemos, riñamos y lo arreglemos, las diapos de Félix Rodríguez de la Fuente. Tú has estado ahí cuando lo he necesitado. Muchas gracias, David.

Mis padres. Recuerdo que en el tercer año de instituto, en una encuesta había una pregunta relacionada con la profesión de mi padre, y yo contesté que era “trabajador”. Ya con el paso de los años, ante el asombro del profesor de filosofía, no puedo más que reafirmar aquella respuesta y añadir que es un trabajador de la vida. Ha trabajado el campo, el azúcar, las máquinas y, ahora, su casa, su huerta, sus gallinas, su ilusión. Y, además, ha aplicado el método científico durante toda su vida, el método aplicado a las pequeñas cosas con su observación y sus resultados. Mi madre, Ramoni, es una luchadora, una “corredora” de fondo, la persona más valiente que conozco, siempre cuidando de todo, de todos, de manera infatigable. De mi familia tengo un cariño y un apoyo inagotable. Me han dado el amor a la vida y la educación, ante esto, solo me puedo quitar el sombrero y agradeceros todo.

De la forma más inesperada, a veces, aparece un número con significado (especial o no). En este caso fue el dos. Dos minutos, tarde. Dos días, una cita. Dos meses, quédate a mi lado. Dos años, y una vida. Una hermosa casualidad, dos aes y un nombre palíndromo, Ana. Un día (el dos) abriste la puerta de abajo y las baldosas del suelo me propusieron una mágica partida de ajedrez. Desde ese momento subir a casa se convierte en una trepidante aventura. Ahora (año dos) escribo estas líneas en el lugar de estudio compartido y no quiero salir. Ana, contigo quiero viajar a Ítaca, sentarme en cualquier sitio y echar la vista atrás, recordar este tiempo, a tu lado. Todo futuro es maravilloso.

Pablo Pérez-Merino
Divino Pastor, 20 de septiembre de 2015 *(2015, International year of light)*